Kobe University Repository : Kernel

PDF issue: 2024-07-08

Magma ascent processes inferred from microlite and vesicle textures of the ejecta from the 1914-1915 eruption of Sakurajima volcano

中村, 敬介

(Degree)
博士（理学）

(Date of Degree)
2006-03-25

(Date of Publication)
2012-06-05

(Resource Type)
doctoral thesis

(Report Number)
甲3542

(URL)
https://hdl.handle.net/20.500.14094/D1003542

※ 当コンテンツは神戸大学の学術成果です。無断複製・不正使用等を禁じます。著作権法で認められている範囲内で、適切にご利用ください。

PhD Thesis

Magma ascent processes inferred from microlite and vesicle textures of the ejecta from the 1914-1915 eruption of Sakurajima volcano

(桜島 1914-1915 年噴火噴出物におけるマイクロライトと気泡組織から見たマグマ上昇過程について)

平成　　18 年　　1 月

神戸大学大学院自然科学研究科

学籍番号：011d860n

中村　敬介

Abstract

Vesicle and microlite textures of volcanic ejecta may record vesiculation, degassing and crystallization processes of magma during eruption. Efficiency of degassing depends on decompression rate of magma, indicating that vesicularity changes in response to decompression rate. Microlite crystallization takes place during magma ascent due to volatile exsolution and accompanying increase in liquidus temperature. There is a time lag between volatile exsolution and accompanying crystallization microlite, resulting in the variation of microlite texture in response to the magma ascent process. Textural changes of plagioclase microlite in the volcanic products erupted at the 1914-1915 eruption of Sakurajima volcano and were investigated. The aim of this study is to examine magma ascent process from vesicle and plagioclase microlite texture.

There is a linear correlation between logarithms of population density and crystal size of plagioclase microlite. Marsh (1998) suggested that exponential increase in nucleation rate despite of the same growth rate in closed system caused linear correlation. On the other hand, Eberl et al. (1998) showed that size-dependent growth and growth dispersion of nucleated crystals caused various relation between logarithms of population density and crystal size. Textural changes of plagioclase microlite in the run products of 1-atmosphere melting/crystallization experiments using the pressed powder of scoria erupted at the 1707 eruption of Mt. Fuji were analyzed to examine how linear correlation between logarithms of population density and crystal size of plagioclase microlite produces in the closed system.

The 1914-1915 (Taisho) eruption of Sakurajima volcano, Kyushu Japan continued for about 1 year, and erupted Plinian fall pumice, followed by extrusion of lava flows in three periods (Taisho 1 lava, Taisho 2 lava and Taisho 2' lava, respectively). Firstly, Geological feature and stratigraphy of the deposit, chemical feature of the volcanic products, magmatic condition and pre-eruptive melt compositions were investigated in chapter 3 and chapter 4, respectively. Classification of volcanic products in terms of microlite, vesicle texture and pre-eruptive melt compositions were conducted in chapter

5. Finally, the relations between textural changes of microlite and magma ascent process were discussed by the observed texture and the results of previous decompression experiment in chapter 5.

The column height of Plinian phase of the eruption estimated from isopleth of Plinian fall deposit and average bulk density (c.a. 770 kg/m^3) of Plinian fall pumice of total 350 pumices by the method of Carey and Sparks (1986) is 15-18 km. The magma discharge rate estimated from the method of Sparks (1986) is 5×10^3 m^3/s. Total volume of the deposit estimated from isopach map by the equation of Hayakawa (1985) is 0.29 km^3 (DRE). The thickness of the Plinian fall deposit located at about 4 km east from Minami-dake is c.a. 2 m. Most pumices collected from the deposit in the lower to middle parts of the deposit (0-1.5 m) show white in appearance with low bulk density (700 kg/m^3). In addition to white pumice, darker colored pumices with high bulk density (>1000 kg/m^3) are observed in the upper part of the deposit (1.5-2.0 m).

The phenocryst assemblage is almost the same in all volcanic products. It is plagioclase + orthopyroxene + augite + magnetite. Olivine phenocrysts (microphenocrysts) are present slightly in Taisho 2 and 2' lavas. SiO_2 contents of bulk-rock compositions of all volcanic products is in range of 62-59 wt.%. An contents of core of plagioclase phenocrysts show the bimodal distribution around An_{85} and An_{58}. Orthopyroxene and augite can be divided into two types in terms of their Mg# of core, low Mg# orthopyroxene (Mg#<66: type-B opx) and high Mg# orthopyroxene (Mg#>66: type-A opx). Augite phenocryst can be divided into three types according to the Mg#, low Mg# augite (Mg#<69: type-b cpx), relatively high Mg# augite (69<Mg#<75: type-a cpx) and high Mg# augite (type-c cpx) included in Taisho 2 and Taisho 2' lava. Olivine phenocryst can coexist only type-c augite. Pre-eruptive melt composition change from silicic (SiO_2 = 70 wt.%) to basic (SiO_2 = 62 wt.%) from Plinian and Taisho 1 phase to Taisho 2 and Taisho 2' effusive phase due to magma mixing, suggesting it not suitable to compare magma ascent process of Taisho 2 and 2' lavas with others. Difference among white pumice, darker colored pumice and Taisho 1 lavas is due to the difference of decompression rate.

White pumices are classified into two types according to vesicularity and

plagioclase microlite texture. Type-1 is white Plinian fall pumices with high vesicularity (>60 vol.% estimated from mapping image) low modal content and number density of the microlite (modal content <1.0 vol.% or number density $<10^{14}$ m^{-3}) with small size variation less than 30 μm. Type-2 is white Plinian fall pumices with high vesicularity (>55 vol.%), intermediate modal content (1.0-11 vol.%, 30-100 μm length) and number density ($1\text{-}10\times10^{14}$ m^{-3}) of the microlite. Darker colored Plinian fall pumices show low vesicularity (25-50 vol.%), intermediate to high modal content (8-16 vol.%, 30-100 μm length) and number density ($5\times10^{14}\text{-}2\times10^{15}$ m^{-3}) of the microlite. Lava flows show low vesicularity (< 25 vol.%, about 100 μm length), high modal content (>16 vol.%) and intermediate number density ($1\text{-}5\times10^{14}$ m^{-3}) of plagioclase microlites. Hence, volcanic products are classified into type-1, -2 and -3 pumice and lava flows according to vesicularity and plagioclase microlite texture.

Decompression induced crystallization experiment using rhyolitic melt indicate that modal content and number density of microlite change in response to amount of decompression (ΔP) and decompression rate ($\Delta P/\Delta t$). Efficient nucleation takes place during 4 hours (Couch et al., 2003). Residual water contents in Plinian fall pumices are c.a. 0.4 wt.% despite of pumice type, suggesting that ΔP of all pumices is almost the same. Effective degassing occurred from type-1 to type-3 pumices. Degassing takes place effectively as decompression rate of magma decrease, indicating that decompression rate of magma decrease from type-1 pumices to type-3 pumices.

Combined with previous decompression experiments, stratigraphy of the volcanic products and microlite and vesicle texture of volcanic products, early to middle stage of Plinian phase, type-1 and type-2 white pumices mainly erupted at the same time at the highest decompression rate during the whole phase of the eruption. Textural variations of microlite between type-1 and type-2 reflect the slight difference of decompression rate of magma, perhaps due to the difference in center of conduits and near the margin of conduits (e.g., Taddeucci et al., 2004; Gurioli et al., 2005). Type-1 pumices ascended in the center of conduit. Type-2 pumices ascended in the margin of conduit slightly slightly lower decompression rate than type-1 pumice, , resulting in more modal content and number density of plagioclase microlite in type-2 pumices in spite of the

almost same vesicularity.

Late stage of Plinian phase, the proportion of type-1 and type-2 white pumices decrease and type-3 darker colored pumice erupted. The difference of type-1 and type-2 white to type-3 darker colored pumice reflects the decrease in decompression rate. Type-1 and type-2 white pumice erupted at late stage of Plinian phase may represent the magma ascended rapidly in the center of conduit. Type-3 pumices with the highest number density of microlite show vesicularity of around 40-50 vol.%, indicating that nucleation of microlite occur effectively during late stage of Plinian phase. Decrease in microlite number density and change of CSD slope from steep to shallow within type-3 pumices is in proportional to the decrease in vesicularity, expect the most vesicular type-3 pumice. Number density of microlite of least vesicular type-3 pumices is the almost same as those of lavas, indicating that decompression rate decrease continuously from late stage of plinian phase to Taisho 1 lava effusive phase and that crystallization process change from nucleation-dominated crystallization to growth-dominated crystallization during late stage of Plinian phase in type-3 pumices or Taisho 1 lava effusive phase.

In the late stage of effusive phase, pre-eruptive melt composition of magma became basic due to magma mixing, suggesting it not suitable to compare the change of decompression rate with the others in terms of microlite texture. The effect of chemical change of pre-eruptive melt, however, reflect not plagioclase microlite texture but the An content of plagioclase microlite.

In chapter 6, 1-atmoshere closed system melting/crystallization experiments were conducted by using pressed powder of scoria erupted at the 1707 eruption of Mt. Fuji to examine textural change of microlite with time. Modal content and number density of plagioclase microlites in the run products quenched to 1120 ℃ or 1170 ℃ from initial melting temperature (1200 ℃, 1220 ℃, 1227 ℃ and 1235 ℃) show rapid increase in short time during cooling period (within 8 minutes). Modal contents of plagioclase microlite slightly increase and number density of microlite slightly decrease during the annealing period of constant temperature around 1120 ℃ or 1170 ℃. These results indicate that crystallization processes are divided into two processes. The first process

is nucleation-dominated crystallization. Growth of nucleated microlite, i.e., growth-dominated crystallization is the second process of crystallization. During the period of nucleation-dominated crystallization, nucleation and growth dispersion of nucleated microlite cause linear shape of CSD with steep slope. Change of CSD slope from steep to shallow and decrease in intercepts of CSD occurs during the period of growth-dominated crystallization. These changes of the shape of CSDs from step to shallow with time are the results of growth dispersion and size-dependent growth of microlite.

Acknowledgement

I wish to express my sincere gratitude to Professor Hiroaki Sato for critical comments, fruitful discussions, teaching analytical and experimental technique and encouragements throughout this study. I learned so much from his indepth knowledge of earth science.

I would to thank to Dr. Keiko Suzuki-Kamata for useful comments, encouragements and interesting talks about volcano and so on.

I would to acknowledge to Professor Kozo Uto, Professor Yoshiaki Tainosho and Professor Noboru Nakamura for their counsel and valuable comments on this thesis, and encouragements.

I would to acknowledge to Dr. Naotaka Tomioka, Dr. Ichiro O-nishi, Dr. Jun-ichi Ito and Mr. Mitsuhiro Sugita for cooperation for EPMA analyses and useful comments.

I would to thank to Dr. Tatsuo Kanamaru, Dr. Toshio Arai and Mr. Yu-ta Matsuo for XRF analyses.

I would to acknowledge Dr. Daisuke Fukushima, Professor Tetsuo Kobayashi, Professor Kazuhiro Ishihara and all the members of Sakurajima volcano research members of Disaster Prevention Research Institute Kyoto University during field observation.

I would to thank all the members of volcanology group in Kobe University for their discussions and encouragements.

Contents

Chapter 1: Introduction

Difference in eruption styles such as Plinian explosion versus lava effusion has been considered to reflect different modes of magma degassing (i.e., volatile exsolution and expansion and open system gas separation from melt) (Eichelberger et al.,1986; Jaupart and Allegre,1991). Jaupart and Allegre (1991) numerically showed that slow ascent of magma allows efficient magma degassing, resulting in effusive eruptions, whereas fast ascent of magmas prohibits the efficient magma degassing, resulting in explosive eruptions. Most of volcanoes, which consist of silicic magma, shifts eruption style from explosive to effusive in a single eruption, suggesting that modes of magma degassing change during eruption. Textures of volcanic products such as color, vesicularity, vesicle texture and microlite texture and chemical feature of these such as bulk rocks, groundmass glass and mineral chemistry record various phenomena occurring during the eruption. Magma mixing or mingling processes during the explosive eruption are recorded in the color and chemical heterogeneity of bulk rock and/or groundmass glass of volcanic products. For example, chemically and texturally heterogeneous clasts erupted at the 79 AD eruption of Vesuvius during Plinian phase of eruption due to magma mingling (Gurioli et al., 2005). On the other hand, Gardner et al. (1998) suggested that difference of decompression rate and degassing processes reflected the textural difference such as vesicularity, color, and microlite texture in spite of almost the same chemical feature at the 1992 eruption of Crater peak. Vesicle number density is proportional to the 3/2 power of decompression rate for homogeneous vesicle nucleation (Toramaru, 1995). Vesicularity of volcanic products changes in response to degassing process; i.e., closed-system gas expansion or escape of gas from the system (Martel et al., 2000). Moreover volatile exsolution from melt increases the liquidus temperatures of melt and consequently sometimes induces crystallization of microlite (Hammer and Rutherford, 2002; Couch et al., 2003; Martel and Schmidt, 2003). According to the previous decompression experiments, number density and modal content of microlite change drastically in response to amount of decompression (ΔP) and decompression rate ($\Delta P/\Delta t$) relating to magma ascent rate, suggesting that

vesicle and plagioclase microlite texture reflect the magma ascent and degassing process.

CSD (Crystal Size Distributions) and VSD (Vesicle Size Distributions) are one of the common methods to describe quantitatively the texture of minerals and vesicle in the rocks. Shape of VSD plots reflects vesiculation and degassing process of vesicle during magma ascent (e.g., Simakin et al., 1999; Blower et al., 2001; Blower et al., 2002). The relation between crystal size and number density of crystal; the relation of slope and intercept of CSDs, record various phenomena during crystallization (e.g., Hammer et al., 1999).

At first, author reviewed the previous studies of CSD, especially, in term of the factors that determine the shape of CSD plot and the relation between size and number density of crystals and reveals the feature in CSD of plagioclase microlite in volcanic products in chapter 2. Then, author discussed the significance in investigating the CSD of plagioclase microlite to understand the magma ascent process and the unsolved problem about CSD studies.

The 1914-1915 (Taisho) eruption of Sakurajima volcano, Kyushu Japan, represents the largest eruption in the last 400 years in Japanese volcanoes, and continued for about 1 year, erupted Plinian fall pumice, followed by extrusion of lava flows in three periods (Koto, 1916). These volcanic products are expected to have different microlite and vesicle textures. The main aim of this study is to reveal magma ascent process in terms of vesicle and microlite textures.

Author investigated geological features of Plinian fall pumices, Taisho 1 lava, Taisho 2 lava and Tasiho 2' lava in chapter 3. Author also estimated the eruption column height and eruption rate of the Plinian phase of the eruption by using the methods of Carey and Sparks (1986), Sparks (1986) and computer program, conflow (Mastin and Ghiorso, 2000: USGS Open file and http://volcan.wr.usgs.gov/Projects/Mastin/), which are meaningful data in discussing decompression rate of magma in the conduit.

Magmatic conditions in the magma chamber and during magma ascent are important factors in discussing magma ascent processes. Magma mixing processes,

volatile content, magmatic temperature, and melt composition related in melt viscosity may affect the conditions of microlite crystallization. In chapter 4, magmatic conditions were estimated by analyzing whole rock, glass and mineral composition of these products.

Next I demonstrated the difference of textures of the explosive and effusive eruption products of the 1914-1995 eruption of Sakurajima volcano in terms of texture of plagioclase microlites (modal content, number density and CSDs) and texture of vesicle (vesicularity, VSDs, vesicle number density) of the volcanic products and discussed the relative change of decompression rate.

Finally, author experimentally produced microlite texture by using pressed powder of scoria erupted at the 1707 eruption of Mt. Fuji and discussed time-dependence change of microlite texture, CSDs growth-dispersion, and size-dependent growth of plagioclase microlite.

Chapter 2: Previous studies about CSD (Crystal Size Distribution)

2.1 Introduction

In this chapter, I review the previous studies about CSDs. Articles on CSDs are classified into 4 types: (1) theory of CSDs, (2) analyses method of CSDs, (3) estimating of nucleation and growth rate by analyzing CSDs and (4) discussing the cause of change of CSD plots.

Articles on (1) are explanation about theological equation of CSDs (Marsh, 1988; Marsh, 1998), the correlation between the system in which crystallization occur and crystallization mechanism (Morishita, 1992; Morishita, 1995), the relation between growth-dispersion of crystals and change of CSDs (Eberl et al., 1998) and correlation between intercept and slope of CSDs (Zeig and Marsh, 2002).

Textural data available from slab or thin sections are 2-dimengional data. Articles on (2) deal with the methods to convert 2-dimensional data to 3-dimensional data (Higgins, 1994; Peterson, 1996; Sahagian and Proussevith, 1998 and Higgins, 2000).

There is commonly linear relation between Ln (n) (logomachies of population density) and size of crystal about CSDs. Articles on (3) are to estimate nucleation and growth rate of crystals by using theological equation for steady state open-system proposed by Randolph and Larson (1971). Cashman (1992), Crips et al. (1994) and Hammer et al. (1999) estimated crystallization time according to the record of eruption sequence. Cashman and Marsh (1988) and Burkhard (2002) calculated crystallization time by the thermal model. Higgins (1996a) or Nakagawa et al. (2002) correlated CSDs or crystal size to the growth rate estimated by these studies and estimated the residence time of magma in the magma chamber.

Recently, studies about CSDs are focused on the shape of CSD plots, how the kinked CSDs generate and the difference of CSDs cause in the same outcrop with different morphology (for example difference of surface and center of thick lava, sill and complex, lava flow and Plinian fall pumice in the single eruption.), which are

associated with (4).

In this chapter, I focus on the change of CSDs. Marsh (1998) discussed that exponential increase in nucleation rate caused various types of CSDs such as linear and kinked CSDs. Models of Marsh (1998), however, assume that growth rate of crystals is nearly constant regardless of change of temperature. Recently, new models about the change of CSDs have been proposed (Eberl et al., 1998; Taddeucci et al., 2004). According to the models of of Eberl et al. (1998), change of growth rate, growth dispersion and size-dependent growth of crystals cause the various change of the shape of CSD plots.

I review the theory of CSDs briefly and review at first. Then I discuss how kinked CSDs could be proposed and that how slope and intercept of CSDs change, especially in terms of the chemical and physical change of magma. Finally I estimate the relation between the slope and the intercept of CSD (size and number density of crystal), reveal the characteristic feature of microlite and discuss the significance in investigating the CSD of plagioclase microlite to understand the magma ascent process and the unsolved problem about CSD studies.

2.2 **Theory of CSD (Crystal Size Distribution)**

CSD (Crystal Size Distribution) is useful to discuss the textures of igneous rocks quantitatively, especially the relation between crystal size and number of crystals. Logomachis of (n: population density) is plotted against crystal size (L). In open-steady system, population density of crystal is expressed as a function of crystal size (L) as follow (Marsh, 1988);

$$n = n^0 \exp(-L/G\tau) \quad (2\text{-}1)$$

Equation (2-1) is rearranged by taking natural logarithm,

$$\ln(n) = \ln(n^0) - L/G\tau \quad (2\text{-}2)$$

where, G is growth rate of crystal. n^0 is population density of size class 0 (nucleation density). τ is crystallization time. Equation (2-2) indicates that there is a linear correlation between In (n) and L. $G\tau$ expresses the average size of crystal.

Nucleation rate (J) is defined as follow;

$$J = n^0 * G \quad (2\text{-}3)$$

Marsh (1998) tried to explain the cause of change of CSDs in terms of change of nucleation rate, chemical and physical condition of melt and change or difference of the system of crystallization. Characteristic of Marsh (1998)'s model is that growth rate of crystal is nearly constant against change of temperature and that nucleation rate increase exponentially against the increase in temperature.

On the other hand, Eberl et al. (1998) suggest that change of both nucleation and growth rate of crystal and dispersion of growth of crystals affect the shape of CSDs. Eberl et al. (1998) discussed the dispersion of growth rate and degree of dispersion based on LPE effect (Law of Proportionate Effects) (for more details see Eberl et al. (1998)) cause the change of the shape of CSDs.

CSD of natural samples commonly show linear correlation between In n and L in relatively small size class (Cashman, 1992; Hammer et al., 1999). According to the increase in size class of crystal size, CSDs, however, tend to be convex upwards (e.g., Tomiya and Takahashi, 1995; Morrissey, 1997; Higgins, 2002). In the case of the same outcrops, intercept and slope of CSDs change in response to the occurrence and morphology of samples (for example, from surface to inner part of a lava flow, basement to central part of a complex and pumice, pyroclastic deposit and lava flow of a cycle of eruption).

2.3 **Change of CSDs caused by the change of chemical and physical conditions of melt**

There are three reasons to generate the nucleation, growth, and resorbing of crystals;

1) increase in magmatic temperature above liquidus temperature or decrease of magmatic temperature below liquidus temperature,

2) change of melt composition,

3) decrease or increase in H_2O content of magma.

These chemical or physical changes of magma affect the crystallization process such as nucleation, growth of crystal and resorbing of crystal. In the case of thick lava flows or complex, slow cooling of magma affects the change in CSDs in response to stratigraphy. On the other hand, magma mixing in the magma chamber, crystal settling and compaction of crystals also affect the shape of CSDs. I discuss how these conditions of magma occur and affect the shape of CSDs

2.3.1 **Magma mixing**

One of the features of many volcanoes is magma mixing between silicic low temperature magma and basic high temperature magma.

Tomiya and Takahashi (1995) compared the CSDs of plagioclase of Us-b Plinian fall pumice erupted at the 1663 eruption Usu volcano with those of Ko-Usu lava dome sample erupted at the 1769 eruption Usu volcano. CSDs of plagioclase with low An content (type-A) included in Us-b show gentle slope. Plagioclase included in crystal clots of Ko-Usu samples (type-C) show relatively high An content. CSDs of them have steep slope and their size is smaller than the type-A plagioclase. CSDs of plagioclases included in Ko-Usu (type-A and type-C) show concave up and characteristic of both of CSDs of Us-b and of the type-C crystal clots (Fig. 2-1). Tomiya and Takahashi (1995) suggested that origin of plagioclases CSDs of gentle slope part of larger size was derived from the silicic low temperature magma. They thought that plagioclases of small size with steep slope were nucleated due to the rapid cooling of high temperature magma during the injection of high temperature magma into the low temperature magma within the magma chamber after the 1663 eruption. The same kind of discussion is done by Higgins (1996a) who analyzed CSDs of plagioclase included in dacitic lava erupted at Mt. Kameni during the past 2000 ys.

Higgins and Roberge (2003) analyzed CSDs of plagioclase included in matrix from andesite of Soufriere Hills volcano. CSDs of plagioclase included in matrix show slightly concave up. Higgins and Roberge (2003) suggested that concave up CSDs were generated by Ostwald ripening process induced by repeated magma mixing.

A steep, straight CSD developed by nucleation and growth of crystals during cooling of andesite magma in the magma chamber. Injection of hotter mafic magma into the magma chamber caused solution of small crystals and growth of large crystals (Ostwald ripening). During this period, CSD became less steep and extended to larger crystal sizes (Fig. 2-2).

Amma-Miyasaka and Nakagawa (2002) analyzed CSDs of plagioclase and olivine from the volcanic products (essential and xenoliths) erupted during the 1940 eruption at Miyake-jima. CSDs from zenoliths are gentle slope and their size is large. CSDs from essential products were steep slope and their sizes were small. Plagioclase and olivine CSDs from the products, which were mixed with essential and xenoliths, are concave up.

In summary, one reason for change in CSDs is that crystallization processes change due to change of melt compositions or magmatic temperature due to magma mixing (e.g., Tomiya and Takahashi, 1995; Higgins, 1996a; Higgins and Roberge, 2003). The decrease in magmatic temperature during cooling period yields nucleation, resulting in steep CSDs. The increase in magmatic temperature due to injection of hotter magma into magma chamber leads to solute of small crystal and growth of large crystal, resulting in gentle CSDs. The other reason for change of CSDs is that mixing of magmas (or magma and xenoliths) with different size and population of crystal makes kinked CSDs (Amma-Miyasaka and Nakagawa, 2002).

2.3.2 **Ostwald ripening**

Higgins and Roberge (2003) suggest that change of magmatic temperature due to magma mixing yield Ostwald ripening of crystal and concave up CSDs. Other kind of discussions about the relation between the shape and change of CSDs and Ostwald ripening are given by Miyazaki (1991), Miyazaki (1996), Higgins (1998), Higgins (2002) and Zeh (2004).

Higgins (1998) divided plagioclase chadacrysts enclosed by olivine into three types in terms of crystallinity of plagioclase (40 vol.%, 50 vol.% and 80 vol.%) and

analyzed CSDs of them from Lac-St-Jean anorthosite complex. Intercept of CSDs decreased and slope of CSDs became gentler in response to the increase in crystallinity of plagioclase chadacryst, suggesting that plagioclase chadacrysts were affected by coarsening (Fig. 2-3). Model of Higgins (1998) is as follows; Increase in undercooling induced nucleation and growth of plagioclase, resulting in linear CSDs. By about 25vol.% solidification, latent heat did not eliminate effectively, resulting in increase in magmatic temperature. Nucleation of plagioclase was inhibited and conditions were suitable for textural coarsening of plagioclase and olivine to occur (Ostwald ripening). The same kind of discussion was done by Higgins (2002).

Zeh (2004) categolized three texturally distinct zones (Z-1 to -3) and in the matrix (Z-4) of garnet-epidote- biotite gneiss from the Moine Supergroup and analyzed CSDs of accessory apatite, titanite and allanite included in each zone (Fig. 2-4). Evolution of CSDs of each mineral was modeled by the model of Eberl et al. (1998). Zeh (2004) suggested that the apatite CSD evolution from Z-1 to Z-4 was consistent with open-system LPE growth accompanied and followed by supply controlled random ripening, whereas that transformation of original titanite CSD was more consistent with Ostwald ripening, temporarily accompanied by McCabe growth, which was a model of size-indipendent growth of crystals proposed by McCabe (1929). Zeh (2004) suggested that the allanite CSDs also pointed to Ostwald ripening between Z-3 and Z-4. The evolution of CSDs of accessory minerals is influenced by reaction with surrounding rock-forming minerals, deformation, coarsening of matrix and increase in temperature. Zeh (2004) thought that fast nucleation and growth of accessory minerals during Z-1 was initiated by contact metamorphism, whereas that subsequent growth and annealing (Z-2 to -4) resulted from regional metamorphism event.

Miyazaki (1991) investigated the relation between compositional zoning and crystal size of garnet and between CSDs and spatial distribution of garnet from the Nagasaki metamorphic rocks in the Nomo and Nishisonogi peninsulas. Core compositions of garnet are constant regardless of size variation, suggesting that most of crystals nucleate at the same time and size variation is due to Ostwald ripening. Miyazaki (1991) divided CSDs of the garnet into two types. The CSD of first type is

consistent with theological prediction of LSW distribution. The CSD of second type is wider than theological prediction. The later one shows heterogeneous spatial distribution such as in cluster or layer. Miyazaki (1991) suggested that the heterogeneity of spatial distributions results in a heterogeneity of concentration of garnet, causing the wide distribution.

According to the simulation of Miyazaki (1996) about the relation between stratigraphy and CSDs, in the case of two-layer system consisting of smaller mean size layer (S-layer) and larger mean size layer (L-layer), final CSDs of each layer depend on the initial size distribution in each layer (Sd_{g0}). When the standard deviation of the initial size distribution of each layer is small, mass transport from the S-layer to the L-layer is more likely to occur. On the other hand, as Sd_{g0} become larger, the mass transport becomes slower, and Ostwald ripening takes place within each layer rather than between layers. CSD of crystals in the S-layer becomes more symmetric and wider than a Lifshitz-Slyozov-Wagner (LSW) distribution due to removal of the solute from the S-layer. On the other hand, CSD of crystals in the L-layer approaches the LSW distribution.

Ostwald ripening is a reason for the change of shape of CSDs. Fluctuation of magmatic temperature may cause nucleation, growth and resorbtion of crystal, causing the Ostwald ripening. Homogeneity or heterogeneity of spatial distribution of crystal and difference of CSDs between layers affect the degree of Ostwald ripening; i.e., a kinds of self-organization of crystal (Nishiyama, 1991), resulting in the difference in shape of CSDs.

In summary, magma mixing, effect of latent heat and metamorphism induce the increase in temperature, resulting in gentle CSDs due to Ostwald ripening.

2.3.3 **Change of melt composition, crystal settling and compaction of crystal**

Higgins (2002) illustrated that crystal size became smaller from basement to critical zone by analyzing CSDs of plagioclase, olivine and clinopyroxene from the Kiglapait intrusion and suggested that variation of CSDs was mainly due to Ostwald

ripening. Higgins (2002) indicated that there was a possibility of settling and compaction of large crystal.

Boorman et al. (2004) categorized Group 1 to Group 4 in terms of texture and stratigraphy and measured CSDs of orthopyroxene and plagioclase from Bushveld complex, South Africa. CSDs of orthopyroxene revealed that crystal size became smaller from basement to critical zone due to the settling and compaction of large crystals, which crystallize first from the melt (Fig. 2-5). By the time magma cooled till the liquidus temperature of plagioclase, melt removed from basement to critical zone due to compaction of orthopyroxene.

In the complex, because of large cooling time of magma, there is a possibility of settling and compaction of crystal, resulting that intercept of CSDs decreased and slope of CSDs became gentler from basement to critical zone.

2.3.4 **Difference of cooling rate of magma**

From surface to inner part of lava flow or lava lake, basement to center of sill, which are thinner compared with complex, there is a tendency for variation of CSDs. Wilhelm and Worner (1996) illustrated the correlation between stratigraphy and rock texture by analyzing CSDs of plagioclase from basaltic or andesitic flow (Colonnade flow), complex (HiTi-unit) and sill (Thumb Point Sill) spreading in Victoria Land. Cashman and Marsh (1988) revealed that slope of CSDs of plagioclase, ilmenite and magnetite became steep according to the increase in depth from the surface from the Makaopuhi lava lake, Hawaii. Burkhard (2002) suggested that slope of CSDs of plagioclase, pyroxene and Fe-Ti oxide microlite became gentler from surface to inner part of basaltic pahoehoe lava flow erupted at Pu' u O'o-Kupaianaha eruption (Fig. 2-6).

These changes of CSDs are thought to be due to the difference of cooling rate from surface to center of lava flow, resulting in the difference of growth time of crystals.

2.3.5 **Change of nucleation rate**

Concave down CSDs of chlorite at small size part are observed from chromitite layer spreading Gabbronorite Zone I , Stillwater complex (Fig. 2-7a) (Waters and Boudreau, 1996). The same kinds of CSDs are observed CSDs of garnet in politic rocks from the chlorite, garnet and sillimanite zones of the Waterville Formation (Cashman and Ferry, 1988) (Fig. 2-7b). CSDs of these types are interpreted to be the results of two processes: 1) initial continuous nucleation and growth of crystals, and 2) later loss of small crystals due to annealing (Cashman and Ferry, 1988).

Cashman and Ferry (1988) revealed that CSDs of olivine, pyroxene and magnetite from Isle of Skye showed linear correlation between In (n) and crystal size due to one process: continuous nucleation and growth of crystals.

The difference of concave down CSDs and linear CSDs reflect the difference in the thermal histories of regional vs. contact metamorphosed rocks. Contact metamorphism involves high temperature for short durations, resulting in linear CSDs. On the other hand, regional metamorphism involves prolonged cooling from high temperatures, primary linear CSDs are later modified by annealing to concave down shapes (Cashman and Ferry, 1988).

Sato (1995) remarked that the difference in CSDs of microlite between pahoehoe lava erupted at the 1781 eruption at Izu-Oshima and LA aa lava erupted at the 1986 eruption at Izu-Oshima, in spite of almost the same chemical composition (Fig. 2-8a). One-atmosphere melting/crystallization experiment on the lavas showed that a 20 ℃ difference in initial-melting temperature near liquidus temperature can cause the difference of nucleation processes between homogeneous nucleation and heterogeneous nucleation and the large difference of CSDs of run products (Fig. 2-8b).

2.3.6 **Increase in liquidus temperature**

Armienti et al. (1994) revealed that CSDs of plagioclase, olivine and magnetite from the volcanic product of the 1991-1993 eruption, Mt Etna become kinked around 300μm or 500μm. Previously, I discuss that magma mixing induces nucleation and kinked CSDs. Armienti et al. (1994), however, proposed that magma ascent cause the

kinked CSDs; high nucleation condition occurs during magma ascent. H_2O in the melt affect the liquidus temperature of plagioclase. Recent decompression induced crystallization experiment revealed decompression cause the uprise of liquidus temperature and cause to crystallize a lot of microlite (Hammer and Rutherford, 2002; Couch, 2003; Couch et al., 2003). Significant characteristic of microlite is small size and large number of crystals, compared with phenocryst. Previous analyses of microlite CSD were done by Cashman (1992), who analyzed microlite CSDs of the Plinian fall pumice and lava dome samples from the 1980-1986 eruption of Mt. St. Helens (Fig. 2-9a), Hammer et al. (1999), who measured microlite CSDs of the pre-climactic volcanic products from the 1991 eruption of Mt. Pinatubo (Fig. 2-9b) and Taddeucci et al. (2004), who analyzed CSDs of plagioclase, olivine, pyroxene and magnetite microlite of volcanic ash erupted at the 2001 eruption of Mt. Etna. Results of these studies indicate that intensity of eruption (explosive vs. effusive) affect the CSDs of plagioclase microlite. In the case of explosive eruption such as Plinian, variation of microlite texture is large; some samples have no microlite and others have a lot of small microlite (Cashman, 1992; Hammer et al., 1999; Taddeucci et al., 2004). In the case of lava effusive eruption, relatively small amount of large microlites nucleate and grow, resulting in gentle CSDs (Cashman, 1992).

Variation of CSD, number density and size of microlite is thought to be the difference of volatile exsolution process during magma ascent.

2.4 **Discussions**

2.4.1 **Comparisons of previously established CSDs**

(1/Slope; $G\tau$) and (intercept; Ln (n^0)) of CSDs represent the size and number density of crystals, respectively. The relation between intercept and 1/(slope) is, therefore, useful to interpret the texture of the rocks. There have been some attempts to discuss the textural change based on the intercept and slope of CSDs (Marsh, 1998; Petrick et al., 2003; Boorman et al., 2004). These studies reveal the negative relation

between slope (n^0) and 1/(slope) ($G\tau$) of CSDs in the same samples. There is no discussion of the relation between n^0 and $G\tau$ among all kinds of rocks or minerals. Hence, analyzed data of plagioclase CSDs were compared with other data. Intercepts of CSDs (Ln (n^0)) were plotted against Ln ($G\tau$) (Fig. 2-10a and 10b). Origin of CSD data, rock type and mineral type were summarized in Table 2-1.

2.4.1.1 **The relation of the intercept and slope of CSDs**

Intercept of CSDs compiled is Ln (n^0; population density; number density of crystals of class sizes 0). In the case of volcanic rocks, there is a linear correlation between Ln (n^0) and Ln ($G\tau$) despite of the difference of rock samples or minerals. Number of crystals decrease exponentially as $G\tau$ increases. In the case of kinked CSDs of volcanic rocks, there is a linear relation between Ln (n^0) and Ln ($G\tau$) in both gentle slope parts with large size classes (phenocryst) and steep slope parts with small size classes (microlite) despite of the difference of volcanoes. $G\tau$ of most of phenocrysts or microphenocrysts is in range of 0.002 cm (20 μm) to 0.1 cm (1000 μm) and population density (n^0) of them is in range of e^{10} cm^{-4} (2.2×10^4 cm^{-4}) to e^{20} cm^{-4} (4.9×10^8 cm^{-4}). $G\tau$ and population density of microlite range from 0.001cm (10μm) to 0.00003 cm (0.3 μm), and e^{25} cm^{-4} (7.2×10^{10} cm^{-4}) to e^{38} cm^{-4} (3.2×10^{16} cm^{-4}), respectively. There is also a linear relation between Ln (n^0) and Ln ($G\tau$) in minerals included in the rocks expect volcanic rocks. $G\tau$ and population density of the minerals in most of complex is in range of 0.3 cm (3000 μm) to 0.002 cm (20 μm), and e^3 cm^{-4} (2×10 cm^{-4}) to e^{13} cm^{-4} (6.6×10^7 cm^{-4}), respectively. $G\tau$ in complex is slightly larger compared with $G\tau$ in volcanic rocks and population density in complex is slightly smaller than population density in volcanic rocks. Hematite in pseudotachylytes (Petrik et al., 2003), framboidal pyrite (Wilkin et al., 1996) and accessory apatite, titanite and allanite in a garnet-epidote-biotite gneiss (Zeh, 2004) have similar textural feature with microlite in volcanic rocks. $G\tau$ and population density of the minerals in most of complex is in range of 0.001 cm (10 μm) to 0.0001 cm (1 μm), and e^{20} cm^{-4} (4.9×10^8 cm^{-4}) to e^{36} cm^{-4} (4.3×10^{15} cm^{-4}), respectively. The linear trends of these

minerals overlap the trend of minerals in volcanic rocks.

In summary, there is a linear relation between Ln (n^0) and Ln ($G\tau$) in all minerals of all kind of rocks, suggesting that if number density of crystals is decided, then size of crystals is also determined unique.

There is one exception, which is the CSDs of plagioclase, pyroxene and Fe-Ti oxide from the basaltic pahoehoe lava erupted at the Pu'u O'o-Kupaianaha erutption, Kilauea volcano (Burkhard, 2002). Number density is smaller relative to the crystal size.

2.4.1.2 **Relation between crystal size and number density from the numerical equation**

Previously, Zeig and Marsh (2002) and Petrik et al. (2003) investigate the correlation between the intercept and slope of CSDs. In this study, the negative relation between negative relation between slope log (n^0) and log 1/(slope)($G\tau$) of CSDs are discussed by using the numerical equation of CSDs and modal contents of crystals.

Volumetric number density is gained by integrating the equation of (2-2).

$$Nt = \int n(L)\, dL = n^0 G\tau \qquad (2\text{-}4)$$

Total lengths of total crystals per units volume is

$$Lt = \int Ln(L)\, dL = n^0 (G\tau)^2 \qquad (2\text{-}5)$$

Hence, average length of crystal (Sn) is defined as follows;

$$Sn = Lt/Nt = G\tau \qquad (2\text{-}6)$$

On the other hand, average length of crystal is calculated from the equation of Hammer et al. (1999)

$$Sn = (\varphi/Na)^{1/2} \qquad (2\text{-}7)$$

Volumetric number density per unit volume can be estimated by the equation of Hammer et al. (1999) from average length of crystal and areal number density as follows;

$$Nt = Na/Sn \qquad (2\text{-}8)$$

Assuming that crystal length estimated from equation (2-5) and (2-6) and number density estimated from equation (2-4) and (2-7) are equal, respectively, relation among population density, crystal length ($G\tau$) and modal content is as follows from equation of (2-4), (2-6), (2-7) and (2-8);

$$\varphi = n^0 (G\tau)^4 \qquad (2\text{-}9)$$

Equation (2-9) is rearranged by taking natural log,

$$\ln (n^0) = \ln (\varphi) - 4\ln (G\tau) \qquad (2\text{-}10)$$

Equation (2-10) indicates that there is a linear negative relation between $\ln (n^0)$ and $\ln (G\tau)$.

2.4.2. **Causes of the relation between number density and crystal size**

Crystallization begins from melt when magmatic temperature become below the liquidus temperature of minerals. There are two possibilities for magmatic temperature to be below the liquidus temperature; (1) increase in liquidus temperature due to the decrease in H_2O content in the melt and (2) decrease in magmatic temperature below the liquidus temperature. The difference between magmatic temperature and liquidus temperature i.e., undercooling rate, affects the crystallization processes. In the case of large undercooling, nucleation rate increase, resulting that many small crystals nucleate. On the other hand, in the case of small undercooling, crystallization process is dominated by growth on existing crystal (Swanson, 1977). Reasons for rapid change of undercooling are magma mixing and decrease in H_2O contents due to magma ascent. These changes induce the crystallization of microlite, which is characteristic in volcanic rocks. On the other hand, in the case of complex, migration of magma is within the ground, indicating that it seems to be difficult to decrease the H_2O contents drastically. H_2O is preserved as a hydrous mineral such as hornblende and biotite, which crystallize from melts during slow cooling. Hence, there is rare difference of number density between phenocryst in volcanic rocks and crystals in plutonic rocks, supporting this hypnosis. Difference of crystal size between phenocryst in volcanic rocks and crystals in plutonic rocks is due to whether magma

erupts or not. In the case of complex, slow cooling of magma in the ground induces low undercooling, resulting that growth of pre-existing crystals, Ostwald ripening and nucleation of small number of crystals take place due to equilibrium crystallization. Final textures of rocks show equigranular texture. On the other hand, in the case of volcanic rocks, decompression induced decrease in H_2O content during the eruption or rapid cooling of mafic magma due to magma mixing causes the increase in liquidus temperature, resulting that crystallization pressed in non-equilibrium condition. Final texture of volcanic rocks is porphyritic texture, containing both phenocryst, which is large size with low number density and microlite, which is small size with large number density.

2.4.3 **Significance of studying microlite texture in understanding eruption mechanism**

Microlites in volcanic rocks nucleate maybe during magma ascent due to decrease in solubility of H_2O in the melt. Efficiency of degassing depends on decompression rate of magma. Large decompression rate of magma induce incomplete H_2O exsolution and vesicle growth (Martel and Schmidt, 2003), resulting in incomplete chemical re-equilibration to final pressure. Low decompression rate of magma lead to complete H_2O exsolution and vesicle growth. Hence, it is expected that whether exsolution of H_2O occur completely or incompletely affect microlite texture. Actually, in the case of explosive eruption such as Plinian, variation of microlite texture is large; some samples have no microlite and others have a lot of small microlite (Cashman, 1992; Hammer et al., 1999; Taddeucci et al., 2004). It is thought that large decompression rate of magma lead to incomplete exsolution of H_2O, resulting in incomplete nucleation of microlite. On the other hand, in the case of lava effusive eruption, relatively small amount of large microlites nucleate and grow, resulting in gentle CSDs (Cashman, 1992). Low decompression rate of magma may induce effective degassing of H_2O, resulting in effective crystallization of microlite. Hence, it is important to reveal the stratigraphy of volcanic products and analyze the microlite

texture (CSD) of these volcanic products to understand the eruption mechanism, especially, transition of decompression rate during eruption from Plinian to lava effusive phase.

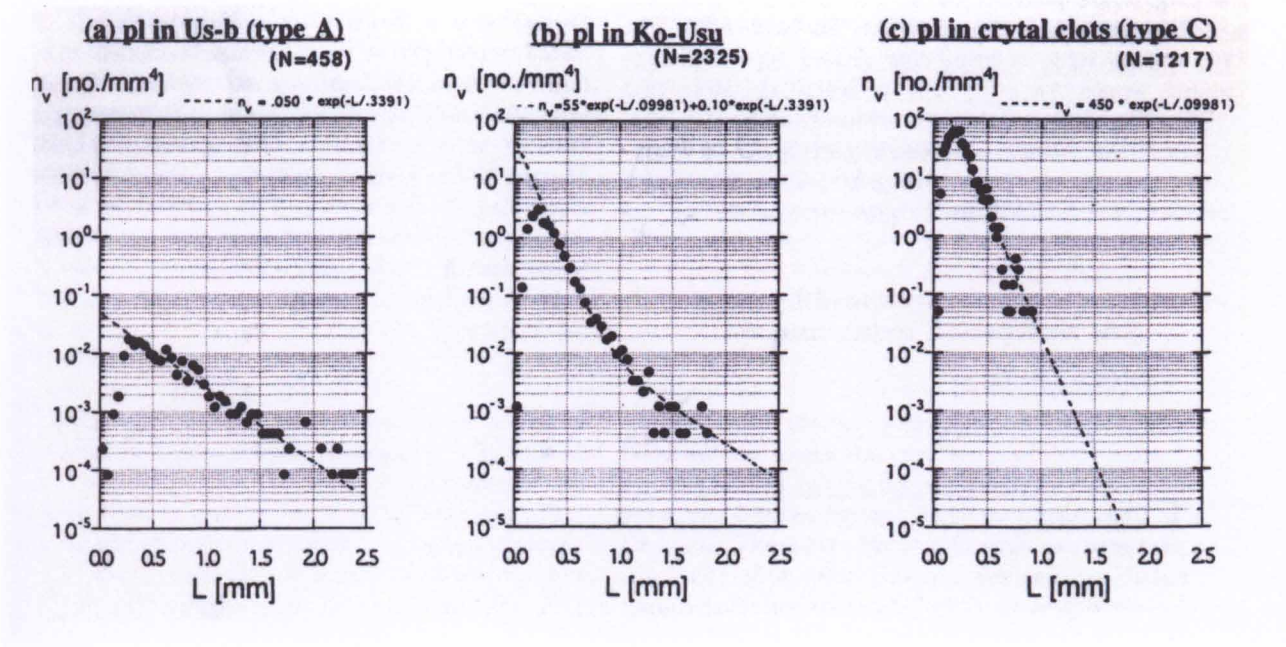

Figure 2-1 Change of CSDs of plagioclase due to magma mixing (after Tomiya and Takahashi, 1995). (a) CSD for plagioclase in Us-b essential fragments (1663). Most of the plagioclase phenocrysts are type-A. (b) CSD for plagioclase in Ko-Usu lava. Most of the plagioclases are type-C, which would have crystallized from a rapidly cooling mafic magma. (c) CSD for plagioclase in crystal clots in Ko-Usu.

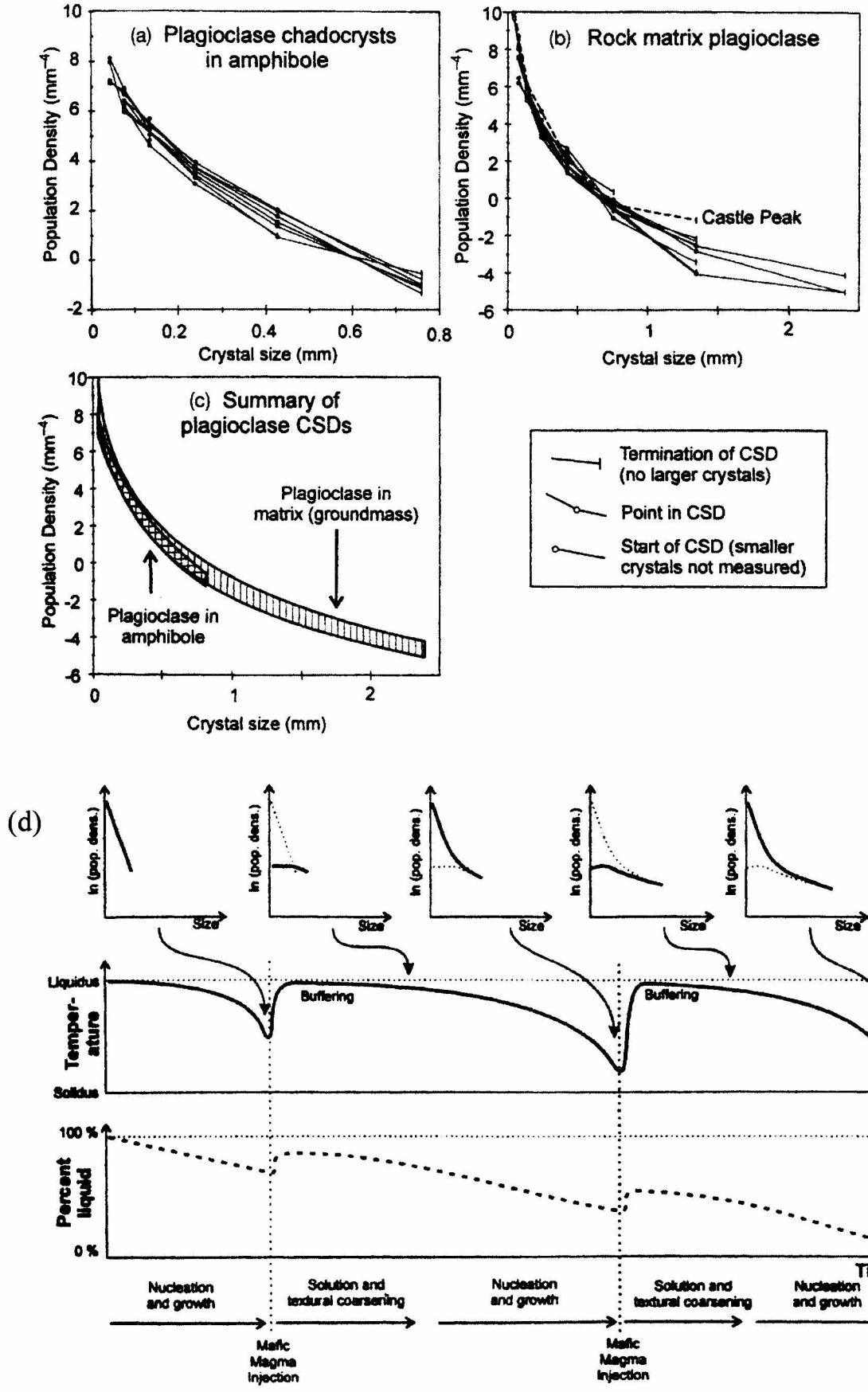

Figure 2-2 CSDs of plagioclase of the volcanic products from Soufriere Hills (after Higgins and Roberge, 2003)(a), (b), (c) and model of magma mixing induced kinked CSDs (d).

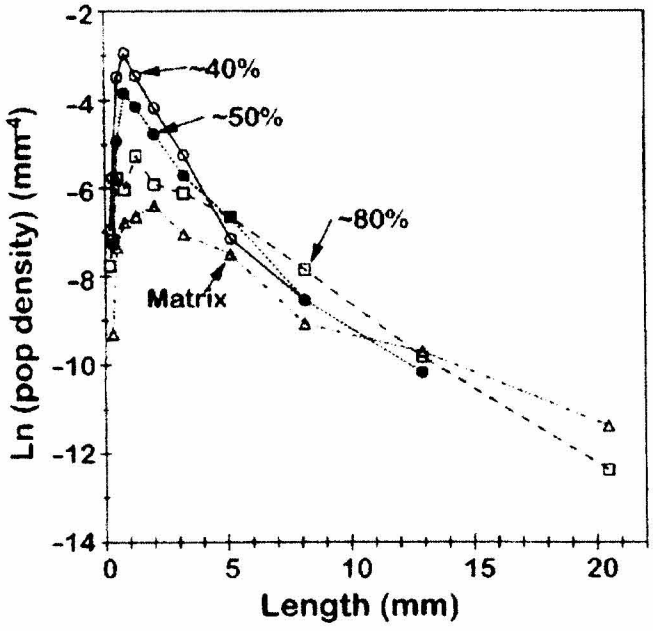

Figure 2-3 CSD of plagioclase in matrix and enclosed by olivine from Lac-St-Jean Anorthosite complex (after Higgins, 1998).

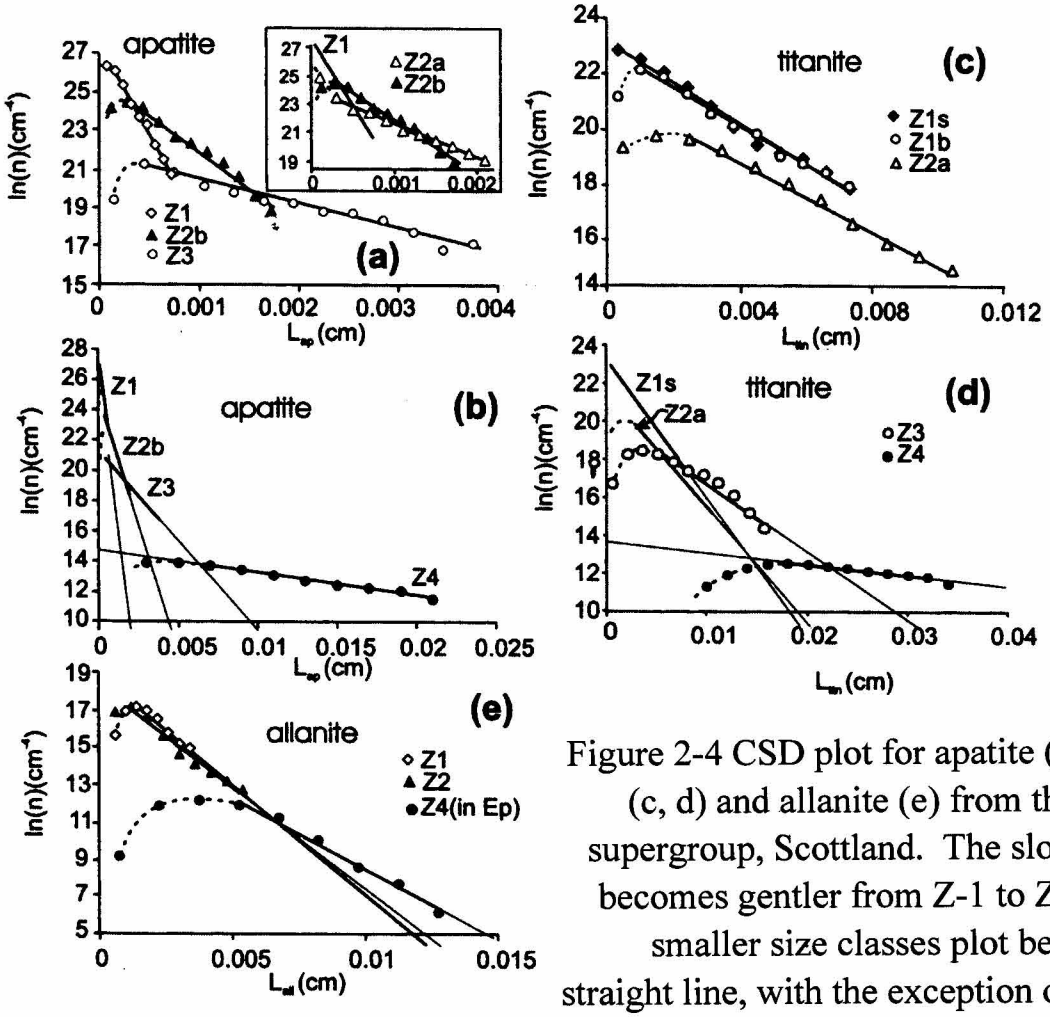

Figure 2-4 CSD plot for apatite (a, b), titanite (c, d) and allanite (e) from the Moine supergroup, Scottland. The slope of CSDs becomes gentler from Z-1 to Z-4, and the smaller size classes plot below the straight line, with the exception of apatite from Z-2. (after Zeh, 2004)

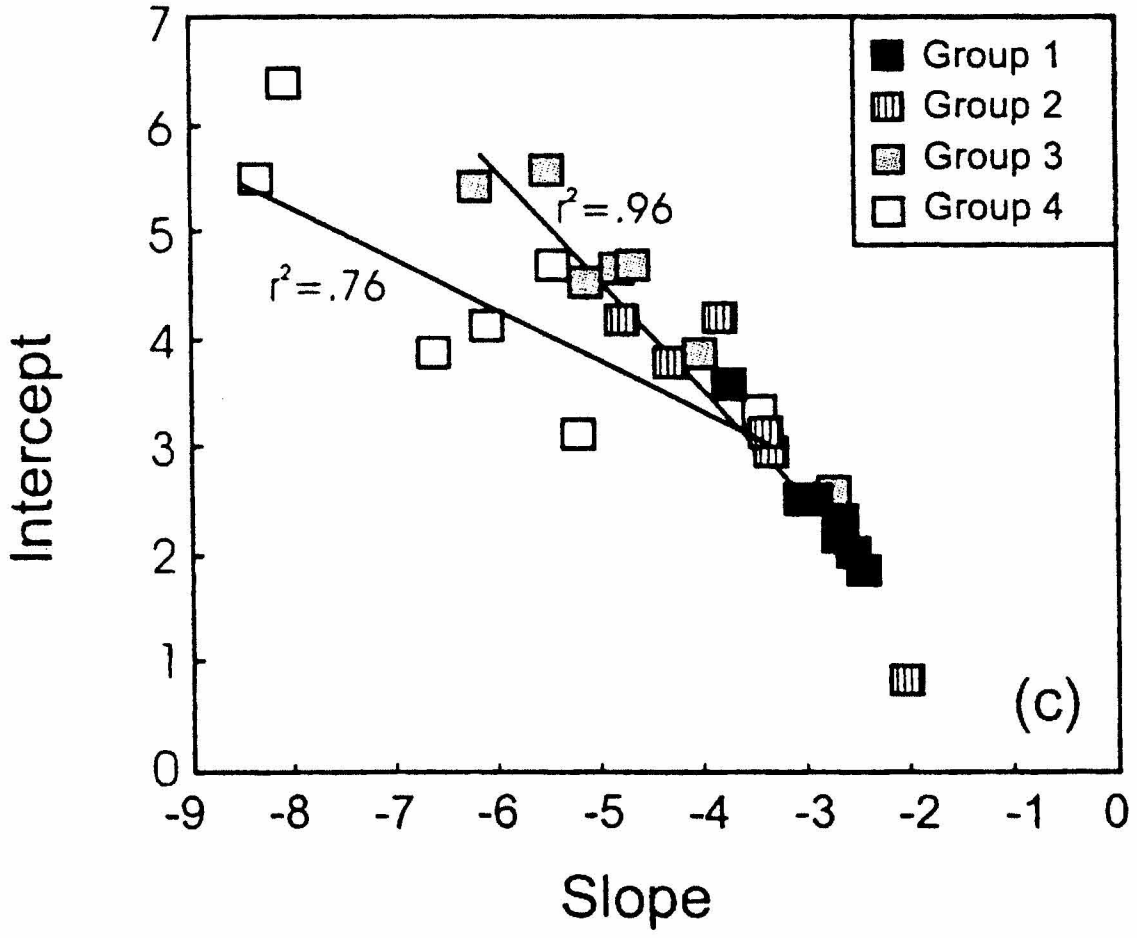

Figure 2-5 CSD slope plotted against the intercept for orthopyroxene from Bushveld complex, South Africa. (after Boorman et al., 2004).
There is a negative relation between intercpet and slope.

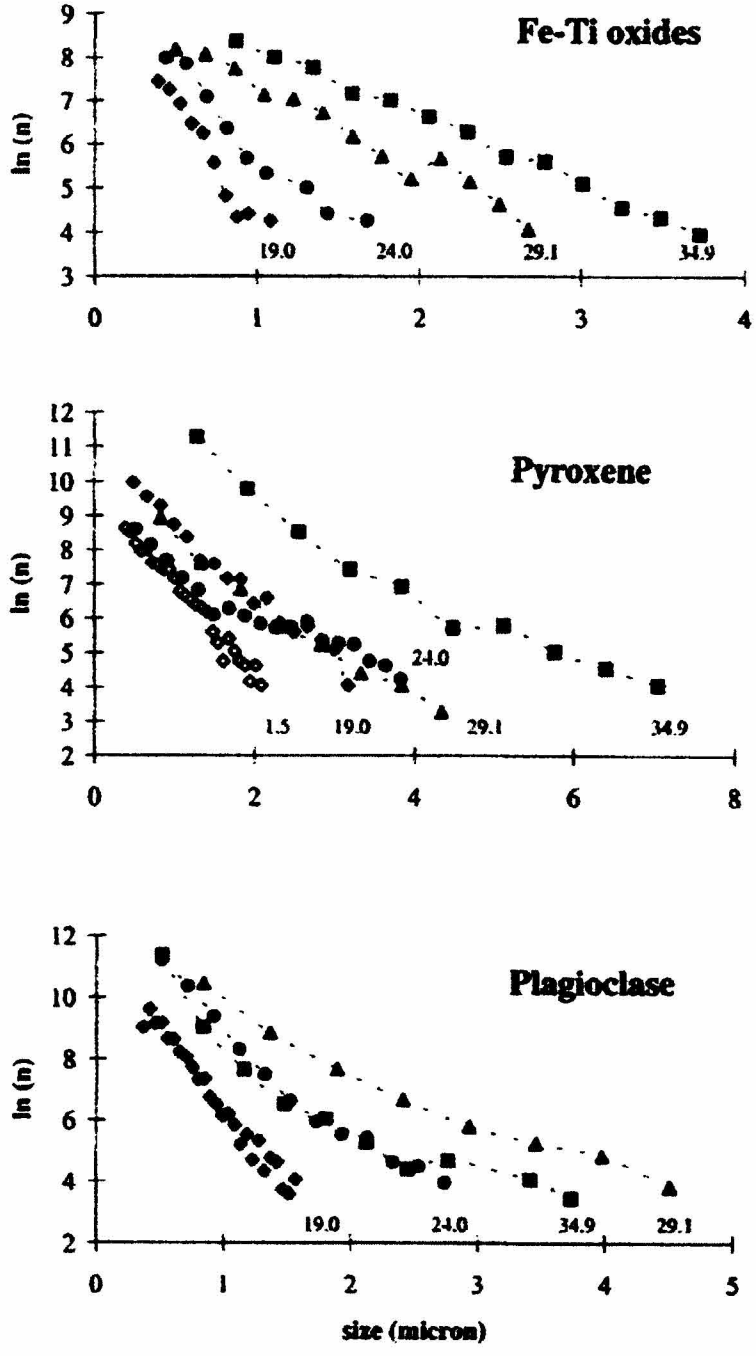

Figure 2-6 CSDs of Fe-Ti oxide, pyroxene and plagioclase in the basaltic glass from Kilauea, Hawaii (after Burkhard, 2002). Symbols refer to the different distance from the original lava-air interface and marked in millimeters. open diamond 1.5 mm; filled diamond 19 mm; circle 24 mm; triangle 29.1 mm; square 34.9 mm.

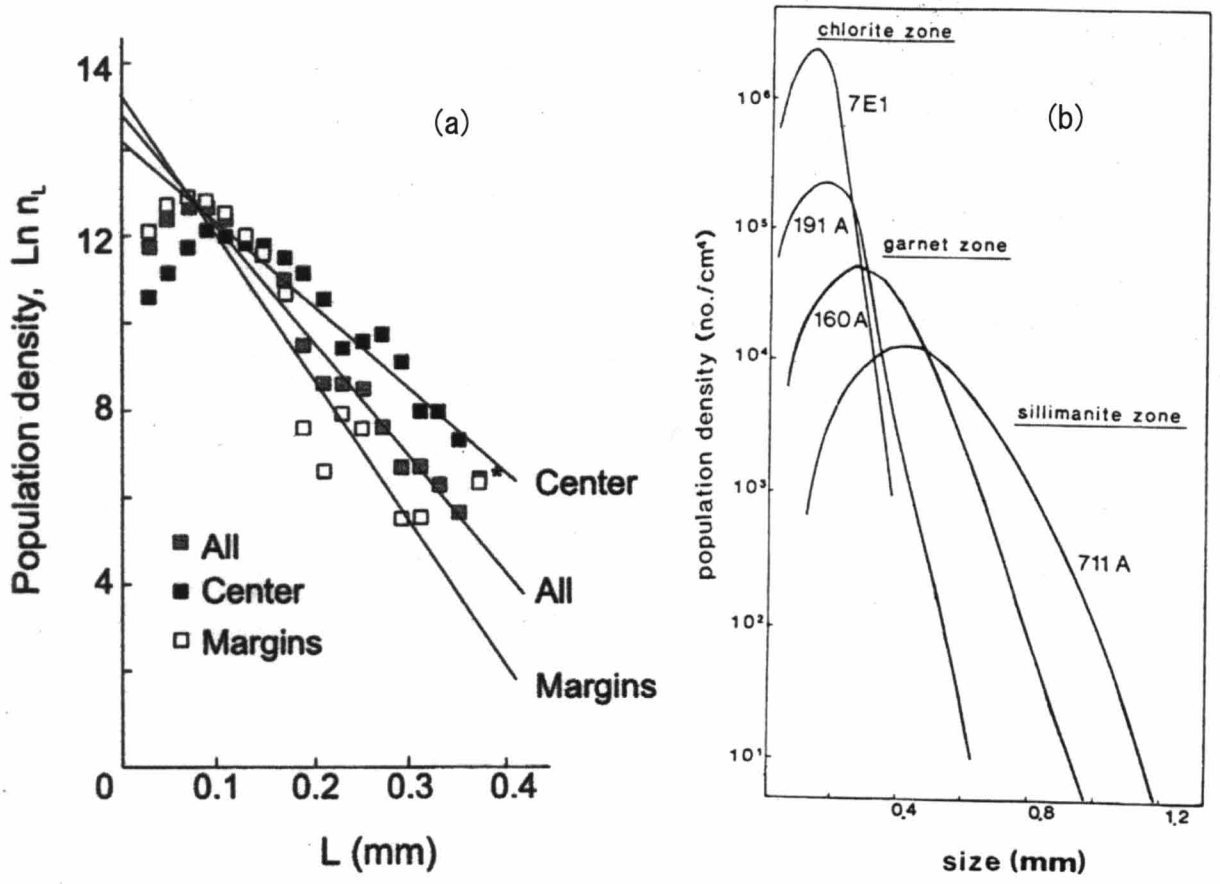

Figure 2-7 Concave down CSDs of chromite from the Stillwater complex (a; after Waters and Boudreau, 1996) and of garnet in pelitic rocks from the chlorite, garnet and sillimanite zones of the Waterville Formation (b; Cashman and Ferry, 1988).

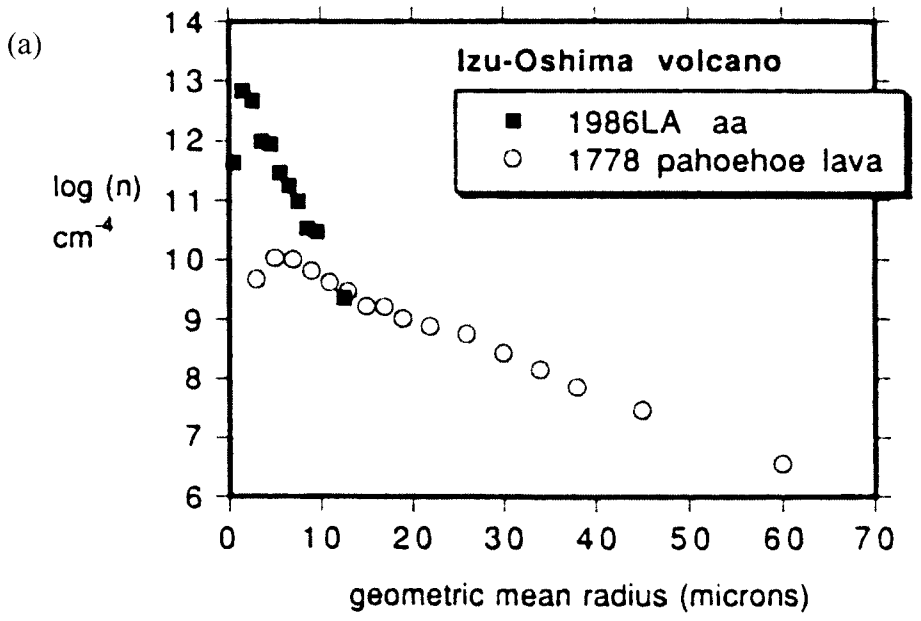

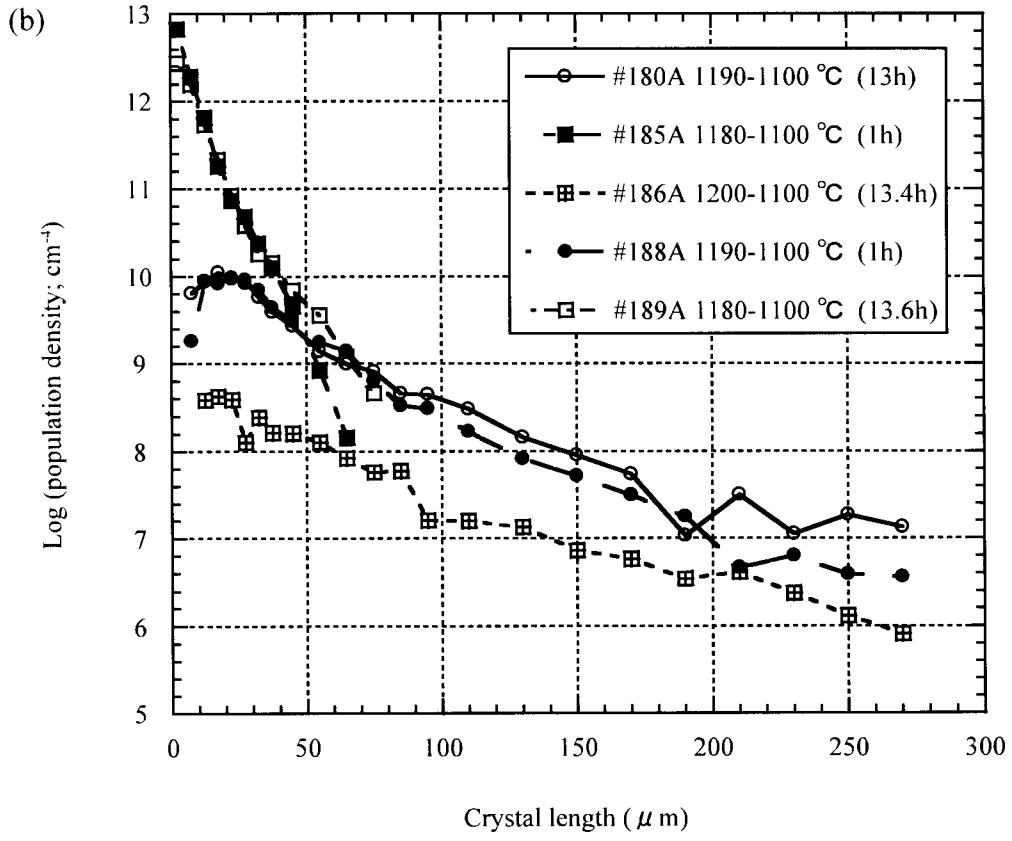

Figure 2-8 (a) CSDs of plagioclase microlite from the 1778 pahoehoe lava and 1986 LA aa lava of Izu-Oshima volcano (after Sato, 1995) and (b) CSDs of plagioclase microlite inrun products of Sato (1995). CSD analyses are done in this study.

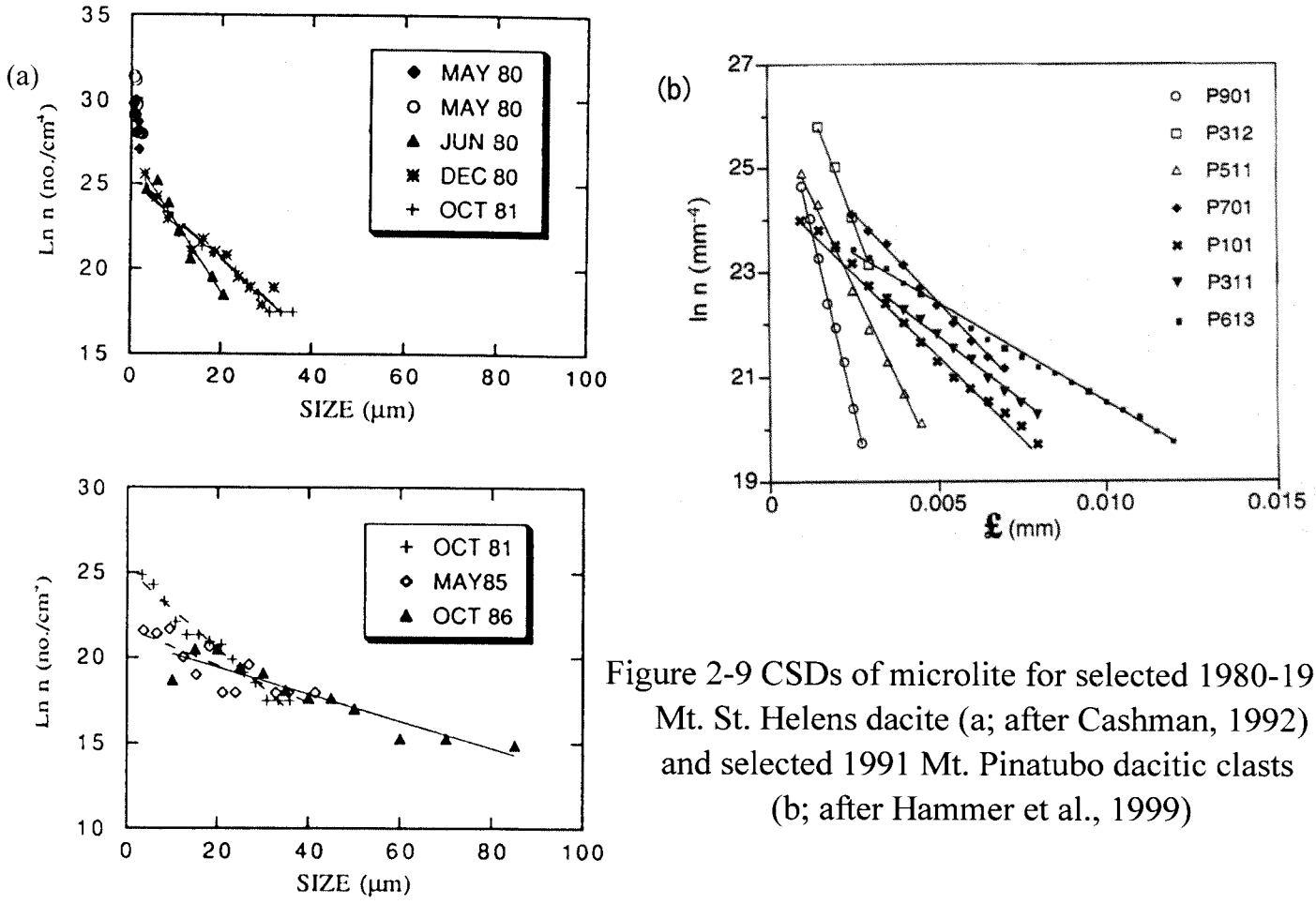

Figure 2-9 CSDs of microlite for selected 1980-1986 Mt. St. Helens dacite (a; after Cashman, 1992) and selected 1991 Mt. Pinatubo dacitic clasts (b; after Hammer et al., 1999)

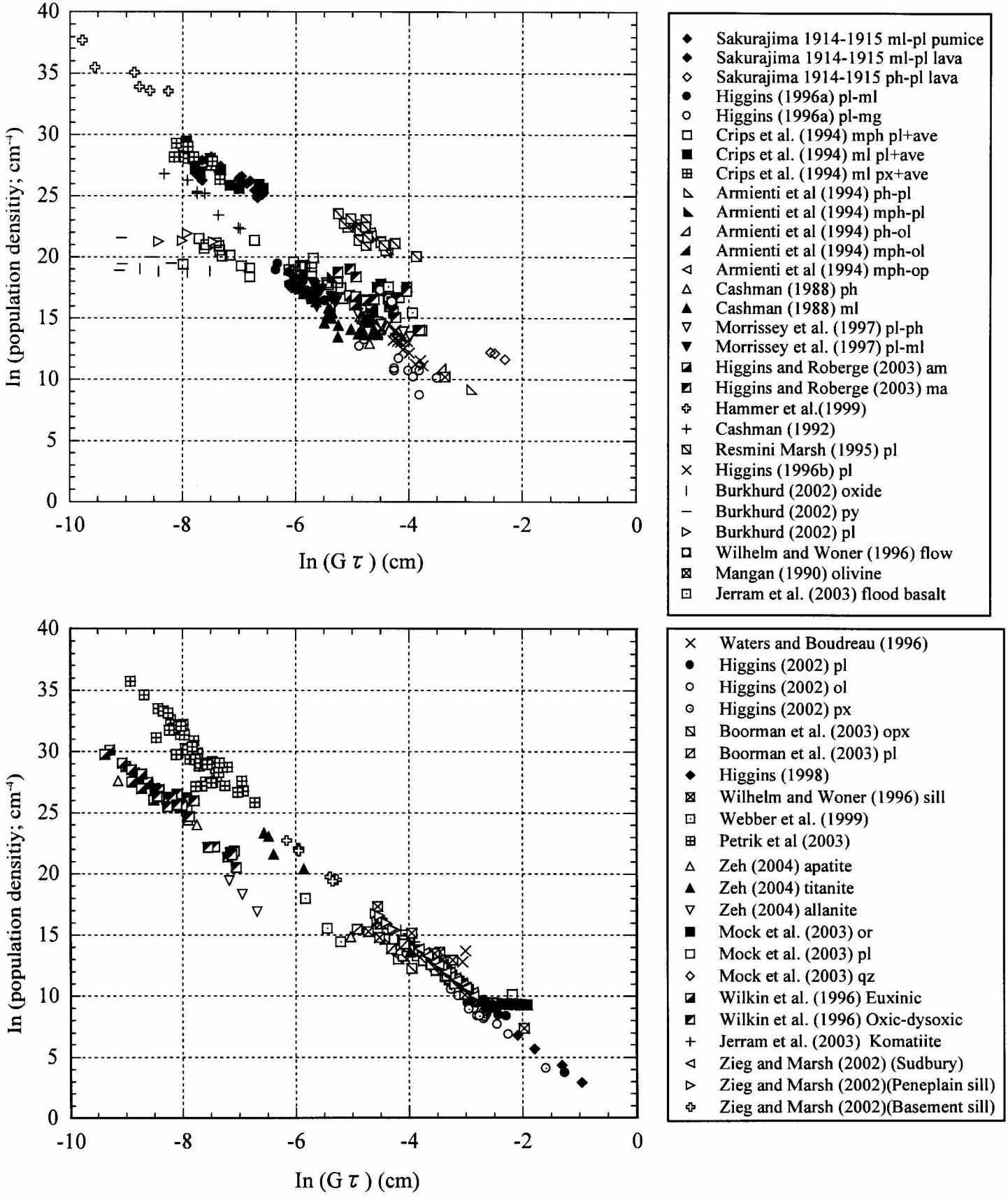

Figure 2-10 Relation between In (population density) and In (G τ) of CSDs of volcanic rocks (a) and other rocks (b).

Table 2-1 List of compiled CSD data and type of rocks and minerals

	rocks	phenocryst			microphenocryst or microlite		
Arimienti et al. (1994)	volcanic rock	plagioclase	olivine		plagioclase	olivine	oxide
Boorman et al. (2004)	plutonic rock	plagioclase	orthopyroxene				
Burkhard (2002)	volcanic rock				plagioclase	pyroxene	oxide
Cashman (1988)	volcanic rock	plagioclase			plagioclase		
Cashman (1992)	volcanic rock				plagioclase		
Crips et al. (1994)	volcanic rock				plagioclase	pyroxene	
Hammer et al. (1999)	volcanic rock				plagioclase		
Higgins (1996a)	volcanic rock	plagioclase			plagioclase		
Higgins (1996b)	volcanic rock	plagioclase					
Higgins (1998)	plutonic rock	plagioclase					
Higgins (2002)	plutonic rock	plagioclase	olivine	pyroxene			
Higgins and Roberge (2003)	volcanic rock	plagioclase	amphibole				
Jerram et al. (2003)	volcanic rock	plagioclase					
Mangan (1990)	volcanic rock	olivine					
Morrissey (1997)	volcanic rock	plagioclase			plagioclase		
Mock et al. (2003)	plutonic rock	plagioclase	orthoclase	quartz			
Petrik et al. (2003)	pseudotachylyte	hematite					
Resimi and Marsh (1995)	volcanic rock	plagioclase					
Webber et al (1999)	plutonic rock	garnet					
Wilhelm and Worner (1996)	volcanic rock	plagioclase					
	plutonic rock	plagioclase					
Wilkin et al. (1996)	sedimental rock	pyrite					
Zeh (2004)	metamorphic rock	apatite	titanite	allanite			
Zieg and Marsh (2002)	plutonic rock	plagioclase					

Chapter 3: Geological study of the 1914-1915 eruption of Sakurajima volcano

3.1 Introduction

The main purpose of this study is to understand ascent process of magma during eruption. Most of volcanoes, which consist of silicic magma, shifts eruption style from explosive to effusive in a single eruption, suggesting that magma ascent process and degassing process change during a single eruption. It is meaningful to compare the textures of vesicle and microlite between explosive volcanic products and effusive ones to understand degassing process and magma ascent process. The 1914-1915 eruption of Sakurajima volcano is one of the most suitable volcano to estimate the change of magma ascent process, because the eruption is the largest eruption within historical records in Japan, eruption style sifted from Plinian phase to lava effusive phase in a single eruption and outcrops of the Plinian fall deposits and lava flows are easy to identify due to good preservation. Before comparing the texture of vesicle and microlite of the volcanic product to discuss the degassing and magma ascent process, it is significant to understand characteristic the eruption, especially Plinian phase of eruption by investigating the feature of the Plinian fall deposit.

I discuss geological feature of Plinian fall deposits and lava flows of the 1914-1915 eruption of Sakurajima volcano from the field observation, at first, in this chapter. Then, feature of Plinian fall deposits are investigated in laboratory analyses. At last, parameters which represent the characteristic of eruption such as column height, eruption rate and decompression rate of Plinian phase of eruption were estimated from the feature, distribution and thickness of the Plinian fall deposits.

3.2 Geological setting and the 1914-1915 eruption of Sakurajima volcano

3.2.1 Geological setting

Sakurajima is a volcanic island located on the southern rim of Aira caldera in the

southern Kyushu, Japan (Fig. 3-1a). It has elliptical shape base with NS and EW axes of 9 and 12 km, respectively. The volcano consists of two main cones, Kita-dake (1117 m height) and Minami-dake (1040 m height), and many parasitic domes.

Many tephrochronological and ^{14}C dating studies have been carried out to reveal the activity of Sakurajima volcano (e.g., Kobayashi, 1986; Okuno et al., 1997; Okuno, 2002). Tephra layer observed around Aira caldera is summarized in Table 3-1 and Figure 3-2 based on Kobayashi (1986) and Okuno (2002). Tephra layers derived from Sakurajima volcano are divided into 17 layers and named Sz/P1 through Sz/P17 from top to the bottom of stratigraphy according to Kobayashi (1986b) and Okuno (2002). Tephra layers derived from Aira caldera and other volcano or caldera are in italics. The activity of Sakurajima volcano is classified into three stages, "Old Kita-dake" stage, "Young Kita-dake" stage and "Minami-dake" stage (Kobayashi, 1986). The activity of "Old Kita-dake" stage started about 26 ka BP (Okuno et al., 1997) after a large-scale Plinian and pyroclastic flow eruption, which formed the Aira caldera (Aramaki, 1984) (Aira-Tn Tephra in Table 3-1). During the "Old Kita-dake" stage, three tephra derived from Sakurajima volcano are identified, Sz-Tk6/P17, Sz-Tk5/P16 and Sz-Tk4/P15, respectively. "Young Kita-dake" stage started from 12.8 ka BP (Okuno et al., 1997). 7 tephras erupted from Sakurajima volcano during the "Young Kita-dake" stage. Mt. Haruta, Yunohira, Mt. Hurihata and Hikinohira are lava domes distributed the western part of the volcano, which generated during "Kita-dake" stage. "Minami-dake" stage has continued its activity since ca 4.5～1.6 ka BP before till now (e.g., Okuno et al., 1997). Mt. Nabe is a pumice cone, which was active in "Minami-dake" stage.

According to the historical records, there occurred four gigantic eruptions within the last 1,000 years. They are Bunmei (1471-1476 A.D., the same as follows), An-ei (1779), Taisho (1914-1915), and Showa (1946) eruptions (Fukuyama, 1978; Fukuyama and Ono, 1981; Kobayashi, 1982). Distribution of these lava flows are shown in Figure 3-1b.

Bulk rock chemistry of these lava flows changed systematically from silicic to basic with time (Yanagi et al., 1991; Takahashi et al., 2001; Uto et al., 2005), and core composition of plagioclase phenocrysts of them changed from unimodal to bimodal,

suggesting that magma mixing continuously occurred in the magma chamber (Yanagi et al., 1991).

3.2.2 **Sequence of the 1914-1915 eruption of Sakurajima volcano**

The 1914-1915 (Taisho) eruption began with seismic activity on the morning of January 10, 1914. Seismic activity continued for a few days. The distributions of Plinian fall deposit are shown in Figure 3-1b and Figure 3-3. Explosive Plinian eruption began on morning of January 12, 1914, and Plinian fall pumice began to erupt first at from the western vent and then from the eastern vent (Koto, 1916). From western part, Plinian fall pumice erupted from V.w1 vent (Fig. 3-1c) (Ishihara et al., 1985). The explosive activity continued for one and half a days (about 34 hours). In the evening on January 13, lava flows (Taisho 1 lava) began to extrude from both western and eastern flanks of the mountain at the evening of January 13, 1914 and the extrusion had continued for about two weeks. In the western flank, at first, lava extruded from V.w2 and 3 vents, and then from V.w4 to 7 vents, all of which are located to the western lower flank of V.w1 vent (Ishihara et al., 1985). The eastern vents for the Taisho 1 lava flow were buried beneath the following lava flows and their accurate position is obscure. In February 1914, the second lava flow (Taisho 2 lava) extruded from the eastern flank. The extrusion had continued until fall of 1914. In the end of March to the beginning of April of 1915, the secondary lava flow (Taisho 2' lava) appeared from the flow fronts of the Taisho 2 lava flow. Five vents were observed in the eastern part of Sakurajima volcano during the 1914-1915 eruption (Koto, 1916). The volume of pumice is 0.6 km^3 (not DRE) and that of lava flows is 1.34 km^3 (Ishihara et al., 1981; Kobayashi, 1982). The volume of Plinian fall deposit is discussed in detail later.

3.2.3 **Magma supply system**

Magma supply system has been studied by using seismic and ground deformation

data. Mogi (1958) and Yokoyama (1971) estimate that the depth of magma chamber is 7-10 km by applying the deformation model of elastic body to the ground deformation around Sakurajima at the 1914-1915 eruption. On the other hand, Yokoyama (1986) suggested from ground deformation data that two magma sources exist beneath the volcano, one is shallow (about 2 km depth) and vertically directive and the other is deep (about 8 km depth) and obliquely, directly beneath volcano. Present seismic and geophysical study revealed the existence of two magma chambers; one is just beneath the volcano about 3-6 km and the other is beneath the Aira caldera beneath 10km (Ishihara 1989; Ishihara 1991; Ishihara 1995) (Fig 3-4a). Magma supply rate to the magma chamber beneath the Aira caldera may be c.a. 10 million m^3/s (e.g., Ishihara 1995; Nagaoka et al., 2001) estimated from the inflation volume of Aira caldera since the 1779 eruption of Sakurajima volcano and leveling data. Moreover, A-type earthquake generate before the recent Bulcanian eruption beneath the 15 km from the south-west of the volcano, suggesting the uprise of magma (Fig. 3-4b). Takahashi and Takahashi (1995) and Takahashi et al. (2001) proposed that magma chamber 10 km beneath from Aira caldera represent the felsic magma and that mafic magma supply from south-west of Sakurajima volcano beneath 15 km depth. Takahashi and Takahashi (1995) and Takahashi et al. (2001) suggest that magma mixing occur at magma chamber 3-6 km beneath the volcano.

3.3 **Analytical methods**

3.3.1 **Grain size analysis**

6 samples from Plinian fall deposits were dried by a oven at 120 ℃ more than 24-hours. After then, samples were sieved with a set of sieves having an interval of one phi ($\phi = -\log_2 d$; where d is a diameter of a particle in millimeter) and covering a range of mesh-size from -6 ϕ (64 mm) to 4 ϕ (1/32 mm). -3 to -4 ϕ pumices were used to analyze density, and residual water content analyses. -6 to 2 ϕ samples were used to component analyses.

3.3.2 **Component analysis**

6 samples from Plinian fall deposit were further analyzed by each size down to 2 ϕ (1/4 mm) into three main components of pyroclastic rocks: essential glass (pumice fragment and vitric fine ash), liberated crystals (plagioclase and pyroxene) and accidental lithic fragment. Each component from 0 ϕ (1 mm) to 2 ϕ (1/4 mm) fraction was separated by thin section. Each component from -6 ϕ to 0 ϕ (1 mm) fraction was separated by handpicking with naked eyes and under a binocular microscope. For size fractions of larger than -3 ϕ (8 mm), all the grains were counted and separated, and then each weight percentage is determined directly on a laboratory balance. For size fractions of -2 ϕ (4 mm) to 0 ϕ (1 mm), a minimum of 500 grains were counted and separated, and then each weight percentage is also determined directly on a laboratory balance. For size fraction of 0 ϕ to 2 ϕ and <2 ϕ, minimum 100 grains were counted from the thin section.

3.3.2 **MP and ML measurement**

In this study, the maximum diameter of Plinian fall pumice and lithic fragment were described as MP and ML respectively. MP and ML measurement were carried out at 10 outcrops of Plinian fall pumice deposits. Isopleth map was made from the ML. MP and ML were measured at three methods.

The first method is to measure five to one largest Plinian fall pumice and three to one largest lithic fragments found in a 2 m^2 to 0.25 m^2 at each out crop of Plinian fall deposits. Then, the arithmetic mean of each set of the measurements were calculated and defined as the maximum diameter.

3.3.3 **Analytical method of density of Plinian fall pumices**

50 pumice samples for each unit, hence total 350 samples, were analyzed for bulk

density.

Bulk density of Plinian fall pumices was analyzed at Kobe University using helium pycnometer (Micrometicics Accupyc 1330; Shimadzu Co.Ltd. Japan), which utilizes helium gas. Firstly, total weight of pumice was measured. Then surface of pumice was coated by melted paraffin, and the volume of pumice was measured using Micrometicics Accupyc 1330. Bulk density was calculated from the values of pumice weight and volume. Bulk vesicularity was calculated from the equation of Houghton and Wilson (1989), assuming that magmatic density is 2400 kg/m^3 and converted to crystal-free vesicularity using total phenocryst mode.

3.4 **Characteristics of Plinian phase of the 1914-1915 eruption of Sakurajima volcano**

3.4.1 **Features of Plinian fall pumice deposits**

The distributions of sampling points and isopach map of Plinian fall deposit investigated in this study are shown in Figure 3-3. Plinian fall deposit is distributed in the whole of Sakurajima Island and western part of Osumi peninsula, around Tarumizu City, Kihoku Town and Fukuyama Town due to the wind direction.

Most of outcrops in the island are more than 1 m thickness. In the western part of island (Loc.P1), Plinian fall deposits show no grading maybe due to up wind (Fig. 3-5). On the other hand, in the eastern parts of island, Plinian fall deposit show normal grading due to leeward (Fig. 3-6). Thickness of the outcrops in Osumi peninsula is less than 0.5 m. Plinian fall deposits outside of island show normal grading (Fig. 3-7). Grain size distribution shows the unimodal main peak around -1 -0 ϕ. The Plinian fall deposit consists of essential pumice fragments, accidental lithic fragment (Fig. 3-8(b)) isolated (free) crystals and matrix volcanic ash. Pumice fragments are divined into white-brown pumice and slightly darker colored pumice in color (Fig. 3-9a). Most of pumice fragments show subangular in shapes (Fig. 3-9a). Lithic fragments are subangular to angular in shapes and consist of andesitic rocks. Volcanic ash (<2 mm in

diameter) consists of micro-pumice (37.5±16 number %) (in other word, essential glass (ash)), isolated (free) crystals (58.0±18 number %) and accidental lithic fragments (4.5±5.1 number %) (Fig. 3-8b and 3-9b). Isolated crystals are plagioclase, orthopyroxene, augite, and Fe-Ti oxide and contain a lot of broken crystals as pointed out by Yasui and Suganuma (2003). There are not clear difference of vesicle texture between pumice and micro-pumice in the volcanic ash.

3.4.2 **Change of density of Plinian fall pumice from lower to upper parts of the deposit**

In the Loc.P1 Plinian fall deposit which is about 2 m thickness (Fig. 3-10), from 0809A to 0809E (from basement to 1.5 m), density of most Plinian fall pumices are about 700 kg/m^3. Most of pumices in the lower to middle parts of the deposit (from 0809A to 0809E) are white-brown pumices. On the other hand, pumices in the upper part (from 0809F to 0809G; 1.5-2.1 m) are white pumices and darker colored pumices and their average density is about 950-1000 kg/m^3.

3.4.3 **Features of lava flows**

The distributions of historical lava flow within 1000 years ago are shown in Figure 3-1. Taisho 1 lava flows were speared at western and southeastern part of the island. The Taisho 2 lavas were distributed at the southeastern parts of the island (Fig. 3-1c). The Taisho 2' lavas were observed at the rim of Taisho 2 lava flows. Blocky lava flow is divided into two parts according to the rock textures (Fig. 3-11). The first is clinker part of lava. The second is massive part of lava. In the case of western part of Taisho 1 lava flow, Taisho 1 lava flows separated near to middle parts of lava flows are mantled by pyroclastic flows deposits (Fig. 3-12) (Kobayashi 1986), which consist darker brown pumices (Fig. 3-11). On the other hand, Yasui (2001a, 2001b and 2005) investigated textural heterogeneity of matrix glass and phenocryst of plagioclase to discuss the intensity of lava effusive phase. Yasui (2001a and 2001b) concluded that

western part of Taisho 1 lava is clastgenic lava flow due to showing the eutaxitic texture and high proportion of broken plagioclase (Fig 3-13). Phenocryst assemblage is plagioclase + orthopyroxene + augite + magnetite (Fig 3-13). Olivine phenocrysts (microphenocrysts) are present slightly in Taisho 2 and 2' lavas. To investigate crystallization processes of microlite during magma ascent, clinker part of lavas, which represent surface of lava flows and rapidly cooled after eruption from the vents, were collected. In these samples, microlite crystallization might have taken place mostly during magma ascent through conduit. In two locarities (L. 1 and L. 8 points, Fig. 3-1c), it is possible to observe the massive inner part of lava flow, which is slightly white maybe due to high crystallinity of groundmass phase. Hence, several samples were collected from clinker part to massive part to compare the difference of microlite textures.

3.4.4 **Estimation of total volume of Plinian fall deposit**

Figure 3-3 shows the isopach map of Plinian fall deposit. Total volume of Plinian fall deposit was estimated at two methods.

There is a linear relation between logarithm of thickness of the deposit and logarithm of area enclosed by isopach contour (Fig. 3-14),

$$(\text{thickness}) = 2.2\times10^{-2} * (\text{area})^{-0.78} \qquad (3\text{-}1)$$

Assuming that the thickness of the deposit decrease from 0.01 km to 1.0×10^{-5} km, total volume can be estimated by integral the equation (3-1). Total volume of the Plinian fall deposit estimated from the first method is 0.60 km^3 (0.24 km^3 ;DRE), corresponding to the estimation of Kobayashi (1982).

In the case of the first method, there is a possibility of ignoring the co-Plinian ash erupted far away. Total volume of Plinian fall deposit included in co-Plinian ash erupted far was estimated from Isopach map (Fig. 3-3) by the method of arranged 'crystal method' proposed by Hayakawa (1985).

On the other hand, Total volumes of Plinian fall deposit measured by the method proposed by Hayakawa (1985) are 0.77 km^3 (0.31 km^3 ;DRE) using 0.5 m contour and

0.66 km^3 (0.26 km^3 ;DRE) using 1 m contour, respectively, and are slightly larger than total volume estimated by the first method.

3.4.5 **Estimation of column height and eruption rate of Plinian eruption**

Isopleth maps of Plinian fall pumice and lithic fragment were measured by the value of MP and ML and showed in Figure 3-15. Distribution axis, cross-wind and maximum down wind range of Plinian fall deposit were determined from the 4cm contour plot of Plinian fall pumice and 0.8 cm contour plot of lithic fragment, listing in Table 3-2. Density of lithic fragment is assumed to 2500 kg/m^3. According to the analyses of pumice density, 777 kg/m^3, which is average value of 350 samples, was applied. From the obtained average density of pumice, the corresponding size of pumice fragment to the lithic (density = 2500 kg/m^3) for equivalent terminal settling velocity can be calculated by the following equation:

$$y = 2500 * a * \rho^{-1} \qquad (3\text{-}2)$$

(Suzuki et al., 1998), where y is diameter of pumice clast (cm), a is the equivalent size for lithic fragment (1.6 cm), and ρ is density of pumice fragment. Column height of Plinian fall pumice and lithic fragment were estimated by the method of Carey and Sparks (1986), using the 4 cm contour plot of Plinian fall pumice and 0.8 cm contour plot of lithic fragment (Table 3-2). In the case of the Plinian phase of the 1914-1915 eruption, Plinian fall pumice erupted from the two vents located both eastern and western parts of the volcano (Fig. 3-1c). Center of the volcano was assumed to be the vent erupted Plinian fall pumice.

Eruption rate is proportional to the fourth power of the eruption column height, and was calculated after the diagram of Sparks (1986). Magmatic temperature of Plinian fall pumice estimated by Sekine et al. (1979) was 950 ℃, and estimated by pyroxene microlite composition in this study (chapter 4) was around 1000-1100 ℃. Hence in this chapter, magma tic temperature is assuming 1000 ℃.

Estimated column height and wind velocity by Plinian fall pumice and lithic fragment are 15-18 km (Fig. 3-16), 20-30 m/s, respectively. Magmatic temperature is

assumed to be 1000 ℃ and column height is plotted against eruption rate of the graph of Sparks (1986) (Fig. 3-17). Eruption rate is c.a. 5×10^3 m^3/s (Fig. 3-17, Table 3-2), corresponding to c.a. 10^7 kg/s. Duration of Plinian eruption is about 40 hours, slightly larger than actual duration of Plinian phase of eruption, assuming that total volume of the Plinian fall deposit is 0.72 km^3 (not DRE) estimated by the method of Hayakawa (1985). Duration of Plinian eruption is about 16 hours, less than actual duration of Plinian phase of eruption, assuming that total volume of the Plinian fall deposit is 0.29 km^3 (DRE) estimated by the method of Hayakawa (1985).

3.4.6 **Estimation of magma ascent rate**

Magma ascent rate was estimated by using computer program, CONFLOW (Mastin and Ghiorso, 2000: USGS Open file and http://volcan.wr.usgs.gov/Projects/Mastin/). Parameters for calculating magma ascent rate and results are listed in Table 3-3 and Figure 3-18, respectively. Values of conduit diameter were changed from 20 to 35 m to adjust the mass eruption rate estimated from column height. Mamgatic temperature and H_2O content of case (1) (Sekine et al., 1979), (2) and (3) were selected to compare each other. Estimated values are used in discussions of chapter 5 to reveal the correlation among ascent rate of magma, vesicularity and plagioclase microlite texture.

3.5 **Summary**

1. Volume of Plinian fall deposit erupted at the 1914-1915 eruption of Sakurajima volcano is c.a. 0.72 km^3 (0.29 km^3 ;DRE). Column height was 15-18 km. Wind velocity at the eruption was 20-30 m/s. Volume eruption rate is c.a. 5×10^3 m^3/s.

2. Plinian fall deposit pumices collected at Loc. P1 are divined into two types according to the bulk density and color; white pumice with low bulk density (c.a. 700 kg/m^3) and darker colored pumice with high density (c.a. 950 kg/m^3).

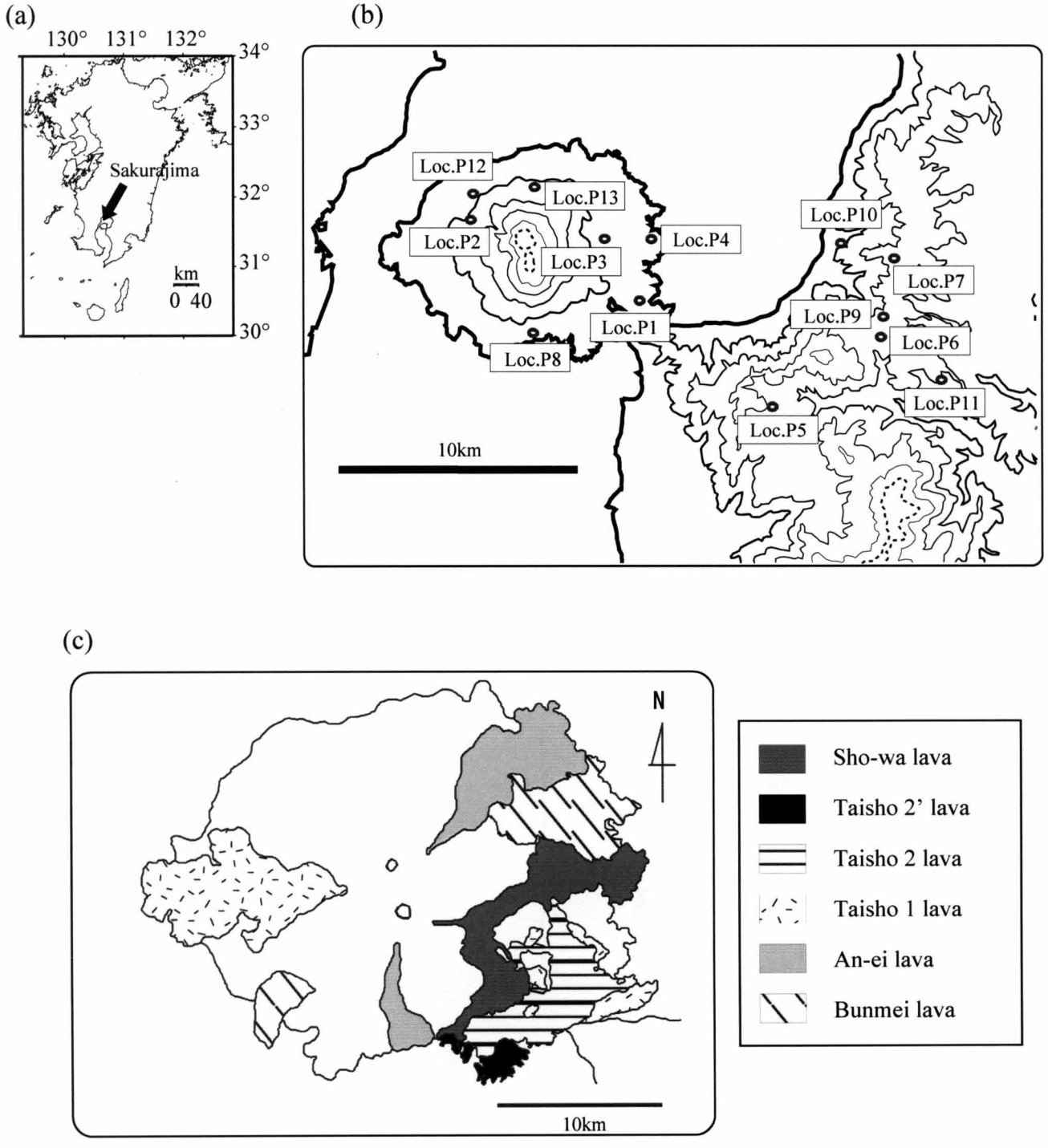

Figure 3-1 Index map showing the location of Sakurajima volcano (a), distribution of Locality points of Plinian fall pumice (b) and distribution of histrical lava flows, modified from Fukuyama and Ono (1981) (c).

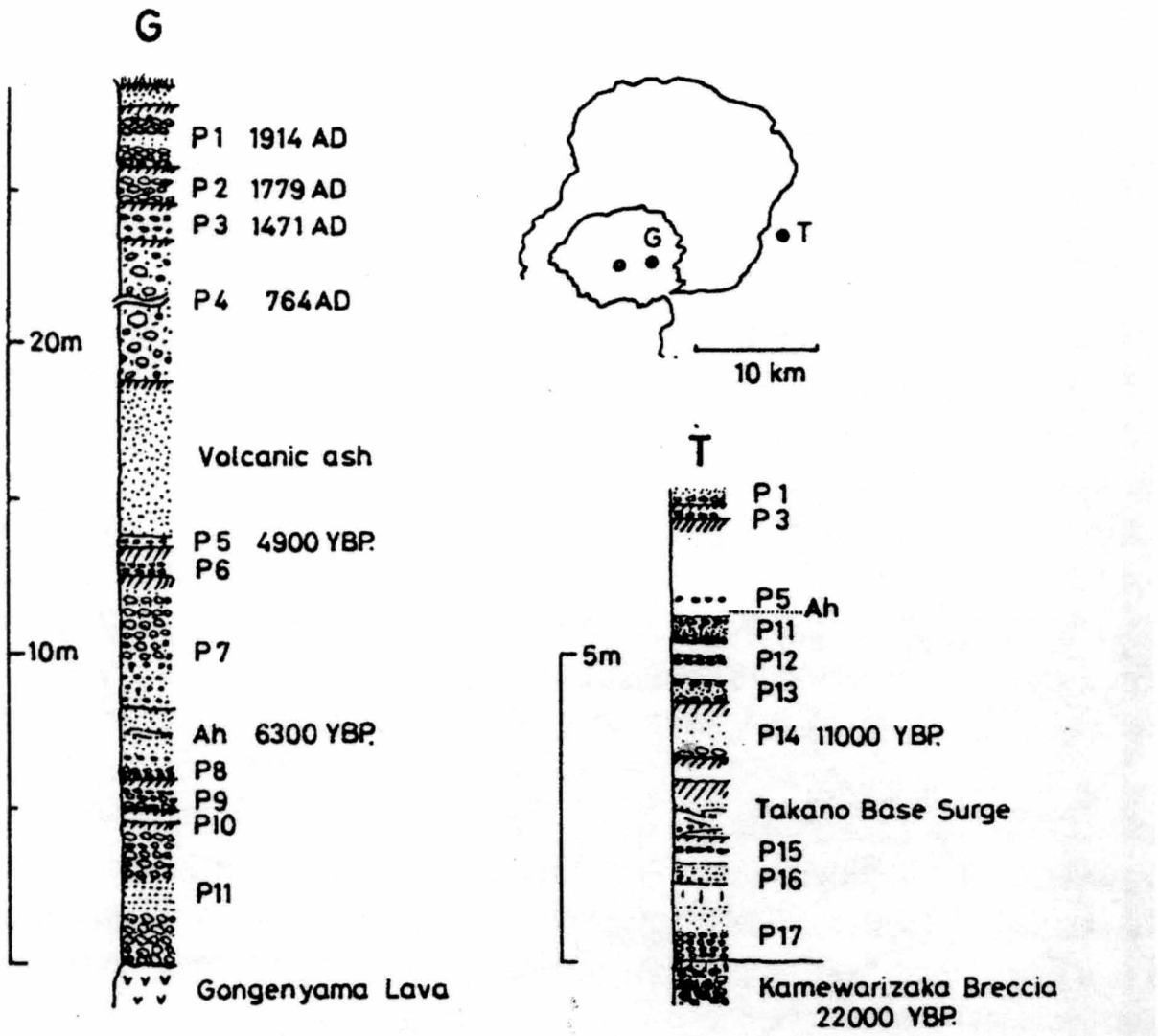

Figure 3-2 Stratigraphic sections of Gongenyama area in Sakurajima volcano and Takano area in Osumi peninsula (after Kobayashi, 1986)

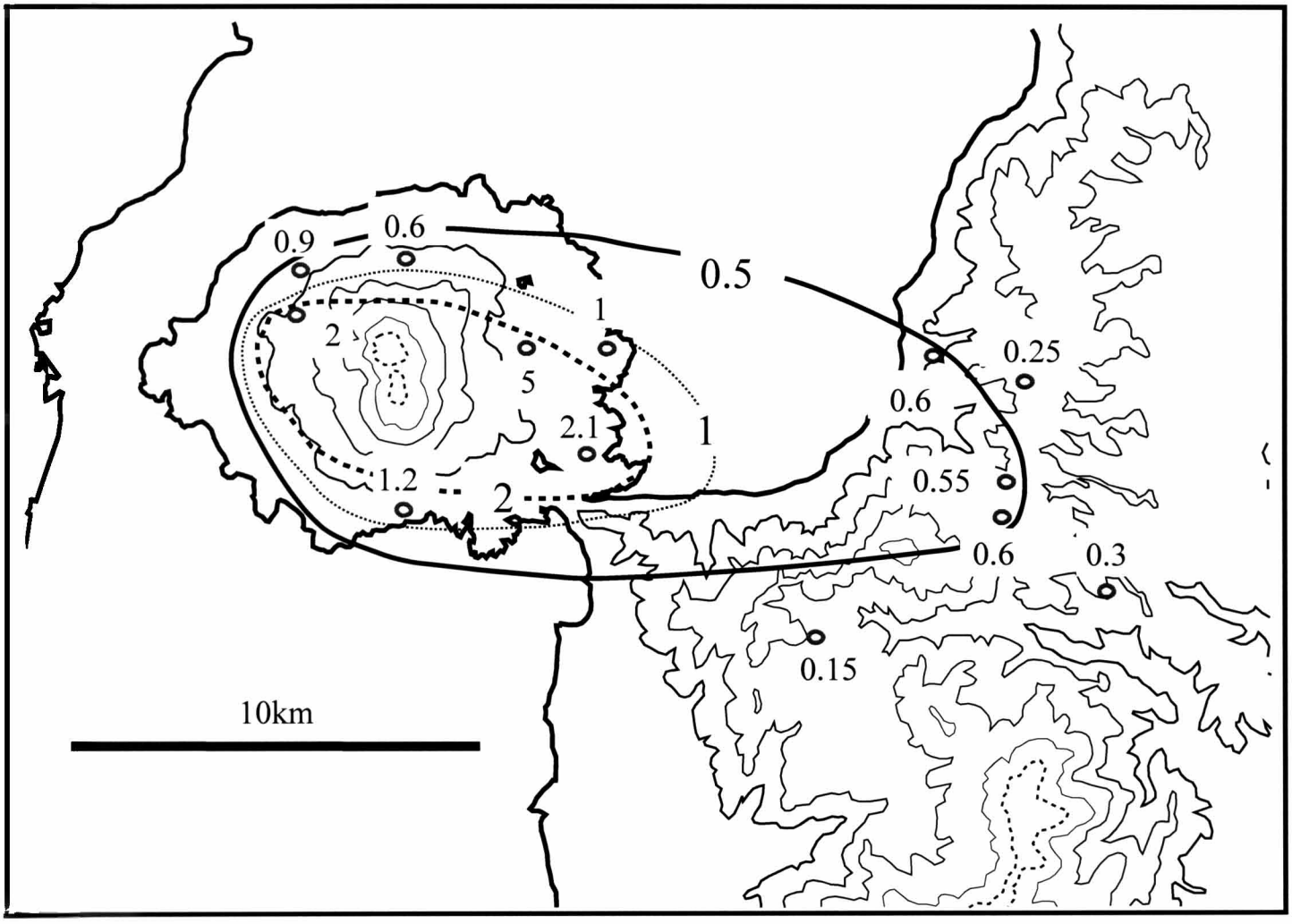

Figure 3-3 Isopach map of the Plinian fall deposits erupted at the 1914-1915 eruption of Sakurajima volcano. (Units are m)

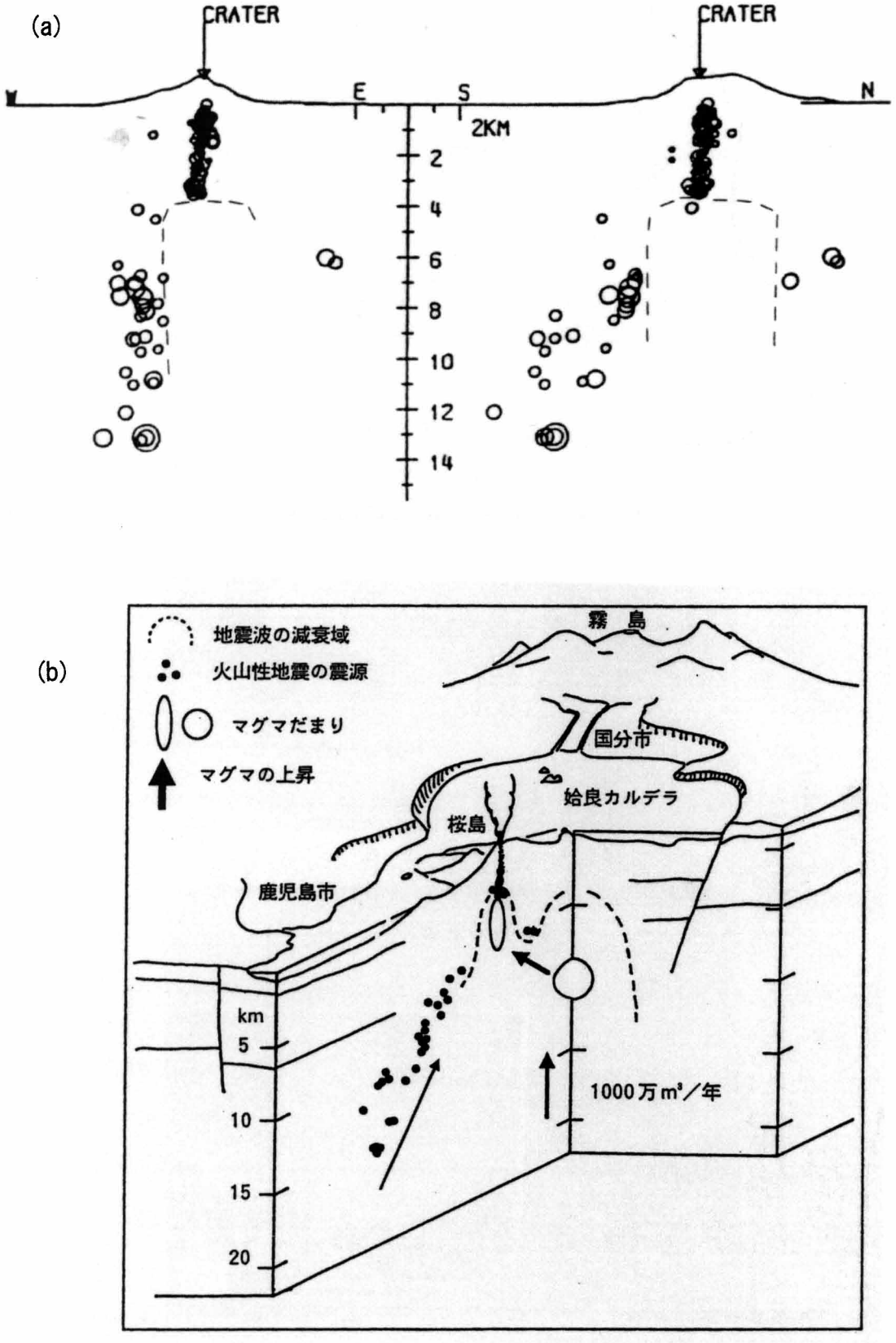

Figure 3-4 (a) Hypocenters of A-type (tectonic) earthquakes during 1975-1986 (after Ishihara, 1988) and (b) magma supply model proposed by Ishihara (1995).

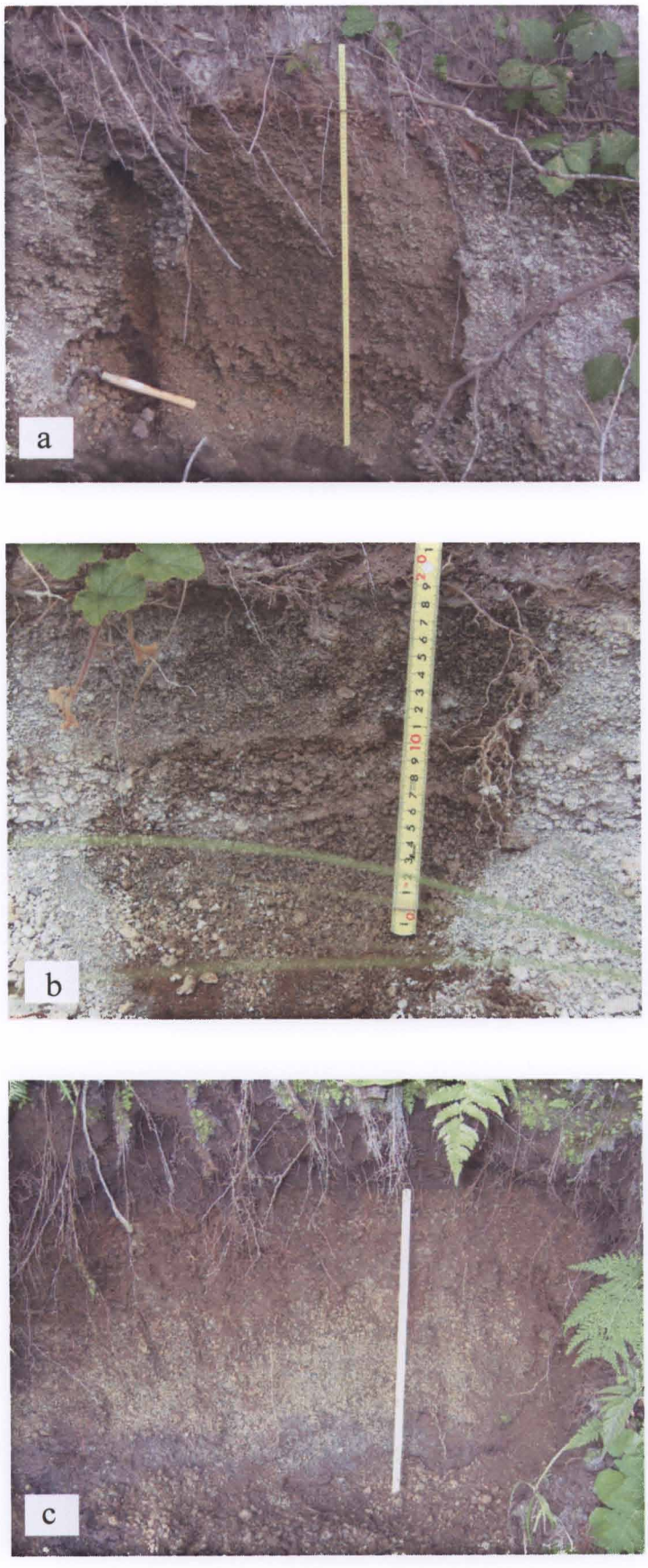

Figure 3-5 Photgraphs of Plinian fall deposits. Loc.P4 deposit, 1 m thickness (a). Loc.P7 Plinian fall deposit, 20 cm thickness (b). Loc.P13 Plinian fall deposit, 1 m thickness (c).

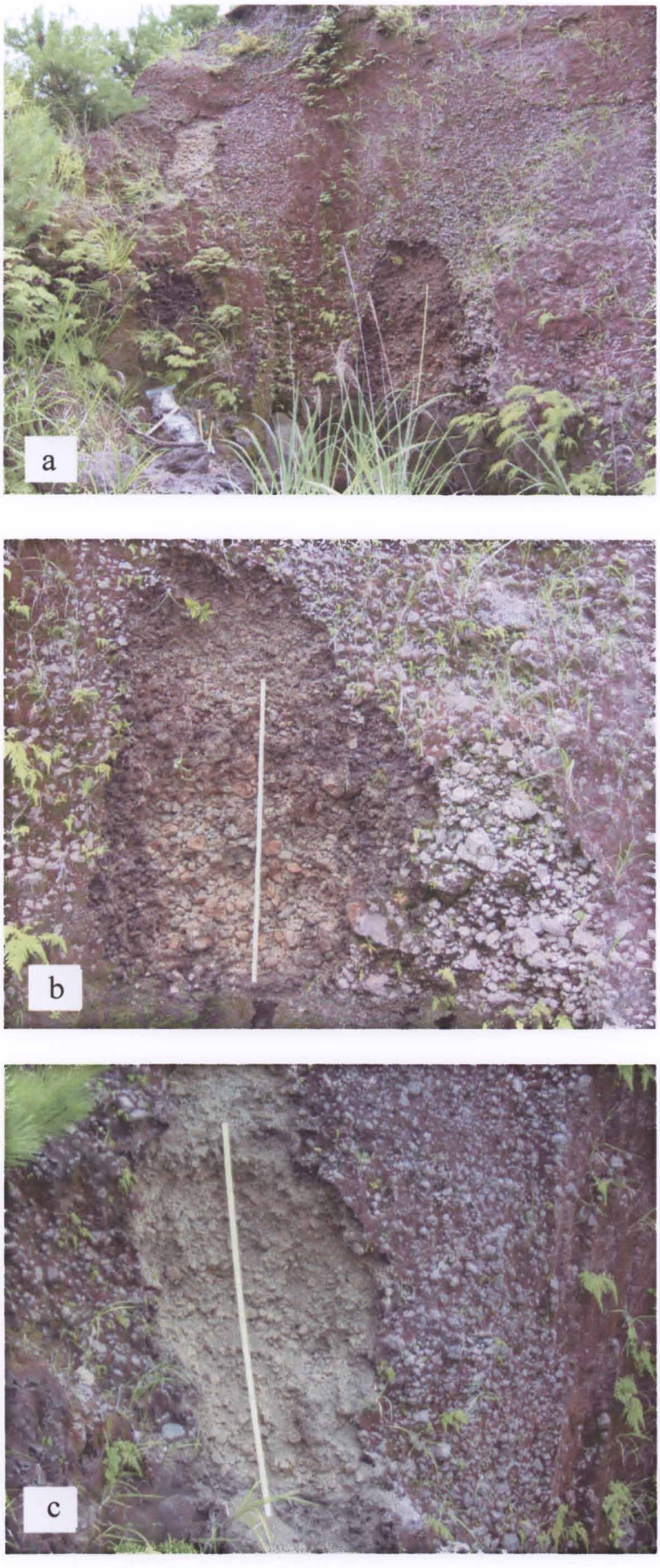

Figure 3-6 Photgraphs of Loc.P3 Plinian fall pumice deposit, 5 m thickness. Overview of Loc.P3 deposit (a). Lower part of Loc.P3 deposit (b). Upper part of Loc.P3 deposit (c).

Figure 3-7 Photgraphs of Loc.P2 Plinian fall pumice deposit, 2 m thickness. Overview of Loc.P2 deposit (a). Lower part of Loc.P2 deposit (b). Upper part of Loc.P2 deposit (c).

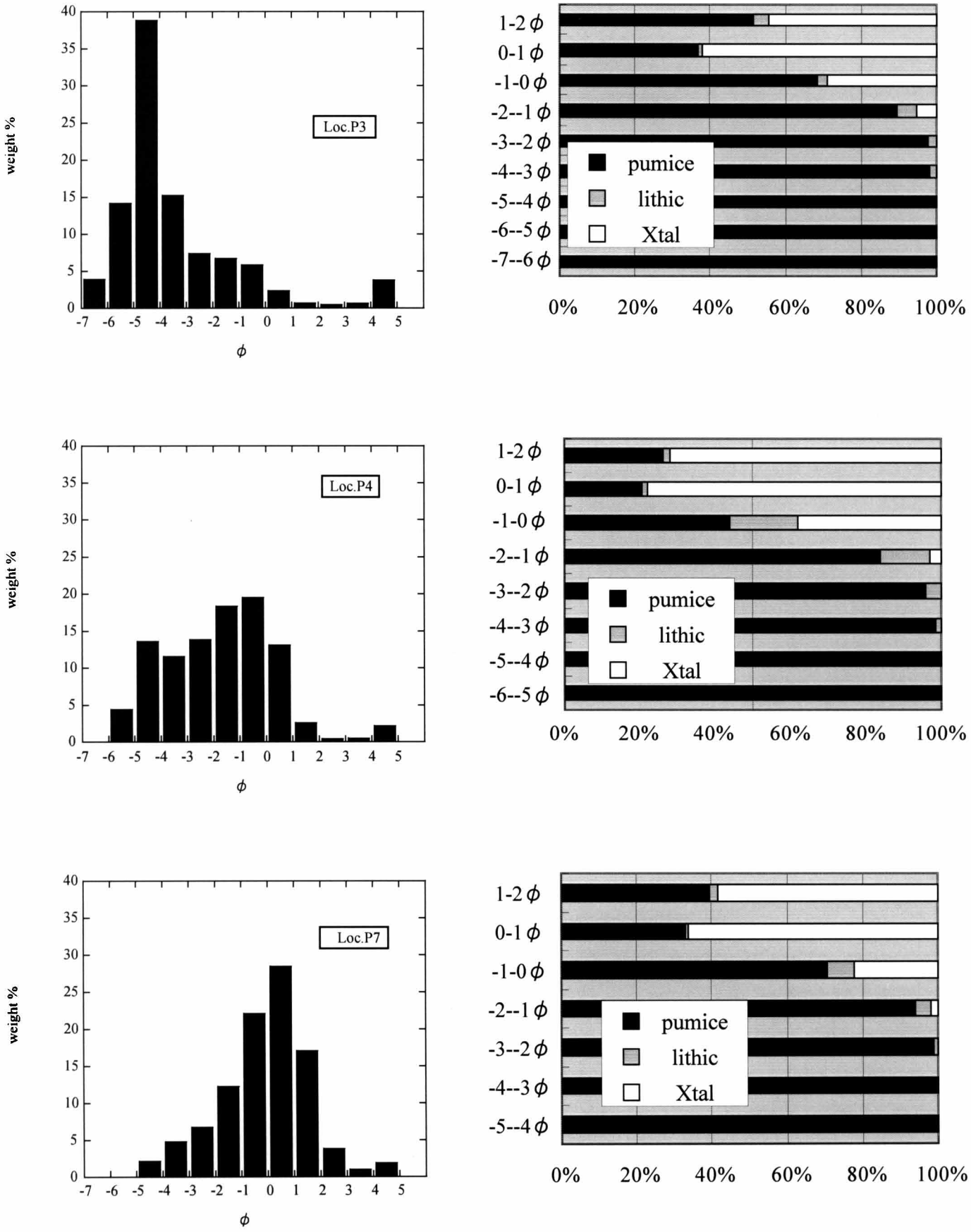

Figure 3-8 (a) Grain size distribution of Plinian fall deposits and (b) component analyses of each grain size.

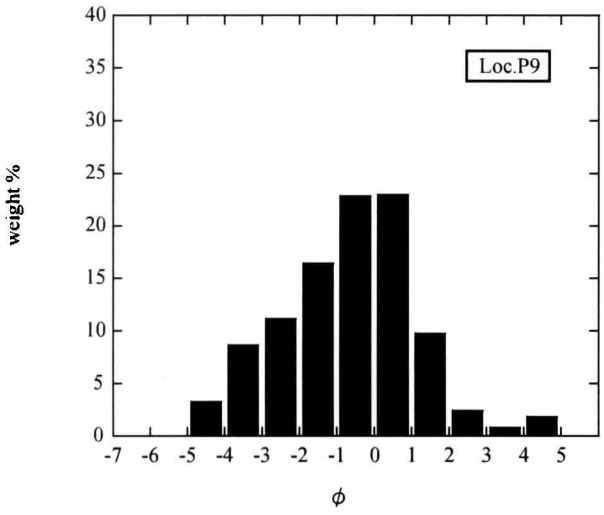

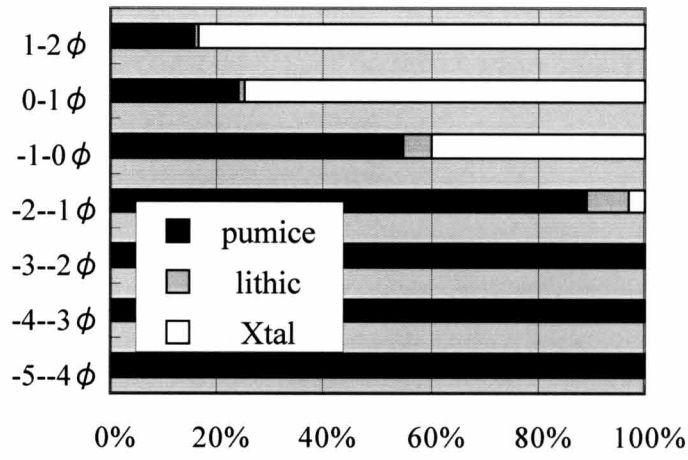

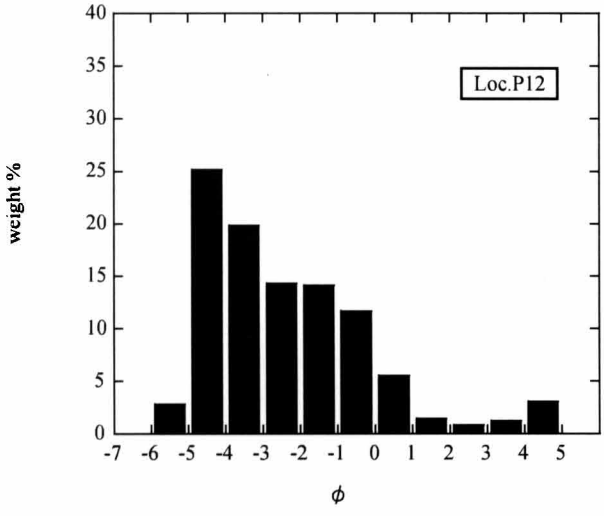

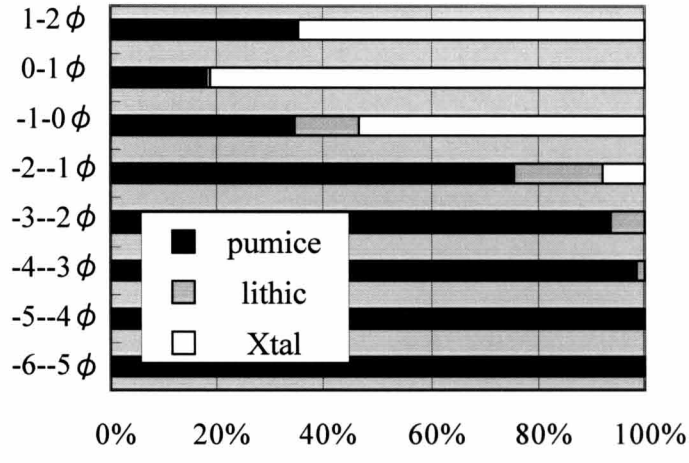

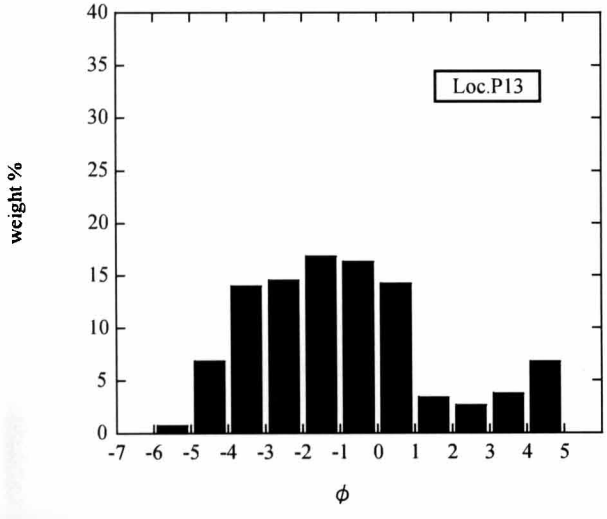

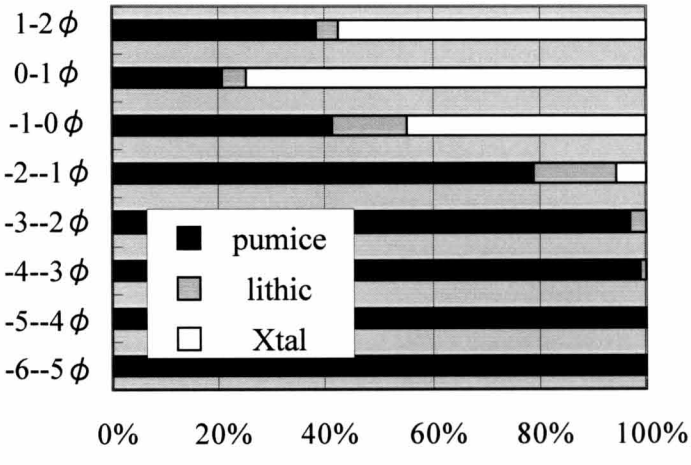

Figure 3-8 (continued)

(a)

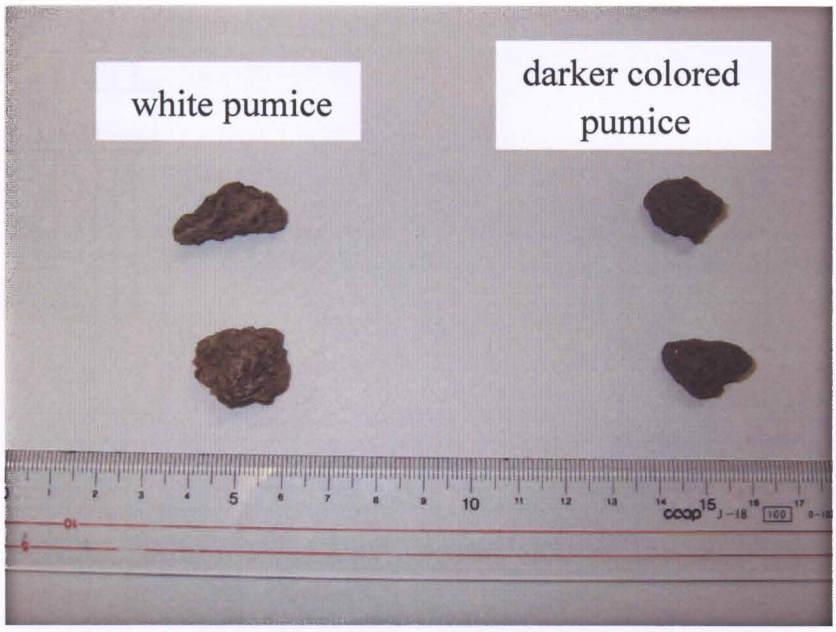

(b)

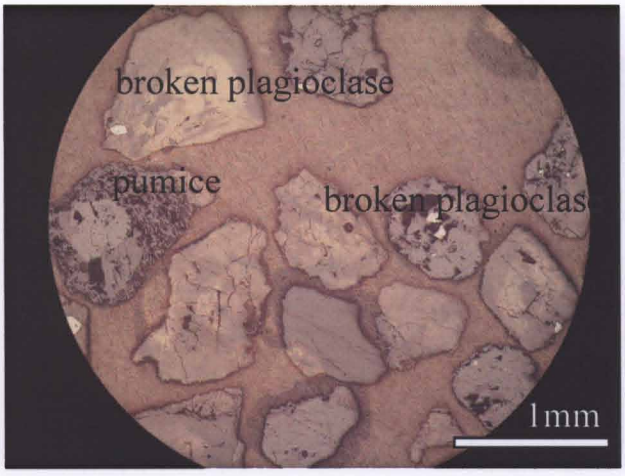

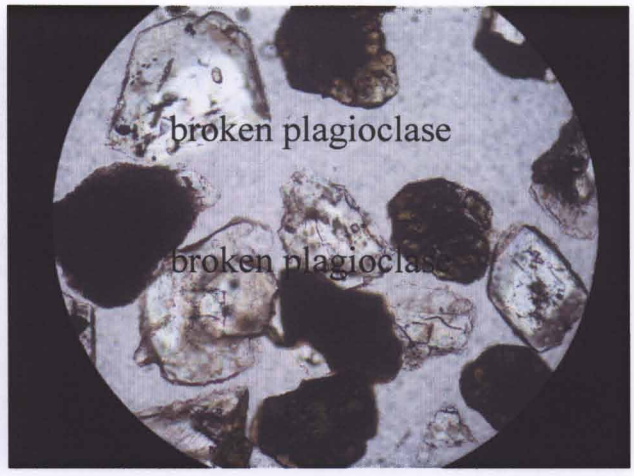

Figure 3-9 (a) Photographs of low density white pumices and high density darker colored pumices. (b) Microphotographs of the components (0-1 ϕ) of the deposit.

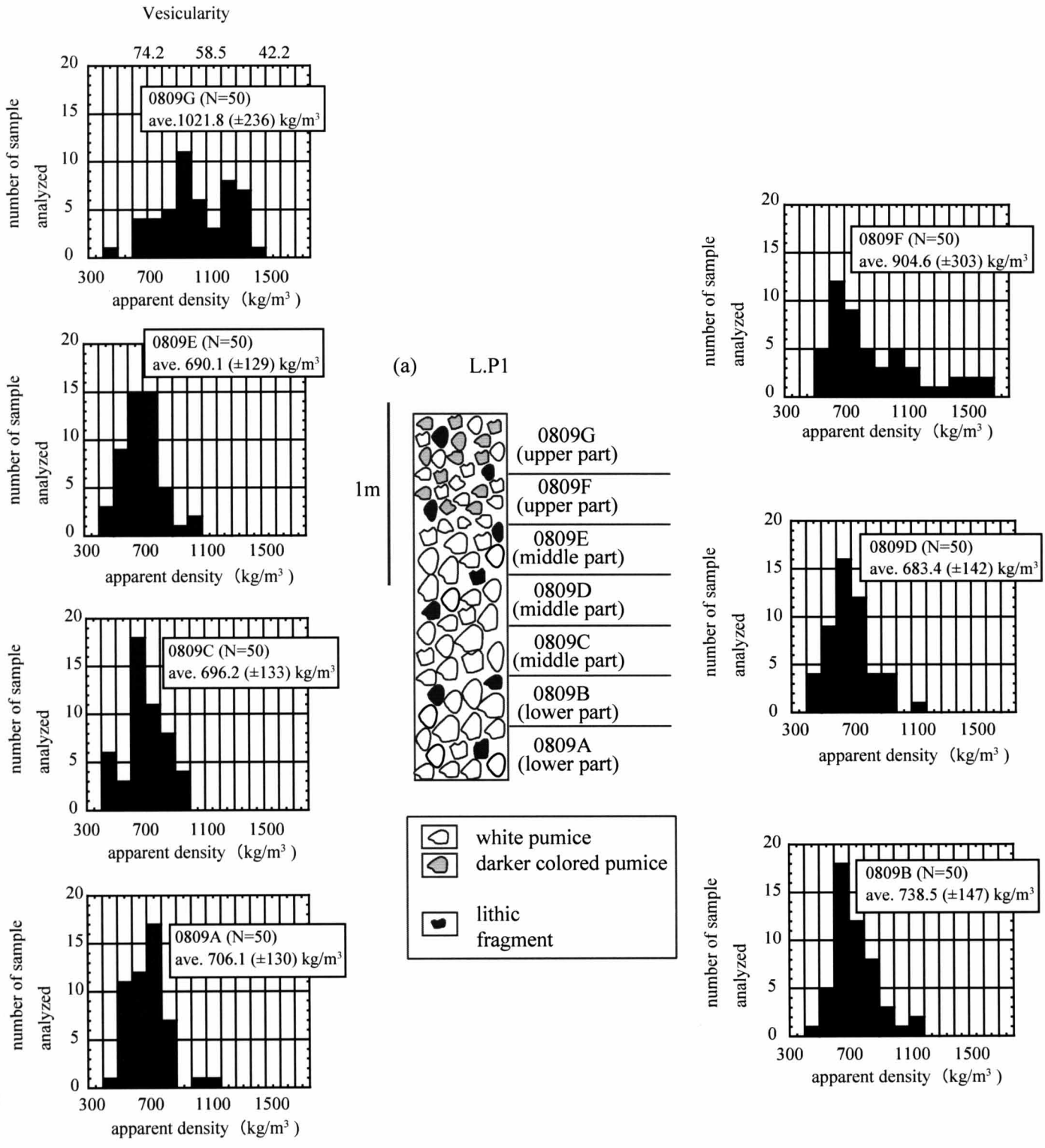

Figure 3-10 Columner section of Loc.P1 Plinian fall deposit and bulk density histograms of Plinian fall pumices from the deposit. N is number of pumices measured.

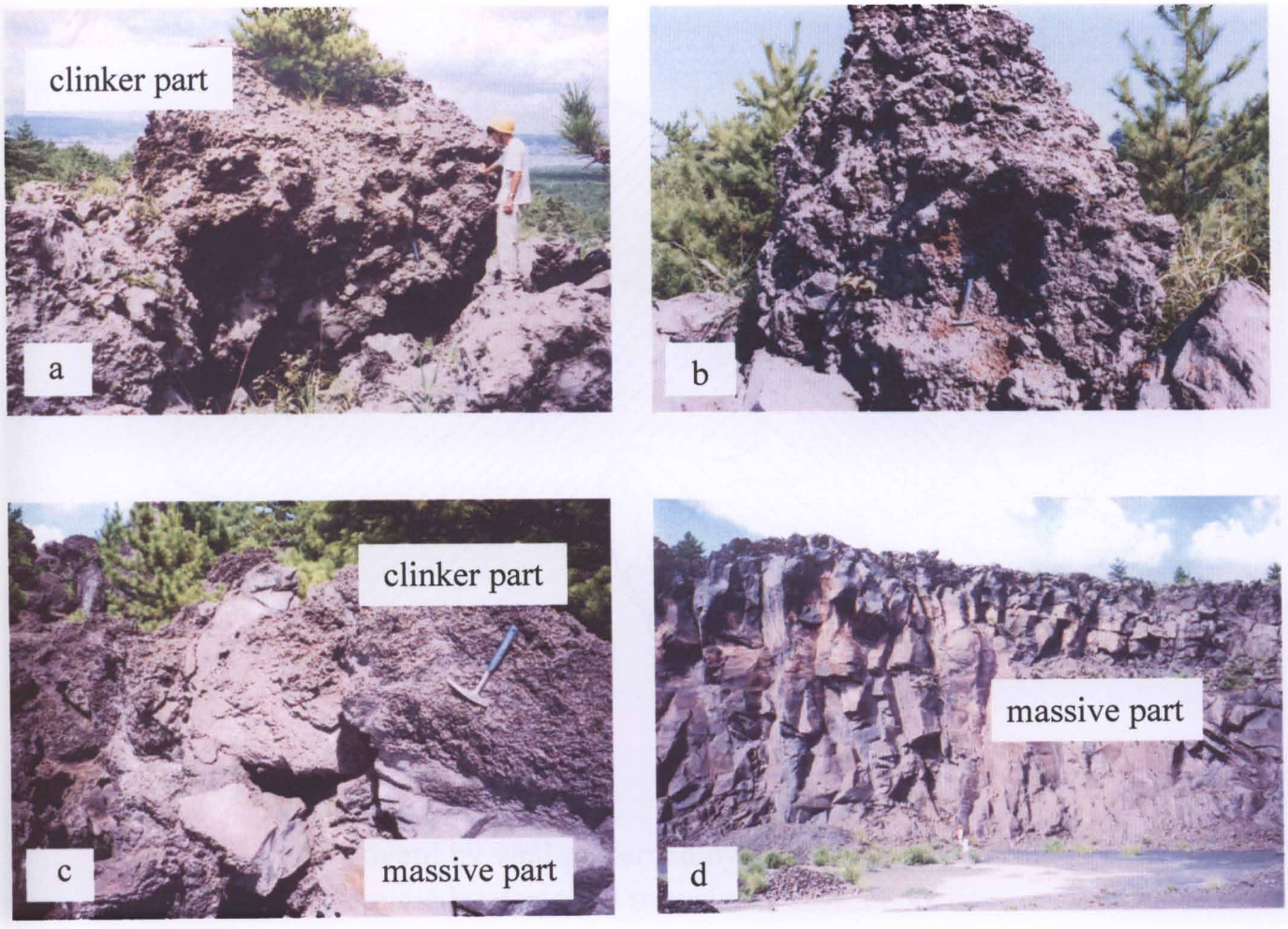

Figure 3-11 Photographs of the outcrops of Taisho lava flows. Clinker part of Taisho 1 lava flow coverd by pyroclastic flow (a) and (b). Texture of block lava of Taisho 2' lava (c). Massive sheet-like lava of Taisho 2' lava (d).

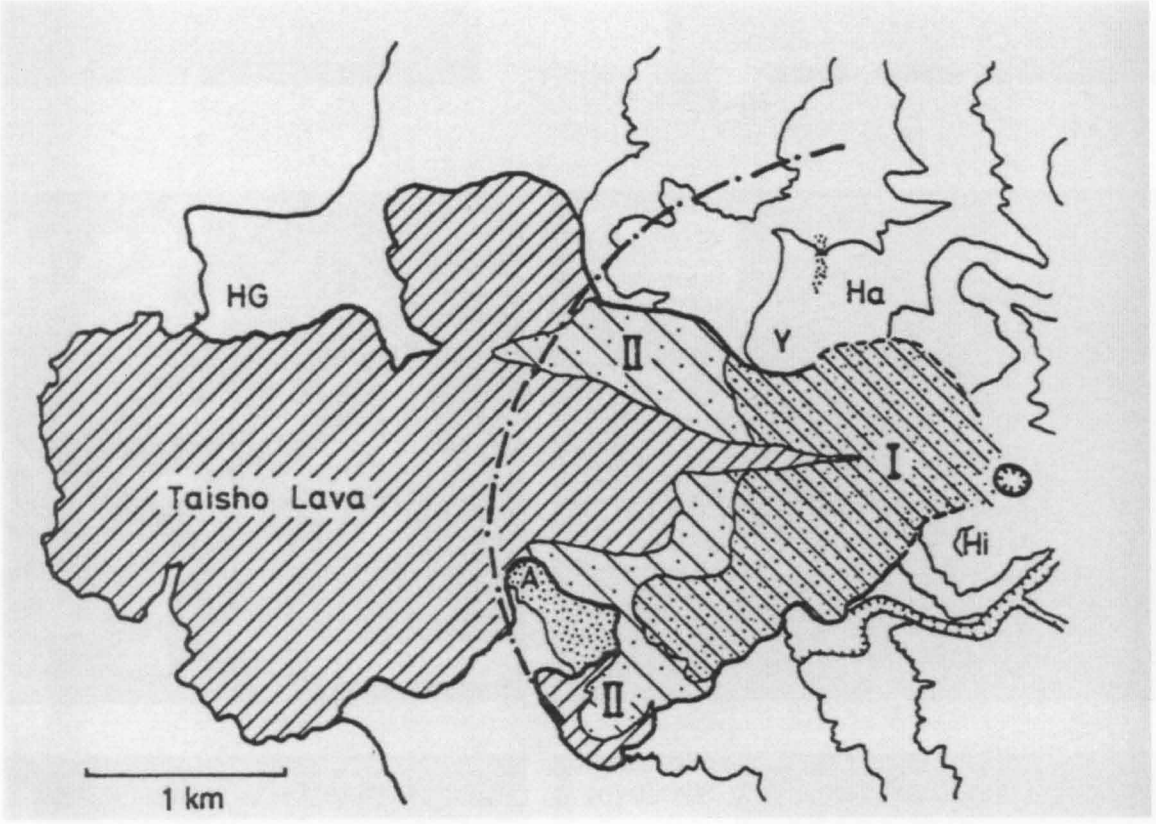

I : area coverd by well preserved pyroclastic flow deposits
II : area coverd by destoried pyroclastic flow deposits

Figure 3-12 Distribution of lava flow and pyroclastic flow in the western part of volcano. (after Kobayashi, 1986)

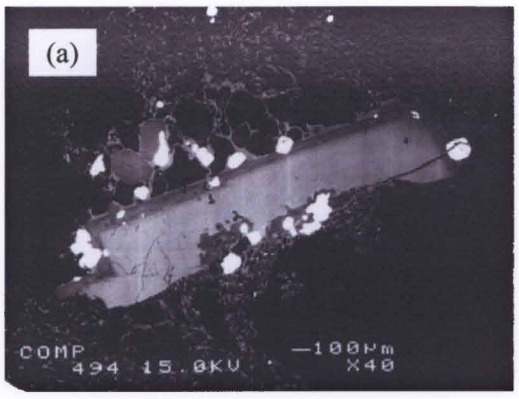

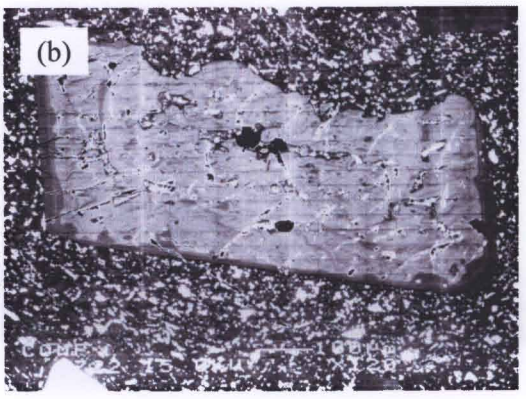

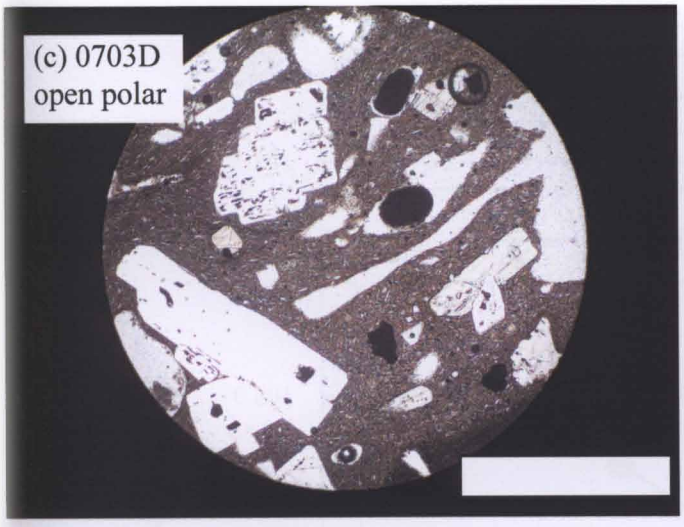

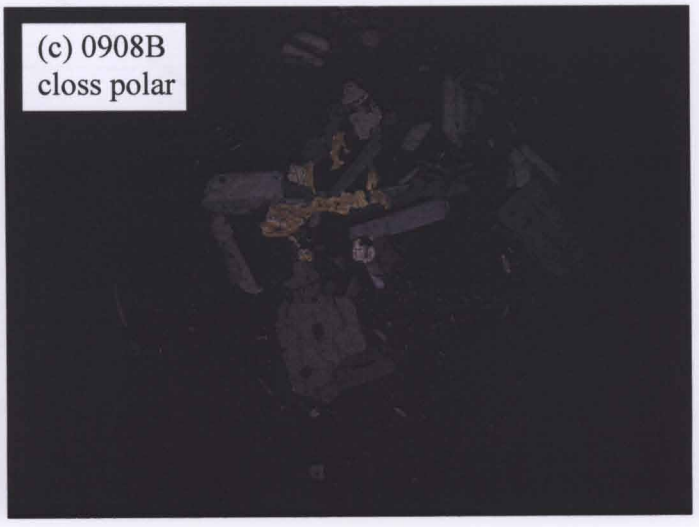

Figure 3-13 BSE images of broken plagioclase in the Plinian fall pumice (a) and lava flows (b) and microphotographs of the volcanic products (c), (d), (e) and (f).

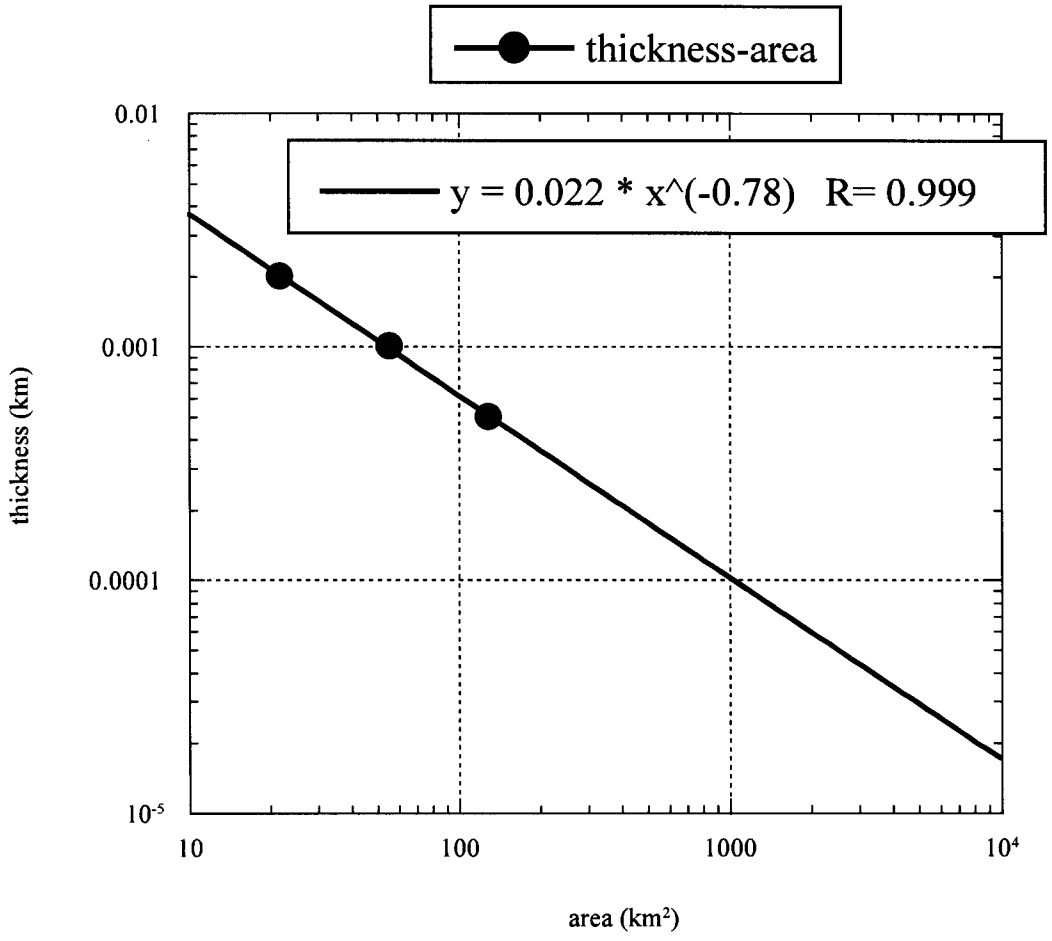

Figure 3-14 Logarithmic plot of isopach map data from Fig. 3-4.

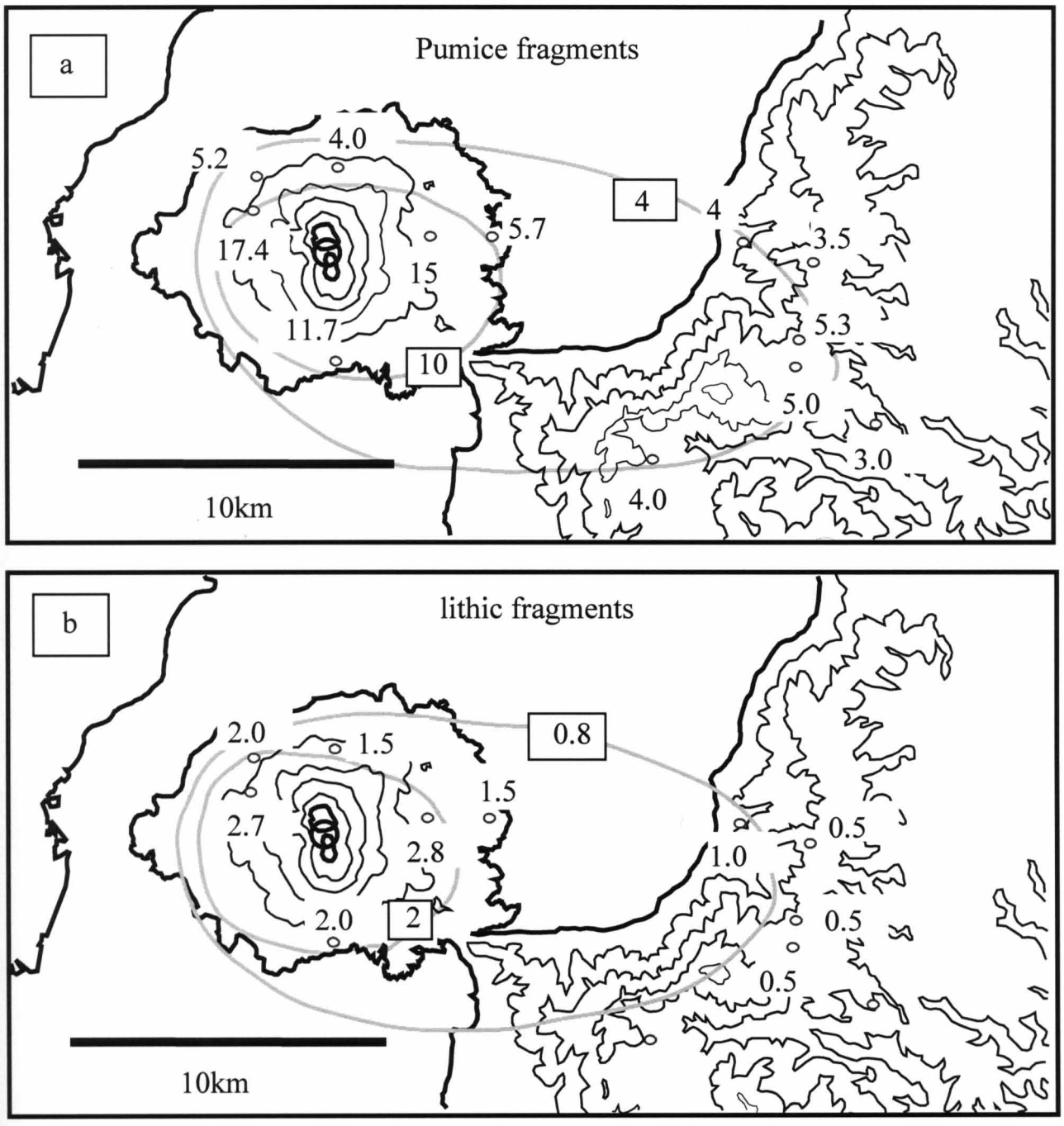

Figure 3-15 Isopleth map for Pulinian fall pumice fragments (a) and lithic fragments (b) of the 1914-1915 eruption of Sakurajima volcano. (Units are cm)

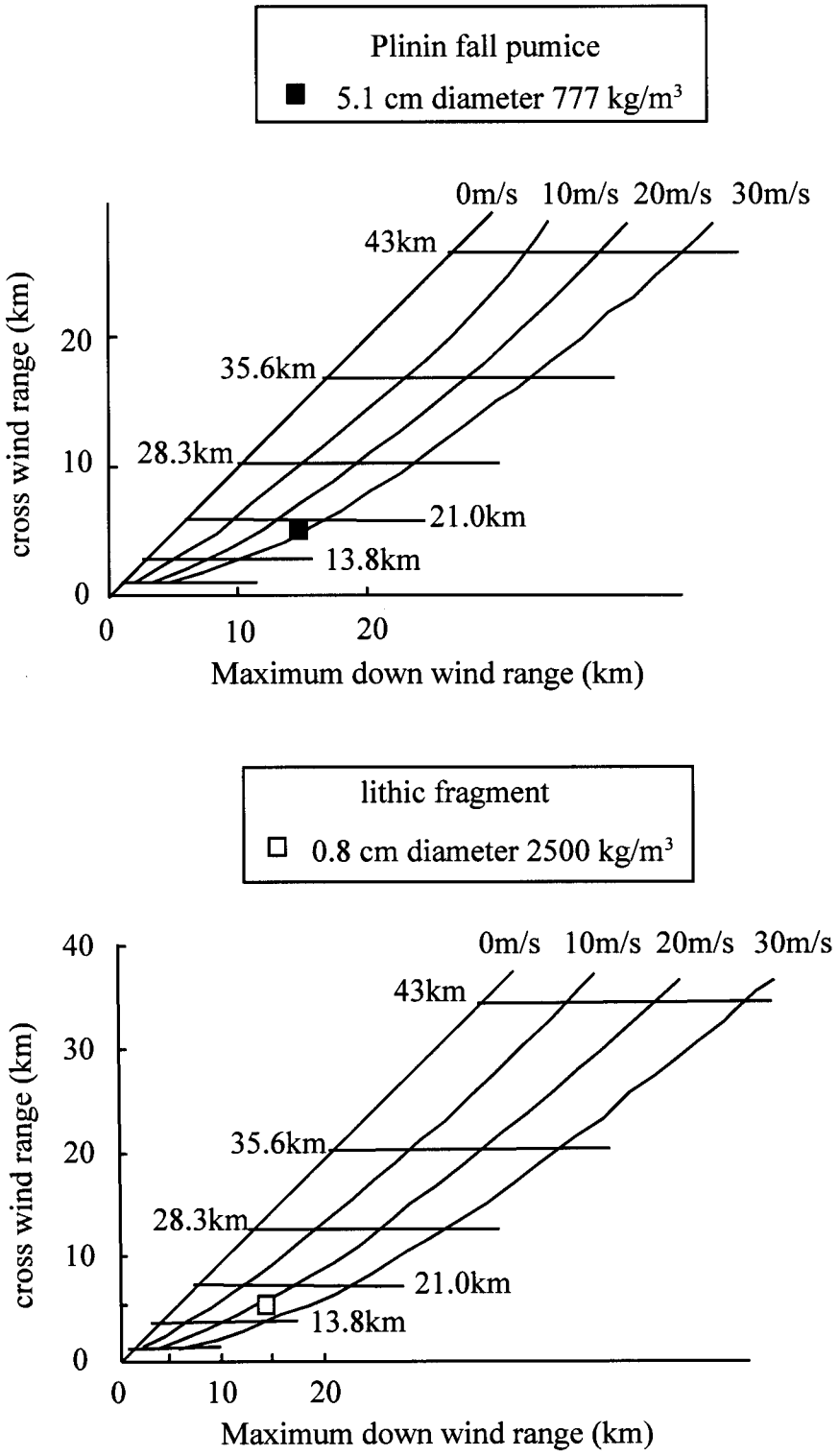

Figure 3-16 Crosswind range versus maximum downwind range for 5.1 cm-diameter and 777 kg/m^3 Plinian fall pumice and 0.8 cm-diameter and 2500 kg/m^3 lithic. (Modified from Carey and Sparks, 1986).

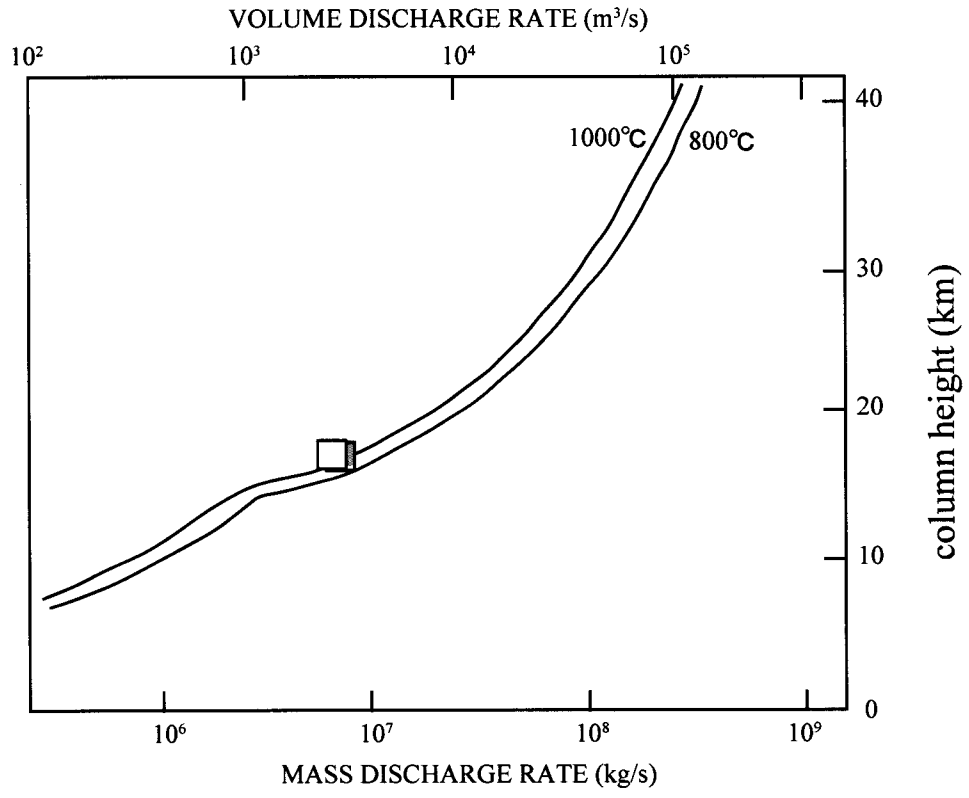

Figure 3-17 Estimation of the eruption rate from the column height by the method of Sparks (1986).

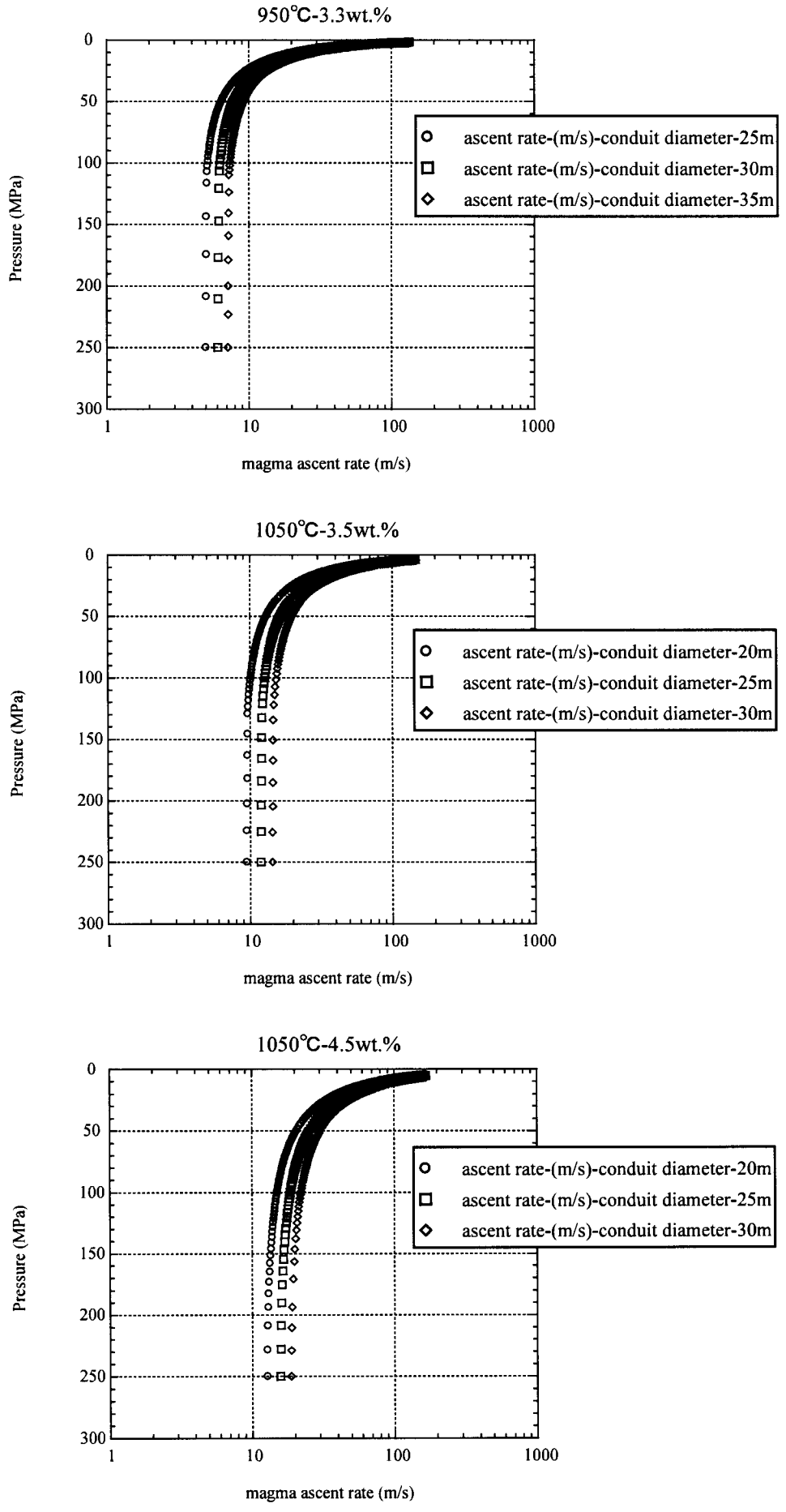

Figure 3-18 Magma ascent rate as a function of Pressure estimated from CONFLOW program.

Table 3-1 eruptive history and stratigraphy of Aira-caldera and Sakurajima volcano

Stage	Tephra name	Abbrevation	Calendar/calibrated age
"Minami-dake" stage	Sakurajima Taisho/P1	Sz-Ts/P1	AD 1914
	Sakurajima An-ei/P2	Sz-An/P2	AD 1779-1782
	Sakurajima Bunmei/P3	Sz-Bm/P3	AD 1471-1476
	Sakurajima Tenpyohoji/P4	Sz-Tn/P4	AD 764-766
	Sakurajima Minamidake Ash	Sz-Mn	4.5-1.6 ka BP
"Young Kita-dake" stage	Sakurajima P5	Sz-P5	5.6 ka BP
	Sakurajima P6	Sz-P6	3.8 ka BP
	Sakurajima Takatoge2/P7	Sz-TK2/P7	5.0 ka BP
	(Ikedako Tephra)	*Ik*	6.4 ka BP
	Sakurajima P8	Sz-P8	6.5 ka BP
	(Kikai-Akahoya Tephra)	*K-Ah*	7.3 ka BP
	Sakurajima P9	Sz-P9	7.5 ka BP
	Sakurajima P10	Sz-P10	7.7 ka BP
	Sakurajima Sueyoshi/P11	Sz-Sy/P11	8.0 Ka BP
	Yonemaru Tephra	*A-Yn*	8.1 ka BP
	Sumiyoshi-ike Scoria	*A-Sm*	8.2 ka BP
	Sakurajima Uwaba/P12	Sz-Ub/P12	9.0 ka BP
	Sakurajima Takatoge3/P13	Sz-Tk3/P13	10.6 ka BP
	Shinjima Pumice	*A-Sj*	12.8 ka BP
	Sakurajima-Satsuma/P14 Tephra	Sz-S/P14	12.8 ka BP
"Old-Kita-dake" stage	*Takano Base Surge*	*A-Tkn*	19.1 ka BP
	Sakurajima Takatoge4/P15	Sz-Tk4/P15	24 ka BP
	Sakurajima Takatoge5/P16	Sz-Tk5/P16	25 ka BP
	Sakurajima Takatoge6/P17	Sz-Tk6/P17	26 ka BP
	Aira-Tn Tephra	*AT*	29BP ka
	Kenashino Tephra	*A-Kn*	30 ka BP
	Fukaminato Tephra	*A-Fkm*	31 kaBP
	Otsuka Pumice	*A-Ot*	32.5 ka BP

Table 3-2 Eruption dynamic parameters of the 1914-1915 eruption of Sakurajima volcano

frag. Type	ρ	column height	wind velosity	magmatic temperature	eruption rate	total vol.					duration
						m^3					hours (caluculated from DRE)
cm	kg/m^3	km	m/sec	℃	m^3/sec	Estimated from Fig. 3-14		Hayakawa (1985)			
							DRE		DRE		
lithic	2500	15	20		1.0E+03						
						6.0E+08	2.4E+08				33 (11)
								7.7E+08	3.1E+08	0.5m contour	43 (17)
pumice	777	18	30	1000.0	5.0E+03			6.6E+08	2.6E+08	1m contour	37 (14)
								7.2E+08	2.9E+08	average	40 (16)

Table 3-3 Magmatic conditions for CONFLOW calculations

pre-eruptive melt composition	ave (wt.%)	mode of Xtal (pl vol.%)		H_2O (wt.%)	temperature (°C)	conduit diameter (m)	depth (m)	pressure (MPa)	mass eruption rate (kg/m)
SiO_2	70.39	10	case (1)	3.3	950	35	10000	250	1.58E+07
TiO_2	0.79	10	case (2)	3.3	950	30	10000	250	9.87E+06
Al_2O_3	14.42	10	case (3)	3.3	950	25	10000	250	5.63E+06
FeO	4.04	10	case (4)	3.5	1050	20	10000	250	6.75E+06
MnO	0.13	10	case (5)	3.5	1050	25	10000	250	1.32E+07
MgO	0.99	10	case (6)	3.5	1050	30	10000	250	2.29E+07
CaO	3.19	10	case (7)	4.5	1050	20	10000	250	8.95E+06
Na_2O	3.24	10	case (8)	4.5	1050	25	10000	250	1.72E+07
K_2O	2.81	10	case (9)	4.5	1050	30	10000	250	2.95E+07
Total	100								

Chapter 4: Petrological study of the volcanic products erupted at the 1914-1915 eruption of Sakurajima Volcano

4.1 Introduction

I discuss petrological feature of Plinian fall pumice and lava flows in this chapter. Previous petrological studies about Sakurajima Volcano were carried out by Sekine et al. (1979), Yanagi et al. (1991), Takahashi et al. (2001) and Uto et al. (2005). Yanagi et al. (1991), Takahashi et al. (2001) and Uto et al. (2005) focused on magma mixing mechanism beneath the volcano. Bulk rock chemistry of historical or pre-historical lava flows changed systematically from silicic to basic with time (Yanagi et al., 1991; Takahashi et al., 2001; Uto et al., 2005), and core composition of plagioclase phenocrysts of them changed from unimodal to bimodal, suggesting that magma mixing continuously occurred in the magma chamber (Yanagi et al., 1991).

Magma mixing or mingling varies the pre-eruptive magmatic condition in the magma chamber such as melt compositions, temperature and viscosity and is one of the most important phenomena to discuss the eruption mechanism. Recent petrological and theoretical studies revealed that injection of mafic magma to magma chamber is one of the trigger for the eruption (e.g., Murphy et al., 1998). Moreover, it is thought that chemical and physical change of magma induced magma mixing affect the microlite texture of volcanic products.

Previous chapter, it is clear that Plinian fall pumices are distinguished into two types according to their surface color and density; white-brown pumice and darker pumice. In the case of the 1914-1915 eruption of Sakurajima volcano, therefore, volcanic products are divided into five types; white-brown pumice, darker colored pumice, Taisho 1 lava, Taisho 2 lava and secondary lava. Previously proposed reasons of the difference in texture of volcanic products are (1) due to the difference in magma ascent rate which yield to the difference in degree of degassing resulting in the difference in vesicularity and density of the volcanic products (e.g., Gardner et al., 1998; Polacci et al., 2001), (2) due to magma mixing or mingling induced chemical

heterogeneity (e.g., Yasui, 1995; Takeuchi and Nakamura, 2001; Venezsky and Rutherford, 1997; Clynne, 1999), and (3) due to both magma mixing and the difference in decompression rate (e.g., Gurioli et al., 2005). In the case of (1), vesicularity and modal content of groundmass phase reflect the apparent texture of volcanic product in spite of almost the same whole rock or matrix glass (pre-eruptive matrix glass) compositions. Modal contents of microlite increase and vesicularity decrease in response to the decrease in decompression rate. In the case of (2), magma mixing is thought to be a significant trigger for the eruption. During the explosive eruption, magma mixing occurs insufficiently due to the rapid ascent of magma (Koyaguchi, 1986), resulting that volcanic products show various chemical heterogeneities such as large variation of bulk SiO_2 contents, mineral assemblages and heterogeneity of matrix glass composition (e.g., Yasui, 1995; Takeuchi and Nakamura 2001; Venezsky and Rutherford, 1997; Clynne, 1999). Chemical heterogeneities reflect the texture of volcanic products such as white, gray and banded pumice (or scoria). Both magma mixing and decompression rate of magma change the texture of volcanic products. Gurioli et al. (2005) suggested that complex change in eruption dynamics took place during the 79 AD eruption of Vesuvius from the detailed analyses of textural feature of vesicle and microphenocryst and chemical composition.

Purposes in this chapter are (1) to classify the volcanic products in terms of chemical features and (2) to reveal the effect of magma mixing to the eruption mechanism by analyzing whole rock, mineral and matrix glass compositions and combining these data with geophysical data. It is important to check the chemical feature of volcanic products in discussing the relative change of decompression rate of magma from the textural change of vesicularity and groundmass mineral of volcanic products, because it is thought that magma mixing change the chemical and physical condition of magma and affect crystallization process of microlite.

4.2 **Analytical method**

Localities of sampling points are shown in Figure 4-1. Plinian fall pumice

samples analyzed in this study were collected from L.P1 outcrop, which is located about 4 km east from Minami-dake, in Nagasakibana-quarry (Fig. 4-1). The thickness of the Plinian fall deposit is ca. 2 m (Fig. 3-10). Most of pumices in the lower to middle parts of the deposit are white pumices. Both white and darker colored pumices are observed in the upper part of the deposit. Matrix glass and minerals of both white and darker colored pumice were analyzed. Clinkery types of lava flows located at L.1, 4, 6 and 8 were selected for mineral analyses (Table 4-1).

4.2.1 **Analytical method of whole rock composition**

Whole-rock major element contents of the volcanic products erupted at the 1914-1915 eruption of Sakurajima volcano are listed in Table 4-1. Major chemical composition was determined by using Rigaku 3270 X-ray fluorescence spectrometer (XRF) system at Kobe University following the analytical procedure of Yamada and Sato (1998).

4.2.2 **Analytical method of minerals and glass compositions**

Analytical samples of Plinian fall pumices were collected from Loc.P1. Plinian fall pumices of -2 ϕ --3 ϕ size were separated from other size and selected for mineral analyses. Plinian fall pumice samples were divined into upper parts and middle to lower parts of deposits. The former is mainly slightly darker colored pumices. The latter is mainly white pumices. Clinkery types of lava flows located at L.1, 4, 6 and 8 were selected for mineral analyses. Lava flow in L. 1 is the most felsic in whole rock composition. Lava flow in L. 4 is the most felsic in whole rock composition in Taisho 2 lava. Lava flow in L. 6 is the most mafic in whole rock composition in Taisho 2 lava. Lava flow in L. 8 is the Taisho 2' lava flow.

Glass and mineral composition analyses of volcanic product were performed on a JEOL JXA-8900R at the Venture Business Laboratory of Kobe University. Glass composition analyses of volcanic products were done under the following conditions:

15 kV acceleration voltage, 12 nA beam current, 5-10 μm beam size, 4 s counting time for Na and 20 s counting time for other elements with Bence-Albee correction. Plagioclase and pyroxene composition analyses of volcanic products were done the under the following conditions: 15 kV acceleration voltage, 12 nA beam current, 10 s counting time for Na, 100 s counting time for Mg and Fe and 20 s counting time for other elements with Bence-Albee correction. Olivine composition analyses were done under the following conditions: 20 kV acceleration voltage, 50 nA beam current, 10 s counting time for Na, 100 s counting time for Ni and Ca and 20 s counting time for other elements with Bence-Albee correction. Mineral composition analyses of run products were done the under the following conditions: 15 kV acceleration voltage, 12 nA beam current, 10 s counting time for Na, 20 s counting time for other elements with Bence-Albee correction

4.3 **Result**

4.3.1 **Result of whole rock compositions**

Results of whole rock compositions are listed in Table 4-2. Figure 4-2a and Figure 4-2b show FeO*/MgO-SiO_2 and SiO_2-K_2O diagram, respectively. Taisho lava flow and Plinian fall pumice are calc-alkalic in composition. They belong to Medium-K series. Harker diagram for major element oxides plotted against SiO_2 contents are shown in Figure 4-3. SiO_2 content decreases slightly as eruption progress from 63.5 wt.% to 59.8 wt.%. While, Fe_2O_3, CaO and MgO content increase as SiO_2 content decreases linearly from 7.00 wt.% to 8.24 wt.%, from 2.13 wt.% to 3.32 wt.% and from 5.54 wt.% to 7.35 wt.%, respectively, Na_2O and K_2O content decrease linearly from 3.8 wt.% to 3.3 wt.% and from 1.9 wt.% to 1.4 wt.%, respectively with the decrease in SiO_2 content.

4.3.2 **Result of mineral and glass compositions**

The phenocryst assemblage is almost the same in the white and darker Plinian fall pumices and lava flows (Table 4-1). It is plagioclase + orthopyroxene + augite + magnetite. Olivine phenocrysts (microphenocrysts) are present slightly in Taisho 2 and 2' lavas. There observed glomeroporphyritic textures (or crystal clot) included in plagioclase, pyroxene and magnetite.

4.3.2.1 **Plagioclase**

Plagioclase phenocrysts (>100 μm in length; see also chapter 5) are almost euhedral and up to 4.0 mm in length. Plagioclase phenocrysts are classified into six types based on their texture, composition and zoning pattern. BEIs of representative plagioclase of each type and their zoning profile of An (=100*Ca/(Ca+Na)) content, FeO* content and MgO content are listed in Figure 4-4. Histograms of An contents of each types plagioclase is shown in Figure 4-5. Selected electron probe analyses are listed in Table 4-3.

Type-1 plagioclase is characterized by An-rich clear core (An_{83-92}). The calsic core has homogeneous compositions about An, MgO and FeO*. Zoning pattern from mantle to rim is various pattern, some show complex oscillatory zoning and others show no oscillatory zoning. Compositional range of rim of type-1 plagioclase is An_{49-76}.

Type-2 plagioclase has An-rich and An-poor core, showing patch-like texture in the core. An-rich parts cover most of core parts and enclose An-poor parts. The boundary of An-rich and An-poor parts is sharp. An contents of plagioclase are inversely in proportional to the MgO contents. An-rich parts show low MgO contents (~0.03 wt.%) and overlap with core of type-1 plagioclase. An-poor parts show high MgO contents (~0.08 wt.%). Type-2 plagioclase has melt inclusion in the core. Zoning pattern from mantle to rim shows various patterns, some show complex oscillatory zoning and others show no oscillatory zoning. Compositional range of rim of type-2 plagioclase is An_{41-76}.

Type-3 plagioclase is characterized by An-pore core (An_{46-68}) with small-amplitude oscillatory zoning about An from core to rim from $An_{77.3}$ to $An_{45.8}$.

MgO contents of core of type-3 plagioclase (~0.08 wt.%) show relatively higher than those of type-1 and An-rich parts of type-2 plagioclase (~0.03 wt.%), overlap with An-poor parts of type-2 plagioclase show slight reverse zoning from core to rim.

Type-4 plagioclase has melt inclusion rich core with An_{60-80} and shows honeycomb textures. There is no clear boundary between An-rich part and An-poor part, indicating that the core has heterogeneous composition about An, FeO* and MgO. Melt inclusion is relatively larger compared with those in dusty parts of type-6 plagioclase. Type-4 plagioclase shows various compositional textures from mantle to rim.

Type-5 plagioclase has melt inclusion rich mantle, showing honeycomb texture in the mantle. Core of type-5 plagioclase is characteristic in An-rich (type-1) or An-poor (type-3) in composition.

Type-6 plagioclase is observed only in Taisho 2 and Taisho 2' lava flows. Type-6 plagioclase has dusty zoned core or mantle surrounded by An-rich outer mantle and sodic rim.

4.3.2.2 **Orthopyroxene**

Orthopyroxene phenocrysts (>100 μm) are euhedral to subhedral, up to 0.8 mm in length. Orthopyroxene phenocrysts can be divided into Type-A and Type-B based on their Mg# (=100*Mg/(Mg+Fe^{2+})). Type-A orthopyroxene has Mg#-rich core (Mg#>68), while type-B orthopyroxene has Mg#-poor core (Mg#<68). Most of type-A orthopyroxene phenocrysts exhibit normal zoning in terms of Mg#, while most of Type-B orthopyroxene phenocrysts exhibit weak reverse zoning. Orthopyroxene of both types in Taisho 2 and Taisho 2' lava have pigeonite rim. Mg# of pigeonitic rim in Taisho 2 and 2' lava overlaps with pigeonite microlite. Compositional range of core and rim of them and zoning profile of Mg# are shown in Figure 4-6 and Figure 4-7, respectively. Average compositions of core and rim with 1σ are summarized in Table 4-4.

4.3.2.3 **Augite**

Augite phenocrysts (>100 μm) are euhedral to subhedral, up to 1.2 mm in length. Core compositions of augite phenocrysts range from Mg#=66 to Mg#=78 and can be divided into type-a, type-b and type-c. Augite phenocrysts of type-a have Mg#-rich core (75>Mg#>69). Most of type-a augite exhibit oscillatory zoning from core to rim and normal zoning in rim in terms of Mg#. Augite phenocrysts of type-b have Mg#-pore core (Mg#<69). Most of type-b augite exhibit weak reverse zoning in rim in terms of Mg#. In Taisho 2 and Taisho 2' lava flow, some of both types augite phenocrysts have clear reverse zoning rim in terms of Mg#. Type-c phenocrysts have the most Mg#-rich core (Mg#>75) and are included in Taisho 2 and Taisho 2' lava flow. Augite of all types in Taisho 2 and Taisho 2' lava have pigeonitic rim. Mg# of pigeonitic rim of augite phenocrysts overlaps with Mg# of pigeonite microlite. Compositional range of core and rim of them and zoning profile of Mg# are shown in Figure 4-8 and Figure 4-9, respectively. Average compositions of core and rim with 1σ are summarized in Table 4-4.

4.3.2.4 **Olivine**

Olivine phenocrysts or microphenocrysts are euhedral, up to 0.2 mm in length. Olivine phenocrysts are present slightly in Taisho 2 and 2' lavas. Fo (=100*Mg/(Mg+Fe^{2+})) contents of core of olivine phenocrysts or microphenocrysts are in range of Fo_{69} to Fo_{81}. Most of olivine phenocrysts or microphenocrysts show normal zoning from core to rim and have reaction rim of pigeonite. Average compositions of core with 1σ are summarized in Table 4-5.

4.3.2.5 **Groundmass minerals**

The microlite assemblages in all samples are orthopyroxene, pigeonite, augite, titanomagnetite, and plagioclase.

Table 4-6 shows the average compositions of plagioclase microlites. Anorthite content of plagioclase microlites of Plinian fall pumices ranges from An_{46} to An_{50}. Anorthite content of those of Taisho 1 lava flows is about An_{50}. That of Taisho 2 and 2' lava flows is, however, about An_{52-62}, which is more anorthitic in compositions. FeO and MgO contents of plagioclase microlite are negative correlation with An content of plagioclase microlite.

Orthopyroxene and pigeonite predominate in Taisho 1 lava flows. Augite, pigeonite and orthopyroxene are the main phase of pyroxene microlite in Taisho 2 and 2' lava flows. Compositional ranges in Mg# of pyroxene microlite are shown in Figure 4-10 and Table 4-7. In most of pumices, microlites (crystallites) are too small to analyze. Available data for pumices are from crystalline darker Plinian fall pumices collected from the upper part of the deposit.

4.3.2.5 **Glass composition**

The matrix glass of both Plinian fall pumices and lava flows have rhyolitic compositions (Table 4-8). SiO_2 contents of matrix glass of Plinian fall pumices is in a range of 68-73 wt.%, and is slightly correlated with the modal content of the groundmass. Matrix glass compositions of Taisho 1 lava flows have more evolved compositions (SiO_2 contents are 75-78 wt.%), compared with those of Plinian fall pumices. SiO_2 contents of matrix glass of Taisho 2 and 2' lava flows ranges from 71-77 wt.% and from 73-74 wt.%, respectively, which are slightly more basic compositions compared with Taisho 1 lava flows. CaO, MgO, Al_2O_3 and FeO* contents of matrix glass decrease from Plinian fall pumices to Taisho 1 lava flows and slightly increase from Taisho 1 lava flows to Taisho 2 and 2' lava flows. K_2O contents of matrix glass increases from Plinian fall pumices to Taisho 1 lava flows and slightly decreases from Taisho 1 lava flows to Taisho 2 and 2' lava flows.

Per-eruptive melt compositions are estimated from groundmass glass and microlite mineral compositions, modal content of glass and microlite mineral and density of groundmass glass and microlite minerals (Table 4-9). Groundmass glass

and calculated pre-eruptive melt compositions at magma chamber are shown in Table 4-9 and Figure 4-11. SiO_2 contents of melt composition of Plinian fall pumice and Taisho 1 lava flow are around 67-70 wt.%. Those of Taisho 2 and Taisho 2' lava flow are around 69-64 wt.%, which are slightly lower than those of Plinian fall pumice and Taisho 1 lavas. CaO content of groundmass glass and pre-eruptive melt increases linearly in response to the decrease in SiO_2 contents.

4.4 **Discussions**

4.4.1 **Overview of magma mixing**

Many disequilibrium features are observed in 1914-1915 andesite of Sakurajima volcano. They are ;

1) Bimodal distribution of core of plagioclase, orthopyroxene and clinopyroxene phenocrysts

2) Existence of normal and reverse zoning plagioclase, orthopyroxene and clinopyroxene phenocrysts.

3) Occurrence of dusty zoned plagioclase phenocrysts.

These features are considered to be the evidence of magma mixing. Figure 4-3 and Fig 4-11 show the linear trend of whole rock and groundmass glass chemical composition, verifying that magma mixing occurred. Per-eruptive melt compositions of magma in the magma chamber, which also change in response to magma mixing, were estimated from groundmass glass and microlite mineral compositions, modal content of glass and microlite mineral and density of groundmass glass and microlite minerals (Table 4-9). SiO_2 contents of melt composition of Plinian fall pumice and Taisho 1 lava flow are around 67-70 wt.% (Fig. 4-11), indicating that microlite crystallize from chemically homogeneous melt. Those of Taisho 2 and Taisho 2' lava flow are around 69-64 wt.%, which are slightly lower than those of Plinian fall pumice and Taisho 1 lavas. Pre-eruptive melt compositions became chemically heterogeneity as the eruption proceed, indicating that magma mixing occurred in the magma chamber

or conduit during the eruption.

4.4.2 **Magma mixing revealed by phenocrysts assemblage**

The 1914-1915 andesite of Sakurajima volcano included various types of plagioclases, two types of orthopyroxene and three types of augite. In this section, origins of these mineral assemblages are discussed in relating to magma mixing.

4.4.2.1 **Pyroxene and olivine**

Both orthopyroxene and augite phenocrysts divide into two or three types in terms Mg# of core and compositional change from core to rim. High Mg# orthopyroxene (type-A) and augite (type-a), which show slight normal zoning at rim, are thought to be driven from mafic magma. On the other hand, Low Mg# orthopyroxene (type-B) and augite (type-b), which show slight reverse zoning at rim, are thought to be crystallized from felsic magma. Type-c augite and olivine microphenocrysts observed in Taisho 2 and 2' lava are thought to be driven from more non-differentiation mafic magma.

Equilibrium relations between olivine and pyroxene phenocryst, microphenocryst or phenocryst rim were examined by the method of Sakuyama (1979) (Fig. 4-12) to identify the above discussions. This method examines Mg-Fe^{2+} partitioning between them to clarify the equilibrium relations. Average compositions with 1 σ of each minerals are shown in Figure 4-12a for olivine-orthopyroxene relations and Figure 4-12b for olivine-augite relations, respectively. Solid circles are compiled equilibrium pairs determined experimentally in basaltic to andesitic systems, and dashed line shows the equilibrium partition coefficient between olivine and pyroxene. The core of olivine cannot coexist in equilibrium with core of type-A, type-B orthopyroxene, type-b augite and type-a augite. Core of some type-c augite and sharp reverse zoning rim of type-b augite both contained in Taisho2 and Taisho2' lava can coexist in equilibrium with core of olivine (Fig. 4-12). These results indicate that there are three end-member

magmas; felsic end-member magma, mafic end-member magma and more non-differentiation mafic end-member magma. Early to middle stage of the eruption, felsic end-member and mafic end-member mixed and erupted as Plinian fall pumice and Taisho 1 lava. Late stag of the eruption more non-differentiation mafic end-member magma mixed with felsic and mafic end-member magma and erupted as Taisho 2 and 2' lava. Linear trend of harker diagram indicates that mafic end-member magma and more non-differentiation mafic end-member magma are both the same origin.

4.4.2.2 **Magmatic temperature**

Pre-eruptive magmatic temperature of both mafic end-member magma and felsic end-member magma were calculated from the coexisting orthopyroxene and augite pairs using QUILF program of Lindsley and Frost (1992). Magmatic temperature of more non-differentiation mafic end-member magma was also estimated from the coexisting augite olivine pair using the method of Loucks (1996). Assumption of lithostatic pressure is 2000 bar, corresponding with 8-10 km.

Temperature of felsic end-member magma estimated from Low Mg# augite and Low Mg# orthopyroxene pairs is 988-1039 ℃. That of mafic end-member magma estimated from High Mg# augite and high Mg# orthopyroxene is 1051-1082 ℃, which is slightly higher than that of felsic end-member magma. Temperature of mafic end-member magma estimated from high Mg# augite and olivine is 1138-1208 ℃.

Pre-eruptive mixed magmatic temperature was calculated from rim of orthopyroxene and augite phenocrysts and is 1026-1078 ℃.

4.4.2.3 **Plagioclase**

Plagioclase phenocrysts are divined into six types according to An content of core and morphology, and are recorded in various phenomena occurring in the magma chamber or during magma ascent.

Bimodal distributions of the core composition of plagioclase phenocryst between

An_{58} (type-3) and An_{85} (type-1) were thought to be a result of magma mixing in previous studies (Sakuyama, 1981; Yanagi et al., 1991). Origin of type-1 plagioclases is mafic magma. On the other hand, type-3 plagioclases are derived from silicic magma. Moreover, patch-like (type-2) or honeycomb plagioclase (type-4 and -5), and dusty zoned plagioclase (type-6) are caused for reheating and recrystallization of plagioclase at higher temperature (Kawamoto, 1992; Tsuchiyama, 1985; Nakamura and Simakita, 1996; Tsune and Toramaru, 2004). Reheating of plagioclase require heat, suggesting that injection of high temperature mafic magma to the low temperature silicic magma occurred in the magma chamber. Tsuchiyama (1985) and Nakamura and Simakita (1996) experimentally produce dusty zoned plagioclase (type-6) by reheating plagioclase above its equilibrium solidus temperature but below its liquidus. Type-6 plagioclase include in only Taisho 2 and Taisho 2' lava flow. Difference in temperature between felsic end-member magma and mafic end-member magma is about 12-94 ℃. Difference in temperature between felsic end-member magma and more non-differentiation mafic end-member magma is about 99-120 ℃. Large difference of temperature between felsic and more non-differentiation mafic magma may induce the reheating of sodic plagioclase, resulting in crystallization of dusty zoned plagioclase. Hence, bimodal distributions of the core composition of plagioclase phenocryst between An_{58} (tyepe-3) and An_{85} (type-1), existences of patch-like (type-2) or honeycomb plagioclase (type-4 and -5), and dusty zoned plagioclase (type-6) indicate that high An plagioclase with clear core (type-1) may be driven from mafic magma and that the origin of low An plagioclase (type-3) may be felsic magma.

Ever proposal causes of oscillatory zoning of An content from core to rim are (1) fractional crystallization, (2) magma mixing, (3) change in total pressure, (4) change in temperature, (5) change in H_2O content and (6) change of undercooling. (1) and (2) cause the change of melt composition and affect the An content. On the other hand, (3), (4), (5) and (6) induce the change of partition coefficient of Ca and Na, affecting the An content. Magma mixing induces several physical change of magma such as change of melt compositions, temperature and H_2O content, indicating that multiple cause induce oscillatory zoning of An content. Tsune and Toramaru (2004) mathematically

simulated the evolution the plagioclase texture by mixing of evolve and non-evolve magma and illustrated that dusty zoned plagioclase crystallize in case that degree of melt SiO_2 contents of both mafic and felsic end-member magma is large. In the case of small difference in melt SiO_2 content of mafic and felsic end-member magma, mixing induced textural evolution of plagioclase phenocrysts are dominant by the oscillatory zoning from mantle to rim. Decrease in bulk rock and pre-eruptive melt SiO_2 contents of Taisho 2 and 2' lava suggests that newly more non-differentiation mafic end-member magma injected to the already mixed magma in the magma chamber and that degree of SiO_2 contents of pre-eruptive melts became large. Actually, pre-eruptive melt estimated from groundmass glass and modal content of microlite change from silicic in Plinian fall pumice and Taisho 1 lava (SiO_2 = 67-70 wt.%) to basic in Taisho 2 and Taisho 2' lava (SiO_2 = 64-69 wt.%) (Fig 4-11). By combining petrograhical data of plagioclase, experimental results of Tsuchiyama (1985) and Nakamura and Simakita (1996) and the simulation of Tsune and Toramaru (2004), it interpreted that dusty mantle of type-6 plagioclase crystallize during the mixing period of more non-differentiation mafic end-member magma and previously mixed magma during eruption due to reheating, consistent with the interpretation of coexistence pairs of orthopyroxene, augite and olivine and chemical change of pre-eruptive groundmass glass composition. Type-2, type-4, and type-5 plagioclase crystallized during all phase of mixing period. Oscillatory zoning of An content from core to rim of type-3 plagioclase and from mantle to rim of type-1 and -2 plagioclases in the products of 1914-1915 eruption is thought to be a result of (1) magma mixing of mafic and felsic end-member magma, (2) change of temperature, (3) change of total pressure and (4) change of H_2O content of magma.

4.4.3 **Trigger of eruption**

4.4.3.1 **Injection of mafic magma to the magma chamber**

Trigger for eruption is to uprise of magma from magma chamber due to increase

in buoyant force of magma and/or increase in overpressure of magma chamber due to injection of new magma to the magma chamber, vesiculation of volatile content or tectonic movement around the magma chamber (Aramaki, 1975). Recently, it has been cleared that injection of mafic magma to the felsic magma chamber plays an important role in the trigger of the eruption (e.g., Blake, 1981; Folch and Marti, 1998; Sparks et al., 1977). Injection of mafic magma to the magma chamber induces increase in pressure of magma chamber or buoyant force of magma according to the following processes;

(a) Increase in the total volume of magma in the magma chamber (Blake, 1981) and volume of magma body exceed the volume of magma chamber.

(b) Crystallization of injected high-temperature magma by the cooling of overlying low-temperature magma leads to the volatile saturation in high temperature magma. Then, the exsolved volatile phase is supplied to high-temperature magma, resulting in pressure increase in low-temperature magma (Folch and Marti, 1998; Coombs et al., 2002).

(c) Injected high-temperature magma heats the overlying low-temperature magma until it exsolves volatile phase (Sparks et al., 1977), resulting in increase in pressure of low-temperature magma.

In the case of the 1914-1915 eruption of Sakurajima volcano, there are many petrological evidence of magma mixing. In the previous section, it is clear from the bimodal composition of plagioclase An contents and pyroxene Mg# contents that magma mixing occurred before the eruption. Dusty zoned plagioclase and Low Mg# augite with high Mg# rim both contained in Taisho 2 and 2' lava flows erupted at the late stage of lava effusive phase. These results indicate that magma mixing continued during the eruption.

Associated with the increase in overpressure of magma chamber due to the tectonic movement around the magma chamber, in the case of the 1707 eruption of Mt Fuji, large seismic activity generated 48 days before the large eruption, suggesting that tectonic movement around the magma chamber with critical condition caused the large eruption. On the other hand, the migration or intrusion of magma also cause

generation of the seismic activity, called as volcanic earthquakes (A-type earthquake) and causes the explosive eruption such as the 1991 eruption of Mt Pinatubo. Mogi (1957) and Yokoyama (1971) estimate that the depth of magma chamber is 7-10 km by applying the deformation model of elastic body to the ground deformation. Yamashina (2001) discussed that volume of magma chamber about 10 km beneath Aira caldera estimated from leveling data and the inflation volume at the center of Aira caldera (0.8-1.3 km^3) is smaller than the volume of volcanic product erupted at the 1914-1915 eruption (Plinian fall pumice, ash (0.29 km^3) and lava flow (1.34 km^3)). Magma supply rate to the magma chamber beneath the Aira caldera may be c.a. 10 million m^3/s (Nagaoka et al., 2001) estimated from the inflation volume of Aira caldera since the 1779 eruption of Sakurajima volcano and leveling data. In this case, total inflation volume is 1.3 km^3, which is slightly smaller than total volume of volcanic products erupted at the 1914-1915 eruption (about 1.63 km^3; DRE). Yamashina (2001) suggested that magma supply far beneath the 10 km magma chamber just before or during the eruption. Actually, large earthquake started on the morning of January 10, 1914 according to the historical record (O-mori, 1916). Takahashi and Takahashi (1995) and Takahashi et al. (2001) proposed that magma chamber 10 km beneath from Aira caldera represent the felsic magma and that mafic magma supply from south-west of Sakurajima volcano beneath 15 km depth (Fig. 3-4b). Takahashi and Takahashi (1995) and Takahashi et al. (2001) suggest that magma mixing occur at magma chamber 3-6 km beneath the volcano. It is not well known about magma supply system beneath Sakurajima volcano. Both petrological feature and leveling data, however, indicate that seismic activity begun on the morning of January 10, 1914 was associated with the injection of mafic magma into the magma chamber during the seismic activity period and trigger the explosive eruption.

4.4.3.2 **Magmatic condition in the chamber**

Injection of mafic magma is a trigger for the eruption of the 1914-1915 eruption of Sakurajima volcano. Analogue experiments of magma mixing revealed that magma

mixing occur ineffectively in the case of explosive eruption (Koyaguchi, 1986), resulting that explosive volcanic products show chemically or texturally heterogeneity. Actually, chemically heterogeneous volcanic products erupted at the Plinian phase of the eruption within a single eruption cycle in many volcanoes such as the 1991 eruption of Mt Pinatubo (Polacci et al., 2001), the 2.2 ka eruption at Mt Rainier (Venezky and Rutherford, 1997) and the 1915 eruption of Lassen peak (Clynne, 1999). Chemical heterogeneities of matrix glasses of volcanic products are observed in the late stage of effusive phase (Taisho 2 and Taisho 2' lava). White pumice, darker colored pumice and Taisho 1 lava, however, show the almost same chemical features of bulk rock composition, matrix glass composition and phenocryst assemblage. Bimodal distribution of An contents of plagioclase phenocryst in the both white and darker colored Plinian fall pumices is a strong evidence of magma mixing. Hence, it is thought that mafic and felsic magma mixed efficiently before the eruption in the magma chamber.

Magma mixing processes in the magma chamber are for example (1) convective entrainment (Snyder and Tait, 1996), (2) gravitational overturn introduced by vesiculation (Huppert et al., 1982; Blake and Ivey, 1986) and (3) turbulent fountaining by injection (Campbell and Turner, 1988). In the case of (1), injected mafic magma is dragged upward and is mixed with limited amount of superior felsic magma, resulting in erupting of chemically heterogeneous pumice. Mixing model of (1) cannot be explained the mixing process of the 1914-1915 eruption. In the case of (2), (3), stratified two magma with different density mixed efficiently in the magma chamber, resulting in chemically homogeneity of magma. Associated with (2), recent studies revealed that volatile or fluid play an important role in magma mixing processes. Generation of bubbles in the boundary layer in the stratified magma chamber has been proposed by Murphy et al. (2001) and Coombs et al (2002) as a formation mechanism of mafic inclusion. Huppert et al. (1982) suggest that transfer of heat from underlying mafic magma to overlying felsic magma introduce the crystallization and exsolution of volatile of underlying mafic magma, resulting in the generation of bubble. Generation of bubbles in the underlying mafic magma leads to the decrease in the density, resulting

in the intimate magma mixing. Simakin and Botcharnikov (2001) also suggested that generation of bubbles in the stratified magma chamber leads to large-scale convective mixing of magma. In the case of Sakurajima volcano, difference in magmatic temperature of both magmas is relatively small, compared with other volcanoes such as the 2.2 ka eruption of Mt Rainier (Venezky and Rutherford, 1997) and Soufriere Hills volcano (Murphy et al., 1998; Murphy et al., 2001). It is doubtful that efficient vesiculation of mafic magma occur due to cooling by overlying silicic magma. In the case of (3), driving force for magma mixing is injection of mafic magma to the silicic magma chamber. Campbell and Turner (1988), however, pointed out that magma mixing induced by injection occur little or did not occur in the case of large difference of viscosity of two end-member magma such as basaltic magma and granitic melt. In the case of the 1914-1915 eruption of Sakurajima volcano, efficient magma mixing may be induced by gravitational overturn introduced by vesiculation (Huppert et al., 1982; Blake and Ivey, 1986) and/or turbulent fountaining by injection (Campbell and Turner, 1988). However, further studies to understand the mechanism of mixing process in the magma chamber are needed.

4.4.3.3 **Models for the trigger of eruption and for the textual change of phenocrysts**

By combining the petrochemical data of this study and previous geophysical works on the 1914-1915 eruption of Sakurajima volcano, estimated magma mixing and eruption model are as followed (Fig. 4-13).

Firstly, magma supply and magma mixing occurred continuously at the magma chamber maybe beneath the Aira caldera (Fig. 4-13a) after the 1779 eruption of Sakurajima volcano. During this period, core of type-2 and type-4 plagioclase, reverse zoning mantle of type-3 and honeycomb mantle of type-5 plagioclase and rim of orthopyroxene and augite crystallized. Before the 1914-1915 eruption, magma chamber beneath the Aira caldera was occupied with the mixed magma (bulk SiO_2 content was about 62-63 wt.%).

Injection of mafic magma to the magma chamber began on the morning of

January 10, 1914, resulting in the occurrence of seismic activity (Fig. 4-13b). Overpressure in magma chamber increased and exceeded the excess pressure of magma chamber (maybe, more than 10MPa; Tait et al., 1989), resulting in ascent of magma.

From the Plinian phase to Taisho 1 lava effusive phase of eruption, previously mixed magma (bulk SiO_2 content was about 62-63 wt.%) erupted as Plinian fall pumice and Taisho 1 lava flow. Shift from white Plinian fall pumice, darker colored pumice to Taisho 1 lava mainly reflects the decrease in decompression rate of magma because the bulk and pre-eruptive melt composition are almost homogeneous. In the lower part of magma chamber, previously mixed magma mixed with newly injected mafic magma, resulting in decrease of bulk and pre-eruptive melt SiO_2 content and reheating of felsic magma. Dusty mantle of type-6 plagioclase and rim of type-b augite crystallized during this period.

During late stage of lava effusive phase, newly mixed magma (bulk SiO_2 content was about 59 wt.%) erupted as Taisho 2 and 2' lava. Continuous injection of mafic magma and magma mixing occurred in the conduit during magma ascent (Koyaguchi, 1986), resulting in shift of matrix glass compositions from silicic to basic, crystallization of dusty zoned plagioclase, and crystallization of calcic plagioclase microlite (Fig. 4-13c).

4.5 **Summary**

The magmatic processes involved in the product of the 1914-1915 eruption from Sakurajima volcano were investigated on the basis of petrological analyses.

1. The volcanic products from the 1914-1915 eruption of Sakurajima volcano show the evidence of magma mixing; linear compositional trends of whole rock and matrix glass compositions of the erupted materials, bimodal distribution of An content of plagioclase phenocrysts and Mg# content of clinopyroxene and orthopyroxene phenocrysts, and existence of dusty zoned plagioclase.

2. There are three end-member magma; felsic low temperature (988-1039 ℃)

magma with sodic plagioclase and low Mg# pyroxene, basic high temperature (1051-1082 ℃) magma with high An plagioclase and high Mg# pyroxene, and more non-differentiation mafic end-member magma (1138-1208 ℃) with high An plagioclase, high Mg# pyroxene and olivine.

3. Trigger for the eruption is an injection of more non-differentiation mafic end-member magma to the magma chamber before the eruption.

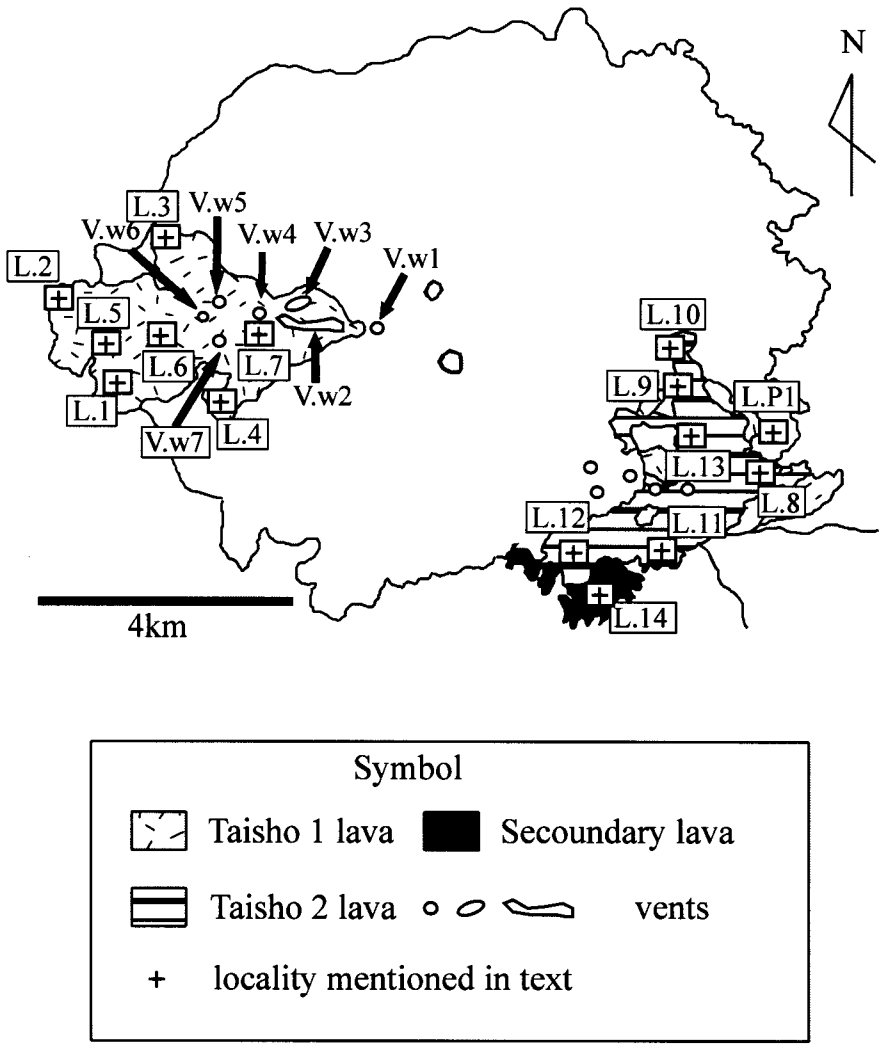

Figure 4-1 Distribution of locality points of Plinian fall pumice and lava flow samples (modified from Fukuyama and Ono, 1981).

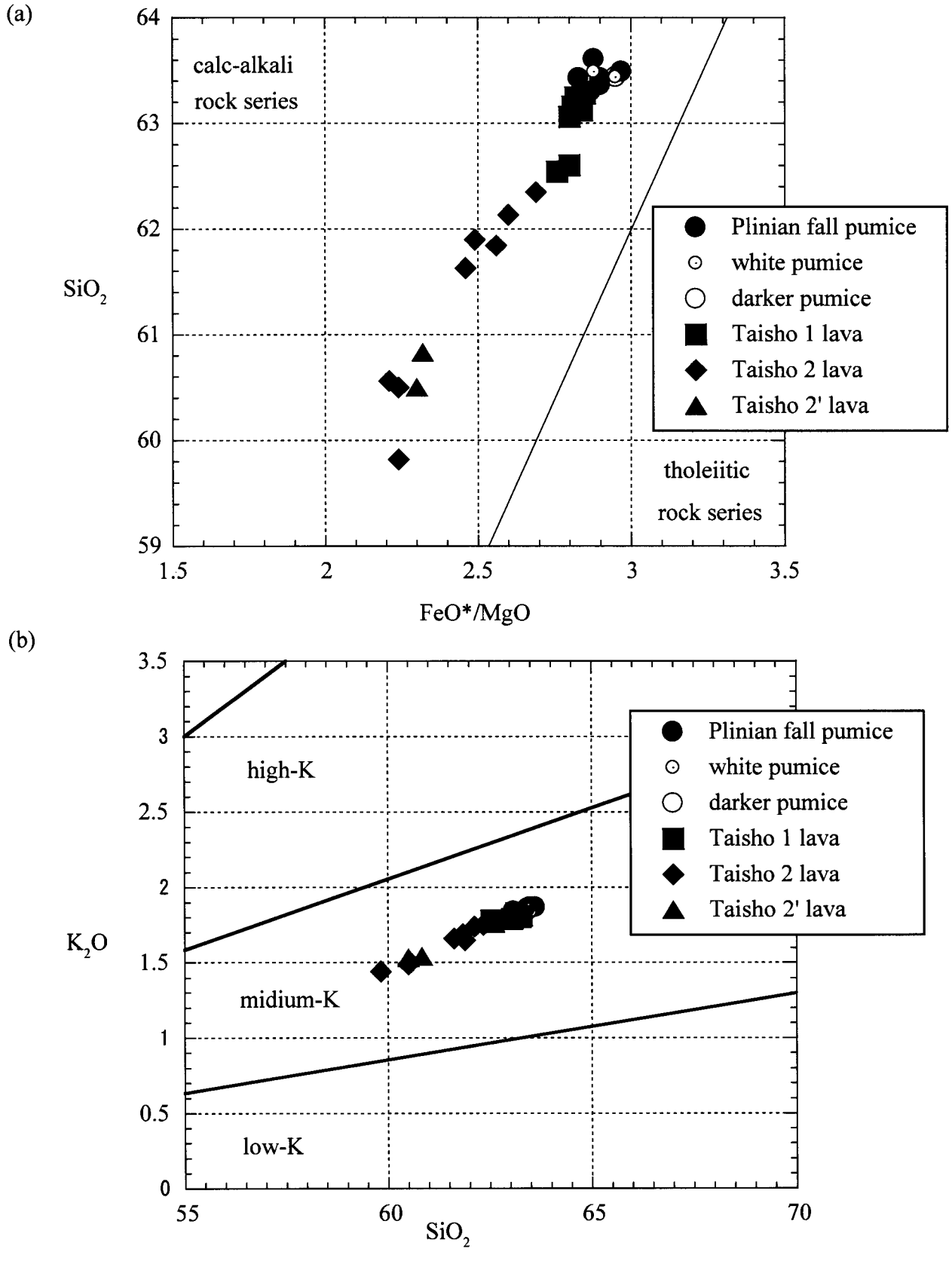

Figure 4-2 (a) FeO*/MgO-SiO_2 diagram of the volcanic products of the 1914-1995 eruption of Sakurajima volcano. Boundary line is based on Miyashiro (1974). Data are recalculated for totals to be 100 wt.%. (b) SiO_2-K_2O diagram of the volcanic products of the 1914-1915 eruption of Sakurajima volcano. The boundary lines of Low-, Midium- and High-K are from Gill (1981). Analyses are recalculated for totals to be 100 wt.%.

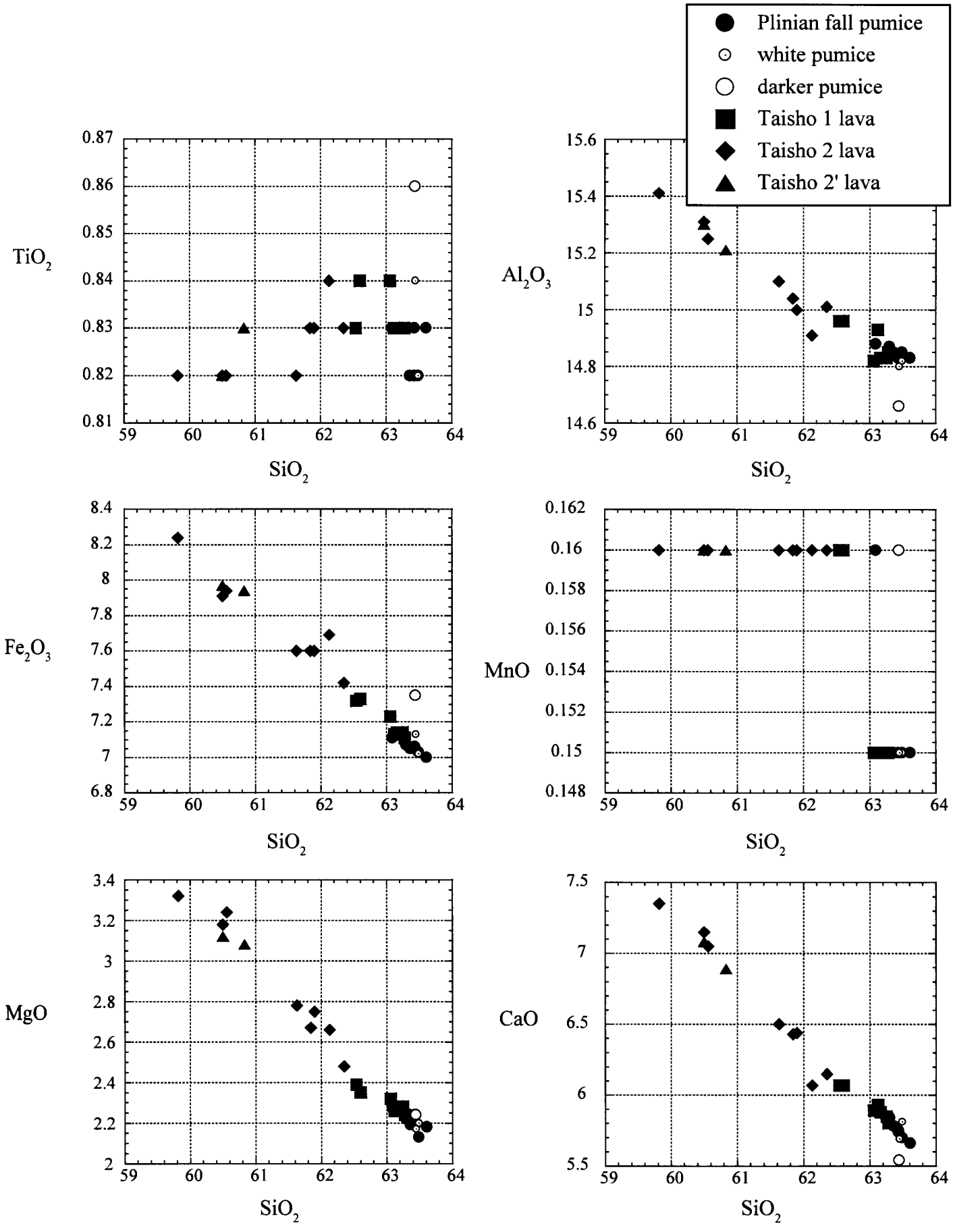

Figure 4-3 Harker diagrams for major oxides from Taisho lava flows and Taisho Plinia fall pumices. Analyses are recalculated for totals to be 100 wt.%.

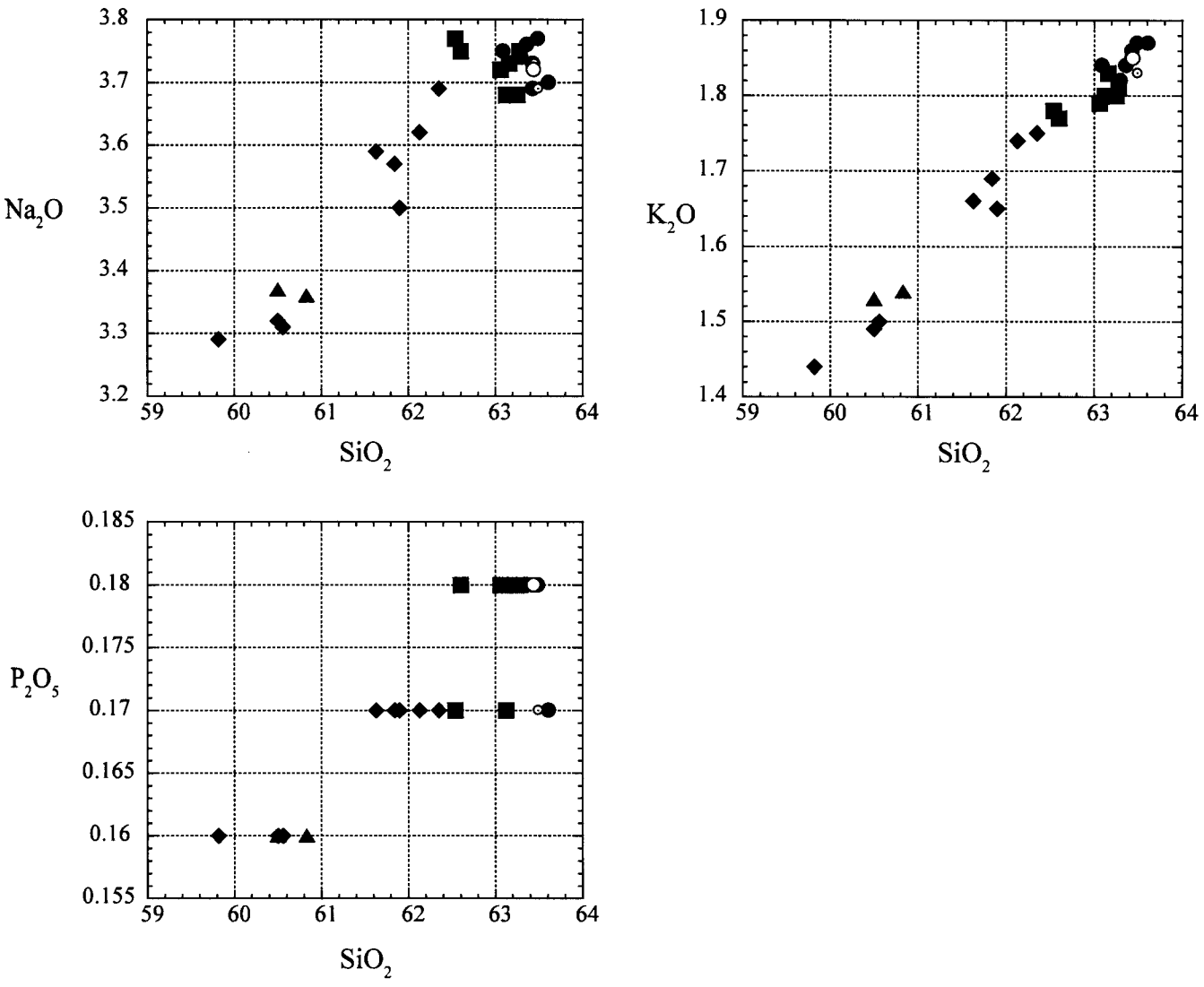

Figure 4-3 (continued)

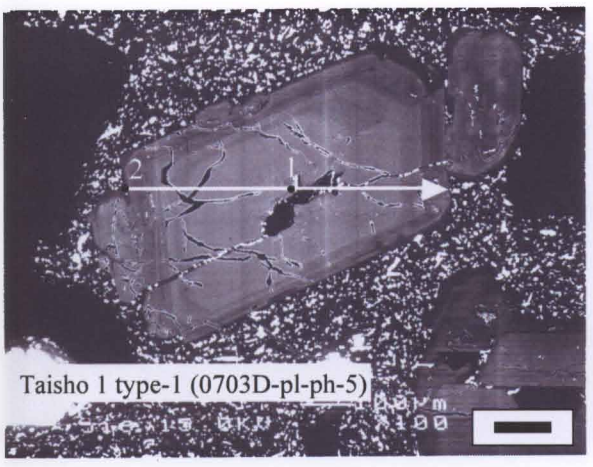

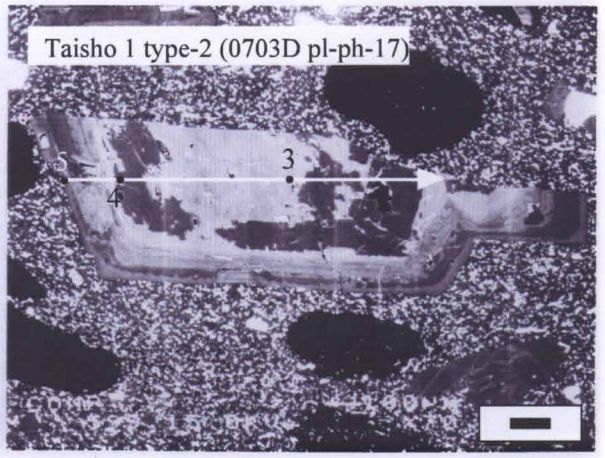

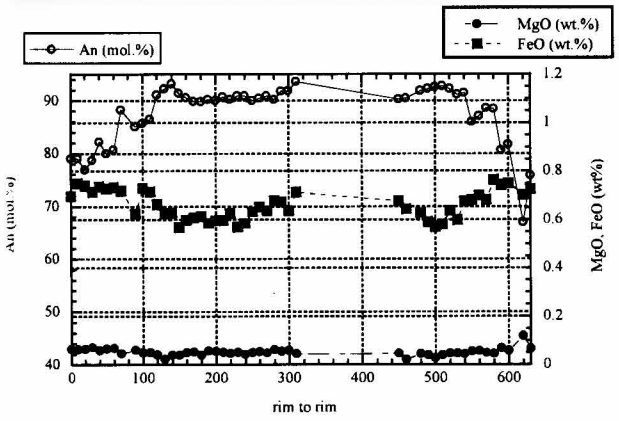

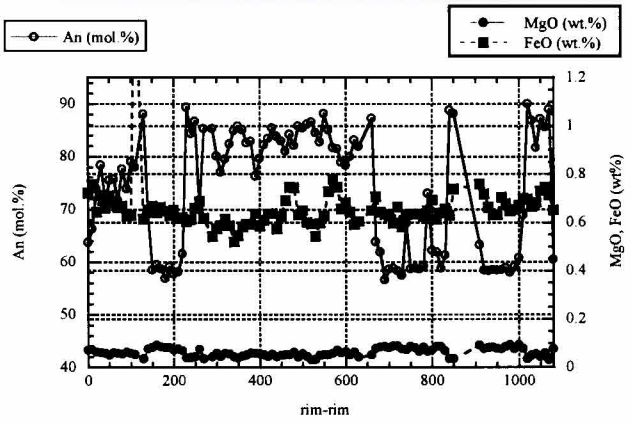

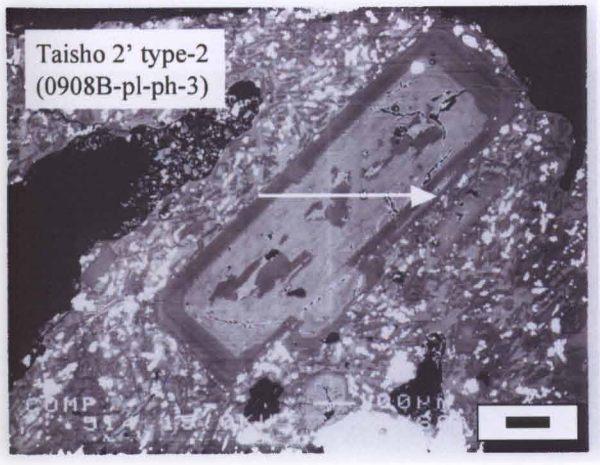

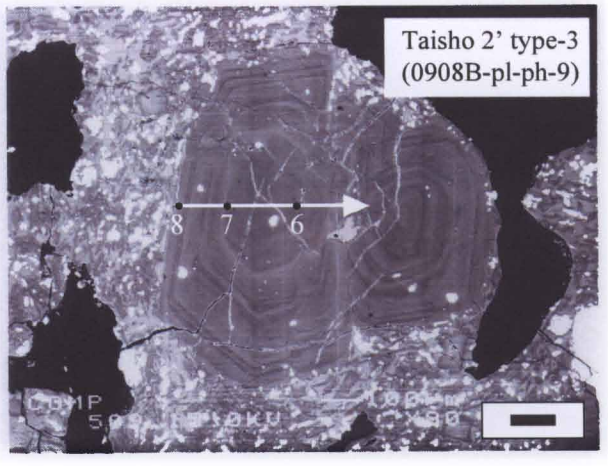

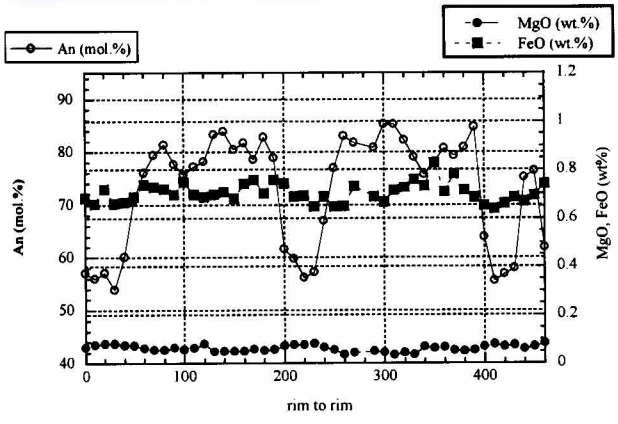

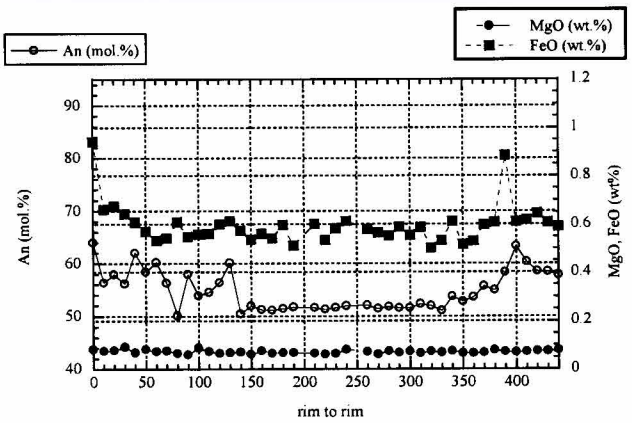

Figure 4-4 Back-scatterd electrom images of plagioclase phenocryst of Taisho lava flows and their line profiles of An, MgO, FeO* content. Solid line of each BSI shows a location of line analysis. Numbers are those listed in Table 4-3. The horizontal black scale bar is 100 μ m in length.

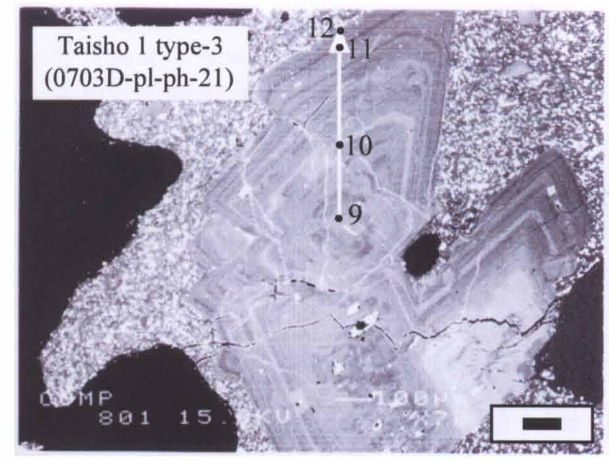

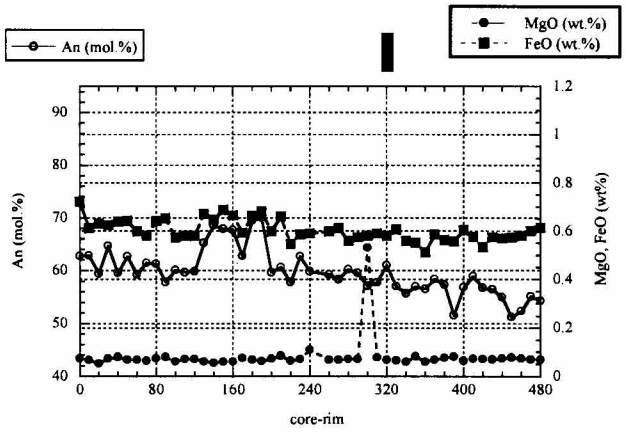

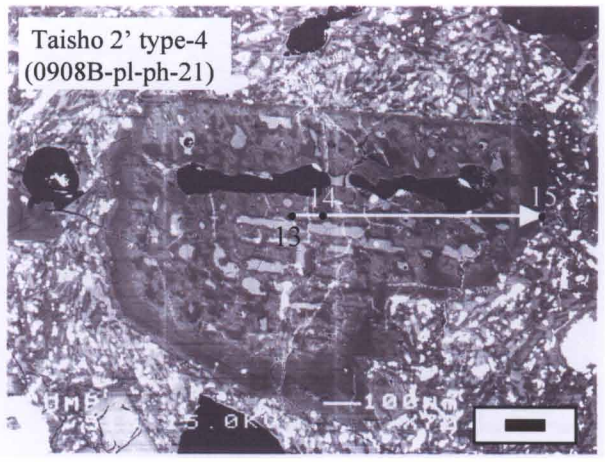

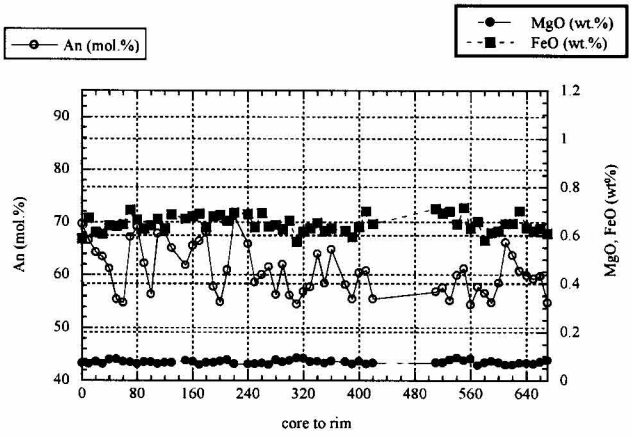

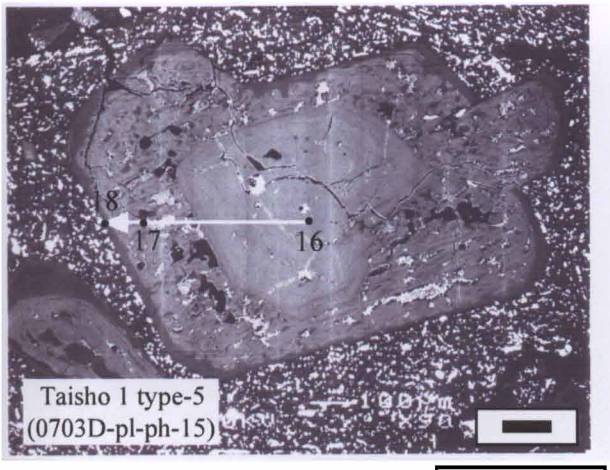

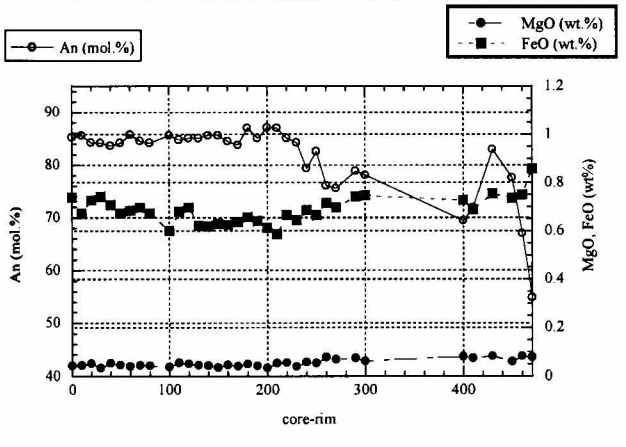

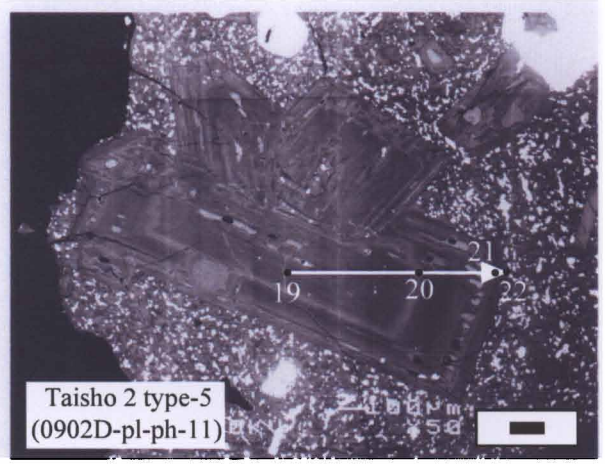

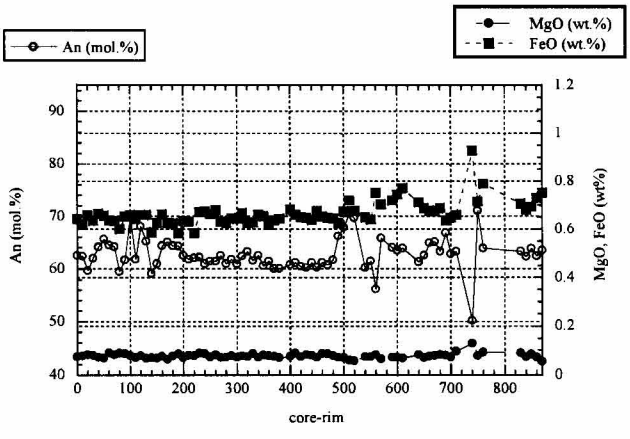

Figure 4-4 (continued)

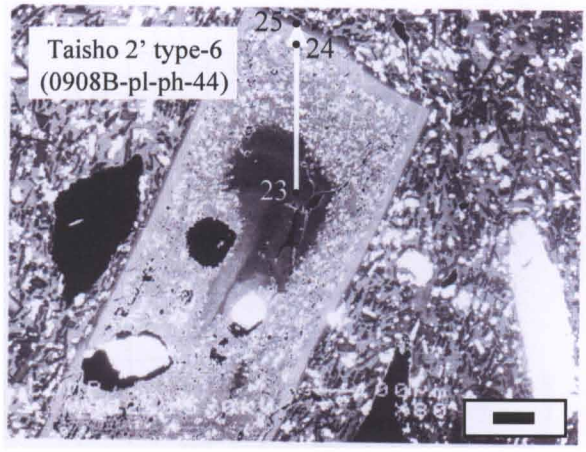

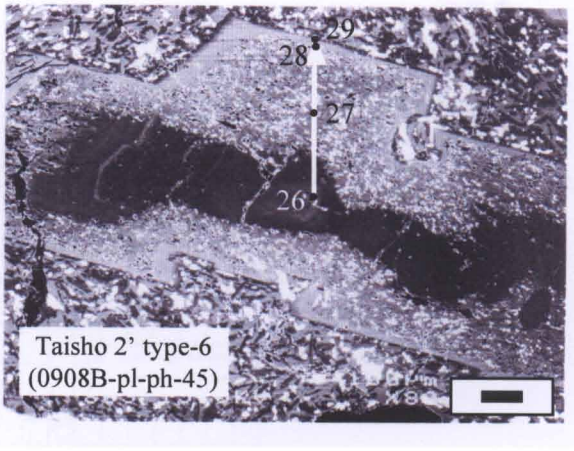

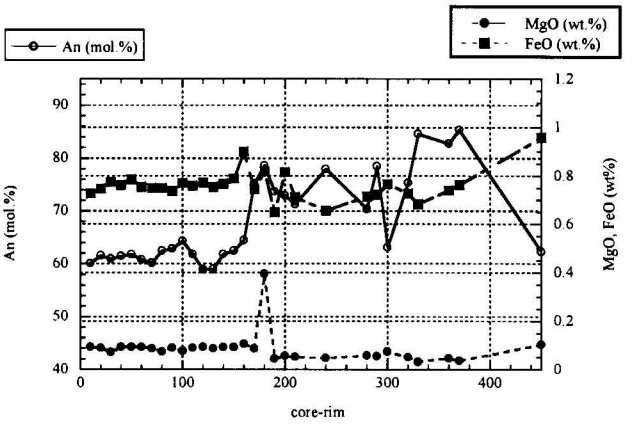

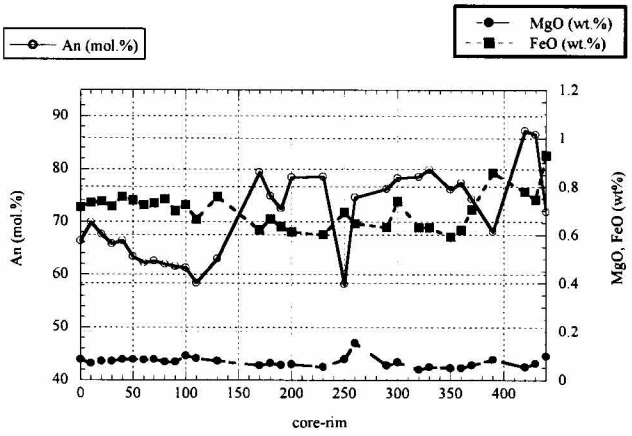

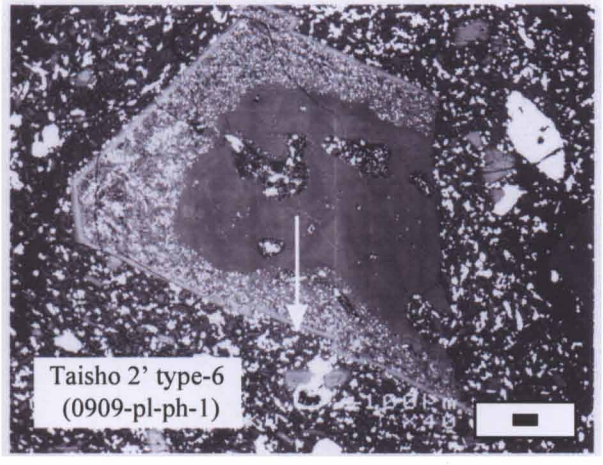

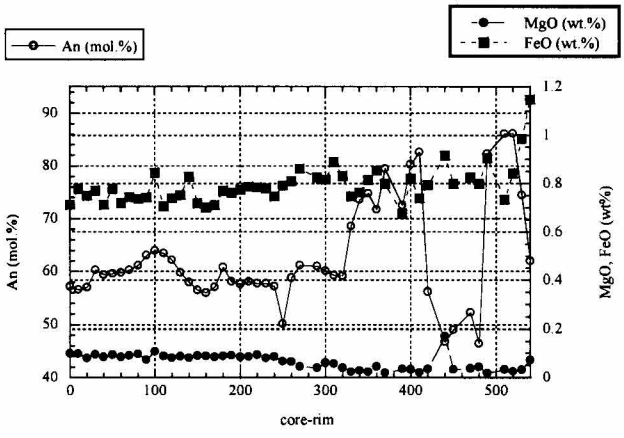

Figure 4-4 (continued)

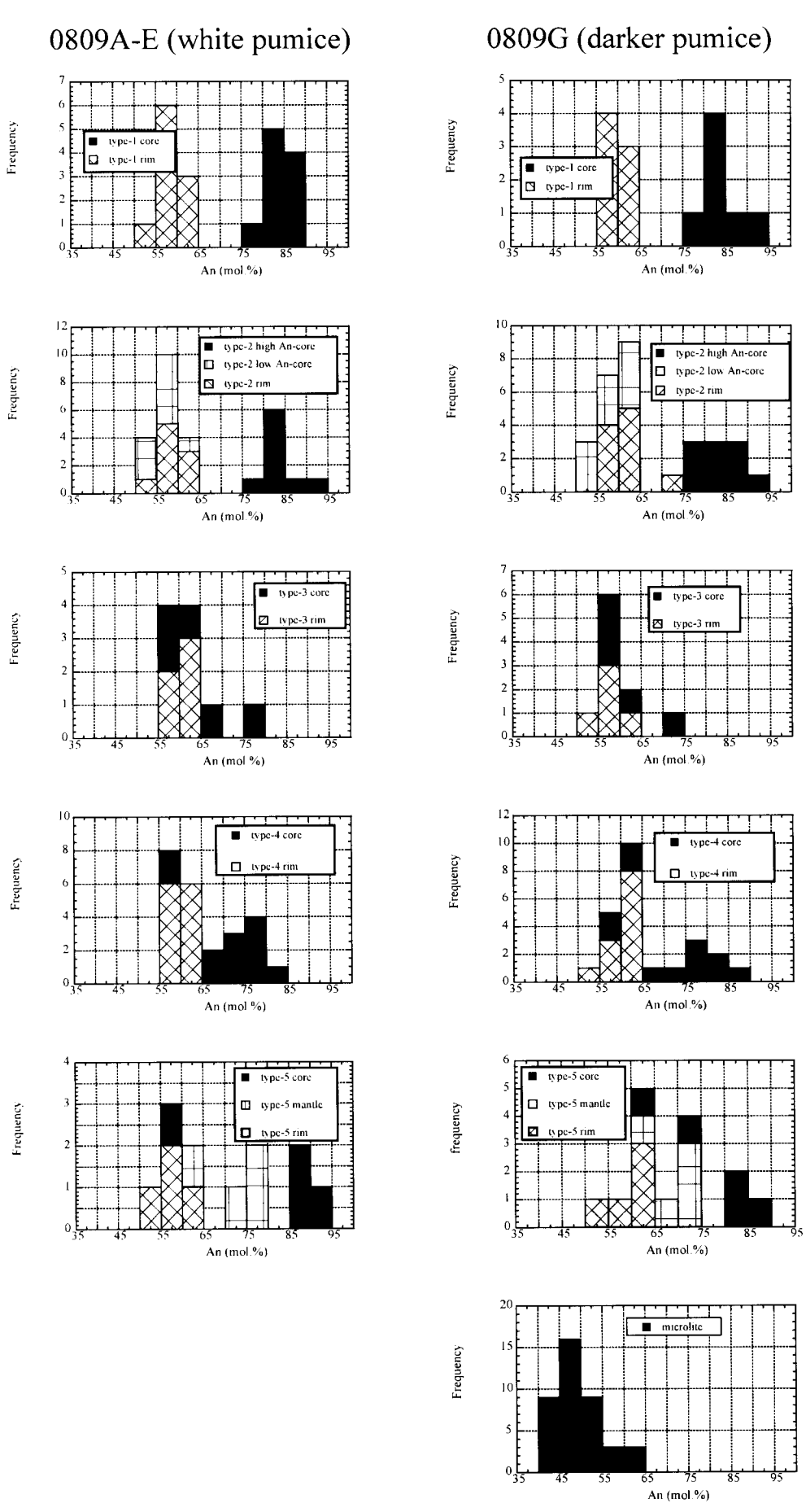

Figure 4-5 Histogram of An content for each textural type of plagioclase phenocryst and plagioclase microlite in the volcanic products.

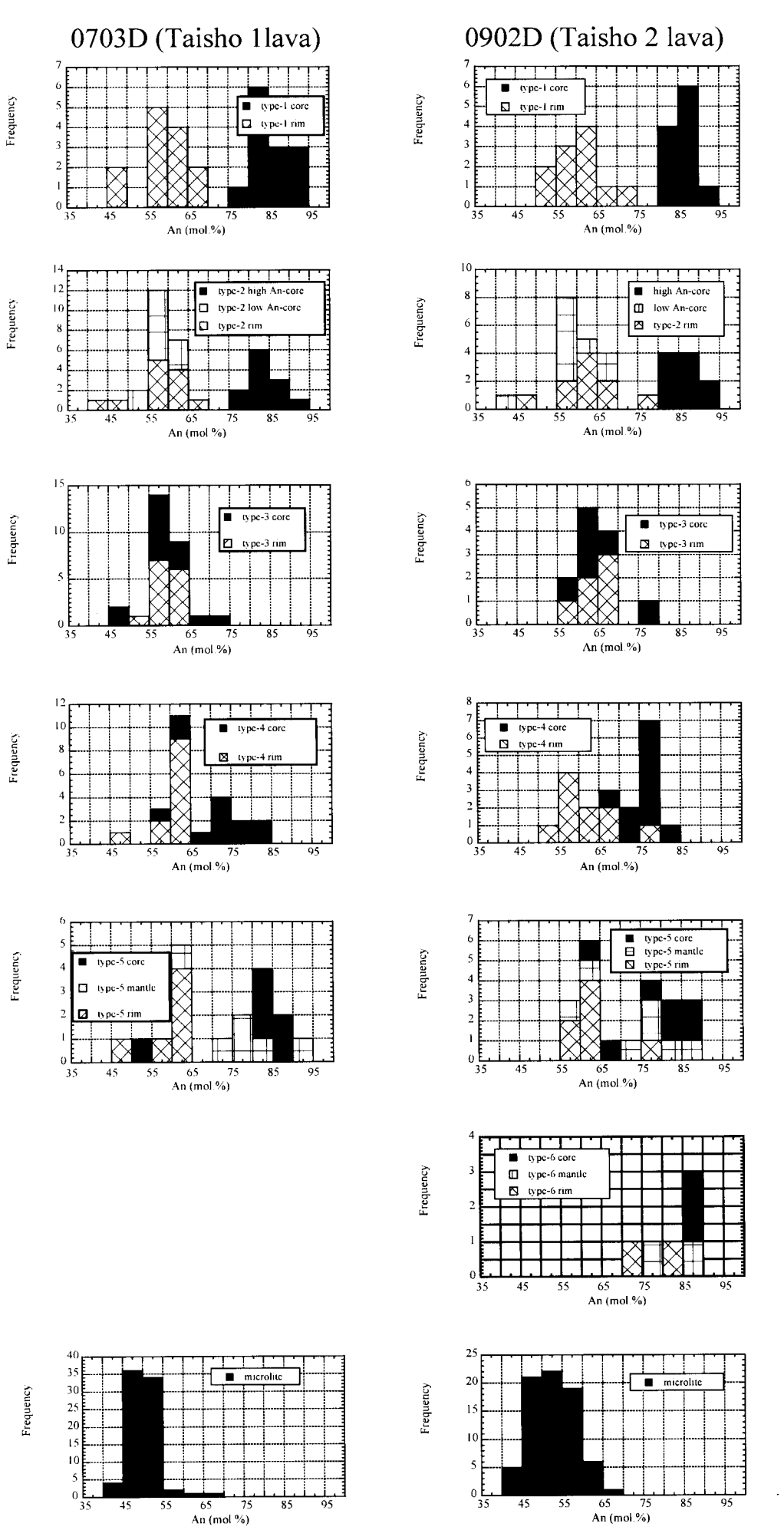

Figure 4-5 (continued)

0910B (Taisho 2 lava)

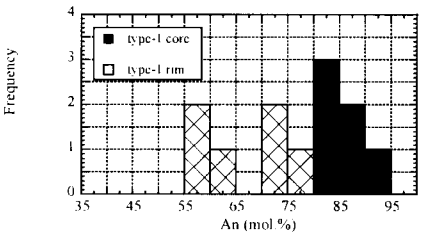

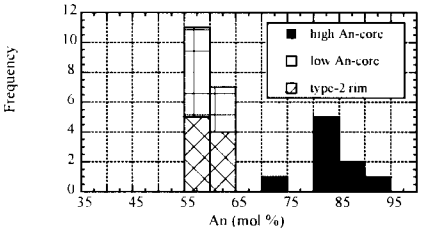

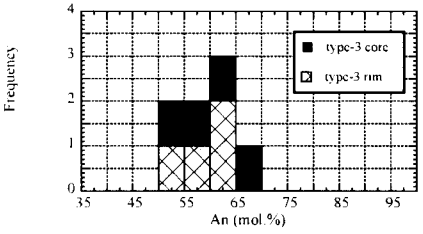

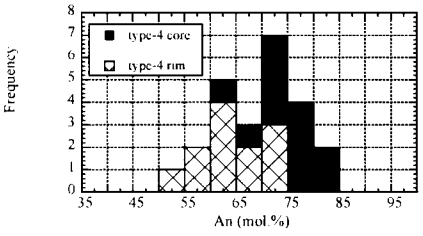

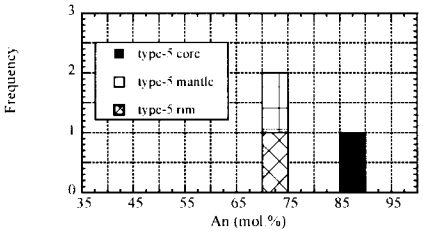

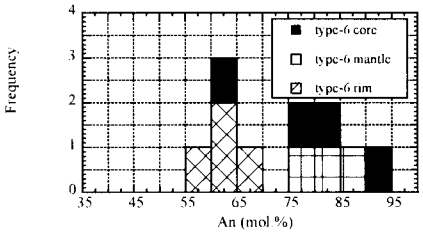

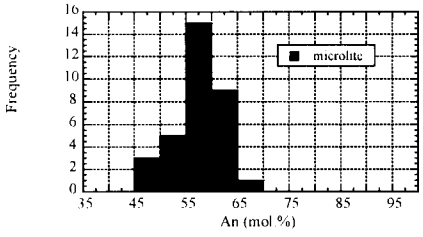

0908B (Taisho 2' lava)

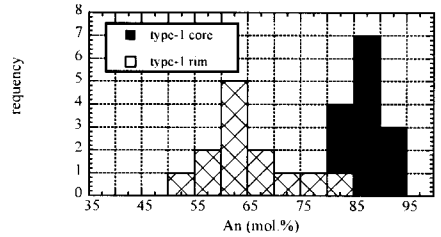

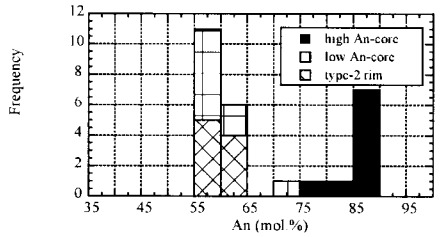

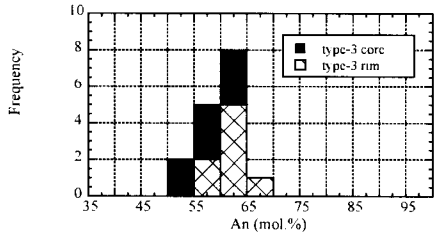

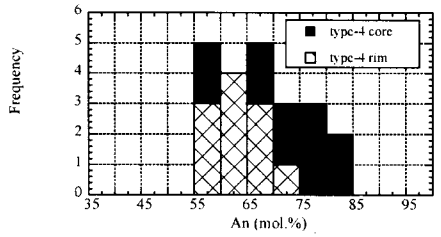

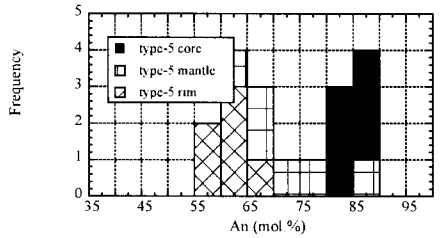

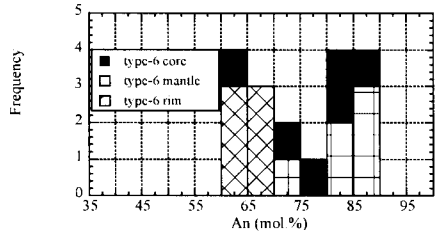

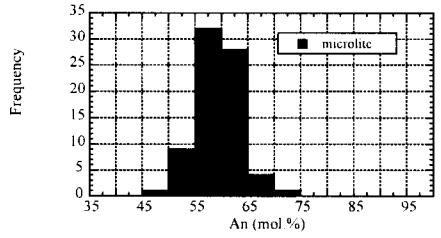

Figure 4-5 (continued)

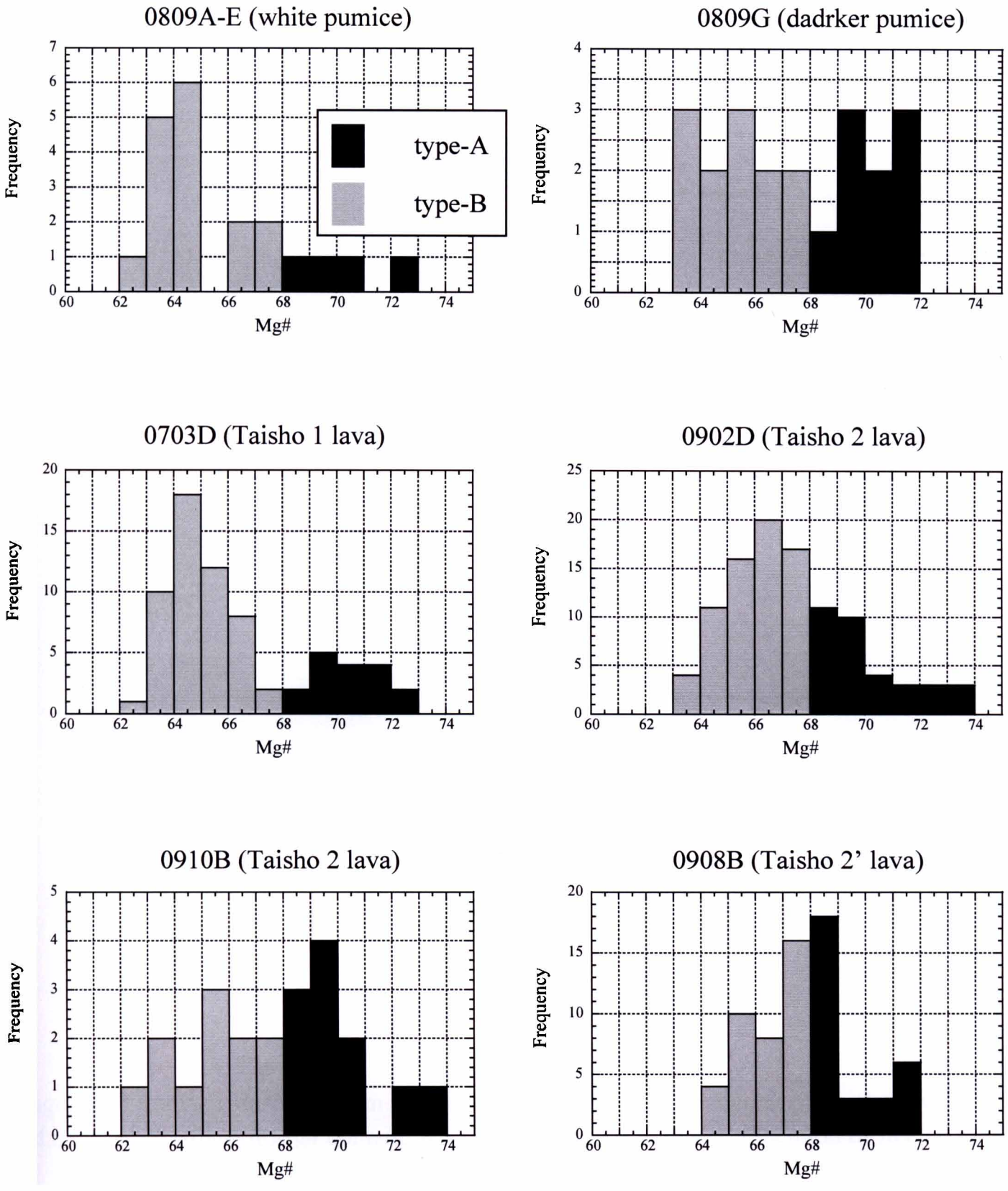

Figure 4-6 Histogram of core of Mg# content for each textural type of orthopyroxene phenocrysts.

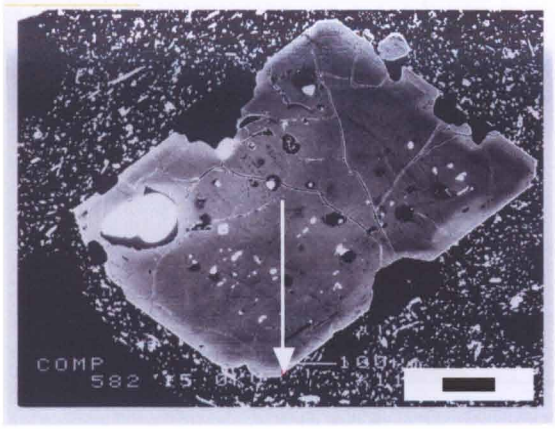

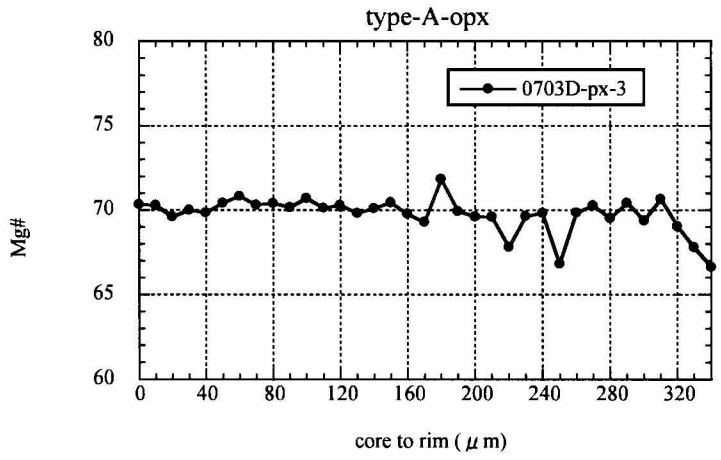

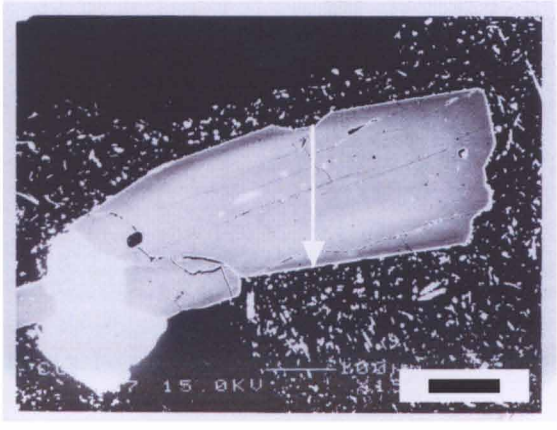

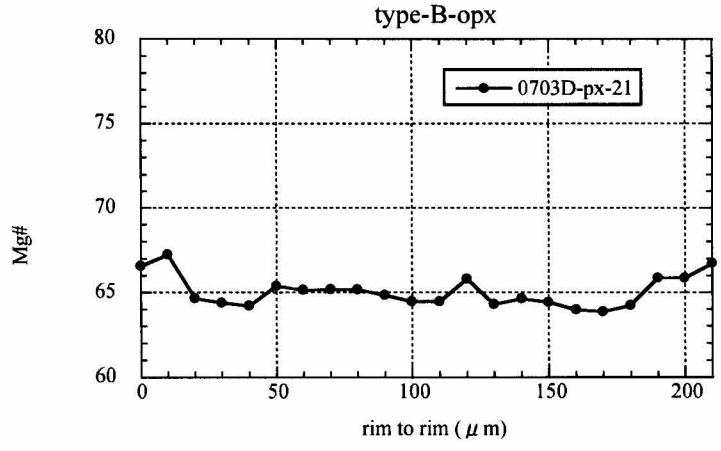

Figure 4-7 Back-scatterd electrom images of orthopyroxene phenocryst of Taisho lava flows and their line profiles of Mg# content. Solid line of each BSI shows a location of line analysis. The horizontal black scale bar is 100 μ m in length.

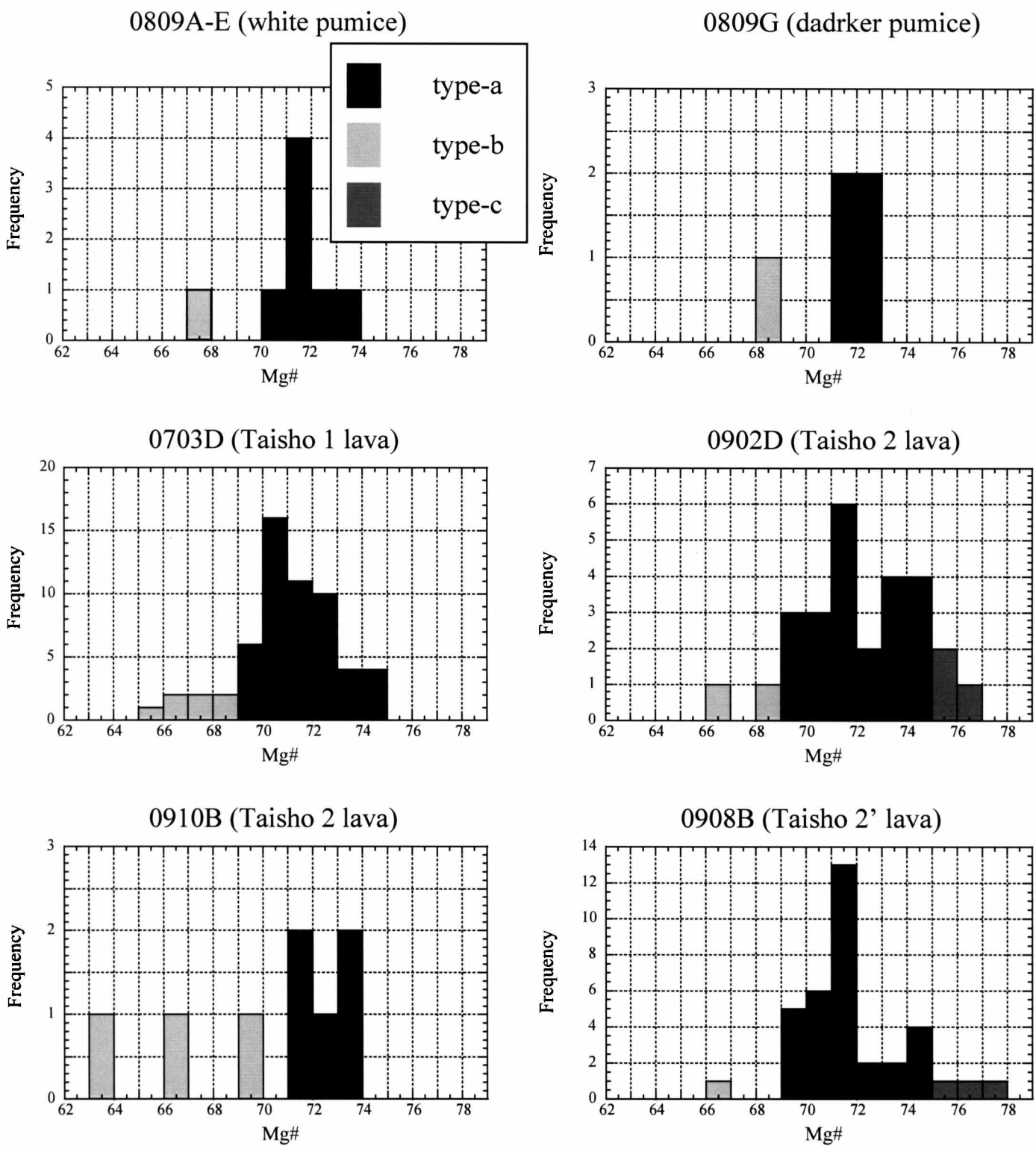

Figure 4-8 Histogram of core of Mg# content for each textural type of clinopyroxene phenocrysts.

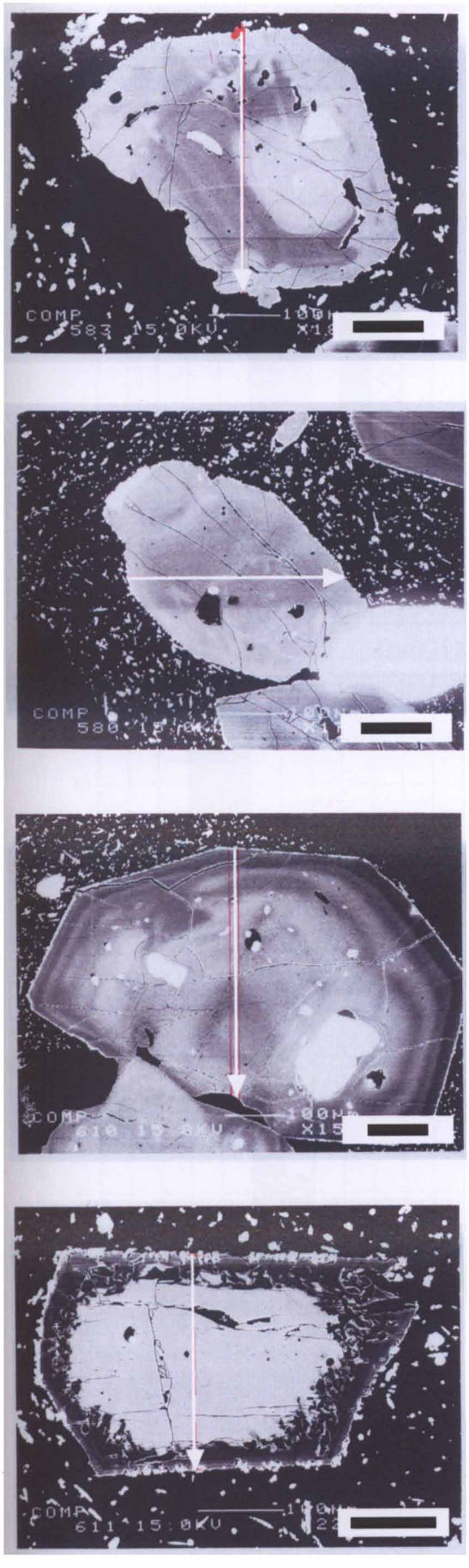

Figure 4-9 Back-scatterd electrom images of clynopyroxene phenocryst of Taisho lava flows and their line profiles of Mg# content. Solid line of each BSI shows a location of line analysis. The horizontal black scale bar is 100 μ m in length.

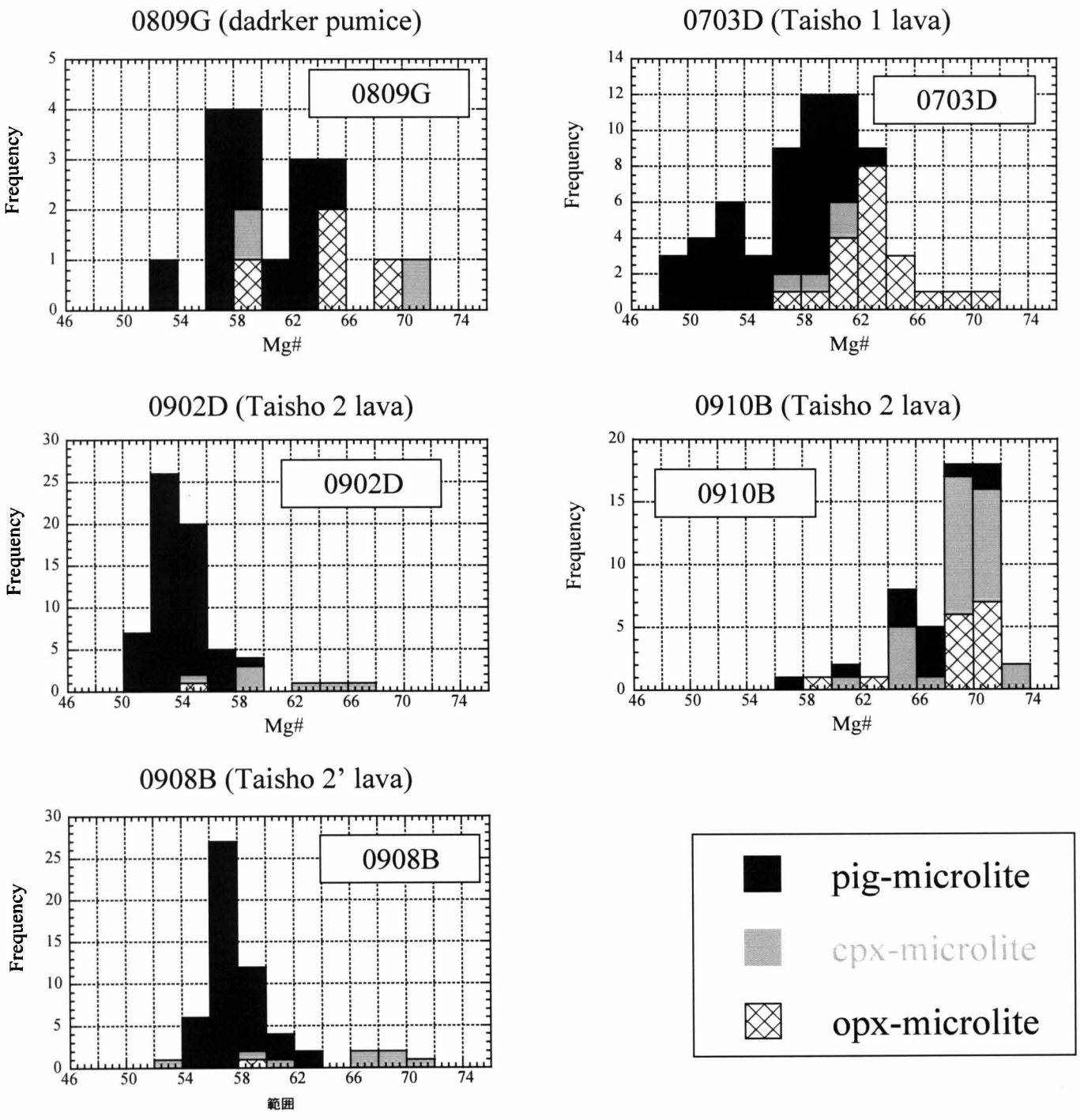

Figure 4-10 Histogram of Mg# content of pyroxene microlite

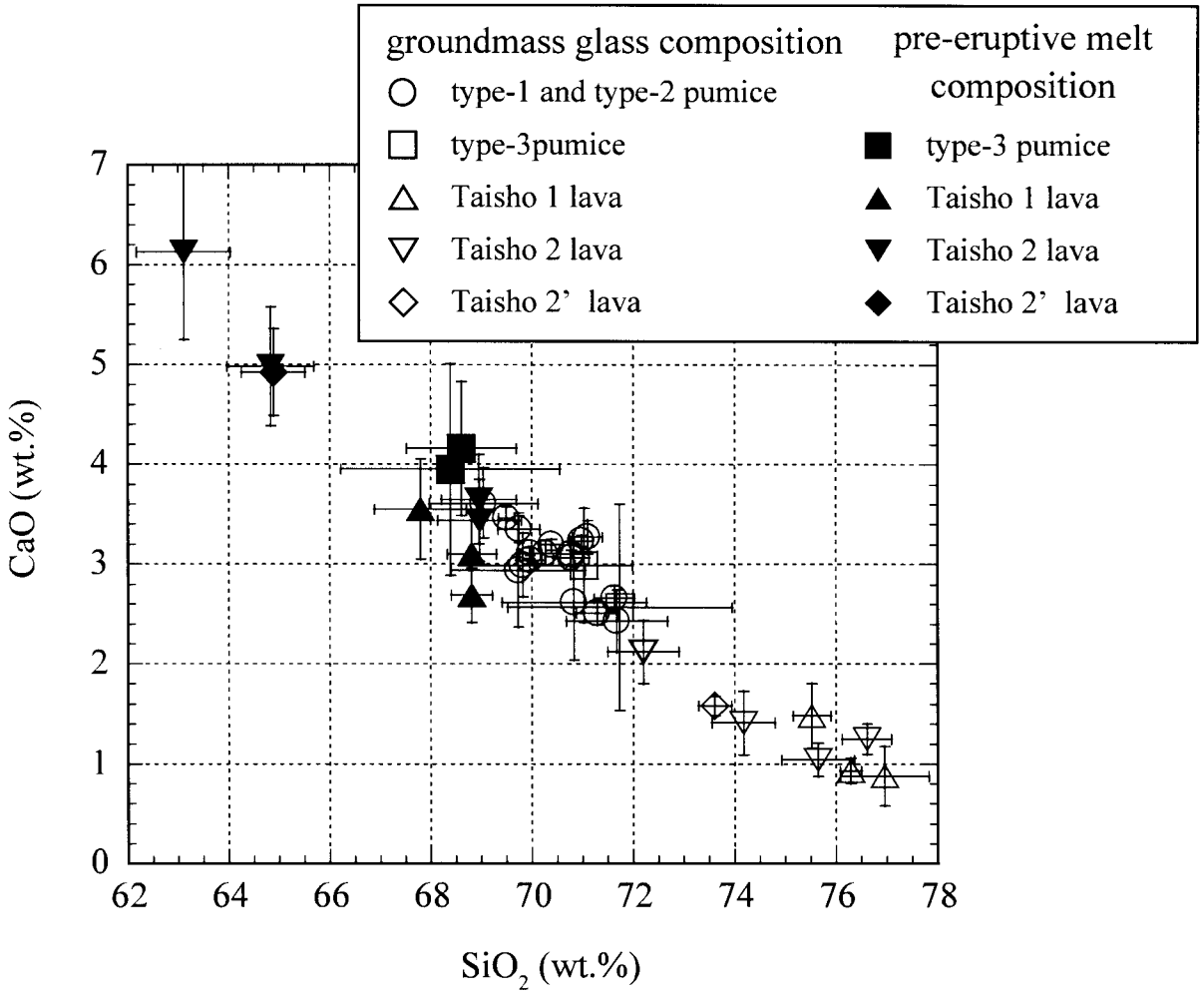

Figure 4-11 matrix glass and recaluclated pre-eruptive melt composition of the volcanic products. Normalized to total 100 wt.%

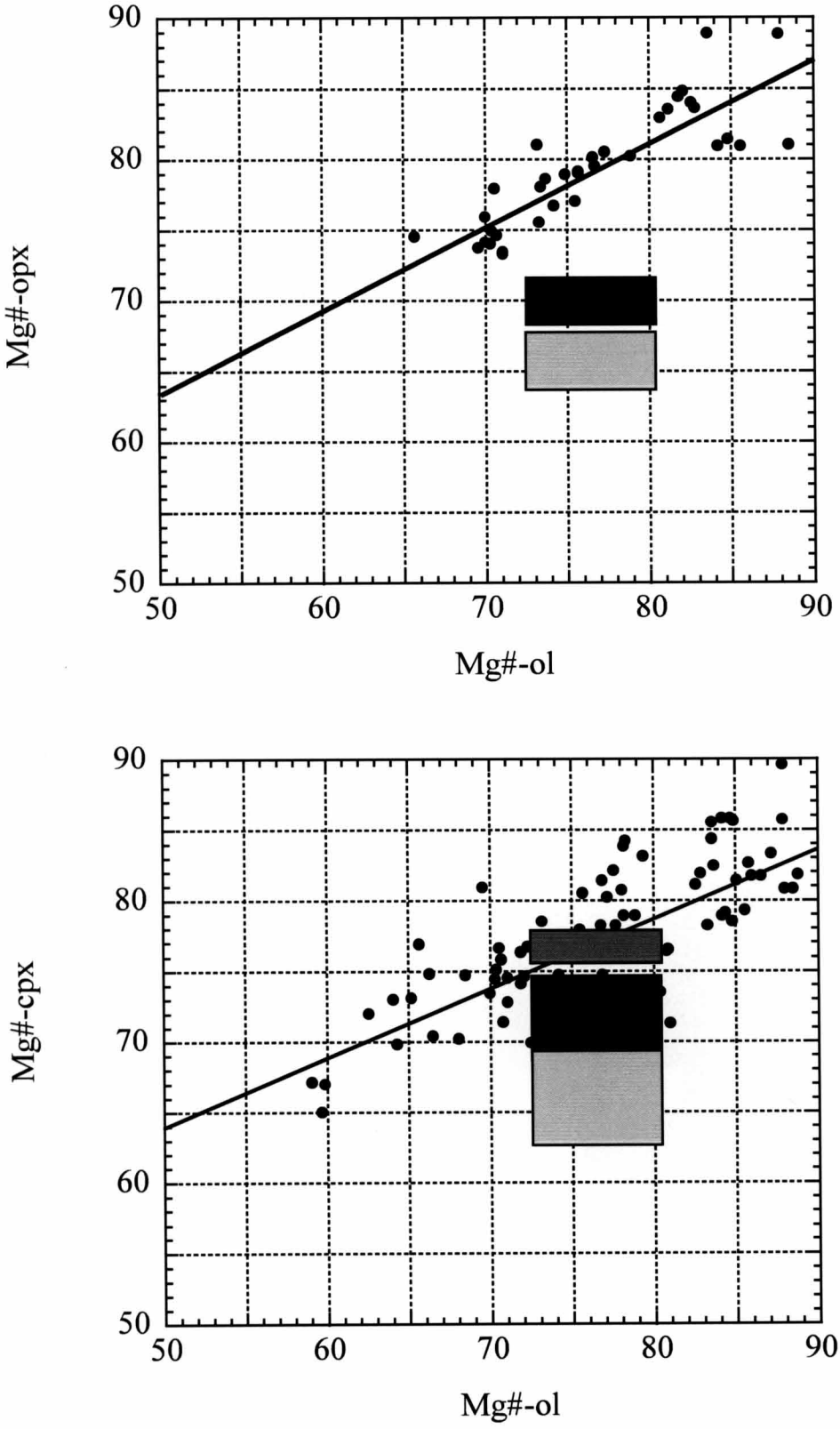

Fig 4-12 Mg-Fe distributions between the core of olivine phenocryst or microphenocryst vs. clinopyroxene (a) and orthopyroxene (b). Solid circles are compiled date of the equilibrium pair determined experimentally in basaltic to andesitic systems. Data sources of (a) are Grove et al. (1982), Grove and Juster (1989), Meen (1990), Draper and Johnston (1992) and Sisson and Grove (1993). Data sources of (b) are Grove et al. (1982), Grove and Juster (1989), Meen (1990) and Draper and Johnston (1992)

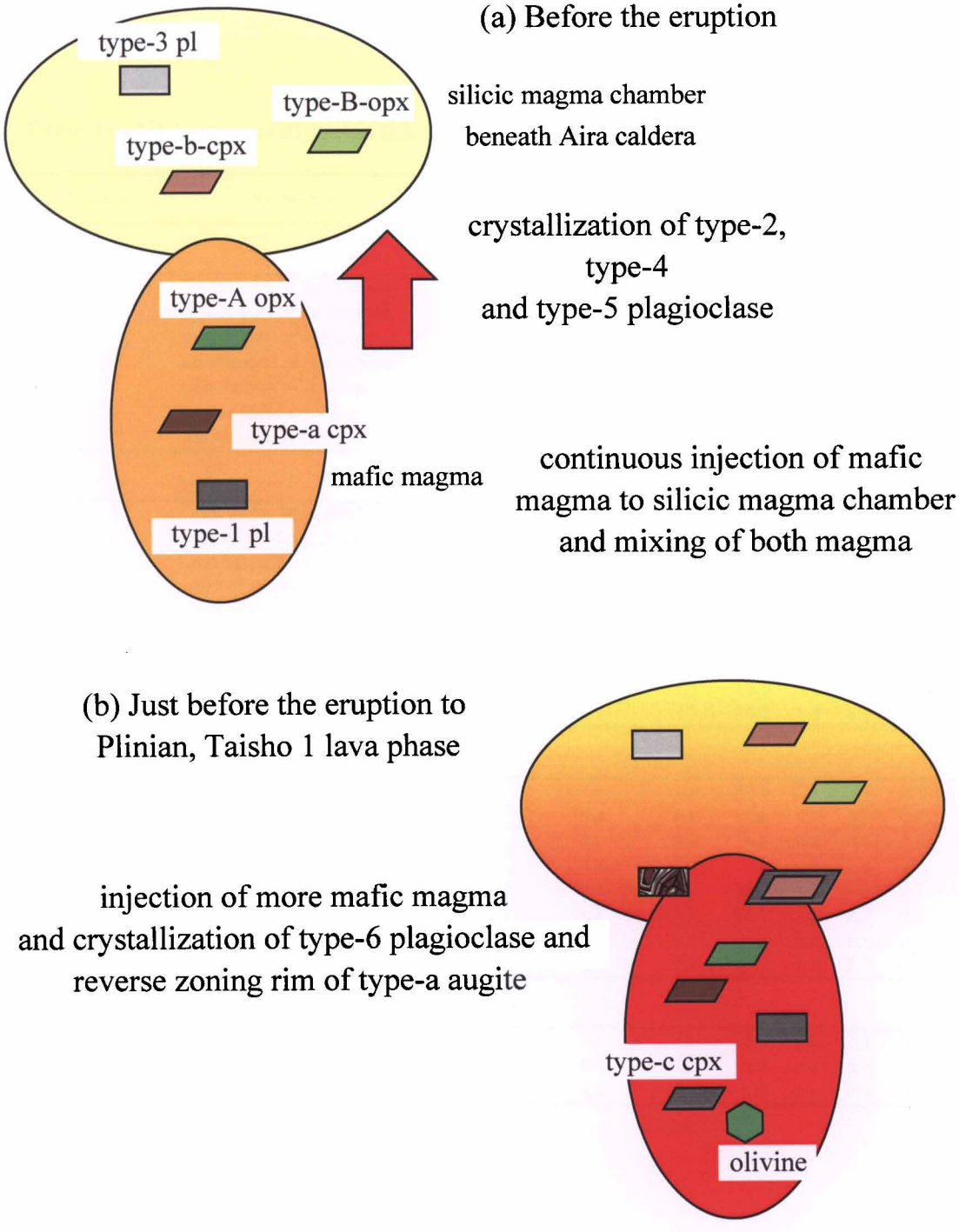

Figure 4-13 Schematic model of evolution of magma chamber and origin of plagioclase, orthopyroxene and augite of each type.

Table 4-1 All samples analyzed in this study and modal abundances of phenocrystic minerals

Sample	Locality	Occurrence	whole rock compositio	mineral compositio	textual analyses	pl	opx	cpx	ol	mt	gl
plinian fall pumice											
0809A		lower part of the deposit	○	○	○	10.2	0.1	0.6	—	0.3	88.8
0809B		lower part of the deposit	○	n.a	○	8.2	0.1	0.2	—	0.2	90.7
0809C		middle part of the deposit	○	n.a	○	14.9	0.1	0.2	—	0.2	86.8
0809D	L. P1	middle part of the deposit	○	○	○	12.2	0.2	0.3	—	0.5	86.8
0809E		middle part of the deposit	○	n.a	○	8.9	0.1	0.1	—	1.4	89.5
0809F		upper part of the deposit	○	n.a	○	9.8	0.1	1.3	—	0.6	88.2
0809G		upper part of the deposit	○	○	○	15.2	0.1	0.8	—	0.9	83.0
Taisho 1 lava											
0703D		rim of the lava, clinker	0	○	○	22.6	2.2	2.1	—	1.9	67.2
0703B	L.1	rim of the lava, massive	○	n.a	○	n.a	n.a	n.a	n.a	n.a	n.a
0703A		rim of the lava, massive	○	n.a	○	n.a	n.a	n.a	n.a	n.a	n.a
1001	L.2	rim of the lava, clinker	○	n.a	n.a	n.a	n.a	n.a	n.a	n.a	n.a
1101	L.3	rim of the lava, clinker	○	n.a	n.a	n.a	n.a	n.a	n.a	n.a	n.a
1002	L.4	rim of the lava, clinker	○	n.a	n.a	n.a	n.a	n.a	n.a	n.a	n.a
1103B	L.5	center of thel lava, clinker	○	n.a	n.a	n.a	n.a	n.a	n.a	n.a	n.a
1102B	L.6	center of thel lava, clinker	○	n.a	○	19.0	3.5	3.4	—	1.5	72.6
1004B	L.7	near the vent Vw1, clinker	○	n.a	○	19.2	1.5	4.7	—	1.5	73.1
Taisho 2 lava											
0902D	L.8	eastern rim of the lava, clinker	○	○	○	24.3	2.0	3.9	0.4	2	67.4
0902C		eastern rim of the lava, clinker	○	n.a	n.a	n.a	n.a	n.a	n.a	n.a	n.a
0807B	L.9	rim of the lava, clinker	○	n.a	n.a	n.a	n.a	n.a	n.a	n.a	n.a
0808B	L.10	rim of the lava, clinker	○	n.a	n.a	n.a	n.a	n.a	n.a	n.a	n.a
0907	L.11	southeastern rim of the lava, clinke	○	n.a	○	25.0	0.8	1.3	0.2	0.8	71.9
0910B	L.12	south rim of the lava, clinker	○	○	○	20.2	2.0	2.7	0.2	2.4	72.5
0910A		south rim of the lava, massive	○	n.a	n.a	n.a	n.a	n.a	n.a	n.a	n.a
0805	L.13	near the vent, clinker	○	n.a	○	23.1	1.5	3.2	0.3	1.6	70.3
Taisho 2' lava											
0908B		center of the lava, clinker	○	○	○	23.0	0.5	2.1	0.2	0.7	73.5
0908A	L.14	rim of the lava, massive	n.a	n.a	○	n.a	n.a	n.a	n.a	n.a	n.a
0909		rim of the lava, massive	○	n.a	○	n.a	n.a	n.a	n.a	n.a	n.a

Table 4-2 Whole-rock chemical composition of Plinian fall pumice and lava flow erupted at 1914-1915 eruption of Sakurajima volcano

	Plinian fall pumice										
sample	0809A	0809B	0809C	0809D	0809E	0809F	0809G	white	white	white	darker
SiO_2	63.61	63.43	63.49	63.43	63.36	63.09	63.30	63.49	63.45	63.44	63.44
TiO_2	0.83	0.82	0.82	0.83	0.82	0.83	0.83	0.82	0.84	0.86	0.86
Al_2O_3	14.83	14.84	14.85	14.83	14.85	14.88	14.87	14.82	14.80	14.66	14.66
Fe_2O_3*	7.00	7.06	7.03	7.05	7.05	7.11	7.07	7.02	7.13	7.35	7.35
MnO	0.15	0.15	0.15	0.15	0.15	0.16	0.15	0.15	0.15	0.16	0.16
MgO	2.18	2.24	2.13	2.19	2.19	2.27	2.22	2.20	2.17	2.24	2.24
CaO	5.66	5.74	5.70	5.75	5.78	5.89	5.84	5.81	5.69	5.54	5.54
Na_2O	3.70	3.69	3.77	3.73	3.76	3.75	3.74	3.69	3.73	3.72	3.72
K_2O	1.87	1.85	1.87	1.86	1.84	1.84	1.82	1.83	1.85	1.85	1.85
P_2O_5	0.17	0.18	0.18	0.18	0.18	0.18	0.18	0.17	0.18	0.18	0.18
FeO*/MgO	2.88	2.83	2.97	2.90	2.90	2.82	2.87	2.88	2.95	2.95	2.95
Na_2O+K_2O	5.57	5.54	5.65	5.59	5.60	5.59	5.56	5.52	5.59	5.57	5.57
SiO_2	62.17	62.48	61.91	62.26	61.82	61.38	61.90	62.23	62.18	62.52	61.86
TiO_2	0.81	0.81	0.80	0.82	0.80	0.81	0.81	0.80	0.82	0.85	0.81
Al_2O_3	14.49	14.62	14.48	14.55	14.49	14.47	14.54	14.52	14.50	14.44	14.60
Fe_2O_3*	6.84	6.96	6.85	6.92	6.88	6.92	6.91	6.88	6.99	7.24	6.99
MnO	0.15	0.15	0.15	0.15	0.15	0.15	0.15	0.15	0.15	0.15	0.15
MgO	2.13	2.21	2.08	2.15	2.14	2.21	2.17	2.15	2.13	2.21	2.25
CaO	5.53	5.65	5.56	5.64	5.64	5.73	5.71	5.70	5.58	5.46	5.85
Na_2O	3.62	3.64	3.68	3.66	3.67	3.65	3.66	3.62	3.66	3.66	3.63
K_2O	1.83	1.82	1.83	1.82	1.80	1.79	1.78	1.79	1.82	1.82	1.76
P_2O_5	0.17	0.18	0.17	0.18	0.17	0.18	0.18	0.17	0.17	0.18	0.17
Total	97.75	98.51	97.50	98.15	97.57	97.29	97.79	98.02	98.00	98.54	98.06

	Taisho 1 lava						
sample	0703D	1001	1002	1004B	1101	1102B	1103B
SiO_2	63.12	62.54	63.06	63.25	62.60	63.28	63.16
TiO_2	0.83	0.83	0.84	0.83	0.84	0.83	0.83
Al_2O_3	14.93	14.96	14.82	14.83	14.96	14.85	14.83
Fe_2O_3*	7.13	7.32	7.23	7.14	7.33	7.11	7.14
MnO	0.15	0.16	0.15	0.15	0.16	0.15	0.15
MgO	2.26	2.39	2.32	2.28	2.35	2.24	2.28
CaO	5.93	6.07	5.89	5.85	6.07	5.80	5.88
Na_2O	3.68	3.77	3.72	3.68	3.75	3.75	3.73
K_2O	1.80	1.78	1.79	1.80	1.77	1.81	1.83
P_2O_5	0.17	0.17	0.18	0.18	0.18	0.18	0.18
FeO*/MgO	2.84	2.76	2.80	2.82	2.80	2.85	2.81
Na_2O+K_2O	5.48	5.55	5.51	5.48	5.52	5.56	5.56
SiO_2	61.82	60.92	62.25	63.09	60.73	61.94	61.95
TiO_2	0.81	0.81	0.83	0.83	0.81	0.81	0.82
Al_2O_3	14.62	14.57	14.63	14.79	14.52	14.54	14.54
Fe_2O_3*	6.98	7.13	7.14	7.12	7.11	6.96	7.00
MnO	0.15	0.15	0.15	0.15	0.15	0.15	0.15
MgO	2.21	2.33	2.29	2.28	2.28	2.20	2.24
CaO	5.81	5.91	5.82	5.84	5.89	5.67	5.76
Na_2O	3.61	3.68	3.67	3.67	3.64	3.67	3.66
K_2O	1.76	1.73	1.77	1.80	1.71	1.78	1.79
P_2O_5	0.17	0.17	0.17	0.18	0.17	0.17	0.17
Total	97.93	97.41	98.72	99.75	97.01	97.89	98.09

Table 4-2 (continued)

	Taisho 2 lava								Taisho 2' lava	
sample	0805	0807B	0808B	0902C	0902D	0907	0910A	0910B	0908B	0909
SiO_2	59.82	61.84	62.13	61.63	61.90	62.35	60.50	60.56	60.83	60.50
TiO_2	0.82	0.83	0.84	0.82	0.83	0.83	0.82	0.82	0.83	0.82
Al_2O_3	15.41	15.04	14.91	15.10	15.00	15.01	15.31	15.25	15.21	15.30
Fe_2O_3*	8.24	7.60	7.69	7.60	7.60	7.42	7.91	7.94	7.94	7.97
MnO	0.16	0.16	0.16	0.16	0.16	0.16	0.16	0.16	0.16	0.16
MgO	3.32	2.67	2.66	2.78	2.75	2.48	3.18	3.24	3.08	3.12
CaO	7.35	6.43	6.07	6.50	6.44	6.15	7.15	7.05	6.89	7.08
Na_2O	3.29	3.57	3.62	3.59	3.50	3.69	3.32	3.31	3.36	3.37
K_2O	1.44	1.69	1.74	1.66	1.65	1.75	1.49	1.50	1.54	1.53
P_2O_5	0.16	0.17	0.17	0.17	0.17	0.17	0.16	0.16	0.16	0.16
FeO*/MgO	2.24	2.56	2.60	2.46	2.49	2.69	2.24	2.21	2.32	2.30
Na_2O+K_2O	4.73	5.27	5.36	5.24	5.15	5.43	4.81	4.82	4.90	4.90
SiO_2	58.95	61.07	61.41	60.36	61.90	60.47	60.36	60.45	60.74	59.78
TiO_2	0.81	0.82	0.83	0.81	0.83	0.81	0.82	0.82	0.83	0.81
Al_2O_3	15.18	14.85	14.73	14.79	15.00	14.56	15.28	15.22	15.18	15.12
Fe_2O_3*	8.12	7.50	7.60	7.45	7.60	7.20	7.89	7.93	7.93	7.88
MnO	0.16	0.16	0.16	0.16	0.16	0.15	0.16	0.16	0.16	0.16
MgO	3.27	2.63	2.63	2.72	2.75	2.40	3.17	3.23	3.08	3.08
CaO	7.24	6.35	6.00	6.37	6.45	5.96	7.13	7.04	6.88	6.99
Na_2O	3.24	3.53	3.58	3.51	3.50	3.58	3.31	3.31	3.36	3.33
K_2O	1.42	1.67	1.72	1.62	1.65	1.69	1.49	1.50	1.54	1.51
P_2O_5	0.15	0.17	0.17	0.16	0.17	0.17	0.16	0.16	0.16	0.16
Total	98.55	98.75	98.84	97.94	100.00	96.99	99.77	99.82	99.85	98.82

Upside data of major element are normalized to 100 wt.% anhydrous.
Fe_2O_3* is total Fe as Fe_2O_3

Table 4-3 Representative chemical composition of plagioclase phenocryst in lavas

sample	0703D-pl-ph-5		0703D-pl-17			0908B-pl-ph-9		
type	type-1		type-2			type-3		
number	1	2	3	4	5	6	7	8
	core	rim	core	core	rim	core	mantle	rim
SiO_2	44.62	49.11	45.79	54.27	52.90	56.49	53.52	52.67
TiO_2	0.00	0.03	0.01	0.05	0.03	0.03	0.03	0.05
Al_2O_3	34.64	31.76	33.81	28.59	29.47	27.35	29.19	29.07
FeO*	0.71	0.70	0.63	0.67	0.72	0.55	0.61	0.94
MnO	0.02	0.04	0.00	0.04	0.02	0.00	0.00	0.04
MgO	0.05	0.06	0.05	0.08	0.07	0.07	0.07	0.08
CaO	18.89	16.01	18.33	11.89	13.01	10.57	12.46	12.89
Na_2O	0.71	2.36	1.36	4.66	4.10	5.43	4.57	4.01
K_2O	0.03	0.08	0.02	0.20	0.20	0.24	0.17	0.19
Total	99.68	100.15	99.99	100.45	100.54	100.75	100.61	99.94
An	93.62	78.97	88.17	58.48	63.67	51.82	60.10	63.96
cation	5.01	5.00	5.02	5.00	5.00	4.99	5.01	5.00

sample	0703D-pl-21				0908B-pl-ph-21			0703D-pl-ph-15		
type	type-3				type-4			type-5		
number	9	10	11	12	13	14	15	16	17	18
	core	mantle	mantle	rim	core	core	rim	core	mantle	rim
SiO_2	52.35	51.10	56.24	55.45	51.29	55.74	55.44	47.26	51.48	55.53
TiO_2	0.04	0.02	0.03	0.03	0.00	0.05	0.02	0.04	0.04	0.05
Al_2O_3	28.43	30.32	27.11	27.45	30.55	28.07	27.60	33.22	30.43	27.26
FeO*	0.72	0.68	0.56	0.62	0.59	0.65	0.61	0.74	0.73	0.86
MnO	0.00	0.00	0.02	0.03	0.02	0.04	0.05	0.03	0.05	0.03
MgO	0.08	0.06	0.08	0.07	0.07	0.08	0.08	0.04	0.08	0.08
CaO	12.36	14.24	10.69	10.80	14.28	11.45	11.08	17.47	14.05	10.73
Na_2O	4.05	3.36	5.54	5.25	3.44	5.22	5.04	1.68	3.43	4.87
K_2O	0.16	0.11	0.28	0.28	0.14	0.23	0.25	0.06	0.13	0.29
Total	98.18	99.90	100.54	99.97	100.37	101.52	100.17	100.53	100.41	99.70
An	62.79	70.06	51.59	53.18	69.66	54.80	54.84	85.20	69.38	54.92
cation	4.99	5.00	5.00	5.00	5.00	5.01	4.99	5.01	5.00	4.98

sample	0902D-pl-ph-11				0908B-pl-44			0908B-pl-45			
type	type-5				type-6			type-6			
number	19	20	21	22	23	24	25	26	27	28	29
	core	mantle	mantle	rim	ccore	mantle	rim	core	mantle	mantle	rim
SiO_2	53.40	50.47	52.50	52.91	53.05	47.04	54.34	51.60	50.46	46.06	50.59
TiO_2	0.05	0.02	0.06	0.01	0.01	0.01	0.02	0.00	0.03	0.00	0.06
Al_2O_3	28.94	30.59	28.73	29.10	28.28	33.17	28.12	29.68	29.78	33.17	30.17
FeO*	0.64	0.72	0.71	0.75	0.73	0.76	0.96	0.72	0.64	0.78	0.93
MnO	0.03	0.00	0.00	0.00	0.01	0.01	0.02	0.01	0.00	0.00	0.02
MgO	0.08	0.06	0.09	0.06	0.09	0.04	0.10	0.09	0.06	0.05	0.10
CaO	12.44	14.22	12.32	12.53	12.20	17.48	12.51	13.46	14.50	17.44	14.62
Na_2O	4.13	3.29	3.95	3.98	4.47	1.66	4.19	3.77	3.05	1.40	3.17
K_2O	0.18	0.11	0.20	0.20	0.29	0.07	0.25	0.20	0.12	0.07	0.15
Total	99.88	99.48	98.55	99.53	99.13	100.23	100.51	99.52	98.63	98.98	99.80
An	62.49	70.46	63.28	63.54	60.10	85.37	62.27	66.36	72.45	87.29	71.84
cation	4.99	5.00	4.98	4.99	5.01	5.01	4.99	5.01	4.99	5.01	5.01

Analysed points are shown in BEIs of Figure 4-4.
FeO* is total Fe as FeO.

Table 4-4 Average compositions of core and rim of pyroxene phenocryst

white Plinian fall pumice (0809A-E)												
	type-A opx		type-a cpx		type-B opx		type-b cpx		opx-rim		cpx-rim	
n	4	stdev	7	stdev	16	stdev	1	stdev	13	stdev	8	stdev
SiO_2	53.04	0.33	51.69	0.47	52.49	0.37	51.40		52.72	0.57	51.74	0.69
TiO_2	0.25	0.05	0.49	0.07	0.26	0.04	0.54		0.26	0.04	0.49	0.04
Al_2O_3	1.13	0.41	1.67	0.27	0.77	0.09	1.58		0.87	0.16	1.68	0.20
FeO*	18.63	0.73	10.13	0.39	21.32	0.82	11.72		20.40	0.92	10.46	0.75
MnO	0.62	0.15	0.46	0.05	0.90	0.09	0.42		0.83	0.07	0.47	0.06
MgO	24.66	0.90	14.51	0.22	22.15	0.79	13.78		22.78	0.74	14.53	0.33
CaO	1.51	0.03	20.03	0.32	1.56	0.19	19.60		1.61	0.08	20.05	0.36
Na_2O	0.04	0.03	0.26	0.03	0.04	0.02	0.32		0.03	0.04	0.30	0.04
K_2O	0.00	0.01	0.00	0.01	0.00	0.00	0.00		0.01	0.02	0.01	0.01
Total	99.89	0.52	99.25	0.79	99.50	0.73	99.35		99.51	0.93	99.72	0.95
Mg#	70.21	1.58	71.85	1.05	64.93	1.55	67.71		66.55	1.65	71.25	1.89
En	69.9		44.7		63.8		42.7		65.2		45.2	
Wo	3.2		39.7		3.3		39.3		3.4		39.4	
Fs	27.0		15.6		33.0		18.0		31.5		15.5	
T (℃)	1051		17		1007		13		1038		28	

darker colored Plinian fall pumice (0809G)												
	type-A opx		type-a cpx		type-B opx		type-b cpx		opx-rim		cpx-rim	
n	9	stdev	4	stdev	12	stdev	1	stdev	19	stdev	4	stdev
SiO_2	53.07	0.43	51.39	0.66	52.39	0.62	51.95		52.97	0.79	52.04	1.12
TiO_2	0.21	0.05	0.50	0.05	0.24	0.08	0.50		0.27	0.04	0.50	0.02
Al_2O_3	0.95	0.10	1.98	0.28	0.94	0.43	1.29		0.97	0.41	2.00	0.71
FeO*	18.49	0.51	10.22	0.22	21.22	0.99	11.55		20.25	0.59	10.59	0.95
MnO	0.63	0.08	0.41	0.08	0.86	0.10	0.62		0.76	0.06	0.49	0.08
MgO	24.61	0.57	14.88	0.28	22.36	0.63	13.93		22.84	0.48	14.22	0.32
CaO	1.55	0.06	20.14	0.16	1.53	0.31	19.67		1.62	0.07	19.73	0.75
Na_2O	0.02	0.03	0.25	0.03	0.03	0.03	0.29		0.05	0.09	0.34	0.17
K_2O	0.00	0.00	0.00	0.00	0.00	0.00	0.00		0.03	0.08	0.04	0.07
Total	99.53	0.55	99.77	0.42	99.57	0.67	99.79		99.76	0.99	99.94	1.10
Mg#	70.34	0.98	72.19	0.81	65.26	1.55	68.26		66.78	0.81	70.54	2.14
En	69.6		47.4		64.4		42.3		65.0		43.7	
Wo	3.2		38.4		3.2		39.7		3.4		39.1	
Fs	27.2		14.3		32.4		18.0		31.6		17.3	
T (℃)	1082		17		988		28		1030		8	

Taisho 1 lava (0703D)												
	type-A opx		type-a cpx		type-B opx		type-b cpx		opx-rim		cpx-rim	
n	15	stdev	50	stdev	52	stdev	8	stdev	17	stdev	17	stdev
SiO_2	52.68	0.67	51.06	0.63	51.99	0.45	50.25	0.60	52.58	0.39	51.33	0.57
TiO_2	0.22	0.05	0.53	0.11	0.28	0.04	0.62	0.14	0.28	0.03	0.51	0.08
Al_2O_3	1.16	0.45	1.97	0.62	0.89	0.28	2.36	0.54	0.92	0.16	1.90	0.46
FeO*	18.25	0.72	10.30	0.59	21.20	0.73	11.50	0.42	20.27	0.59	10.35	0.48
MnO	0.64	0.12	0.46	0.05	0.91	0.08	0.54	0.18	0.81	0.08	0.45	0.06
MgO	24.37	0.59	14.54	0.46	22.00	0.50	13.41	0.57	22.88	0.33	14.52	0.46
CaO	1.53	0.22	20.02	0.43	1.66	0.15	20.07	0.33	1.67	0.06	20.18	0.34
Na_2O	0.05	0.05	0.32	0.18	0.06	0.04	0.29	0.04	0.02	0.02	0.28	0.04
K_2O	0.00	0.01	0.01	0.03	0.01	0.01	0.00	0.00	0.01	0.01	0.01	0.01
Total	98.91	0.78	99.20	0.70	99.00	0.80	99.04	0.87	99.45	0.76	99.54	1.04
Mg#	70.41	1.20	71.56	1.48	64.92	1.13	67.48	1.24	66.80	0.85	71.42	1.47
En	69.6		46.7		64.0		44.3		65.5		46.1	
Wo	3.2		38.8		3.5		38.7		3.5		39.1	
Fs	27.1		14.5		32.4		17.0		31.0		14.9	
T (℃)	1066		7		1012		40		1026		53	

FeO* is total Fe as FeO.
stdev = one standard deviation

Table 4-4 (continued)

Taish 2 lava (0902D)														
	type-A opx		type-a cpx		type-B opx		type-b cpx		type-c cpx		opx-rim		cpx-rim	
n	34	stdev	22	stdev	68	stdev	1	stdev	3	stdev	23	stdev	5	stdev
SiO_2	52.61	0.60	51.21	0.43	52.36	0.57	51.08		50.78	0.22	52.89	0.46	49.85	1.45
TiO_2	0.25	0.05	0.50	0.05	0.28	0.05	0.54		0.47	0.02	0.25	0.05	0.74	0.29
Al_2O_3	1.06	0.38	1.92	0.45	0.83	0.18	1.53		2.60	0.50	0.98	0.30	3.52	1.69
FeO*	18.75	0.98	10.27	0.73	21.01	0.71	11.66		8.48	0.30	19.50	1.43	9.79	3.95
MnO	0.67	0.14	0.46	0.10	0.89	0.07	0.52		0.29	0.05	0.73	0.14	0.34	0.23
MgO	24.54	0.83	14.87	0.41	22.81	0.59	14.47		15.21	0.23	23.23	1.11	14.45	3.75
CaO	1.64	0.18	20.14	0.43	1.63	0.21	19.62		20.71	0.41	1.68	0.13	19.36	7.96
Na_2O	0.04	0.03	0.28	0.05	0.04	0.03	0.30		0.26	0.01	0.02	0.02	0.28	0.11
K_2O	0.01	0.01	0.00	0.01	0.00	0.01	0.00		0.00	0.00	0.01	0.01	0.00	0.00
Total	99.56	0.89	99.65	0.63	99.85	0.82	99.71		98.81	0.31	99.29	0.88	98.33	1.11
Mg#	69.99	1.67	72.10	1.80	65.93	1.19	68.86		76.18	0.65	67.97	2.55	72.44	2.58
En	70.2		48.1		65.8		47.1		50.1		66.1		48.8	
Wo	3.4		38.2		3.4		37.0		38.8		3.5		36.7	
Fs	26.4		13.8		30.8		15.9		11.1		30.4		14.5	
T(℃)	1078		26		1002		46				1078		61	

Taisho 2 lava (0910B)												
	type-A opx		type-a cpx		type-B opx		type-b cpx		opx-rim		cpx-rim	
n	10	stdev	6	stdev	12	stdev	2	stdev	22	stdev	8	stdev
SiO_2	53.3	0.55	51.8	0.57	52.7	0.54	51.4	0.56	53.1	0.59	50.7	1.03
TiO_2	0.24	0.04	0.50	0.09	0.24	0.05	0.54	0.10	0.26	0.04	0.66	0.20
Al_2O_3	1.21	0.37	1.94	0.31	0.77	0.09	1.53	0.25	1.36	1.60	2.96	0.94
FeO*	18.6	0.86	10.3	0.62	21.1	0.93	13.4	0.87	19.0	1.82	10.0	1.38
MnO	0.62	0.10	0.43	0.11	0.85	0.09	0.46	0.08	0.67	0.16	0.33	0.09
MgO	24.4	0.71	14.9	0.46	22.5	0.83	13.9	0.35	23.5	1.77	14.8	0.65
CaO	1.56	0.09	19.8	0.57	1.59	0.15	17.9	0.03	1.78	0.51	19.5	1.08
Na_2O	0.03	0.03	0.27	0.04	0.03	0.02	0.29	0.02	0.09	0.31	0.25	0.05
K_2O	0.00	0.00	0.00	0.00	0.00	0.00	0.01	0.01	0.01	0.02	0.01	0.01
Total	100.0	0.75	99.9	0.67	99.8	0.82	99.3	0.29	99.8	0.79	99.2	0.74
Mg#	70.06	1.51	71.98	1.69	65.53	1.74	64.90	2.06	68.76	2.90	72.49	3.21
En	68.9		46.2		64.4		42.8		66.9		47.7	
Wo	3.2		38.4		3.3		35.7		3.7		37.0	
Fs	27.9		15.4		32.3		21.5		29.4		15.4	
T(℃)	1052		5		982		24		1068		41	

Taisho 2' lava (0908B)														
	type-A opx		type-a cpx		type-B opx		type-b cpx		type-c cpx		opx-rim		cpx-rim	
n	27	stdev	32	stdev	41	stdev	1	stdev	3	stdev	12	stdev	11	stdev
SiO_2	52.97	0.55	51.57	0.42	52.82	0.42	51.59		52.17	0.18	53.20	0.62	51.65	0.73
TiO_2	0.26	0.05	0.48	0.08	0.25	0.05	0.51		0.44	0.03	0.24	0.04	0.52	0.10
Al_2O_3	1.17	0.33	1.81	0.36	0.98	0.21	1.52		2.11	0.09	1.20	0.48	2.05	0.83
FeO*	19.09	0.88	10.43	0.56	20.73	0.59	12.73		8.76	0.66	18.59	2.02	10.47	0.42
MnO	0.70	0.10	0.49	0.06	0.85	0.07	0.69		0.35	0.02	0.61	0.19	0.46	0.10
MgO	24.43	0.57	14.68	0.52	23.15	0.69	14.42		16.08	0.30	24.45	1.52	14.63	0.38
CaO	1.56	0.14	20.41	0.69	1.55	0.22	19.36		20.41	0.26	1.74	0.16	20.03	0.40
Na_2O	0.03	0.02	0.28	0.04	0.03	0.03	0.31		0.21	0.02	0.02	0.02	0.27	0.04
K_2O	0.00	0.00	0.00	0.00	0.00	0.01	0.00		0.01	0.01	0.00	0.00	0.01	0.01
Total	100.2	0.82	100.2	0.52	100.4	0.70	101.1		100.5	0.63	100.0	0.96	100.1	0.42
Mg#	69.52	1.39	71.49	1.49	66.55	1.16	66.88		76.62	1.18	70.10	3.60	71.40	1.00
En	69.4		46.8		66.1		46.9		50.3		69.0		46.0	
Wo	3.3		38.9		3.2		35.7		38.0		3.6		38.6	
Fs	27.4		14.3		30.7		17.4		11.7		27.4		15.5	
T(℃)	1076		10		1013		18				1067		9	

FeO* is total Fe as FeO.

stdev = one standard deviation

Table 4-5 Average olivine phenocryst composition of Taisho 2 and Taisho 2' lavas

sample	0910B		0908B	
	ave	stdev	ave	stdev
n	8		12	
SiO_2	39.23	0.25	38.11	0.53
TiO_2	0.00	0.00	0.00	0.00
Al_2O_3	0.02	0.01	0.01	0.01
FeO*	18.93	1.07	24.34	2.29
MnO	0.26	0.02	0.39	0.06
MgO	43.17	0.98	38.59	1.98
CaO	0.18	0.01	0.16	0.01
Na_2O	0.01	0.01	0.00	0.01
K_2O	0.00	0.00	0.00	0.00
NiO	0.03	0.01	0.02	0.01
Total	101.82	0.37	101.62	0.39
Mg#	80.25	1.25	73.83	2.80
total	3.02	0.00	3.02	0.00

FeO* is total Fe as FeO.
stdev = one standard deviation

Table 4-6 Average plagioclase microlite composition of Plinian fall pumices and lava flows

	Plinian fall pumice		Lava flow							
	Plinian fall pumice		Taisho 1			Taisho 2				Taisho 2'
sample	0809F-a	0809G-a	0703D	1102B	1004B	0902D	0907	0910B	0805	0908B
	ave	ave	ave	ave	ave	ave	ave	ave	ave	ave
n	44	40	78	66	68	74	45	33	58	75
SiO_2	58.7 (2.0)	57.7 (1.9)	56.0 (1.3)	56.7 (1.0)	56.1 (0.9)	56.0 (1.7)	55.8 (1.3)	55.3 (1.5)	53.5 (1.5)	54.3 (1.4)
TiO_2	0.07 (0.03)	0.08 (0.04)	0.06 (0.03)	0.05 (0.03)	0.05 (0.02)	0.06 (0.03)	0.05 (0.03)	0.07 (0.03)	0.05 (0.03)	0.06 (0.03)
Al_2O_3	26.4 (1.3)	26.3 (1.4)	26.6 (0.9)	26.9 (0.8)	26.7 (0.8)	27.2 (1.2)	27.7 (0.86)	28.1 (1.2)	28.3 (1.2)	27.9 (1.0)
FeO*	0.82 (0.13)	0.88 (0.13)	0.88 (0.09)	0.85 (0.11)	0.83 (0.06)1	0.92 (0.10)	0.92 (0.09)	1.12 (0.43)	1.08 (0.11)	1.00 (0.10)
MnO	0.01 (0.02)	0.02 (0.02)	0.02 (0.02)	0.02 (0.02)	0.02 (0.02)	0.02 (0.02)	0.01 (0.02)	0.02 (0.03)	0.02 (0.02)	0.02 (0.02)
MgO	0.11 (0.10)	0.11 (0.05)	0.08 (0.03)	0.08 (0.07)	0.08 (0.01)	0.08 (0.02)	0.10 (0.02)	0.24 (0.37)	0.10 (0.02)	0.10 (0.02)
CaO	9.22 (1.38)	9.60 (1.13)	10.1 (0.8)	10.2 (0.6)	10.1 (0.6)	10.7 (1.2)	11.3 (0.9)	11.0 (1.0)	12.5 (1.23)	12.1 (0.9)
Na_2O	5.55 (0.59)	5.43 (0.58)	5.53 (0.41)	5.56 (0.42)	5.53 (0.27)	5.30(0.58)	5.01 (0.53)	4.47 (0.48)	4.26 (0.66)	4.57 (0.47)
K_2O	0.41 (0.13)	0.42 (0.16)	0.39 (0.07)	0.39 (0.10)	0.35 (0.05)	0.37 (0.09)	0.30 (0.06)	0.29 (0.08)	0.26 (0.08)	0.31 (0.09)
Total	101.3 (0.96)	100.6 (0.97)	99.7 (1.4)	100.8 (0.6)	99.8 (1.3)	100.7 (0.6)	101.1 (0.5)	100.7 (0.8)	100.0 (0.7)	100.4 (0.4)
An	47.7 (5.9)	49.4 (5.2)	50.3 (3.5)	50.4 (3.2)	50.3 (2.6)	52.7 (5.4)	55.6 (4.4)	57.7 (4.5)	61.8 (5.9)	59.5 (4.2)

FeO* is total Fe as FeO.

Table 4-7 Average compositions of pyroxene microlite

	darker colored Plinian fall pumice (0809G)						Taisho 1 lava (0703D)					
	opx		cpx		pig		opx		cpx		pig	
n	4	stdev	2	stdev	12	stdev	20	stdev	4	stdev	44	stdev
SiO_2	52.88	0.84	51.80	0.88	52.16	0.90	52.75	0.67	51.17	0.60	51.93	0.91
TiO_2	0.63	0.57	0.86	0.56	0.50	0.18	0.33	0.08	0.70	0.07	0.44	0.30
Al_2O_3	1.27	0.47	3.13	1.80	1.74	0.54	1.01	0.27	2.25	0.16	1.10	0.57
FeO*	21.32	1.79	13.26	3.40	21.14	2.44	21.76	1.54	18.38	0.79	23.90	1.99
MnO	0.84	0.11	0.56	0.20	0.96	0.10	0.88	0.10	0.85	0.07	1.05	0.08
MgO	21.63	1.50	13.67	1.31	17.56	1.28	21.05	1.39	15.28	1.06	17.04	1.89
CaO	1.96	0.44	15.83	3.54	5.33	2.25	2.25	0.32	10.78	1.12	4.74	1.27
Na_2O	0.12	0.08	0.48	0.04	0.22	0.12	0.07	0.06	0.22	0.04	0.14	0.16
K_2O	0.10	0.15	0.21	0.15	0.14	0.07	0.06	0.04	0.13	0.11	0.08	0.06
Total	100.73	0.86	99.80	0.42	99.75	1.38	100.17	0.87	99.76	0.42	100.42	0.74
Mg#	64.36	3.43	64.87	8.04	59.74	3.55	63.25	3.07	59.66	1.45	55.85	4.40

	Taisho 2 lava (0902D)						Taisho 2 lava (0910B)					
	opx		cpx		pig		opx		cpx		pig	
n	1	stdev	7	stdev	58	stdev	15	stdev	29	stdev	12	stdev
SiO_2	51.30		50.20	1.48	51.20	0.55	53.89	0.55	51.43	0.88	53.04	0.56
TiO_2	0.22		0.76	0.26	0.37	0.08	0.26	0.07	0.79	0.20	0.38	0.10
Al_2O_3	0.63		2.96	1.12	0.79	0.28	1.27	0.47	3.25	0.79	1.59	0.67
FeO*	25.83		16.35	3.17	24.59	1.51	18.88	1.62	12.55	1.39	18.60	2.66
MnO	0.91		0.58	0.10	1.01	0.10	0.60	0.15	0.44	0.07	0.62	0.15
MgO	17.60		14.30	0.93	16.33	1.04	23.50	1.42	15.47	1.20	20.05	1.23
CaO	2.54		13.74	3.28	4.56	0.88	2.04	0.35	15.78	1.93	6.12	2.14
Na_2O	0.01		0.23	0.12	0.14	0.10	0.03	0.04	0.23	0.04	0.08	0.04
K_2O	0.03		0.08	0.11	0.06	0.06	0.02	0.02	0.03	0.02	0.03	0.03
Total	99.07		99.19	0.90	99.05	0.64	100.49	0.54	99.97	0.57	100.52	0.61
Mg#	54.85		61.21	4.02	54.19	2.72	68.88	3.20	68.75	2.40	65.85	4.05

	Taisho 2' lava (0908B)					
	opx		cpx		pig	
n	1	stdev	6	stdev	49	stdev
SiO_2	51.96		51.25	0.72	51.68	0.44
TiO_2	0.29		0.54	0.15	0.35	0.07
Al_2O_3	1.11		2.23	0.80	0.85	0.28
FeO*	24.37		13.99	2.40	23.26	1.14
MnO	0.81		0.50	0.09	0.80	0.07
MgO	19.61		16.03	1.90	17.75	0.85
CaO	1.81		15.63	3.06	4.80	0.94
Na_2O	0.05		0.18	0.12	0.10	0.10
K_2O	0.03		0.03	0.01	0.04	0.02
Total	100.03		100.39	0.49	99.62	0.71
Mg#	58.93		67.19	3.84	57.62	1.97

FeO* is total Fe as FeO.
stdev = one standard deviation

Table 4-8 Average matrix glass compositions of Plinian fall pumices and lava flows

Plinian fall pumice										
sample	0809A-a	0809A-b	0809A-c	0809B-a	0809B-b	0809B-c	0809C-a	0809C-b	0809C-c	0809D-a
	ave	ave	ave	ave	ave	ave	ave	ave	ave	ave
n	10	10	10	10	10	10	9	10	10	9
SiO_2	71.2 (0.4)	70.5 (0.3)	70.8 (0.7)	70.1 (0.4)	71.3 (0.7)	69.1 (1.0)	70.4 (0.6)	71.2 (0.7)	70.9 (1.0)	70.2 (0.2)
TiO_2	0.88 (0.05)	0.80 (0.06)	0.77 (0.03)	0.78 (0.04)	0.84 (0.07)	0.84 (0.02)	0.84 (0.03)	0.84 (0.03)	0.84 (0.05)	0.78 (0.04)
Al_2O_3	13.6 (0.2)	14.3 (0.1)	14.4 (0.2)	14.3 (0.1)	13.6 (0.7)	14.4 (0.16)	14.6 (0.2)	13.7 (0.3)	14.7 (0.3)	14.6 (0.1)
FeO*	4.07 (0.15)	3.85 (0.13)	3.93 (0.15)	4.02 (0.12)	3.79 (0.36)	4.28 (0.26)	4.22 (0.15)	3.96 (0.13)	4.34 (0.08)	3.98 (0.13)
MnO	0.11 (0.02)	0.11 (0.03)	0.11 (0.02)	0.13 (0.04)	0.10 (0.03)	0.12 (0.04)	0.13 (0.01)	0.11 (0.02)	0.14 (0.03)	0.12 (0.03)
MgO	0.69 (0.05)	0.92 (0.04)	0.93 (0.04)	0.99 (0.04)	0.68 (0.28)	1.10 (0.06)	1.09 (0.06)	0.73 (0.05)	1.13 (0.04)	1.00 (0.02)
CaO	2.65 (0.12)	3.04 (0.08)	3.10 (0.12)	3.18 (0.04)	2.42 (0.32)	3.32 (0.17)	3.20 (0.07)	2.50 (0.11)	3.26 (0.14)	3.05 (0.04)
Na_2O	3.18 (0.30)	3.25 (0.32)	3.20 (0.20)	3.22 (0.25)	3.57 (0.61)	3.19 (0.41)	1.89 (0.19)	3.75 (0.42)	1.62 (0.38)	3.82 (0.30)
K_2O	3.02 (0.07)	2.84 (0.04)	2.82 (0.08)	2.79 (0.05)	3.17 (0.17)	2.66 (0.06)	2.77 (0.08)	3.07 (0.09)	2.79 (0.06)	2.81 (0.09)
Total	99.4 (0.5)	99.6 (0.4)	100.0 (0.9)	99.5 (0.7)	99.5 (0.8)	99.0 (1.6)	99.2 (0.8)	99.9 (1.1)	99.7 (1.3)	100.4 (0.4)

Plinian fall pumice									
sample	0809D-b	0809D-c	0809E-a	0809E-b	0809E-c	0809F-a	009G-a	0809G-b	0809G-c
	ave	ave	ave	ave	ave	ave	ave	ave	ave
n	9	9	9	9	9	9	6	9	10
SiO_2	69.7 (1.3)	70.2 (0.5)	69.8 (0.4)	70.3 (0.4)	69.7 (1.2)	72.6 (2.3)	71.4 (1.5)	70.0 (1.0)	71.1 (1.2)
TiO_2	0.80 (0.06)	0.81 (0.03)	0.81 (0.04)	0.85 (0.04)	0.81 (0.05)	0.80 (0.14)	0.71 (0.09)	0.86 (0.04)	0.86 (0.08)
Al_2O_3	14.1 (1.3)	14.6 (0.2)	14.3 (0.1)	14.0 (0.2)	14.3 (0.8)	13.9 (1.9)	14.4 (1.1)	14.1 (0.4)	13.7 (1.2)
FeO*	4.22 (0.68)	4.09 (0.15)	4.54 (0.13)	4.31 (0.17)	4.66 (0.92)	3.67 (0.49)	3.24 (0.45)	4.44 (0.24)	4.31 (0.49)
MnO	0.13 (0.05)	0.13 (0.02)	0.14 (0.02)	0.12 (0.03)	0.14 (0.05)	0.11 (0.02)	0.10 (0.04)	0.12 (0.02)	0.16 (0.04)
MgO	1.13 (0.62)	1.05 (0.04)	1.05 (0.04)	0.87 (0.05)	1.35 (0.98)	0.48 (0.10)	0.49 (0.22)	0.92 (0.23)	0.74 (0.27)
CaO	2.94 (0.57)	3.12 (0.06)	3.48 (0.11)	3.11 (0.13)	3.65 (0.40)	2.60 (1.04)	3.01 (0.56)	3.00 (0.32)	2.63 (0.60)
Na_2O	4.11 (0.41)	3.46 (0.35)	3.55 (0.32)	3.62 (0.21)	3.72 (0.25)	3.88 (0.37)	4.21 (0.44)	3.96 (0.32)	3.82 (0.52)
K_2O	2.84 (0.25)	2.81 (0.09)	2.75 (0.05)	2.84 (0.07)	2.65 (0.24)	3.16 (0.46)	2.94 (1.2)	2.91 (0.11)	3.09 (0.26)
Total	100.0 (0.4)	100.3 (0.8)	100.4 (0.5)	100.1 (0.6)	100.1 (1.7)	101.1 (0.5)	100.5 (1.2)	100.3 (0.6)	100.4 (0.8)

Lava flow								
	Taisho 1			Taisho 2				Taisho 2'
sample	0703D	1102B	1004B	0902D	0907	0910B	0805	0908B
	ave	ave	ave	ave	ave	ave	ave	ave
n	10	9	10	10	8	10	7	9
SiO_2	76.8 (0.9)	77.3 (0.5)	76.4 (0.5)	76.1 (0.6)	76.2 (0.7)	73.0 (0.5)	74.4 (0.6)	73.6 (0.2)
TiO_2	0.86 (0.06)	0.74 (0.04)	0.75 (0.04)	0.93 (0.03)	1.01 (0.05)	0.99 (0.07)	1.05 (0.12)	1.06 (0.05)
Al_2O_3	11.9 (0.5)	11.7 (0.1)	11.8 (0.1)	11.9 (0.1)	11.7 (0.3)	12.3 (0.7)	12.0 (0.7)	12.1 (0.1)
FeO*	2.21 (0.23)	2.66 (0.14)	3.26 (0.09)	3.21 (0.25)	2.78 (0.67)	4.74 (0.40)	3.29 (0.44)	4.23 (0.18)
MnO	0.05 (0.03)	0.05 (0.04)	0.06 (0.03)	0.06 (0.02)	0.07 (0.03)	0.11 (0.02)	0.08 (0.03)	0.08 (0.02)
MgO	0.07 (0.02)	0.18 (0.03)	0.27 (0.02)	0.30 (0.06)	0.13 (0.16)	0.42 (0.04)	0.20 (0.05)	0.52 (0.06)
CaO	0.88 (0.30)	0.94 (0.12)	1.50 (0.32)	1.25 (0.15)	1.05 (0.17)	2.14 (0.33)	1.41 (0.32)	1.58 (0.10)
Na_2O	3.01 (0.54)	3.76 (0.33)	3.43 (0.27)	1.63 (0.31)	3.59 (0.57)	3.81 (0.43)	3.80 (0.39)	2.14 (0.26)
K_2O	4.02 (0.28)	4.04 (0.20)	3.65 (0.07)	3.99 (0.10)	4.21 (0.12)	3.55 (0.14)	4.07 (0.27)	4.69 (0.15)
Total	99.8 (0.5)	101.3 (0.8)	101.2 (0.4)	99.3 (0.6)	100.7 (0.7)	101.1 (0.6)	100.3 (0.9)	100.0 (0.4)

FeO* is total Fe as FeO.

Table 4-9 Examples of estimation of pre-eruptive melt compsositions

	gl		pl		opx		pig		aug		mt		melt
sample	0703D		0703D		0703D		0703D		0703D		0703D		0703D
	ave	stdev	ave	stdev	ave	stdev	ave	stdev	ave	stdev	ave	stdev	
n	10		78		20		44		4		7		
SiO_2	76.95	0.87	56.17	1.05	52.66	0.58	51.72	0.76	51.30	0.75	1.03	1.96	67.80
TiO_2	0.86	0.06	0.06	0.03	0.33	0.08	0.43	0.30	0.70	0.07	20.58	3.62	0.93
Al_2O_3	11.92	0.47	26.68	0.77	1.01	0.28	1.10	0.57	2.25	0.17	1.87	0.62	14.13
FeO*	2.21	0.24	0.88	0.09	21.72	1.49	23.80	1.95	18.43	0.74	73.27	4.29	5.39
MnO	0.05	0.03	0.02	0.02	0.88	0.10	1.04	0.08	0.85	0.07	0.70	0.07	0.16
MgO	0.07	0.02	0.08	0.03	21.01	1.40	16.97	1.87	15.31	1.01	1.35	0.30	2.16
CaO	0.88	0.30	10.13	0.75	2.25	0.32	4.72	1.27	10.81	1.14	1.11	1.29	3.55
Na_2O	3.02	0.53	5.55	0.39	0.07	0.06	0.14	0.16	0.22	0.04	0.04	0.11	3.26
K_2O	4.03	0.28	0.39	0.07	0.06	0.04	0.08	0.06	0.13	0.11	0.05	0.05	2.62
Total	100.00		99.96		100.00		100.00		100.00		100.00		100.00
An			50.3	3.5									
mode (vol.%)	66.9		23.6		2.6		5.6		0.5		0.8		
mineral density	2.4		2.69		3.59		3.32		3.38		5.2		

All data are normalized to tatal 100 wt.%.
FeO* is total Fe as FeO.

Chapter 5: Textural studies of volcanic products erupted at the 1914-1915 eruption of Sakurajima Volcano

5.1 Introduction

Difference in eruption styles such as Plinian explosion versus lava effusion has been considered to reflect different modes of magma degassing (i.e., gas escape from the system) (Eichelberger et al.,1986; Jaupart and Allegre,1991). Jaupart and Allegre (1991) numerically showed that slow ascent of magma allows efficient degassing, resulting in effusive eruptions, whereas fast ascent of magma prohibits the efficient magma degassing, resulting in explosive eruptions. Eruption style in silicic magma may variously change from explosive to effusive in a single eruption, resulting that various types of volcanic products are erupted. Textures such as color, bulk density, microlite texture and vesicle textures and chemical feature such as bulk rocks, groundmass glass and mineral chemistry of these volcanic products record various phenomena occurring during the eruption. Magma mixing or mingling processes during the explosive eruption were recorded in the chemical heterogeneity of bulk rock or groundmass glass, resulting in the difference in color of volcanic products. For example, chemically and texturally heterogeneous clasts erupted at the 79 AD eruption of Vesuvius due to magma mingling (Gurioli et al., 2005). On the other hand, difference of decompression rate and degassing processes induces the textural difference such as bulk density, vesicularity, color, vesicle number density, and microlite texture in spite of almost the same chemical features (e.g., Gardner et al., 1998; Polacci et al., 2001). In the previous chapter, author verified that chemical features of the volcanic products erupted at early stage of the eruption (from Plinian to Taisho 1 lava stage) are almost the same in spite of the difference of bulk density and color, indicating that difference of these features are results of the difference of decompression rate and degassing processes. Decompression rate and degassing processes are recorded in vesicle texture and microlite texture. Vesicle number density is proportional to the 3/2 power of decompression rate for homogeneous vesicle nucleation (Toramaru, 1995).

Vesicularity of volcanic products changes in response to degassing process; i.e., closed-system gas expansion or escape of gas from the system and subsequent coalescence, nucleating and deformation. Moreover volatile exsolution from melt increases the liquidus temperatures of melt and consequently sometimes induces crystallization of microlite (Hammer and Rutherford, 2002; Couch et al., 2003; Martel and Schmidt, 2003). According to the previous decompression experiments, number density and modal content of microlite change drastically in response to decompression rate relating to magma ascent rate, suggesting that vesicle and plagioclase microlite texture reflect magma ascent and degassing process.

The 1914-1915 (Taisho) eruption of Sakurajima volcano, Kyushu Japan, representing the largest eruption in the last 1,000 years in Japan, continued for about 1 year, and erupted Plinian fall pumice, followed by extrusion of lava flows in three periods (Koto, 1916). Total volume of the volcanic products is c.a. 2.0 km^3 (DRE) (Ishihara et al., 1981). These volcanic products are expected to have different plagioclase microlite textures and vesicle textures. The purpose of this chapter is to reveal the transition of the eruption style, especially from Plinian phase to Taisho 1 lava phase, by analyzing chemical feature of groundmass glass, bulk density, vesicularity, vesicle textures, and plagioclase microlite textures of the volcanic products. In this chapter, at first, volcanic products of the eruption were classified in terms of vesicularity and plagioclase microlite texture of the volcanic products. Then, the causes of textural difference are discussed from the aspect of magma ascent processes in relating to plagioclase microlite texture, and degassing process in relating to vesicularity.

5.2 **Analytical methods**

5.2.1 **Textural analyses**

X-ray mapping and BSE (back-scattered electron) images for textural analyses were obtained by JEOL JXA-8900R at the Venture Business Laboratory of Kobe University.

All images were analyzed by using the computer software, MacAspect of Mitani Co.Ltd. Japan. MacAspect can easily calculate many characteristic features such as area, aspect ratio and geometric mean diameter of the object, which are extracted in response to the choice of threshold in gray scale spectrum. Pict formatted digital mapping images and photographs of thin sections were converted into binary images.

X-ray mapping images of Al (Fig. 5-1) were used to acquire CSD, modal content, number density, and average length of plagioclase microlites. In Plinian fall pumice samples, vesicularity also are estimated from the same mapping images. In three lava flow samples, X-ray mapping images of Al and photographs of thin sections were used to analyze CSDs of plagioclase and distinguish plagioclase microlite from plagioclase phenocryst. X-ray mapping analyses were conducted with 15 kV acceleration voltage and 12 nA beam current and dwell time was 100 microseconds. Resolution of images is 1 μm/pixel for Plinian fall pumices and 1, 2 and 4 μm/pixel for lava flows to acquire plagioclase microlite texture. Total area of 1, 2 and 4 μm/pixel images are 300×300 μm^2, 600×600 μm^2, 700×700 μm^2 and 1200×1200 μm^2, respectively. 2 μm/pixel, 350×350 μm^2 images were analyzed for some of Plinian fall pumices, which contain relatively large microlites. For CSDs of Plinian fall pumices, at least two images for each samples were analyzed, since sometimes only a few microlites were included in one image. For CSDs of lava, one image of 1, 2 and 4 μm/pixel images was analyzed and combined for CSDs to cover relatively large microlites. Apparently attached crystals originally separated each other were separated off by drawing lines of minimum thickness (Fig 5-1). In three samples, ×40 photographs of thin section were used to analyze CSDs of plagioclase phenocrysts.

X-ray mapping images of Si (Fig. 5-1) were used to acquire VSD and vesicularity of Plinian fall pumices. Vesicle textures of lava were not analyzed because those vesicles record coalescence, deformation, collapse and compaction of vesicles and do not record the original textures of vesicles. Dwell time at image acquisition was 100 microseconds and resolution of image was 2 μm/pixel in order to analyze vesicle textures. Total number of pixels is 350×350 or 400×400, resulting in total area of 700×700 μm^2 and 800×800 μm^2, respectively. At least two images were analyzed for

each sample. Apparent coalescence vesicles were separated off by drawing lines of minimum thickness (1 pixel, representing 2 μm). Estimated bulk vesicularity was converted to groundmass vesicularity by using total phenocryst modes estimated using point counter (1000 point). BSE photo images were used to obtain the modal content of pyroxene and titanomagnetite microlite in groundmass (Fig. 5-2).

Width (w)/length (l) ratios, area of each microlite or vesicle, reference area, modal content or vesicularity and areal number density (Na) of microlites or vesicles were measured by using MacAspect. To convert areal number density per unit diameter range (Na (Dxy)) to volumetric number density per unit diameter range (Nv (Dxy)) for VSDs of Plinian fall pumices, the method of Sahagian and Proussevitch (1998) was applied. In this study, all vesicles were approximated as sphere. Geometric mean diameter of vesicles is plotted on X-axis of VSDs. Total volumetric number density was estimated from VSDs as follow:

$$Nv = \sum Nv\,(Dxy) \qquad (5\text{-}1)$$

To convert areal number density (Na) to volumetric number density (Nv), and to obtain CSDs of microlite, the method of Higgins (2000) was applied. Width (w)/length (l) ratios, area, and modal content and areal number density of plagioclase were measured by computer software, MacAspect. Aspect ratio, short-(S) intermediate-(I) large-(L) axis of plagioclase, was estimated by the method of Higgins (1994). True crystal length (Lt) and crystal width (Wt) were estimated as follows:

$$Lt = l * I \qquad (5\text{-}2)$$

$$Wt = w * L/S \qquad (5\text{-}3)$$

Volumetric number density of crystals in the length interval Lx to Ly (Nv (Lxy)) is obtained as follow:

$$Nv\,(Lxy) = Na\,(Lxy)/Hxy \qquad (5\text{-}4)$$

Where Na (Lxy) is areal number density of crystals in the length interval Lx to Ly. Hxy is the mean value for a length interval Lx to Ly. Population density of crystals (number density per unit volume per unit crystal length) in the length interval Lx to Ly (n (Lxy)) is obtained as follow:

$$n\,(Lxy) = Nv\,(Lxy)/(Ly-Lx) \qquad (5\text{-}5)$$

Average size (Sn) of crystals was estimated by the method of Hammer et al. (1999).

$$Sn = (\varphi/Na)^{0.5} \qquad (5\text{-}6)$$

Where φ is modal content of plagioclase microlite (vol.%).

In this study, crystal length (Lt) was plotted on X-axis of CSDs for plagioclase. Total volumetric number density (Nv) is obtained as follow:

$$Nv = Na/Sn \qquad (5\text{-}7)$$

5.2.2 **Measurement of bulk density and residual water content of Plinian fall pumices**

50 pumice samples for each unit, hence total 350 samples, were analyzed for bulk density and 35 samples within 350 samples were analyzed for residual water content.

Bulk density of plinian fall pumices was analyzed at Kobe University using helium pycnometer (Micrometicics Accupyc 1330; Shimadzu Co.Ltd. Japan), which utilizes He gas. Firstly, total weight of pumice was measured. Then surface of pumice was coated by melted paraffin, and the volume of pumice was measured using Micrometicics Accupyc 1330. Bulk density was calculated from the values of pumice weight and volume. Bulk vesicularity was calculated from the equation of Houghton and Wilson (1989), assuming that magmatic density is 2500 kg/m^3 and converted to

crystal-free vesicularity using total phenocryst mode.

Residual water contents of Plinian fall pumices were analyzed by Karl-Fisher titration method with Aquacounter AQ-200 (Hiranuma Co.Ltd. Japan) in Kobe University. Water in samples (about 0.1-0.5 g) was extracted by two-step heating. First step is at 120 ℃ for at least 12 hour for the aim of extraction of water attached to the surface of the sample. Second step is at 1000±40 ℃ for about half a hour for extraction of water exsolved in the sample. Bulk rock water contents were converted to groundmass water contents by using total phenocryst modes.

5.3 **Result**

5.3.1 **Density and residual water contents of Plinian fall pumices**

Bulk density (Fig. 3-10) of pumices changes from the lower part to the upper part of the deposit. Most pumices in the lower to middle part of the deposit have density of about 700 kg/m^3 (vesicularities around 74 vol.%). The lightest pumice is 403 kg/m^3, corresponding to vesicularity of 85 vol.%. In the upper part of the deposit from 0809F (1.5-1.8 m) to 0809G (1.8-2.1 m) (Fig. 3-10), ratio of high density pumices increase and as a result, average pumice density exceeds 1000 kg/m^3 (vesicularities less than 62 vol.%). The heaviest pumice is 1678 kg/m^3, corresponding to vesicularity of 35 vol.%. Most of low density pumices are white pumices. High density pumices more than 950-1000 kg/m^3 (64-62 vol.%) show slightly darker colored appearance.

The residual water contents of the groundmass of pumices ranges 0.2-0.6 wt.%. Relation among the bulk density, vesicularity and residual water content are listed in Table 5-1.

5.3.2 **Textures of plagioclase microlites and vesicles of Plinian fall pumices**

Vesicularity of Plinian pumices is inversely correlated with the bulk density (Fig. 3-10). Vesicularities of pumices from the lower to middle part of the deposit estimated

from mapping images of Si are in ranges of 55-75 vol.% (Fig. 5-3a and Table 5-2). On the other hand, vesicularity of darker colored pumices collected from the upper part of the deposit are in a range of 25-51 vol.%. Vesicularities estimated from mapping images are not necessarily the same as those estimated from bulk density because of analytical error (Table 5-2). Vesicularities of white pumice estimated from bulk density (400-1000 kg/m^3) are in range of 60-83 vol.% and those of darker colored pumice are in range of 34-60 vol.%, respectively. Vesicularities estimated from mapping images are 25-75 vol.%. The difference of vesicularity estimated from bulk density and mapping image is due to that (1) vesicularity estimated from mapping images change depending on the mapping area and mapping size, resulting in large analytical error (Table 5-2) and that (2) treatment of apparently coalescenced vesicles also causes the difference of vesicularity. Apparently coalescenced vesicles were separated off by drawing lines of minimum thickness (1 pixel thickness representing 2 μm) in estimating vesicularity from mapping images, causing the estimation of less vesicularity. Therefore, vesicularities calculated from bulk density expect to represent more precious feature of vesicularity of Plinian fall pumice. Average vesicularity estimated from bulk density is around 74 vol.%. On the other hand, Vesicularities of most of white pumice estimated from mapping images, are in range of 65-74 vol.%. Vesicularity estimated from mapping images, therefore, represents the rough features of actual vesicularities. Differences between white and darker colored pumices are around 950-1000 kg/m^3, corresponding to vesicularity estimated from bulk density of 64-62 vol.%. Vesicle number density of Plinian fall pumice erupted at the 1914-1915 eruption of Sakurajima volcano is in range from 4.2×10^{13}-2.7×10^{14} m^{-3}, relatively small values in silicic magma. Number density of vesicles of pumices in the lower to middle part of the deposit ranges in 5.9×10^{13}-2.7×10^{14} m^{-3}. Number density of vesicles of slightly darker colored pumices in the upper part of the deposit are in a range of 4.2×10^{13}-2.0×10^{14} m^{-3}, which is mostly smaller than that of white pumice from the lower to middle part of the deposit expect one sample, which shows lowest vesicularity (Fig. 5-3b). VSDs of all samples show linear correlation between logarithm of population density and geometric mean vesicle diameter. VSDs of lower vesicularity

samples show lower population density at relatively large vesicle sizes compared with higher vesicularity samples, indicating that change of vesicularity is due to the difference of number density of large vesicles (Fig. 5-3). Another feature of vesicle texture is that all pumices analyzed contain some silica-minerals in vesicles.

Plagioclase microlite textures change drastically with eruptive unit (Fig. 5-4, Table 5-3 and 5-4). From the lower to middle parts of the deposit (from 0809A to 0809E), modal content of plagioclase microlite in groundmass vary between in a range of 0.1 to 10.7 vol.%. Volumetric number density (number density as follows) of plagioclase is from 2.5×10^{13}-1.1×10^{15} m^{-3}. In the upper part of the deposit, modal content of plagioclase microlite range in 5.9-16.4 vol.%. Number density of plagioclase microlite is from 2.6×10^{14}-1.8×10^{15} m^{-3}, indicating that pumices in the upper parts of deposit tend to contain larger number of microlites compared with those in the lower to middle part of deposit. Average size of plagioclase microlites is in a range of 2.7-6.4 μm.

5.3.3 **Plagioclase microlite texture of lavas**

Plagioclase microlites in lavas are euhedral and generally equant tabular to skeletal fork-shaped. According to the CSDs of plagioclase of three lava flow samples, difference between microlite and phenocryst (or microphenocryst) is about 100 μm in length (Fig. 5-5). Pyroxene and titanomagnetite microlites are euhedral and sometimes attached to each other. The range in number density of plagioclase microlite in clinkery lava varies between 1.3×10^{14} and 4.9×10^{14} m^{-3} (Table 5-4). The variation of number density is smaller than those of Plinian fall pumices. Modal content of plagioclase microlite in groundmass is in a range of 16-33 vol.%, which are higher than those in Plinian fall pumices. Average size of plagioclase microlite in lavas is 7.1-10.7 μm, which are larger than those in Plinian fall pumices. Modal contents of pyroxene and titanomagnetite microlite are 4.9-10.5 vol.% and 0.5-1.1 vol.%, respectively (Table 5-4). Number density of microlite in clinkery and massive parts of lavas is almost the same and textural differences are correlated with modal content.

5.3.4 **CSDs for plagioclase microlite in Plinian fall pumices and lavas**

CSD plots of plagioclase microlite in Plinian fall pumices and lava flows are shown in Figure 5-6, and Fig 5-7, respectively. CSD plots of most samples, expect for some white pumices, show linear correlation between logarithm of population density and crystal length. Intercept and slope values are estimated by least square fitting. The intercepts of CSDs in Plinian fall pumices are $10^{18.2}$-$10^{20.3}$ m^{-4} and are slightly larger than the intercepts of CSDs of lava flows, which are $10^{18.9}$-$10^{19.5}$ m^{-4}. The slopes of CSDs in lava flows are shallower than the slopes of CSDs in Plinian fall pumices, meaning that size variation of microlite is larger in lava flows compared with that in Plinian fall pumices.

5.4 **Discussions**

5.4.1 **The relation between CSD and An content of plagioclase**

There is a relatively clear correlation between CSDs and An contents of plagioclase (Fig. 5-5). Both population densities and An contents of plagioclase drastically change around 100 μm. Population densities of plagioclase change drastically around 100 μm. Population densities of plagioclase smaller than 100 μm are higher than population densities of plagioclase larger than 100 μm. Within the range of crystal size less than 100 μm, population densities of plagioclase drastically increase, as crystal size decrease. Population densities of plagioclase larger than 100 μm are almost constant regardless the change of crystal size. An contents of core of plagioclase smaller than 100 μm is around An_{50} and nearly constant. On the other hand, there is a large variation of An contents from An_{52} to An_{94} of plagioclase larger than 100 μm. These results suggest that the length difference between microlite and phenocryst (or microphenocryst) is around 100 μm.

5.4.2 **Classification of ejecta by vesicularity and plagioclase microlite texture**

In this chapter, volcanic products are divided in response to vesicularity and plagioclase microlite texture. Plinian fall pumice can be divided into two types in terms of vesicularity. One is Plinian fall pumice with high vesicularity (low density) and white in appearance. The other is Plinian fall pumice with low vesicularity (high density) and darker colored in appearance. While high vesicularity white pumice deposited whole parts of the Plinian fall deposit, low vesicularity darker colored pumice mainly deposited at upper part of the deposit from 0809F to 0809G.

There is no sharp boundary about vesicularity among white pumices. High vesicular white pumice, however, can be classified into two types according to plagioclase microlite texture (Fig. 5-4 and Fig. 5-6b). Hence, Plinian fall pumice can be divided into three types in terms of vesicularity and plagioclase microlite texture. The first type (type-1) is high vesicular (>60 vol.% estimated from mapping image)white Plinian fall pumices with low modal content and number density of plagioclase microlite (modal content <1.0 vol.% or number density $<10^{14}$ m^{-3}). The second type (type-2) is high vesicular (>55 vol.% estimated from mapping image) white Plinian fall pumices with intermediate modal content (1.0-11 vol.%) and number density ($1\text{-}10\times10^{14}$ m^{-3}) of plagioclase microlite. Difference of plagioclase microlite textures is clearly shown in CSDs of both types (Fig. 5-6b). CSDs of type-1 show small size variation less than 30 μm length and low population density at small size (less than 20 μm) compared with the others due to low modal content and number density. On the other hand, CSDs of type-2 show large size variation up to 80 μm, verifying the difference of type-1 and type-2. Darker colored low vesicular pumices (type-3 pumice) show different textural feature of vesicle and plagioclase microlite (Fig. 5-4). The darker colored type-3 pumices show intermediate to high modal content (8-16 vol.%) and number density (5×10^{14}-2×10^{15} m^{-3}) of plagioclase microlite. Vesicularities of type-3 pumices estimated from mapping images are 25-50 vol.%.

Plagioclase microlite textures of lavas are quite different from those of Plinian fall pumice, suggesting that lavas can be divined from the others. The fourth type is lava

flows with high modal content (>16 vol.%), intermediate number density ($1\text{-}5\times10^{14}$ m^{-3}) of plagioclase microlites and low vesicularity. Although modal content of plagioclase microlite in lavas is larger than those in type-3 pumices, number density of plagioclase in lavas is smaller than those in type-3 pumices. CSD slopes of lavas are as steep as CSD slopes of type-2 pumices and slight gentler than those of type-3 pumices (Fig. 5-6 and Fig. 5-7). CSDs of lavas, however, show that size variation of microlite in lavas is large up to 120 μm, resulting in the difference of modal content.

There is no sharp boundary about vesicle texture between type-1 and type-2 in spite of large textural variation of plagioclase microlite. High vesicular white pumices (type-1 and type-2) are deposited whole parts of the Plinian fall deposit. These results imply that textural change of plagioclase microlite occurred continuously between type-1 and type-2 pumice. On the other hand, type-3 pumices are deposit slightly in the low to middle part of the Plinian fall deposit, but are mainly deposited at the upper part of the deposit from 0809F (1.5-1.8 m) to 0809G (1.8-2.1 m) and show quite different texture of vesicle and plagioclase microlite from type-1 and type-2 pumice, indicating that physical or chemical change during Plinian phase of the eruption may reflect the textural difference of type-1, -2 white pumices and type-3 darker colored pumices. Of course, physical or chemical change might occur during the transition of eruption style from Plinian to lava effusion. However, physical or chemical change might occur from early and middle stage to late stage of Plinian phase. For example, chemically and texturally heterogeneous clasts erupted at the 79 AD eruption of Vesuvius due to magma mingling (Guioli et al., 2005). On the other hand, in the case of the 1992 eruption of Crater Peak, the difference of eruptive process and degassing process result in the two types of texturally different clasts, both show chemically homogeneous (Gardner et al., 1998). In the case of the 1914-1915 eruption of Sakurajima volcano, two reasons for textural change from type-1 and type-2 white pumices to type-3 darker colored pumices and/or lavas are considered; (1) is chemical change from silicic to basic due to magma mixing and (2) is decrease in decompression late from early stage to late stage of Plinian phase and to lava effusive phase of the eruption.

5.4.3 **Pre-eruptive melt composition at magma chamber**

In the case of the 1914-1915 eruption of Sakurajima volcano, the reason of textural difference of white and darker colored pumices is due to not chemical change from silicic to basic due to magma mixing, but decrease in decompression late from early stage to late stage of Plinian phase of the eruption. Per-eruptive melt compositions of lavas and darker colored pumices were estimated from the compositions and mode of groundmass glass and microlite mineral (Table 4-8) to evaluate the effect of chemical heterogeneity induced by magma mixing to the textural difference of the volcanic products. Groundmass glass and calculated pre-eruptive melt compositions at magma chamber are shown in Table 4-8, Table 4-9 and Figure 4-11. SiO_2 contents of groundmass glass of type-1 and -2 pumices are 67-70 wt%. Pre-eruptive melt compositions of type-1 and type-2 pumices are similar to the groundmass glass compositions, because type-1 and -2 pumices show lower modal content. Pre-eruptive melt composition of type-3 pumice and Taisho 1 lava flow are around 67-70 wt%, indicating that microlite crystallize from chemically homogeneous melt in Plinian fall pumice and Taisho 1 lavas. Pre-eruptive melt compositions of Taisho 2 and Taisho 2' lava flow are around 69-64 wt%, and are slightly more basic than pre-eruptive melt compositions of Plinian fall pumice and Taisho 1 lavas. Change of pre-eruptive melt compositions from silicic to basic are due to progressing of magma mixing (Yanagi et al., 1991), resulting in difference of An content of plagioclase microlite in lavas. Hence, these results suggest that textural differences of type-1 and type-2 white pumice, type-3 darker colored pumice and Taisho 1 lava are due to not chemical heterogeneity of pre-eruptive melt induced by magma mixing but difference of decompression rate during Plinian phase to early stage of lava effusive phase of the eruption. Moreover, chemical heterogeneity of pre-eruptive melt induced by magma mixing during late stage of effusive phase of the eruption reflected not the plagioclase microlite textures but the An contents of plagioclase microlite.

5.4.4 Relative change of decompression rate of magma during the eruption

At first, relative change of decompression rate is discussed in terms of microlite texture. However, before discussing the relation between plagioclase microlite texture and decompression rate, the effect of cooling induced crystallization after erupted from vent must be considered. In the case of Plinian eruption, relatively small volcanic products quenched rapidly soon after ejected from vent, indicating that crystallization of microlite occur mainly in the conduit. On the other hand, in the case of lava effusion, microlite crystallization may occur during emplacement. Textural changes of plagioclase microlite in clinkery parts of blocky lavas, massive part of blocky lavas and massive part of sheet-like lavas at the same locality, were examined to estimate the crystallization processes during emplacement. Modal contents of microlite in clinkery part of blocky lava, massive part of blocky lavas and massive part of sheet-like lava differ by large, especially in Taisho 1 lava of L. 1 point, in spite of small variation of number density of plagioclase microlite (Table 5-4), suggesting that crystallization process during emplacement is mainly subsequent growth of pre-nucleated microlite.

Previous decompression experiments indicate that crystallization is induced by decompression (Hammer and Rutherford, 2002; Couch et al., 2003; Couch, 2003; Martel and Schmidt, 2003). Also they show that modal content and number density of microlite change in response to amount of decompression (ΔP) and decompression rate ($\Delta P/\Delta t$). Figure 5-8 show the ΔP–logarithm of number density plots of SSD (Single-Step-Decompression) experiment and logarithm of $\Delta P/\Delta t$ –logarithm of number density plot of MSD (Multi-Step-Decompression) experiment. Compiled data of SSD experiment are from Hammer and Rutherford (2002) and Couch et al. (2003). Compiled data of MSD experiments are from Couch et al. (2003). Number densities were calculated from areal number density and modal contents by using the equations of (6) and (7). Low number density of microlite is caused by low $\Delta P/\Delta t$ at MSD experiment and small ΔP, high $\Delta P/\Delta t$ at SSD experiment. Logarithm of number density is in proportional to logarithm of $\Delta P/\Delta t$ in MSD experiment (Fig. 5-8a). To

apply the experimental results to textural change of the volcanic products, decrease in number density of microlite from type-3 pumice to Taisho 1 lava is interpreted as decrease in decompression rate of magma from late stage of Plinian phase to Taisho 1 lava effusion. It is, however, difficult to explain the textural difference between type-1, type-2 pumices and the others. Most high decompression rate experiment in MSD experiment (13.8 MPa/h, crystallization time is 8 hours in this case) corresponds to the 0.15 m/s, assuming that $\Delta P/\Delta t$ is equal to ascent rate of magma. Ascent rate of magma may be larger than this value in the case of early to middle stage Plinian eruption. On the other hand, in the case of constant ΔP at SSD experiment, $\Delta P/\Delta t$ affects the number density of microlite. Number density is in reversely proportional to the $\Delta P/\Delta t$ at first, then constant regardless of the $\Delta P/\Delta t$ (Fig. 5-8b), suggesting that there is a time lag between H_2O exsolution and accompanying crystallization about 1-4 hours. Nucleation takes place during the 1-4 hours. In the case of pre-climactic events of the 1991 eruption of Mt Pinatubo, microlite texture correlate with the interval duration of the eruption, indicating that there is a time interval between H_2O exsolution and accompanying crystallization (<40 min) (Hammer et al., 1999). Moreover, microlite-free pumices observed at large pyroclastic eruption at Mt Mazana (Klug et al., 2002) or large Plinian eruption such as Mt St. Helens 1980-1986 eruption and Mt Pinatubo 1991 eruption (Cashman, 1992; Hammer et al., 1999) are also interpreted as a result of high $\Delta P/\Delta t$. Extremely high $\Delta P/\Delta t$ results in low number density, indicating disequilibrium in crystallization. On the other hand, high number density of microlite indicates high nucleation rate caused by large ΔP and relatively high $\Delta P/\Delta t$. Assuming that initial water content and magmatic temperature is 3.3 wt% and 950 ℃, respectively, estimated by Sekine et al. (1979), and that depth where magma is saturated with H_2O is 3.4 km (80 MPa) beneath Aira caldera, then, ΔP of Plinian fall pumices estimated from residual water contents c.a. 0.4 wt.% (Fig. 5-11) is about 75 MPa. It is expected that ΔP of lavas is slightly larger than ΔP of Plinian fall pumices. The textural difference of plagioclase microlite, therefore, results in the difference in decompression rate. Low modal content and number density of plagioclase microlites in type-1 pumices suggest that crystallization occur under especially high decompression rate. Type-1

pumices had little time to crystallize plagioclase microlite during the rapid ascent of magma because of a time lag between H_2O exsolution and accompanying crystallization of microlite (about <40 min or 1-4 hours) (Hammer et al., 1999; Couch et al., 2003). Medium modal content and number density of plagioclase microlite in type-2 pumices indicate that it had more time to crystallize microlite during magma ascent, compared with type-1 pumices. Type-3 pumices had enough time to nucleate microlite because of relatively low decompression rate, compared with type-1 and -2 pumices, resulting in intermediate to high number density of plagioclase microlite. Intermediate number density of microlite in Taisho 1 lava is due to low decompression rate of magma despite of high decompression. Moreover, pre-nucleated crystals grow during magma ascent and emplacement, resulting in high modal content of plagioclase microlite in lavas, compared with Plinian fall pumices.

While number density of plagioclase microlite increases from type-1 pumice to type-3 pumice, vesicularity decreases from type-1 pumice to type-3 pumice. Number density of microlite is the highest around vesicularity of 40-50 vol.%. Decrease in microlite number density within type-3 pumice is in proportional to the decrease in vesicularity (Fig. 5-4) expect the most vesicular sample. These results suggest that effective nucleation of microlite occurred in type-3 pumice during late stage of Plinian phase. Crystallization process shift from nucleation-dominated crystallization during Plinian phase to growth-dominated crystallization during late stage of Plinian phase to lava effusive phase. These results also indicate that vesicle textures have something to do with decompression rate, too.

5.4.5 **Comparisons of vesicle textures of other volcanic products**

Secondary, relative change of decompression rate and degassing process were estimated from vesicle texture. Firstly, the relation between decompression rate and vesicle number density was discussed, and then the relation between among decompression rate, vesicularity and degassing process was discussed.

Before discussing the relation between decompression rate and vesicle texture,

number density analyzed in this study was compared with those analyzed in the other studies. Previously analyzed vesicle number densities of silicic magma are in range of 3.6×10^{14}-2.9×10^{16} m^{-3} at Mt Mazama Plinian fall pumice, pyroclastic flow and Wineglass welded tuff (microlite-free) (Klug et al., 2002), 1.2×10^{13}-5.3×10^{14} m^{-3} at Towada pumice (Toramaru, 1990), 1.7×10^{14}-1.3×10^{15} m^{-3} at Usu micro pumice erupted the 2000 eruption (microlite-bearing) (Suzuki and Nakada, 2002), 2.0×10^{15} m^{-3} and 8.2×10^{14} m^{-3} at white and gray pumice respectively, erupted at the 1980-1986 eruption of Mt St. Helens (microlite-free and microlite-bearing, respectively) (Klug and Cashman, 1994) and 3.9×10^{14}-1.4×10^{13} m^{-3} at the pumice clasts erupted at the AD.79 eruption of Vesuvius (Gurioli et al., 2005) (Fig. 5-9). Vesicle number density of Plinian fall pumice erupted at the 1914-1915 eruption of Sakurajima volcano is in range from 4.2×10^{13}-2.7×10^{14} m^{-3}, relatively small values in silicic magma. Microlite-free pumices erupted at Mt Mazama and Mt St. Helens show higher number densities compared with microlite-bearing pumices.

Previously analyzed vesicle number densities of volcanic product of mafic magma are in range of 3.0-4.9×10^{9} m^{-3} at the lava erupted at March 1 and July 16, 1991 eruption of Kilauea volcano (Mangan et al., 1993), 1.8×10^{11}-1.9×10^{10} m^{-3} and 18×10^{9}-1.1×10^{8} m^{-3} at the scoria and reticulate respectively, erupted at the Kilauea volcano during AD 1984-1986 (Mangam and Cashman, 1996), and 2.32×10^{11}-8.16×10^{10} m^{-3} at Izu-Oshima scoria (Toramaru, 1990) (Fig. 5-9).

Number density of vesicles is proportional to the 3/2 powers of decompression rate for homogeneous vesicle nucleation (Toramaru, 1995). It is not easily compared with each other because number density change in response to other parameter such as temperature, SiO_2 contents of melt, initial water content, viscosity, interfacial tension of gas/melt of magma and degree of magma mixing/mingling. Microlite-free pumices are, however, observed at large pyroclastic (Mt Mazana) or large Plinian (Mt St. Helens 1980-1986 eruption and Mt Pinatubo 1991 eruption) eruptions. Microlite-bearing pumices are observed at Plinian (Sakurajima 1914-1915 eruption) or phreatomagmatic eruption (Usu 2000 eruption), which is smaller scale eruptions compared with the eruption erupted microlite-free pumices. Intensity of the eruption may have something

to do with the vesicle and microlite texture. In the case of the 1914-1915 eruption of Sakurajima volcano, both microlite texture and vesicle number density indicate that decompression rate of magma was relatively low in explosive eruption enough to crystallize microlite.

5.4.6 **Vesiculation and degassing process of magma**

Number density of vesicle in the volcanic ejecta is proportional to the 3/2 power of decompression rate for homogeneous vesicle nucleation (Toramaru, 1995). In the case that vesiculation process is dominant by simple vesicle nucleation growth/vesiculation and no collapse/coalescence and that volcanic products preserve original number density of vesicle, vesicle number density is a good tool in discussing the relative change of decompression rate. On the basis of vesicle textures, especially deformed vesicle shape, type-1 and type-2 pumice collected from 0809A to 0809E appear to have experienced vesicle nucleation, growth, vesiculation, coalescence, and collapse. Type-3 Plinian fall pumices collected from upper parts of the deposit show lower vesicularity, thicker vesicle walls, irregular vesicle shapes, and large variations of number densities. Difference in VSDs between type-3 pumices and other types (type-1 and type-2 pumices) is mainly the difference of number density of large vesicles. While high vesicular pumices (type-1 and type-2) include relatively large vesicles, low vesicular type-3 pumices contain lesser amount of large vesicles. These results may indicate that large vesicles coalesced and collapsed or that volatile escaped from magma before enough expansion in type-3 pumices. Vesicle textures of all types imply that observed number densities do not necessarily record the original number densities at nucleation time, suggesting it not suitable to discuss the relative change of decompression rate in terms of number density. However, these textural features suggest that vesiculation and degassing process might vary during the Plinian phase of eruption due to the physical change of ascending magma.

H_2O contents of Plinian fall pumices is about 0.4 wt.% (Fig. 5-10) and pre-eruptive H_2O contents of the magma is estimated to be the ca. 3.3 wt.% by Sekine et

al. (1979). If the degassing and expansion of magma take place in closed system and equilibrium condition, numerically expected vesicularity (α) is more than 90 vol.% (Fig. 5-10), exceeding the traditionally accepted "fragmentation vesicularity" of 75-80 vol.% (e.g., Sparks,1978). Here:

$$\alpha = 100 * Vg/(Vg+Vm) \quad (5\text{-}8)$$

V_g is volume of expanded gaseous H_2O. V_m is volume of melt. These values are defined as follows:

$$V_g = n'RT/P \quad (5\text{-}9)$$
$$V_m = (1-n)/\rho_m \quad (5\text{-}10)$$

Here, n is water solubility (wt.%), calculated from the equation of Moore et al. (1998) using estimated matrix glass composition of Plinian fall pumices. R is gas constant (8.31 J/mol/K). P is pressure (Pa). n' is mole wt.% of H_2O vapor. T is magmatic temperature. For T, author used 1223 K as estimated by Sekine et al. (1979). ρ_m is melt density and author used for $\rho_m = 2400$ kg/m^3 estimated by the equation of Lange and Carmichael (1994),

The observed vesicularities calculated from bulk density are lower than the calculated values, suggesting that open-system degassing occurred during the eruption (Fig. 5-10). One more evidences for open-system degassing is the existence of silica-minerals in vesicles. Hoblitt and Harmon (1993) and Martel et al. (2000) noted that silica minerals in vesicles may precipitate during degassing of volatiles from vesicles and indicate the open-system degassing.

Open-system degassing requires a gas flow from vesicles out of the magma column into the basement rocks or upward through the conduit (Eichelberger et al., 1986). Hence, degree of degassing can be controlled by decompression rate and relative magma/conduit permeability. Rhyolitic melt becomes permeable to gas flow in the vesicularity range of 60-70 vol.% and vesicles easily collapse (Westrich and

Eichelberger, 1994). It is, therefore, thought that all pumices may have undergone a two-stage vesiculation; the first stage is closed system expansion of vesicles till reaching vesicularity of 60-70 vol.% (around 15 MPa in this case) and the second stage is gas escape from magma. Magma erupted as type-1 or -2 pumices certainly reached vesicularity of 60-70 vol.%, at which they were potentially permeable. Then slight degassing occurred during magma ascent and fragmentation occurred when reaching vesicularity of 64-83 vol.%. In case of type-3 pumice, effective degassing and foam collapsing of magma occurred when reaching the vesicularity around 60 vol.%, resulting that the final products had the vesicularity of 34-64 vol.%. Both change of decompression rate and relative magma/conduit permeability may enhance effective degassing. Decrease in decompression rate induceds more effective degassing for type-3 pumice, resulting in decrease in vesicularity and being consistent with the inference from the plagioclase microlite texture. In summary, number density of microlite in the volcanic products once increase in response to the decrease in decompression rate from type-1 to type-3 pumice, then, decrease in response to the decrease in decompression rate and vesicularity from type-3 pumice to Taisho 1 lavas. Effective nucleation of microlite occurred in type-3 pumice during late stage of Plinian phase. Crystallization process shift from nucleation-dominated crystallization to growth-dominated crystallization during late stage of Plinian phase to lava effusive phase.

5.4.7 **Estimation of magma ascent rate**

Cashman (1992), Crips et al. (1994) and Hammer et al. (1999) estimated the growth rate of microlite 2.7×10^{-8}-5.2×10^{-11} mm/s, 1.8×10^{-7}-2.6×10^{-8} mm/s and 2.5×10^{-7}-3.6×10^{-8} mm/s, respectively by the combination of the theological equation of CSDs and eruption records. On the other hand, growth rate of plagioclase microlite estimated by experimentally by Couch et al. (2003), Hammer and Rutherford (2002), and Geschwind and Rutherford (1995) are 1.9×10^{-6}-1.4×10^{-8} mm/s, 1.0×10^{-6}-8.5×10^{-10} mm/s and 7.2-14×10^{-8} mm/s, respectively which are slightly larger than those

estimated by the combination of the theological equation of CSDs and eruption records. Theological equation of CSD, however, is true in only steady state open-system. Crystallization of microlite during magma ascent, however, occurs under closed-system condition, indicating that theological equation of CSDs is not necessarily true in this situation. In this study, growth rate of microlite estimated from experimental data of Couch et al. (2003), who investigate decompression induced crystallization by using silicic melt (SiO_2 content; c.a., 70 wt.%) were used (Fig. 5-12). Growth rate were estimated from average size (average size = $(\varphi/Na)^{0.5}$) and decompression time. Maximum and average growth rate are 2.9×10^{-5} mm/s and, 4.7×10^{-6} mm/s, respectively.

In chapter 3, magma ascent rate (decompression rate) was estimated by using CONFLOW program. In this section, magma ascent rate (decompression rate) was estimated from the relation between crystal size and growth rate of microlite to confirm the estimation of the ascent rate of CONFLOW program. Decompression induces volatile exsolution from melt, resulting in the increase in liquidus temperatures of melt and consequently crystallization of microlite. In this chapter, crystallization begins with the exsolution of volatile. CONFLOW program assumes that fragmentation occurs when reaching vesicularity of 75 vol.% in closed-system expansion. Crystallization continues till fragmentation depth. Table 5-5 summarized the results of calculation.

Assuming that magmatic conditions are case (1), (2) and (3) (magmatic temperature is 950 ℃, water content is 3.3 wt.%, conduit diameters are 25 m, 30 m and 35 m, respectively), magma is saturated with H_2O around 80 MPa (3.4-4 km depth, assuming 3.4 km). Volatile exsolution and microlite crystallization occur around 80 MPa. Fragmentation level is 12.6 MPa (about 500 m). In the case of case (1), initial ascent rate and final ascent rate beneath fragmentation level of magma is 5.0 m/s and 18.9 m/s, respectively. Average ascent rate of magma is 9.6 m/s (3.8×10^2 MPa/h). Hence, average time from volatile exsolution and crystallization till fragmentation and stop of crystallization is 302 s. If growth rates are 2.9×10^{-5} mm/s and, 4.7×10^{-6} mm/s, the largest microlite size are 8.8 μm and 1.4 μm, respectively. In the case of case (2), initial ascent rate of magma is 6.1 m/s. Final ascent rate of magma beneath fragmentation level is 22.9 m/s. Average ascent rate of magma is 11.8 m/s (4.7×10^2

MPa/h), resulting that average time from volatile exsolution and crystallization till fragmentation and stop of crystallization is 246 s. If growth rates are 2.9×10^{-5} mm/s and, 4.7×10^{-6} mm/s, the largest microlite size are 7.3 μm and 1.2 μm, respectively. In the case of case (3), initial ascent rate of magma is 7.1 m/s. Final ascent rate of magma beneath fragmentation level is 27.1 m/s. Average ascent rate of magma is 14.0 m/s (5.6×10^{2} MPa/h), resulting that average time from volatile exsolution and crystallization till fragmentation and stop of crystallization is 207 s. If growth rates are 2.9×10^{-5} mm/s and, 4.7×10^{-6} mm/s, the largest microlite size are 6.0 μm and 1.0 μm, respectively.

Assuming that magmatic conditions are case (4), (5) and (6) (magmatic temperature is 1050 ℃, water content is 3.5 wt.%, conduit diameters are 20 m, 35 m and 30 m, respectively), magma is saturated with H_2O around 125 MPa (5-6.3 km depth, assuming 5 km). Volatile exsolution and microlite crystallization occurs around 125 MPa. Fragmentation level is 12.6 MPa (about 500 m). In the case of case (4), initial ascent rate and final ascent rate beneath fragmentation level of magma is 9.5 m/s and 35.6 m/s, respectively. Average ascent rate of magma is 18.4 m/s (4.7×10^{2} MPa/h). Average ascent rate of magma is 11.8 m/s, resulting that average time from volatile exsolution and crystallization till fragmentation and stop of crystallization is 381 s. If growth rates are 2.9×10^{-5} mm/s and, 4.7×10^{-6} mm/s, the largest microlite size are 11.0 μm and 1.8 μm, respectively. In the case of case (5), initial ascent rate of magma is 11.9 m/s. Final ascent rate of magma beneath fragmentation level is 44.5 m/s. Average ascent rate of magma is 23.5 m/s (9.4×10^{2} MPa/h), resulting that average time from volatile exsolution and crystallization till fragmentation and stop of crystallization is 191 s. If growth rates are 2.9×10^{-5} mm/s and, 4.7×10^{-6} mm/s, the largest microlite size are 5.5 μm and 0.9 μm, respectively. In the case of case (6), initial ascent rate and final ascent rate beneath fragmentation level of magma is 14.3 m/s and 53.8 m/s, respectively. Average ascent rate of magma is 28.9 m/s (1.2×10^{3} MPa/h), resulting that average time from volatile exsolution and crystallization till fragmentation and stop of crystallization is 156 s. If growth rates are 2.9×10^{-5} mm/s and, 4.7×10^{-6} mm/s, the largest microlite size are 4.5 μm and 0.7 μm, respectively.

Assuming that magmatic conditions are case (7), (8) and (9) (magmatic temperature is 1050 ℃, water content is 4.5 wt.%, conduit diameters are 20 m, 25 m and 30 m, respectively), magma is saturated with H_2O around 195 MPa (7.8-9.8 km depth, assuming 7.8 km). Volatile exsolution and microlite crystallization occur around 195 MPa. Fragmentation level is 16.7 MPa (about 668 m). In the case of case (7), initial ascent rate and final ascent rate beneath fragmentation level of magma is 12.8 m/s and 46.9 m/s, respectively. Average ascent rate of magma is 24.7 m/s (9.9×10^2 MPa/h), resulting that average time from volatile exsolution and crystallization till fragmentation and stop of crystallization is 289 s. If growth rates are 2.9×10^{-5} mm/s and, 4.7×10^{-6} mm/s, the largest microlite size are 8.4 μm and 1.4 μm, respectively. In the case of case (8), initial ascent rate of magma is 15.7 m/s. Final ascent rate of magma beneath fragmentation level is 57.8 m/s. Average ascent rate of magma is 31.3 m/s (1.3×10^3 MPa/h), resulting that average time from volatile exsolution and crystallization till fragmentation and stop of crystallization is 228 s. If growth rates are 2.9×10^{-5} mm/s and, 4.7×10^{-6} mm/s, the largest microlite size are 6.6 μm and 1.1 μm, respectively. In the case of case (9), initial ascent rate and final ascent rate beneath fragmentation level of magma is 18.8 m/s and 68.6 m/s, respectively. Average ascent rate of magma is 38.0 m/s (1.5×10^3 MPa/h), resulting that average time from volatile exsolution and crystallization till fragmentation and stop of crystallization is 188 s. If growth rates are 2.9×10^{-5} mm/s and, 4.7×10^{-6} mm/s, the largest microlite size are 5.5 μm and 0.9 μm, respectively.

In the case of 2.7×10^{-5} mm/s of growth rate, microlite size is larger than average size of microlite of all types of Plinian fall pumices, and almost the same or slightly smaller than those of the largest observed microlite. On the other hand, in the case of growth rate 4.7×10^{-6} mm/s, microlite size is smaller than those of average size observed in natural samples. Experimental results of Couch et al. (2003) indicate that growth rate of microlite decrease in proportional to the increase in crystallization time (Fig. 5-11). In the case of explosive eruption such as Plinian, crystallization time is short due to rapid ascent and rapid quench after erupting from vent, indicating that growth rate of microlite is expected to be large. Hence, 4.7×10^{-6} mm/s is not suitable to apply

the growth rate of microlite in the volcanic product of the explosive eruption. In the case of 2.7×10^{-5} mm/s, ascent rate estimated from CONFLOW program is almost consistent with ascent rate of type-1 pumice estimated from the correlation between growth rate and the observed largest size. Ascent rate estimated from the correlation between growth rate and the observed largest size is 667-3507 s, which is longer than ascent rate estimated from CONFLOW program. One possible interpretation on the difference between type-1 and other types is that slight difference in decompression rate of magma, perhaps due to the difference of center and near the margin of conduits, and/or due to decrease in eruption rate and/or conduit radius. Polacci et al. (2002) discussed the effects of the intense shear and viscous dissipation at conduit wall causes various textural variation of Plinian fall Pumice.

It is also possible to estimate the ascent rate from the relative equation between $\Delta P/\Delta t$ and logarithm of number density of microlite (Fig. 5-8a), in case of relatively slow decompression rate such as late stage of plinian phase and lava effusive phase, during crystallization process shift from nucleation-dominated crystallization to growth-dominated crystallization. Table 5-6 summarizes the parameter of the relative equation between $\Delta P/\Delta t$ and logarithm of number density of microlite and results of the calculation. Calculation were done under the condition; magmatic temperature is 950 ℃, water content is 3.3 wt.%.

In the case that number density of microlite is 10^{14} m^{-3} (case A), corresponding to lava effusive phase, decompression rates are $8.1\text{-}1.1\times10^{2}$ MPa/h (9.3×10^{-2}-1.2 m/s), which are smaller than those estimated from growth rate of microlite. In the case of 4.7×10^{-6} mm/s of growth rate, the largest size of crystal is 13-180 μm, within the range of observed crystal size. In the case of 2.9×10^{-5} mm/s of growth rate, the largest size of crystal is 80-1100 μm, which is large than those in natural samples. According to the results of decompression induced crystallization experiments, growth rate of decrease in response to the increase in crystallization time, suggesting that 4.7×10^{-6} mm/s is more suitable for growth rate than 2.9×10^{-5} mm/s in the case of case A.

In the case that number density of microlite is 10^{15} m^{-3} (case B), corresponding to late stage of Plinian phase, decompression rates are 1.5×10^{2}-2.6×10^{4} MPa/h

(1.7-2.8×10^2 m/s), slightly smaller or larger than those estimated from growth rate of microlite. In the case of 2.9×10^{-5} mm/s of growth rate, the largest size of crystal is 0.35-59 μm, which are smaller than, or almost the same as those in Plinian fall pumice samples. In the case of 4.7×10^{-6} mm/s of growth rate, the largest size of crystal is 0.056-9.6 μm, which is smaller than the largest microlites in natural samples. In the case of case B, corresponding to late stage of Plinian phase, decompression rate is higher than decompression rate during lava effusive phase, suggesting that 2.9×10^{-5} mm/s is suitable for growth rate of microlite during late stage of Plinian phase.

In summary, estimation of magma ascent rate from growth rate of microlite and the relative equation between $\Delta P/\Delta t$ and logarithm of number density of microlite is as follows:

(1) Early to middle stage of Plinian phase, type-1 pumice; average ascent rate of magma estimated from growth rate of microlite (2.9×10^{-5} mm/s) is about 9.6 m/s (3.8×10^2 MPa/h).

(2) Late stage of Plinian phase, type-3 pumice; ascent rates of magma estimated from growth rate (2.9×10^{-5} mm/s) and the relative equation between $\Delta P/\Delta t$ and logarithm of number density of microlite (10^{15} m^{-3}, in the case of using the equation of ΔP = 35 MPa and ΔP = 110 MPa) is about 1.7-2.1 m/s (1.5-1.9×10^2 MPa/h).

(3) Lava effusive phase, Taisho 1 lava; ascent rate of magma estimated from growth rate (4.7×10^{-6} mm/s) and the relative equation between $\Delta P/\Delta t$ and logarithm of number density of microlite (10^{14} m^{-3}, in the case of using the equation of ΔP = 35 MPa, ΔP = 60 MPa and ΔP = 110 MPa) is about 9.0×10^{-2}-3.8×10^{-1} m/s (8.1-3.4×10 MPa/h).

5.4.8 **Eruption model**

By combining the textural data of the volcanic products, stratigraphy of Plinian fall deposit and historical record of the eruption, the eruption sequence of the 1914-1915 eruption is shown Figure 5-12.

Early to middle stage of Plinian phase, type-1 and type-2 white pumices mainly erupted at the same time at the highest decompression rate during the whole phase of

the eruption. Both two type pumices had the simple vesiculation process, vesicle nucleation, growth/vesiculation, slight coalescence and slight collapse due to high decompression rate. High decompression rate of magma prohibited efficient decompression-induced crystallization of microlite, resulting low or intermediate modal content and number density of plagioclase microlite. Textural variations of microlite between type-1 and type-2 reflected the slight difference of decompression rate of magma. One possible interpretation on the difference between type-1 and type-2 pumices is that slight difference in decompression rate of magma, perhaps due to the difference in center of conduits and near the margin of conduits (e.g., Taddeucci et al., 2004; Gurioli et al., 2005) (Fig. 5-12a). Type-1 pumices ascended in the center of conduit. On the other hand, type-2 pumices ascended in the margin of conduit. Although most of the model of pyroclastic eruptions assume uniform ascent velocity in the conduit above fragmentation level, it is possible that there is a region of annular flow at the transition from bubbly to particle-laden gas jet flow, where variations of ascent velocity of magma may occur (Jaupart and Tait, 1990). Slightly lower decompression rate, near the margin of conduit, allow more time for crystallization of microlite, resulting in more modal content and number density of plagioclase microlite in type-2 pumices in spite of the almost same vesicularity.

Late stage of Plinian phase of eruption, the proportion of type-1 and type-2 white pumices decreased and type-3 darker colored pumice erupted in addition to type-1and type-2 pumices. The difference of type-1 and type-2 white to type-3 darker colored pumice reflects not chemical heterogeneity induced by magma mixing but the decrease in decompression rate. Less vesicularity in type-3 pumices are due to degassing of volatile and are interpreted as decrease in decompression rate of magma, consistent with the interpretation of microlite texture. Decompression rate is proportional to eruption rate and/or the -4 power of conduit radius. According to the historical record, intensity of the Plinian eruption decreased in the afternoon on January 13, 1914 (Kobayashi, 1982). During the 1914-1915 eruption of Sakurajima volcano, as eruption style shifted from explosive to effusive, many vents were newly created (Koto, 1914). These observations suggest there was a possibility of change in eruption rate and/or decrease

in conduit radius during late stage of Plinian phase of the eruption, resulting in decrease in decompression rate and increase in proportion of type-3 pumices. Type-1 and type-2 white pumice erupted at late stage of Plinian phase may represent the magma ascended rapidly maybe in the center of conduit. Pumice with the highest number density of microlite shows vesicularity of around 40-50 vol.%, indicating that nucleation of microlite occur effectively during late stage of Plinian phase. Decrease in microlite number density within type-3 pumice is in proportional to the decrease in vesicularity, expect the most vesicular type-3 pumice. Number density of microlite of least vesicular type-3 pumices is the almost same as those of lavas, indicating that decompression rate of type-3 pumices decrease near the decompression rate of lavas in the late stage of Plinian phase.

In the effusive phase of eruption, pre-eruptive melt composition of magma became basic due to magma mixing, suggesting it not suitable to compare the change of decompression rate with the others in terms of microlite texture. The effect of chemical heterogeneity of pre-eruptive melt, however, reflect not plagioclase microlite texture but the An content of plagioclase microlite (Fig. 5-12b).

5.5 **Summary**

1. Volcanic products of the 1914-1915 eruption of Sakurajima volcano are classified into 4 types according to vesicularity and plagioclase microlite texture.

2. Textural differences of Plinian fall pumice are due to the difference of decompression rate. Type-1 and type-2 white pumices with high vesicularity, low to middle modal content and number density of plagioclase microlite indicate that decompression rate of magma during early to middle stage of Plinian phase of the eruption is the largest of whole phase of the eruption. Proportion of type-1 and type-2 white pumices decrease and that of type-3 darker colored pumice increase in the upper part of the deposit, implying that decompression rate of magma decrease in the late stage of Plinian phase of the eruption. Difference of microlite texture between type-1 and type-2 in early to middle stage and between type-1, -2 pumice and type-3 pumice in

the late stage of Plinian phase reflects the slightly difference of magma ascent rate, perhaps the difference of center and near the margin of conduits.

3. Chemical change of pre-eruptive melt from silicic to basic induced by magma mixing during late stage of effusive phase of the eruption reflected not plagioclase microlite texture but the An content of plagioclase microlite.

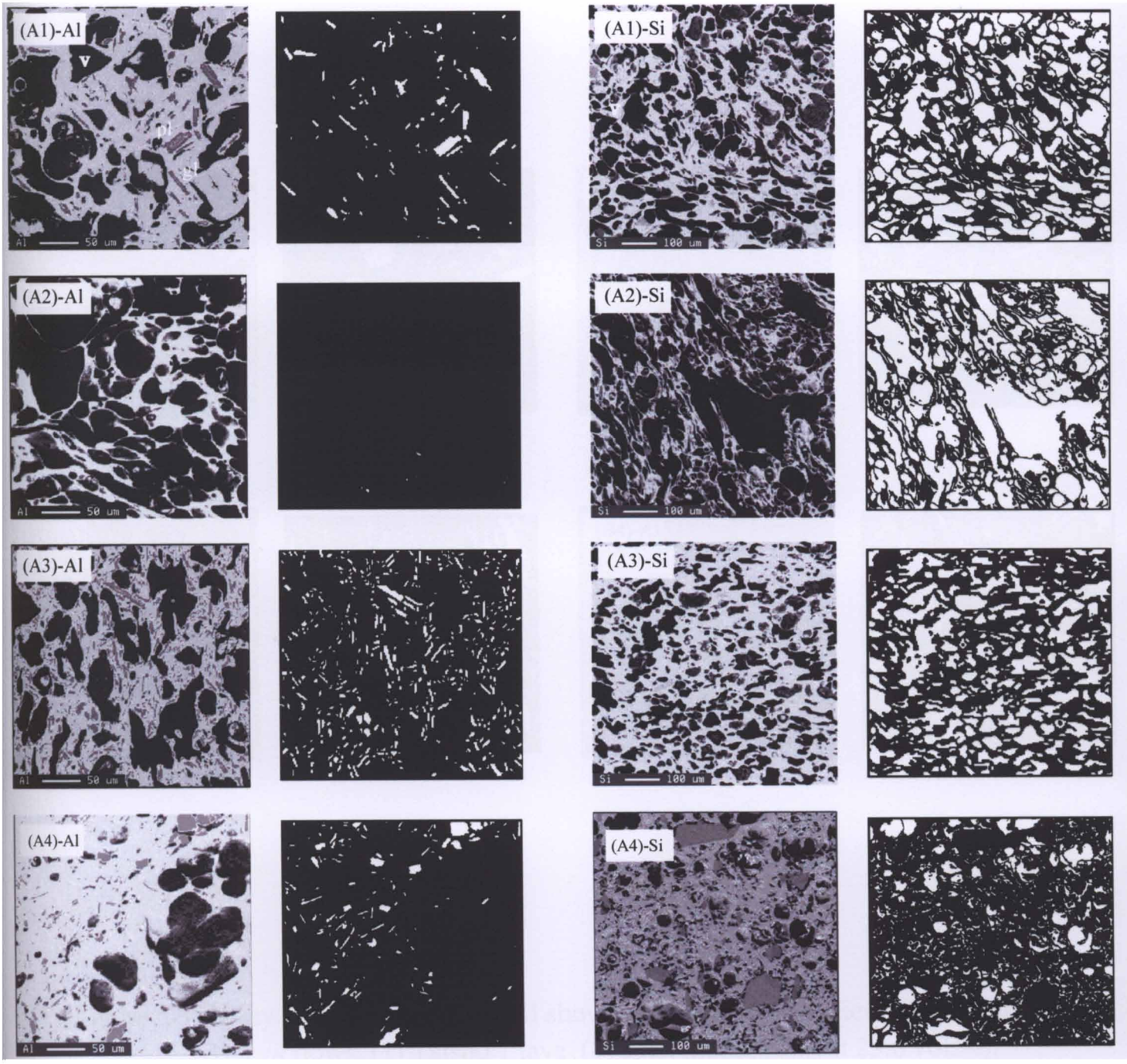

Figure 5-1 X-ray mapping images of Al and Si showing representative microlite and vesicle textual features. (A) Plinian fall pumices: (1) pumice from bottom part of deposit (0809A-a. modal content 6.04 vol.%, vesicularity 60.2 vol.%). (2) low modal content and high vesicularity pumice from lower part of deposit. (0809B-a. modal content 0.45 vol.%, vesicularity 63.2 vol.%). (3) high modal content and low vesicularity pumice from upper part of deposit (0809G-a. modal content 16.3 vol.%, vesicularity 48.2 vol.%). (4) high modal content and low vesicularity pumice from upper part of deposit (0809G-b. modal content 8.12 vol.%, vesicularity 24.7 vol.%).

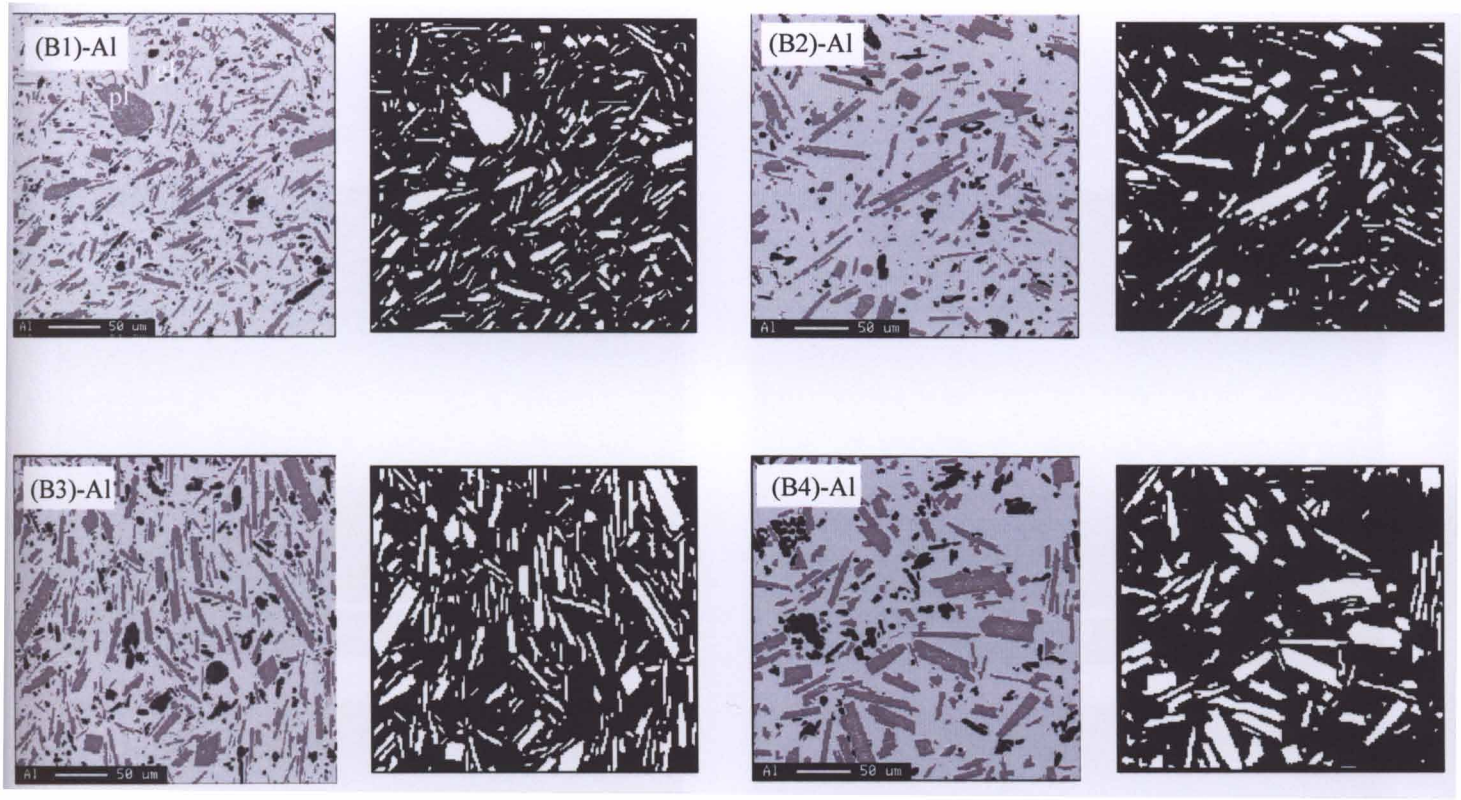

Figure 5-1 X-ray mapping images of Al showing representative microlite textual features.
(B) lava flows: (1) Taisho 1 lava (0703D. modal content 23.6 vol.%).
(2) Taisho 1 lava (1004B. modal content 18.2 vol.%).
(3) Taisho 2 lava (0902D. modal content 21.3 vol.%).
(4) Taisho 2' lava (0908B. modal content 27.0 vol.%)

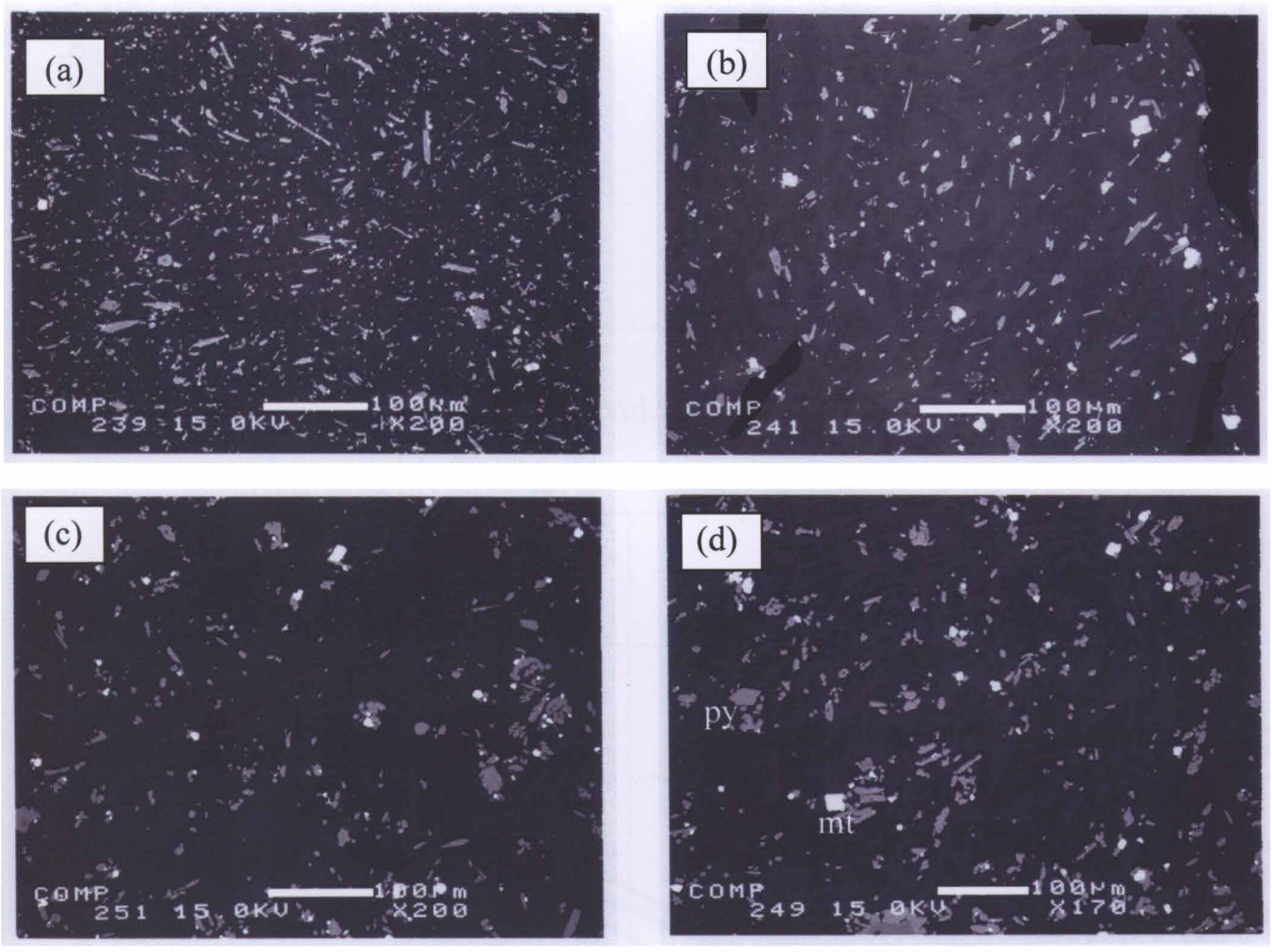

Figure 5-2 BSE image of lava flows showing representative pyroxene and titanomagnetite microlite texture. py, pyroxene; mt, titanomagnetite. (a) Taisho 1 lava (0703D. ϕ of py 8.2 vol.%; ϕ of mt 0.8 vol.%) (b) Taisho 1 lava (1004B. ϕ of py 5.4 vol.%; ϕ of mt 1.1 vol.%). (c) Taisho 2 lava (0902D. ϕ of py 5.6 vol.%; ϕ of mt 0.7 vol.%). (d) Taisho 2' lava (0908B. ϕ of py 7.6 vol.%; ϕ of mt 0.8 vol.%).

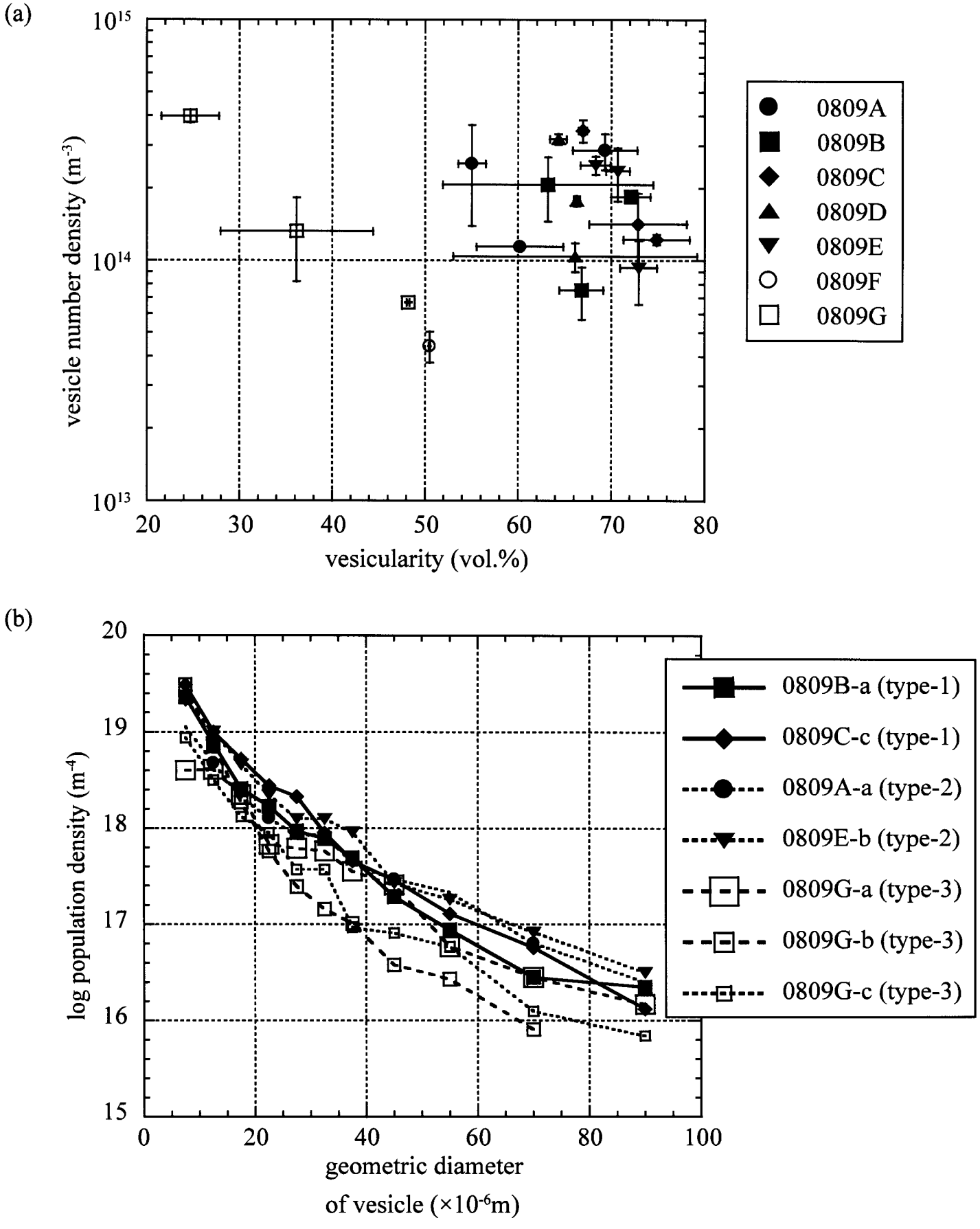

Figure 5-3 (a) Correlation between vesicularity and vesicle number density for Plinian fall pumices. (b) Vesicle size distributions (VSDs) plot for representative vesicles in Plinian fall pumices.

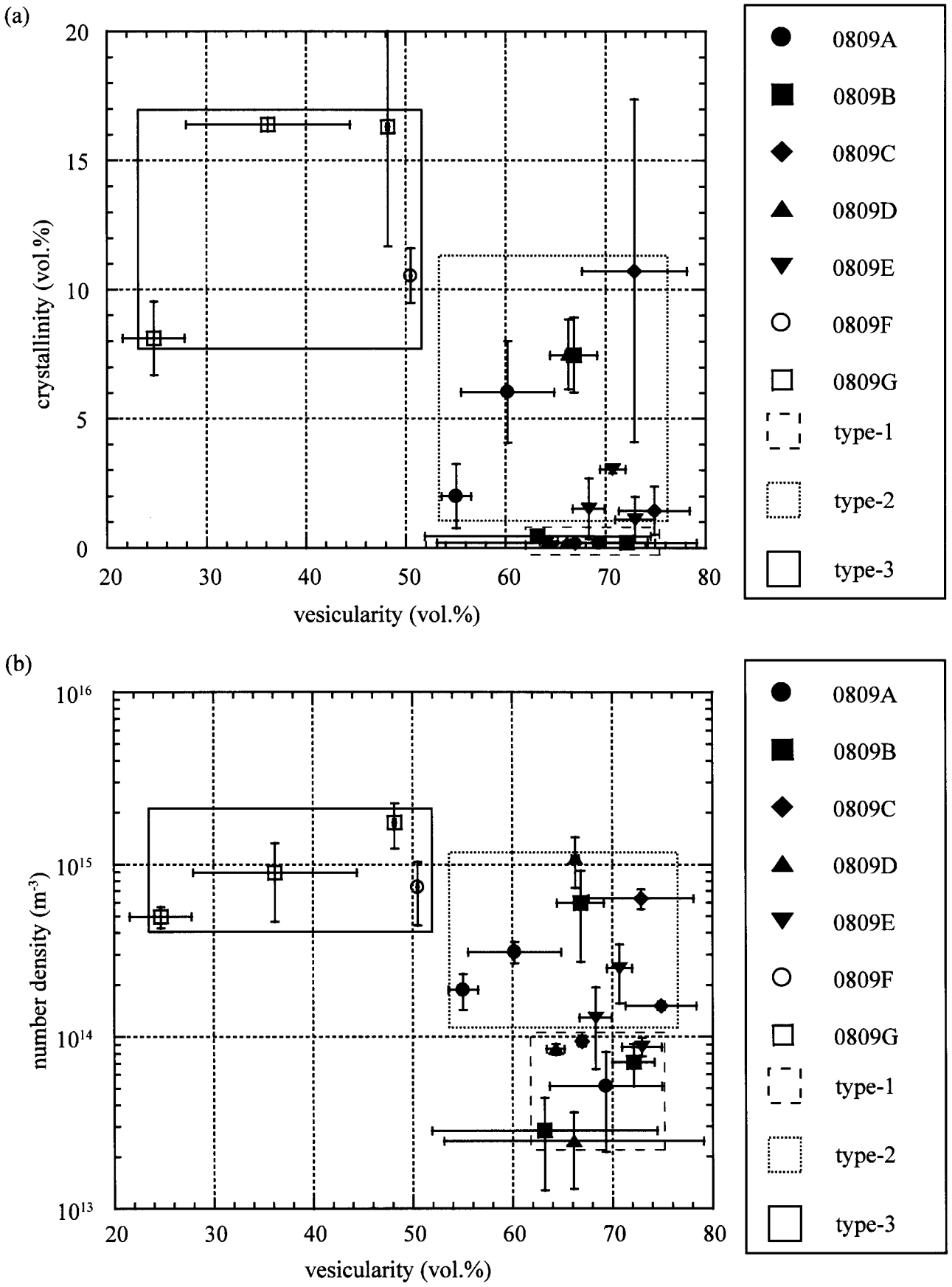

Figure 5-4 Relation between vesicularity and modal content of plagioclase microlite (a) and vesicularity and number density (b). Vesicularities are estimated from mapping images of Si.

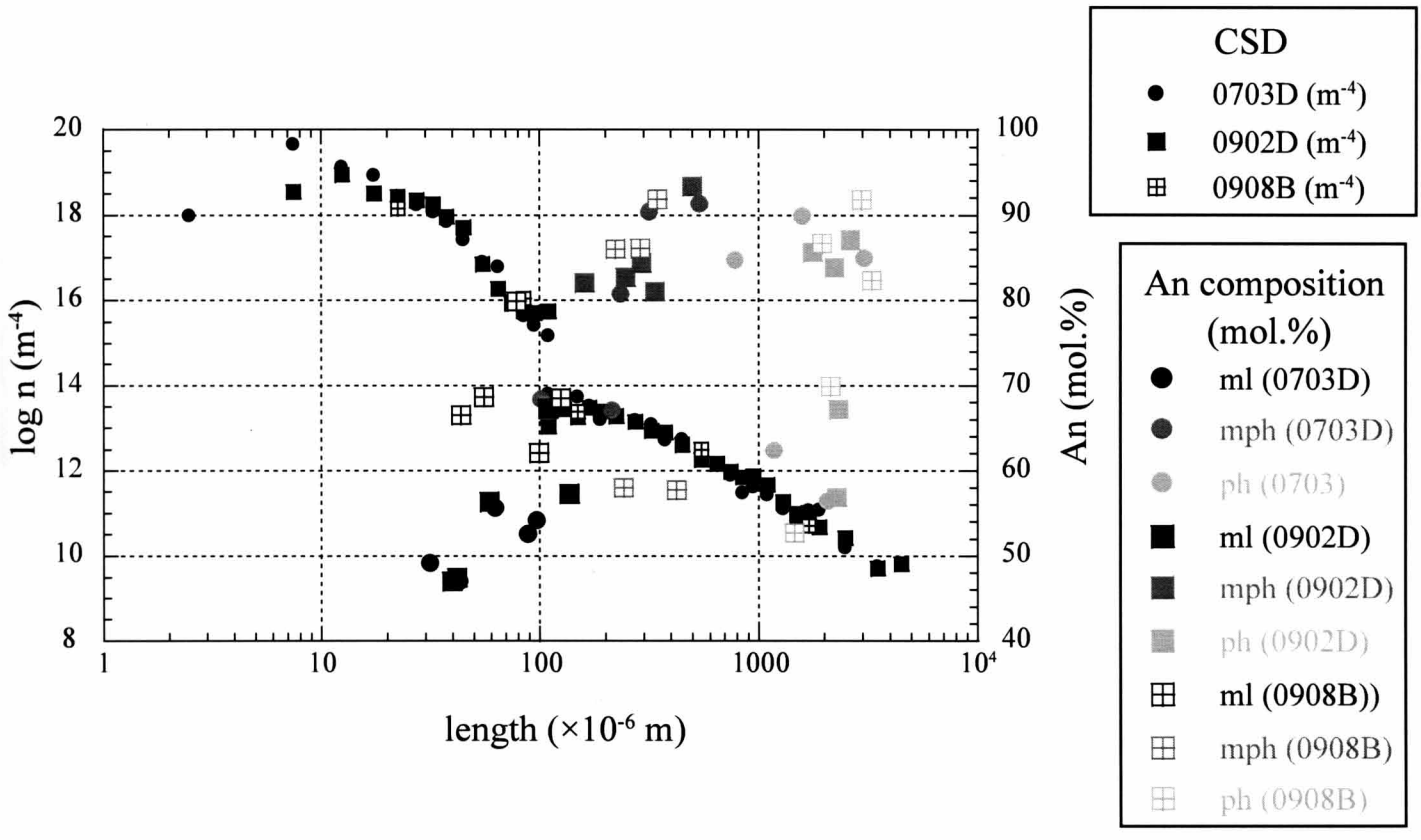

Figure 5-5 Relation between An content and crystal size of plagioclase.

(a)

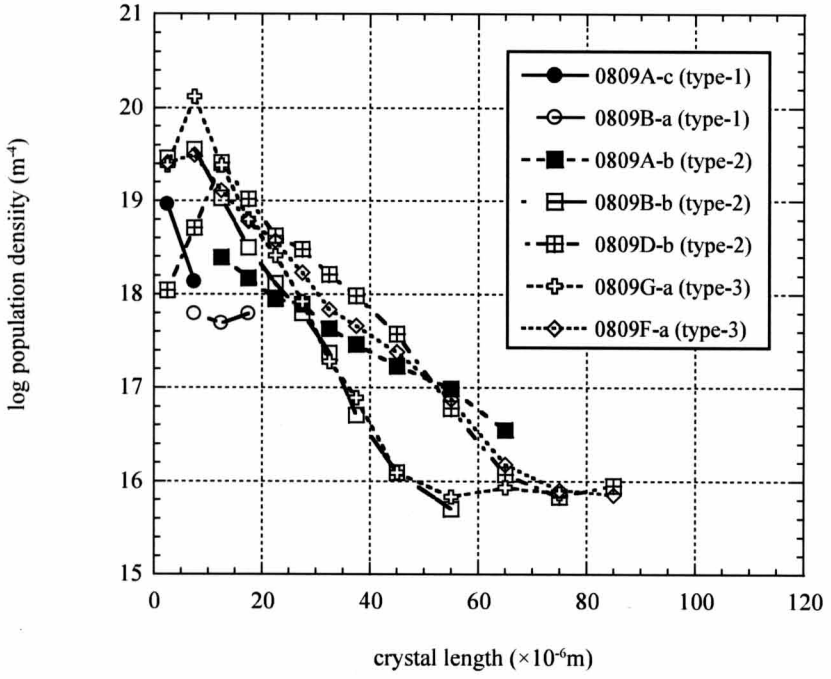

(b)

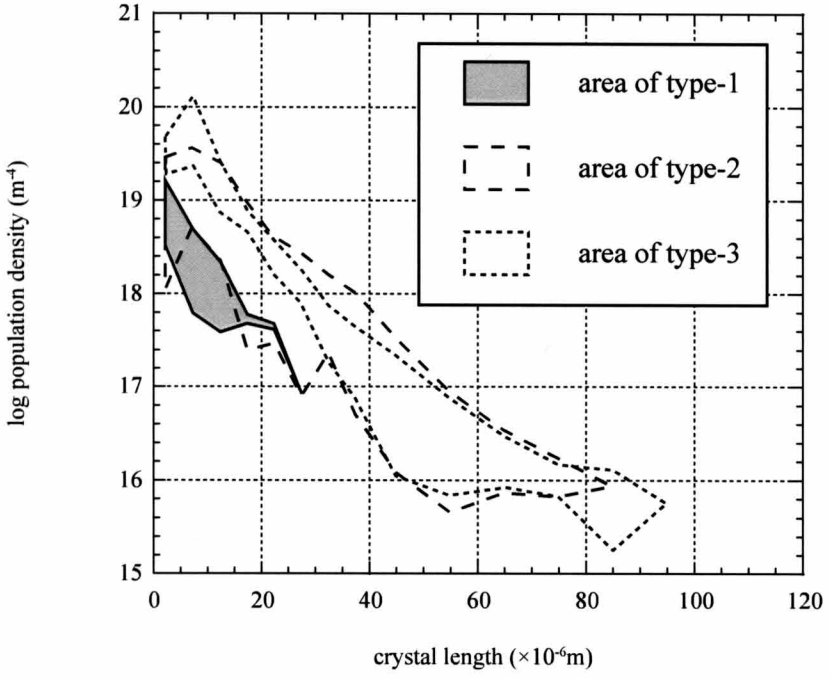

Figure 5-6 Crystal size distributions (CSDs) plots of representative plagioclase microlite in Plinian fall pumices (a) and area of CSDs of each type (b).

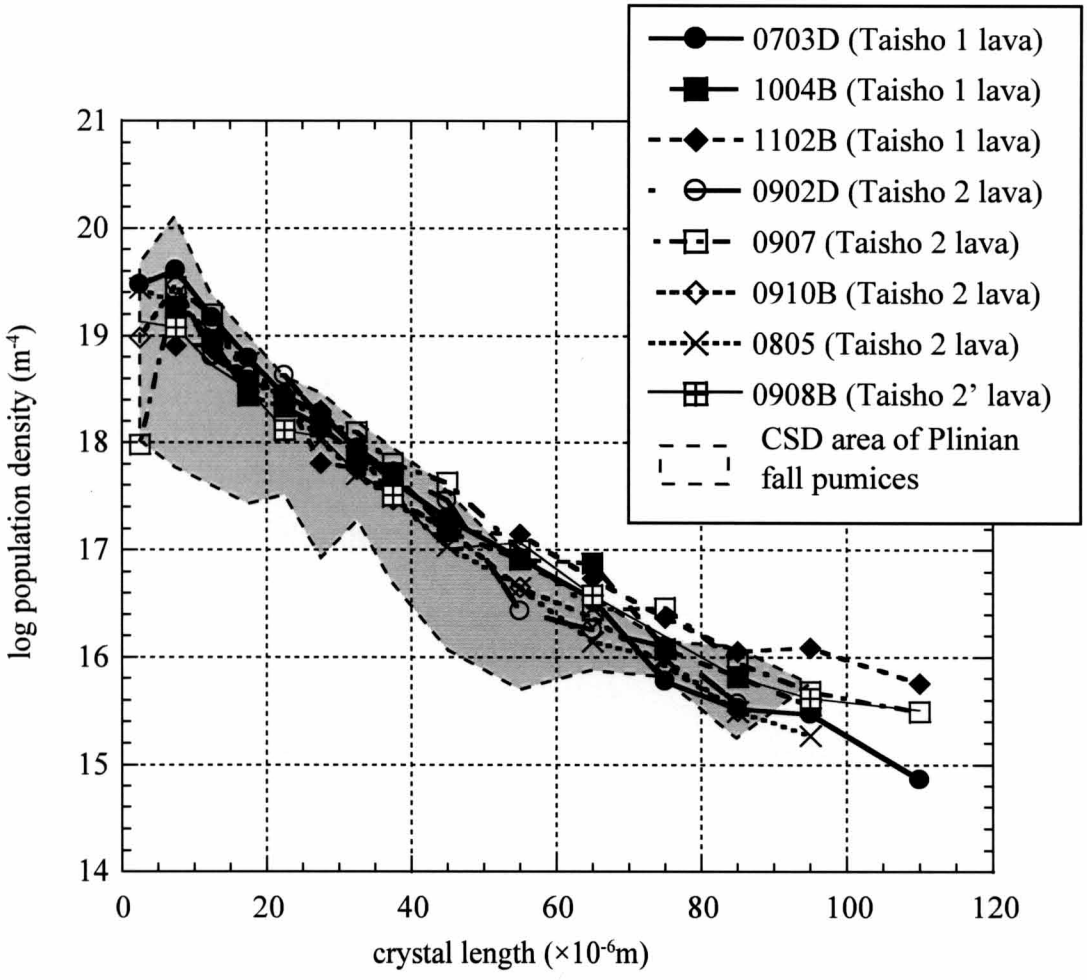

Figure 5-7 Crystal size distributions (CSDs) plots of plagioclase microlite in lavas.

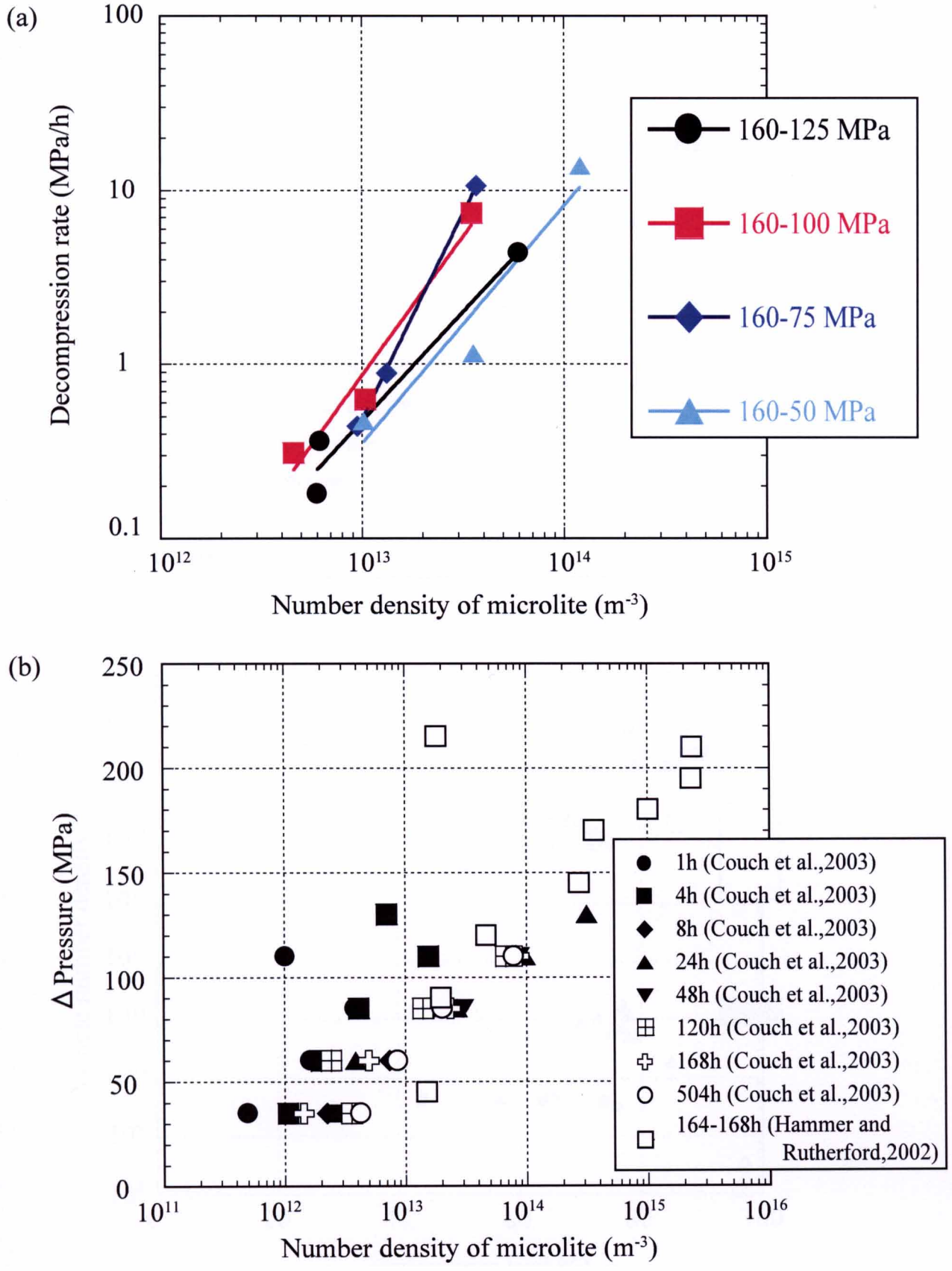

Figure 5-8 Relation between decompression rate and number density of microlite.
(a) MSD experiments of Couch et al. (2003).
(b) SSD experiments of Couch et al. (2003) and Hammer and Rutherford (2002).
Initial pressure before decompression of Couch et al. (2003) and Hammer and Rutherford (2002) are 160 MPa and 220 MPa, respectively.

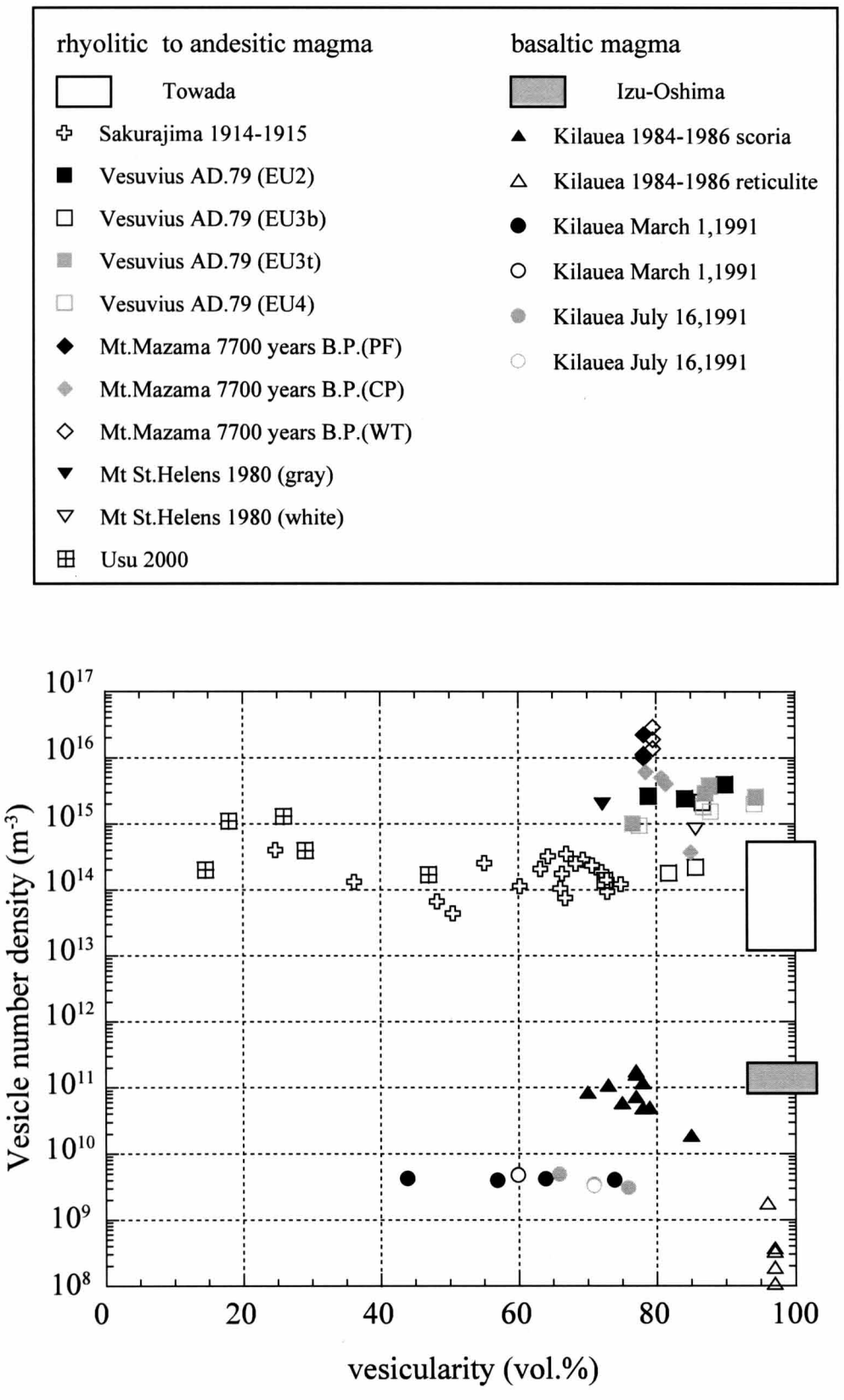

Figure 5-9 Correlation between vesicularity and vesicle number density for volcanic products of other volcanoes.

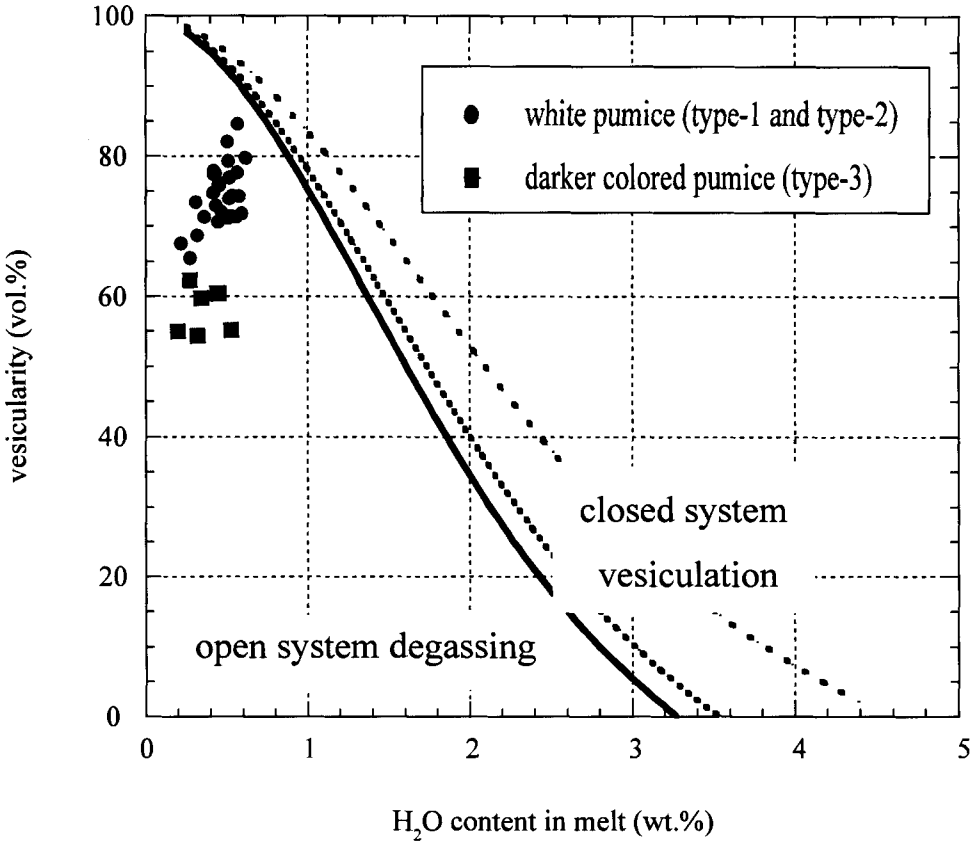

Figure 5-10 Change of vesicularity as a function of water content. Solid curve is estimated equilibrium closed system vesiculation. Vesicularities are calculated from bulk density and phenocryst mode.

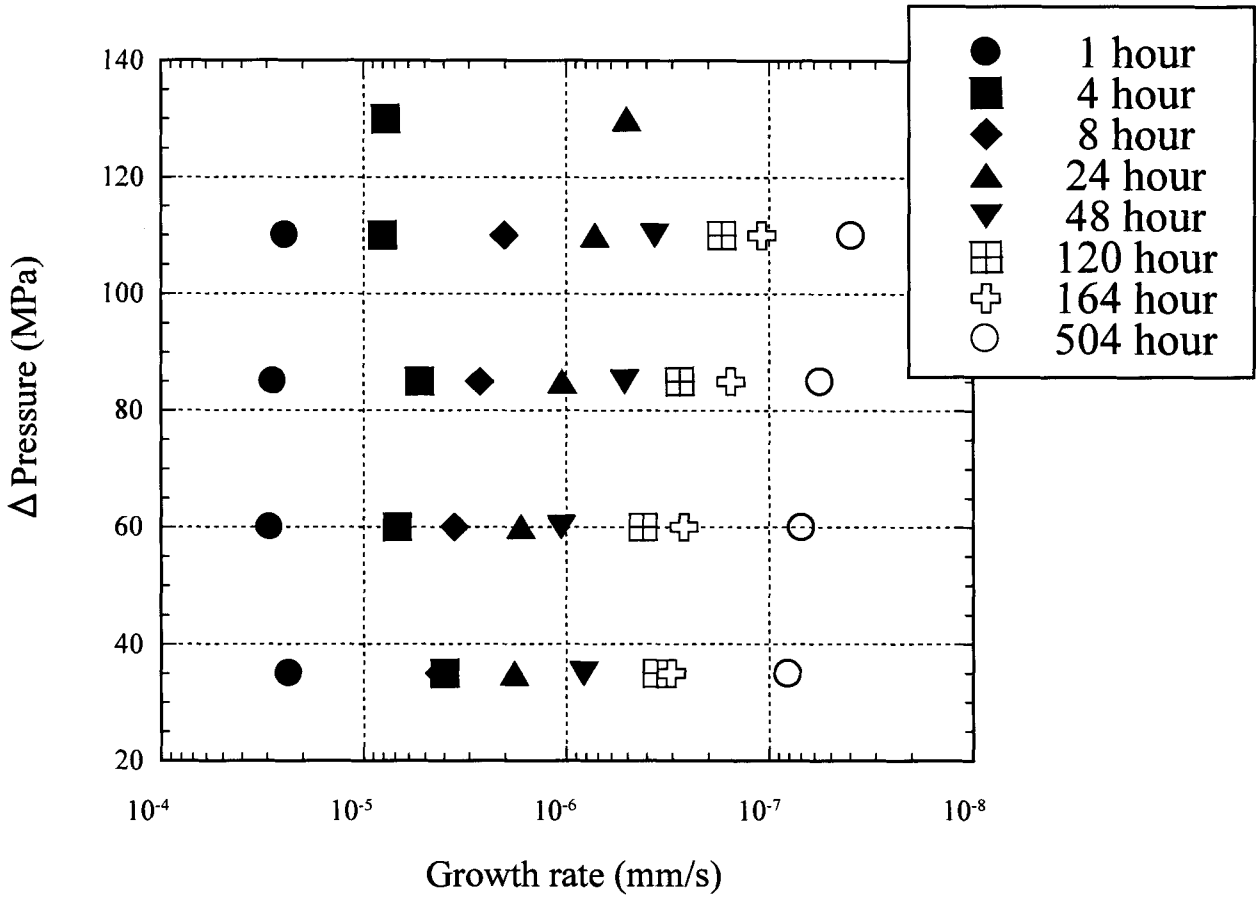

Figure 5-11 Relation between ΔP and growth rate of microlite estimated by SSD experiments of Couch et al. (2003). Y-axis indicate the final pressure after decompression. Initial pressure before decompression is 160 MPa.

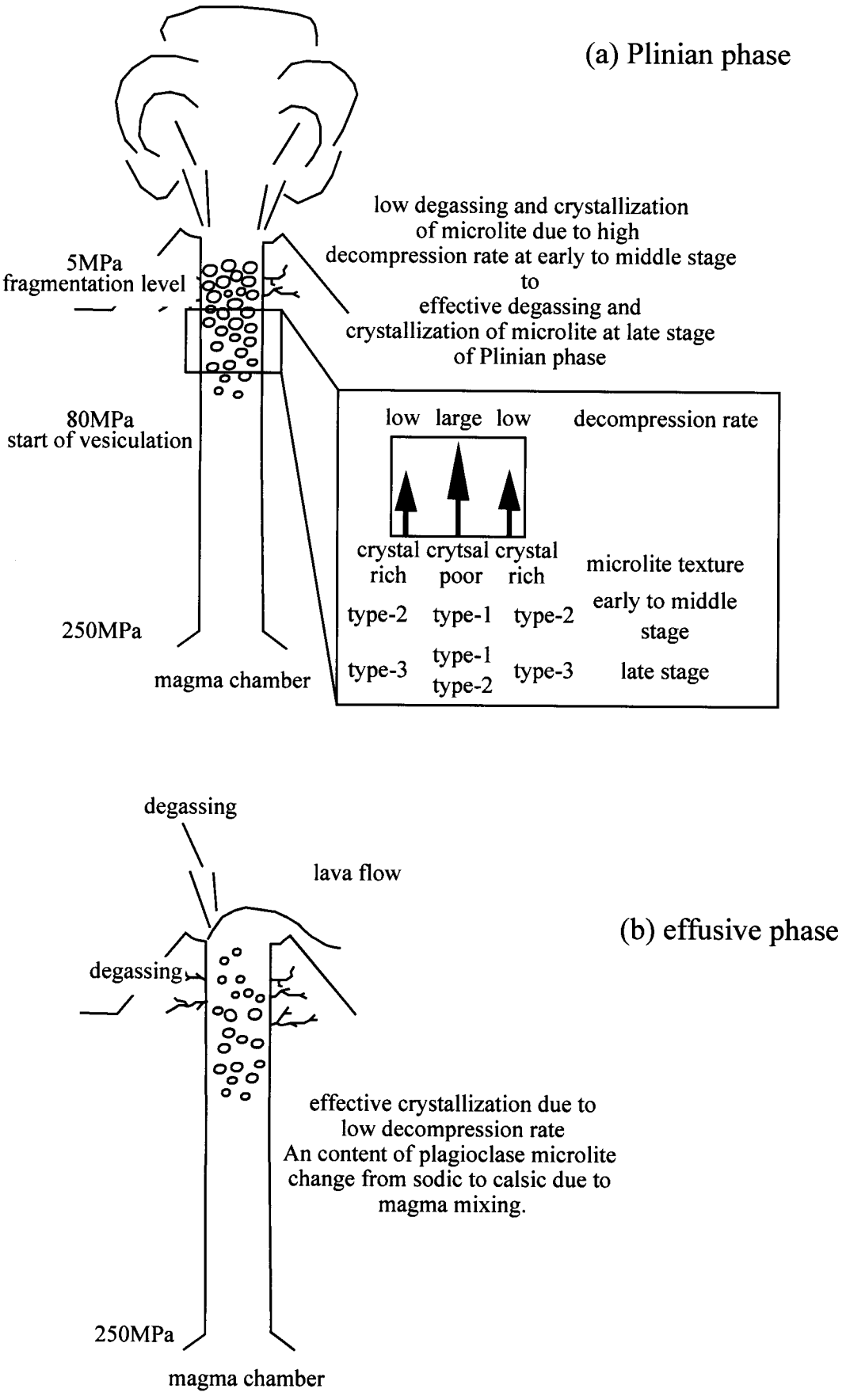

Figure 5-12 Schematic illustrations of sequence of the 1914-1915 eruption of Sakurajima volcano (See text in details).

Table 5-1 water content in the melt and groundmass vesicularity

	water content in melt (wt.%)	groundmass vesicularity (vol.%)		water content in melt (wt.%)	groundmass vesicularity (vol.%)
	0.572	78.2		0.451	71.2
	0.198	56.1		0.475	72.6
collected from 0809A	0.316	74.0	collected from 0809B	0.597	72.4
	0.623	80.1		0.452	76.3
	0.423	77.9		0.521	77.4
	0.510	82.3		0.460	76.3
	0.522	74.5		0.575	84.8
collected from 0809C	0.454	76.6	collected from 0809D	0.425	78.3
	0.513	79.7		0.515	71.8
	0.540	74.9		0.531	72.0
	0.223	68.3		0.451	61.4
	0.368	71.9		0.344	60.7
collected from 0809E	0.420	75.3	collected from 0809F	0.435	78.0
	0.444	61.5		0.530	56.3
	0.442	73.5		0.585	74.8
	0.564	71.9			
	0.320	55.5			
collected from 0809G	0.278	66.2			
	0.322	69.3			
	0.273	63.3			

Table 5-2 Groundmass vesicularity and number density of vesicles of Plinian fall pumices estimated from mapping images

sample	pumice type	no.image analyzed	no.vesicle counted	vesicularity [a] (vol%)	stdev	vesicularity [b] (vol%)	stdev	Nv [b] (m^{-3})	stdev
0809A-a	type-2	2	762	60.2	4.65	53.3	11.8	1.14E+14	3.12E+12
0809A-b	type-2	2	1213	55.1	1.47	53.9	6.3	2.52E+14	1.13E+14
0809A-c	type-1	2	1252	69.4	5.62	59.1	2.8	2.87E+14	4.91E+13
0809B-a	type-1	3	1393	63.2	11.3	69.1	7.1	2.07E+14	6.15E+13
0809B-b	type-2	2	408	66.8	2.36	64.2	7.4	7.52E+13	1.83E+13
0809B-c	type-1	2	772	72.1	2.11	69.0	4.8	1.84E+14	1.81E+13
0809C-a	type-2	2	631	74.9	3.54	60.5	7.4	1.22E+14	1.49E+13
0809C-b	type-2	2	649	72.9	5.21	72.8	5.1	1.42E+14	4.81E+13
0809C-c	type-1	2	1435	67.0	0.44	65.1	2.1	3.47E+14	3.71E+13
0809D-a	type-1	2	595	66.1	13.0	64.0	5.7	1.04E+14	1.43E+13
0809D-b	type-2	2	970	66.3	0.36	66.1	3.4	1.77E+14	8.88E+12
0809D-c	type-1	2	1298	64.3	0.91	64.8	4.2	3.20E+14	1.16E+13
0809E-a	type-1	2	562	72.9	1.98	73.7	2.6	9.33E+13	2.78E+13
0809E-b	type-2	2	1075	70.7	1.27	65.9	2.7	2.35E+14	5.84E+13
0809E-c	type-2	2	1028	68.3	1.60	54.6	2.6	2.49E+14	2.16E+13
0809F-a	type-3	2	373	50.5	0.09	58.8	8.9	4.40E+13	6.43E+12
0809G-a	type-3	2	643	48.2	0.13	50.2	4.3	6.68E+13	3.04E+11
0809G-b	type-3	2	1847	24.7	3.11	26.7	0.6	3.98E+14	2.37E+13
0809G-c	type-3	2	750	36.2	8.24	34.8	13.8	1.32E+14	5.03E+13

Vesicularity (phenocryst-free)
Vesicularity [a] is estimated from mapping image of Si.
Vesicularity [b] is estimated from mapping image of Al.
stdev is one standard deviation.

Table 5-3 Textual data of groundmass phase and CSD data of plagioclase microlite in Plinian fall pumices

sample	type	no.image analyzed	no.crystal counted	φpl (vol.%)	Sn (μm)	maximum size(μm)	Nv (m^{-3})	shape(S=I) I	shape(S=I) L	intercept (m^{-4})	slope (m^{-1})
0809A-a	type-2	2, 2a	264	6.04 (1.96)	5.79 (0.91)	68.1	3.10E+14 (4.3E+13)	1.50	3.03	19.4	5.67E+05
0809A-b	type-2	3	109	1.99 (1.24)	4.66 (1.00)	67.0	1.87E+14 (4.4E+13)	1.50	8.02	18.8	3.37E+05
0809A-c	type-1	2	13	0.19 (0.21)	5.79 (0.91)	6.6	5.15E+13 (3.0E+13)	1.50	1.50	20.3	3.08E+05
0809B-a	type-1	4	19	0.45 (0.19)	5.64 (1.38)	28.6	2.84E+13 (1.6E+13)	1.02	3.03	18.2	3.64E+04
0809B-b	type-2	3, 2[a]	307	7.47 (1.46)	5.23 (0.93)	56.2	5.96E+14 (3.3E+12)	1.50	2.47	20.0	8.36E+05
0809B-c	type-1	3	19	0.22 (0.18)	3.06 (1.14)	n.a.	7.12E+13 (2.0E+12)	n.a.	n.a.	n.a.	n.a.
0809C-a	type-2	2	57	1.44 (0.92)	4.45 (0.93)	26.0	1.51E+14 (8.5E+12)	1.50	2.73	19.6	1.01E+04
0809C-b	type-2	2, 2[a]	276	10.7 (6.63)	5.45 (1.43)	67.9	6.33E+14 (8.4E+13)	1.50	3.63	19.8	5.85E+05
0809C-c	type-1	2	19	0.19 (0.07)	2.68 (0.29)	14.0	9.46E+13 (6.9E+12)	1.50	3.25	20.3	2.13E+05
0809D-a	type-1	2	8	0.20 (0.06)	4.46 (1.14)	n.a.	2.47E+13 (1.2E+13)	n.a.	n.a.	n.a.	n.a.
0809D-b	type-2	2, 2[a]	326	7.49 (1.35)	4.16 (0.71)	89.4	1.08E+15 (3.5E+14)	1.50	6.26	20.1	5.85E+05
0809D-c	type-1	2	20	0.26 (0.11)	3.10 (0.37)	7.2	8.48E+13 (6.2E+12)	1.50	1.85	20.0	2.18E+04
0809E-a	type-1	2	24	1.09 (0.88)	4.83 (1.64)	22.4	8.74E+13 (1.1E+13)	1.50	3.00	18.7	4.31E+04
0809E-b	type-2	2	85	3.04 (0.17)	5.04 (0.54)	43.2	2.49E+14 (9.3E+13)	1.50	3.73	19.4	5.94E+05
0809E-c	type-2	2	49	1.51 (1.18)	4.98 (2.24)	25.8	1.29E+14 (6.5E+13)	1.50	1.79	19.4	9.16E+04
0809F-a	type-3	2, 2[a]	386	10.5 (1.05)	5.31 (0.55)	84.6	7.37E+14 (3.0E+14)	1.50	2.95	19.6	4.92E+05
0809G-a	type-3	2, 2[a]	768	16.3 (4.63)	4.54 (0.02)	78.7	1.75E+15 (5.2E+14)	1.50	2.74	19.9	6.54E+05
0809G-b	type-3	2, 2[a]	402	16.4 (0.26)	5.84 (0.94)	99.1	8.94E+14 (4.3E+14)	1.50	3.59	19.2	4.00E+05
0809G-c	type-3	2, 2[a]	599	8.12 (1.43)	5.47 (0.07)	84.6	4.95E+14 (6.9E+13)	1.50	2.60	19.8	5.70E+05

a: 300×300μm^2 and 650×650μm^2, images were used and combined to analyze textural data and CSDs

Nv[a] estimation from equati(

() is one standard deviation

Table 5-4 Textual data of groundmass phase and CSD data of plagioclase microlite in lavas

sample	no.image analyzed	no.crystal counted	φpl (vol.%)	φpx[a] (vol.%)	φmt (vol.%)	φtotal (vol.%)	Sn (μm)	maximum size(μm)	Nv (m^{-3})	shape(S=1) I	shape(S=1) L	intercept (m^{-4})	slope (m^{-1})
Taisho 1 lava													
0703D	1×3[b]	431	23.6	8.2	0.80	32.6	7.37	116.4	5.89E+14	1.50	2.39	19.5	4.57E+04
0703B	1×3[b]	486	27.4	n.a.	n.a.	n.a.	7.25	99.1	7.18E+14	1.50	2.81	19.6	4.19E+04
0703A	1×3[b]	1033	41.5	n.a.	n.a.	n.a.	8.68	98.6	6.35E+14	1.50	2.94	19.6	3.75E+04
1102B	1×3[b]	303	16.1	4.9	0.88	21.9	9.15	118.5	2.10E+14	1.50	3.31	18.9	3.17E+04
1004B	1×3[b]	237	18.2	5.4	1.14	24.8	8.84	98.9	2.64E+14	1.50	2.79	19.3	4.13E+04
Taisho 2 lava													
0902D	1×3[b]	226	21.3	5.6	0.71	27.6	9.35	86.2	2.60E+14	1.50	2.44	19.5	4.75E+04
0907	1×3[b]	337	17.5	6.5	0.54	24.6	7.06	118.3	4.99E+14	1.50	3.11	19.4	3.92E+04
0910B	1×3[b]	294	24.2	7.8	0.68	32.7	9.09	87.82	3.22E+14	1.50	1.92	19.5	4.93E+04
0805	1×3[b]	343	33.1	10.5	0.70	44.3	10.7	93.5	2.68E+14	1.50	1.50	19.4	4.75E+04
Taisho 2' lava													
0908B	1×3[b]	218	27	7.6	0.75	35.4	12.1	116.4	1.51E+14	1.33	1.72	19.0	3.69E+04
0908A	1×3[b]	486	31.4	n.a.	n.a.	n.a.	12.9	95.3	1.47E+14	1.50	1.71	19.3	4.68E+04
0909	1×3[b]	337	29.7	n.a.	n.a.	n.a.	12.9	118.4	1.39E+14	1.50	2.17	19.0	3.38E+06

b: 300×300μm^2, 600×600μm^2 and 1200×1200μm^2 images were used and combined to analyze textural data and CSDs

Table 5-5 Results of calculation of magma ascent rate from microlite growth rate

case	H_2O (wt.%)	temperature (℃)	conduit diameter (m)	fragmentation level (MPa)	average ascent rate (m/s)	average decompression rate (MPa/h)	growth rate 2.9×10^{-5}mm/s maximum length of crystal (μ m)	growth rate 4.7×10^{-6}mm/s maximum length of crystal (μ m)
case (1)	3.3	950	35	12.6	9.6	3.8E+02	8.8	1.4
case (2)	3.3	950	30	12.6	12	4.7E+02	7.3	1.2
case (3)	3.3	950	25	12.6	14	5.6E+02	6.0	1.0
case (4)	3.5	1050	20	12.6	12	4.7E+02	11.0	1.8
case (5)	3.5	1050	25	12.6	24	9.4E+02	5.5	0.9
case (6)	3.5	1050	30	12.6	29	1.2E+03	4.5	0.7
case (7)	4.5	1050	20	16.7	25	9.9E+02	8.4	1.4
case (8)	4.5	1050	25	16.7	31	1.3E+03	6.6	1.1
case (9)	4.5	1050	30	16.7	38	1.5E+03	5.5	0.9

Table 5-6 Results of calculation of magma ascent rate the relation between number density and decompression rate

decompression rate (MPa/h) of experiment	regression curve	case (A) number density (m^{-3})	calculated ΔP (MPa/h)	ascent rate (m/s)	duration (h)	duration (s)	growth rate 2.9×10^{-5}mm/s maximum length of crystal (μ m)	growth rate 4.7×10^{-6}mm/s maximum length of crystal (μ m)
ΔP=35 (MPa/h)	ΔP = 2.6E-17* Nv ^(1.3)	1.0E+14	8.4	9.3E-02	10	36505	1.1E+03	1.7E+02
ΔP=60 (MPa/h)	ΔP = 1.6E-21* Nv ^(1.6)	1.0E+14	34	3.8E-01	2.5	9053	2.6E+02	4.3E+01
ΔP=85 (MPa/h)	ΔP = 9.0E-32* Nv ^(2.4)	1.0E+14	1.1E+02	1.2E+00	0.8	2769	8.0E+01	1.3E+01
ΔP=110 (MPa/h)	ΔP = 6.1E-19* Nv ^(1.4)	1.0E+14	8.1	9.0E-02	10	37702	1.1E+03	1.8E+02

decompression rate (MPa/h) of experiment	regression curve	case (B) number density (m^{-3})	calculated ΔP (MPa/h)	ascent rate (m/s)	duration (h)	duration (s)	growth rate 2.9×10^{-5}mm/s maximum length of crystal (μ m)	growth rate 4.7×10^{-6}mm/s maximum length of crystal (μ m)
ΔP=35 (MPa/h)	ΔP = 2.6E-17* Nv ^(1.3)	1.0E+15	1.5E+02	1.7	5.7E-01	2050	5.9E+01	9.6E+00
ΔP=60 (MPa/h)	ΔP = 1.6E-21* Nv ^(1.6)	1.0E+15	1.3E+03	15	6.4E-02	231	6.7E+00	1.1E+00
ΔP=85 (MPa/h)	ΔP = 9.0E-32* Nv ^(2.4)	1.0E+15	2.6E+04	2.8E+02	3.3E-03	12	3.5E-01	5.6E-02
ΔP=110 (MPa/h)	ΔP = 6.1E-19* Nv ^(1.4)	1.0E+15	1.9E+02	2.1	4.5E-01	1624	4.7E+01	7.6E+00

Chapter 6: Experimental study of basaltic magma at 1-atmoshpere: time-dependent development of CSD (Crystal Size Distribution) of plagioclase microlite

6.1 Introduction

The characteristic of volcanic rocks is the existence of microlite, i.e., a lot of small crystals crystallized in relatively short time during ascent of magma. The marked features of CSD of microlite are (1) linear correlation between logarithms of population density (crystals per unit cubic per unit length) and crystal size (Cashman, 1992; Hammer et al., 1999) and (2) steep slope and large intercept of CSD plots.

Classical model of CSD developed in the field of chemical industry assumes that nucleation and growth rate of crystals are constant, that crystallization occur under steady state open system and that total number of crystals in the system are constant and preserved (Randorph and Larson, 1971). Linear correlations between logarithms of population density and crystal size generate under the above conditions. Condition of microlite crystallization is, however, not steady state open system but unsteady state batch system. It is expected that crystallization process of microlite in the volcanic rocks is different from crystallization process proposed by classical model of CSDs.

Marsh (1998) suggested that exponential increase in nucleation rate despite of the same growth rate in closed system caused linear correlation between logarithms of population density and crystal size. On the other hand, Eberl et al. (1998) showed that size-dependent growth and growth dispersion of nucleated crystals caused various relation between logarithms of population density and crystal size, resulting in the size variation of crystals.

The aim of this chapter is to investigate experimentally time-dependent change of plagioclase microlite texture by using pressed powder of scoria erupted at the 1707 eruption of Mt Fuji. Author firstly analyzes texture of plagioclase microlite in the run products and discusses the crystallization process of microlite. Then, author investigates how the shape of CSDs of plagioclase microlite in the run products changes

in response to the increase in crystallization time to assess the propriety of model of Marsh (1998) and Eberl et al. (1998).

6.2 Experimental and analytical method

6.2.1 Experimental method

Starting material is fine-grained pressed powder of scoria erupted at the 1707 eruption of Mt. Fuji. Composition of the starting material analyzed by XRF is listed in Table 6-1. Liquidus temperature of starting material is 1227 ℃, and liquidus phase is plagioclase (Hara, 1991).

1-atmosphere experiments employed the platinum wire loop method (Persnall and Brenner, 1974; Donaldson et al., 1975), showing Figure 6-1a. The electric furnace, consisted of vertical double spiral heating element of SiC, was used for experiment. The temperature was monitored by platinum-rhodium thermocouple (type-B), calibrated against the melting temperature of gold. The oxygen fugacity was controlled by a mixed gas of H_2 (10 ml/min) and CO_2 (500 ml/min), yielding a redox condition near the Ni-NiO buffer condition at the temperature of the experiment (Huebner, 1982). The relation of mixed rate of two gases and redox condition are summarized at Appendix 1. The mixed gas flew upward the alumina tube inside the furnace ca. 1 cm/sec.

Figure 6-1b shows the temperature-time schedule of the experiment. Two types of experiments were conducted. The first type is annealing experiments. The sample was firstly held at a certain temperature around 1200 ℃, 1220 ℃, 1227 ℃ and 1235 ℃ (±2 ℃) in 1 hour, then rapidly cooled till room temperature by distilled water by electrically cutting the platinum wire hanging the wire loop. The second types are melting/crystallization experiments. The sample was firstly held at a certain temperature around 1200 ℃, 1220 ℃, 1227 ℃ and 1235 ℃ (±2 ℃) in 1 hour, then rapidly cooled to 1120 ℃ and 1170 ℃ within 8 minutes and kept at the temperature in a certain time (0, 15, 30, 60, 180, 360 and 720 minutes), after which the charges are dropped into the distilled water by electrically cutting the platinum wire hanging the

wire loop.

6.2.2 **Textural analyses**

All images were analyzed by using the computer software, MacAspect of Mitani Co.Ltd. Japan. Analytical conditions are listed in Table 6-2. ×350 and ×150 BSE photo images of the run products (Fig. 6-2, 3, 4, 5, 6, 7 and 8) were used to obtain the modal content, volumetric number density (number density) and CSD of plagioclase microlite in groundmass. Pict formatted digital BSE photo images were converted into binary images. In the case of ×350 images, 1 pixel represents 0.5 μm. In the case of ×150 images, 1 pixel represents 1.0 μm. Width (w)/length (l) ratios, area of each microlite or vesicle, reference area, modal content, and areal number density (Na) of microlites were measured by using MacAspect. Estimation method of volumetric number density, CSD and average size are the same as the methods described in chapter 5. Morphologies of plagioclase microlite follow in the registration of Hammer and Rutherford (2002).

6.2.3 **Compositional analyses**

Glass and mineral composition analyses of the run products were performed on a JEOL JXA-8900R at the Venture Business Laboratory of Kobe University. Glass composition analyses of both volcanic and run products were done under the following conditions: 15 kV acceleration voltage, 12 nA beam current, 5-10 μm beam size, 4 s counting time for Na and 20 s counting time for other elements with Bence-Albee correction. Plagioclase, olivine and pyroxene analyses of volcanic products were done the under the following conditions: 15 kV acceleration voltage, 12 nA beam current with focused beam, 10 s counting time for Na and 20 s counting time for other elements with Bence-Albee correction.

6.3 **Result**

6.3.1 **Textural and compositional variation of plagioclase microlite of the run products**

Figure 6-9 show the TTT (time-temperature-transformation) plots of the run products. The run products of annealing experiments expect 1235 ℃ experiments include plagioclase microlite, which are thought to be a remain of staring material. All run products of melting/crystallization experiments contain plagioclase microlite. In the case of melting/crystallization experiments cooled until 1120 ℃, olivine microlites appear around 30 minutes in addition to plagioclase microlite. Pigeonitic pyroxenes appear around 3-6 hours. On the other hand, in the case of melting/crystallization experiments quenched at 1170 ℃, only plagioclase microlite crystallize.

Table 6-3 and Figure 6-10 summarized the textural data of the experiments. Number densities and modal contents of plagioclase microlite in the run products of annealing experiments at 1200 ℃, 1220 ℃ and 1227 ℃ are in range of 5.1×10^{13}-2.2×10^{14} m^{-3}, and 4.6-7.3 vol.%, respectively. There were few plagioclase microlite in the run products of annealing experiment at 1235 ℃. Number densities of plagioclase included in the run products of 1200-1120 ℃, 1220-1120 ℃ and 1227-1120 ℃ experiments are in range of 3.9×10^{14}-1.1×10^{15} m^{-3}, 2.0×10^{14}-6.0×10^{14} m^{-3} and 5.1×10^{13}-1.6×10^{14} m^{-3}, respectively. Modal contents of plagioclase microlite in the run products of 1200-1120 ℃, 1220-1120 ℃ and 1227-1120 ℃ experiments are in range of 26.8-33.1 vol.%, 25.2-42.8 vol.% and 24.2-39.9 vol.%, respectively. Number densities of plagioclase included in the run products of 1200-1170 ℃ and 1227-1170 ℃ experiments are in range of 3.2-5.4×10^{14} m^{-3} and 3.6-1.9×10^{14} m^{-3}, respectively, which is smaller than 1200-1120 ℃ and 1227-1120 ℃ experiments. Modal contents of plagioclase microlite in the run products of 1200-1170 ℃ and 1227-1170 ℃ experiments are in range of 13.1-17.5 vol.% and 10.3-23.1 vol.%, which are smaller than modal contents of plagioclase microlite in the run products of 1200-1120 ℃ and 1227-1120 ℃ experiments. On the other hand, number density of plagioclase microlite in the run products of 1235-1120 ℃ and 1235-1170 ℃

experiments is in range of 9.7×10^{12}-7.1×10^{13} m^{-3} and 1.4-4.5×10^{13} m^{-3}, respectively, which is one or two magnitude of order smaller than plagioclase microlite in the run products of 1200-1120 ℃, 1220-1120 ℃ and 1227-1120 ℃ experiments, or 1200-1170 ℃ and 1227-1170 ℃ experiments. Modal contents of plagioclase microlite in are in 1235-1120 ℃ and 1235-1170 ℃ experiments range of 9.6-38.4 vol.% and 10.3-21.7 vol.%, respectively.

Table 6-4 and Figure 6-11 show the results of compositional analyses of plagioclase microlites. An contents of plagioclase in the run products of annealing experiments are from $An_{75.8}$ to $An_{76.6}$. An contents of plagioclase decrease in response to the increase in crystallization time and initial temperature (Fig. 6-11). For example, Compositional range of An contents of plagioclase microlite in the run products is from $An_{75.8}$ to $An_{72.7}$ in 1200-1120 ℃ experiments and from $An_{70.9}$ to $An_{64.4}$ in 1235-1120 ℃ experiments.

6.3.2 **CSDs of plagioclase microlite of run products**

Figure 6-12, 13, 14 and 15 show the CSDs of plagioclase microlite in the run products. Table 6-T summarized the intercepts and slopes of CSDs. Most of microlite is less than 250μm in length. The intercepts of CSDs in annealing experiments at 1200 ℃ and 1227 ℃ are 18.8 m^{-4} and 17.8 m^{-4}, respectively. The intercepts of CSDs in 1200-1120 ℃, 1220-1120 ℃ and 1227-1120 ℃ experiments are in range of 18.9-19.6 m^{-4}, 19.3-18.7 m^{-4} and 19.6-18.7 m^{-4}, respectively, which are slightly larger than those of annealing experiments. All the CSDs of melting/crystallization experiments show slightly show concave up. The intercepts of CSDs in 1200-1170 ℃and 1227-1170 ℃ experiments are in range of 18.9-19.3 m^{-4} and 18.1-19.3 m^{-4}, respectively, which are almost the same as those in 1200-1120 ℃, 1220-1120 ℃ and 1227-1120 ℃ experiments. In the case of 1200-1120 ℃ and 1200-1170 ℃ experiments, CSDs of 1200-1170 ℃ experiments show steeper slope than CSDs of 1200-1120 ℃ experiments. On the other hand, CSDs of 1227-1170 ℃ experiments show shallower slope than CSDs of 1227-1120 ℃ experiments. The

intercepts of CSDs in 1235-1120 ℃ and 1235-1170 ℃ experiments are in range of 17.4-18.4 m^{-4} and 19.6-18.7 m^{-4}, respectively. CSDs of both 1235-1120 ℃ and 1235-1170 ℃ experiments show gentler slopes, compared with the others.

6.4 **Discussions**

6.4.1 **Nucleation and growth process**

Run products of melting/crystallization experiments of 1200-1120 ℃, 1220-1120 ℃ and 1227-1120 ℃ experiments, which are sub or around liquidus temperature of staring material, show quite different texture in terms of modal contents and number density of plagioclase microlite, compared with annealing experiments at 1200 ℃, 1220 ℃ and 1227 ℃. These results indicate that drastic textural changes occur during short time in the cooling period. Average size of plagioclase microlite in the run products increase in response to the crystallization time. Degree of textural change is not so large compared with 1200-1120 ℃ and 1227-1120 ℃ experiments, 1200-1170 ℃ and 1227-1170 ℃ experiments show the same textural change.

The crystallization behavior is basically divided into four stage (Solmatov, 1995); metastable stage, nucleation stage, relaxation stage and quasi-equilibrium stage. The metastable stage is defined as the period during which melt is supersaturated for the phase until the nucleation take place. The nucleation stage is the period during which nucleation occur at maximum order of magnitude. The relaxation stage is defined as the period during which system is approaching a quasi-equilibrium state with small supersaturation since nucleation ceases. The quasi-equilibrium stage is the period during which melt and crystal are maintained nearly at equilibrium due to crystal growth. These two stages (relaxation stage and quasi-equilibrium stage) are defined for both phases. Drastic increase in number density and modal content of plagioclase microlite within short time in cooling period and slight decrease in number density and increase in modal content during the period of constant temperature around 1120 ℃ or 1170 ℃ indicate that crystallization processes divide into two processes.

Nucleation-dominated crystallization is the first process of crystallization. This process is defined as metastable stage and nucleation stage. In the case of this experiment, cooling period from 1200 ℃, 1220 ℃ and 1227 ℃ to 1120 ℃ or 1170 ℃ is defined as the stage of nucleation-dominated crystallization process. Due to increase in small microlite during nucleation period, average size of microlite slightly decrease in 1200-1120 ℃, 1227-1120 ℃, 1200-1170 ℃ and 1227-1170 ℃ experiment. Growth-dominated crystallization is the second process of crystallization. During this process, growth of nucleated crystals takes place. Growth-dominated crystallization process is defined as relaxation stage and quasi-equilibrium stage. The phase of growth-dominated crystallization process is the period of annealing at 1120 ℃ or 1170 ℃. Modal content and average size of microlite increases in response to the increase in crystallization time during the stage of growth-dominated crystallization process of crystallization due to growth of nucleated crystals. Table 6-5 summarized the incremental growth rate of plagioclase in run products. Average growth rate of microlite is defined as follow:

$$Gi = (Sn_b - Sn_a)/(t_b - t_a) \qquad (6\text{-}1)$$

where, t_a and t_b are the duration of each experiment.

On the other hand, run products quenched from 1235 ℃ to 1120 ℃ or 1170 ℃, which is slightly above the liquidus temperature of starting material, show different textural change with time. Number density of microlite in the run products of 1235-1120 ℃ and 1235-1170 ℃ experiments is in range of 9.7×10^{12}-7.1×10^{13} m^{-3} and 1.4-4.5$\times10^{13}$ m^{-3}, respectively, which is one magnitude of order smaller than those of 1200-1120 ℃ 1220-1120 ℃ and 1227-1120 ℃ experiments. Plagioclase microlite in the run products of #060 and #052 show the least modal contents. Modal contents of plagioclase microlite in the 1235-1120 ℃ and 1235-1170 ℃ experiments increase in response to the increase in crystallization time. Average size of microlite decreases with time in 1235-1120 ℃ experiments. These results indicate that the period of nucleation-dominated crystallization process of 1235-1120 ℃ and 1235-1170 ℃ experiments occur longer time than that of 1200-1120 ℃, 1220-1120 ℃, 1227-1120 ℃, 1200-1170 ℃ and 1227-1170 ℃ experiments and that

nucleation rate of plagioclase microlite in 1235-1120 ℃ and 1235-1170 ℃ experiments is smaller than that in 1200-1120 ℃, 1220-1120 ℃, 1227-1120 ℃, 1200-1170 ℃ and 1227-1170 ℃ experiments.

Efficiency of nucleation of plagioclase microlite depends of initial melting temperature in the case of basaltic magma (Sato, 1995). Sato (1995) demonstrated that about 20 ℃ difference around liquidus temperature affect the final number density of microlite in melting/crystallization experiment by using pressed powder of basaltic magma erupted at the 1986 eruption of Izu-Oshima volcano.

According to the previous mathematical study about nucleation process, homogeneous nucleation rate (J_{hom}) is described as follows (e.g., Toramaru, 1990; Cashman, 1990; Solomatov, 1995; Toramaru, 2001);

$$J_{hom} \propto \exp(-\Delta G_{hom}/RT_m) \quad (6\text{-}2)$$

$$\Delta G_{hom} = 4\pi Rc^2\gamma/3 \quad (6\text{-}3)$$

$$Rc = 2v\gamma Tm/(T-T_m) \quad (6\text{-}4)$$

where, ΔG_{hom} is the thermodynamic driving force for transformation from melt to crystal in the case of homogeneous nucleation. R is a gas constant. T_m is a magmatic temperature. Rc is the critical size of nuclei. γ is the interfacial tension between crystal and melt. T is the liquidus temperature. On the other hand heterogeneous nucleation rate (J_{het}) is expressed as follows (e.g., Cashman, 1990);

$$J_{het} \propto \exp(-\Delta G_{het}/RT_m) \quad (6\text{-}5)$$

$$\Delta G_{het} = f(\theta) * \Delta G_{hom} \quad (0 \leqq f(\theta) \leqq 1) \quad (6\text{-}6)$$

$$f(\theta) = (2+\cos\theta) * (1-\cos\theta)^2/4 \quad (6\text{-}7)$$

where, ΔG_{het} is the thermodynamic driving force for transformation from melt to crystal in the case of heterogeneous nucleation. θ is a contact angle between crystal, melt and substrate and of the total surface area of the catalyzing substrate (in other word, dependent on crystal size, number density and state of dispersion).

Difference of microlite texture between 1200-1120 ℃ and 1200-1170 ℃ experiment, 1227-1120 ℃ and 1227-1170 ℃ experiment and 1235-1120 ℃ and 1235-1170 ℃ experiment is due to the difference of the undercooling rate. In the case of the experiments cooled until 1120 ℃ and 1170 ℃, the undercooling is 107 ℃

and 57 ℃, respectively. According to the equation (6-4), the critical size of nuclei is inversely proportional to the undercooling. The equation (6-2) and (6-3) indicate that difference of the critical size in nuclei affects the thermodynamic force for crystallization, resulting in the difference of number density of microlite. In the case of the experiments cooled until 1170 ℃, small undercooling enhance the critical size of nuclei and the thermodynamic driving force for crystallization. The number densities of the run products cooled until 1170 ℃, therefore, are smaller than the number densities of the run products cooled until 1120 ℃. Differences of modal con tents of microlite are due to the difference of chemical equilibrium.

Effect of initial melting temperature to the number density of plagioclase in the run products was discussed by Sato (1995). The critical size for nuclei is large at initial temperature, which is near the liquidus temperature. Rapid cooling from near liquidus temperature to sub-liquidus temperature and subsequent nonequilibrium state of cluster-size distribution is a result of variation of number density of plagioclase microlite. One more possibility for the reason of textural difference is heterogeneous nucleation. In the case of homogeneous nucleation, it takes long time from supersaturated state to subsequent nucleation. For example, it takes more than 300 hours in nucleation of plagioclase from basaltic magma near liquidus temperature (Hara, 1991) and more than 45 minutes from the $CaMgSi_2O_6$-$CaAl_2Si_2O_8$ system (Tsuchiyama, 1983). Rapid increase in number density of plagioclase microlite of 1200-1120 ℃, 1220-1120 ℃, 1227-1120 ℃, 1200-1170 ℃, 1227-1170 ℃, 1235-1120 ℃ and 1235-1170 ℃ experiments during cooling period until 1120 ℃ or 1170 ℃ suggests that heterogeneous nucleation takes place in all experiments. According to the equation (6-5), (6-6) and (6-7), pre-existent crystals reduce the thermodynamic force for crystallization and enhance the nucleation rate in the case of heterogeneous nucleation. In the case that initial melting temperature is 1200 ℃, 1220 ℃ and 1227 ℃, there is a possibility that crystals included in the starting materials imperfectly melted. On the other hand, in the case of 1235 ℃ experiment, there are few unmelted crystals in the run products of annealing experiment at 1235 ℃. These unmelted crystals may affect the condition of heterogeneous nucleation process. In the case of 1200-1120 ℃,

1220-1120 ℃, 1227-1120 ℃, 1200-1170 ℃ and 1227-1170 ℃ experiments, existence of unmelted crystals enhance heterogeneous nucleation, resulting in high number density of plagioclase microlite. In the case of 1235-1120 ℃ and 1235-1170 ℃ experiments, heterogeneous nucleation take place less effectively, because most of crystals in the starting materials melted during annealing at 1235 ℃.

These studies reveal not only initial temperature but also final temperature affects the final texture of plagioclase microlite in the run products.

6.4.2 **Development of CSD with crystallization time**

CSD plots of run products also systematically change with time. In the case of 1200-1120 ℃, 1220-1120 ℃, 1227-1120 ℃, 1200-1170 ℃ and 1227-1170 ℃ experiments, intercepts of CSD slightly decrease and slope of CSD become gentle with increase in crystallization time. These results indicate that number density of small microlite decrease and that number density of large microlite increase in response to the increase in crystallization time. Marsh (1998) discussed that log-linear correlation of CSD is due to exponential increase in nucleation rate in closed system. However, results of this study indicate that nucleation occur during cooling period of run products from 1200 ℃, 1220 ℃ and 1227 ℃ to 1120 ℃ or 1170 ℃ and that crystallization process shift from nucleation to growth of nucleated crystals. Linear correlation between logarithms of population density and crystal size is due to (1) exponential increase in nucleation rate during cooling period to 1120 ℃, or 1170 ℃ (Marsh, 1998), (2) nucleation interval (Toramaru, 1991) or (3) growth dispersion of nucleated crystals (Eberl et al., 1998). However, during period of annealing at 1120 ℃ or 1170 ℃, effective nucleation rarely occur, indicating that model of Marsh (1998) is not suitable. Cause of log-linear correlation is due to nucleation interval (Toramaru, 1991) or growth dispersion of nucleated crystals (Eberl et al., 1998). Interpretations of change of CSD slope from steep to shallow are (1) crystal ageing; in other word, Ostwald ripening and textural coarsening (Waters and Boudreau, 1996; Higgins, 1999), (2) surface (reaction)-control growth (Eberl et al., 1998; Zeh, 2004) and (3) supply

(diffusion)-control growth (Eberl et al., 1998; Zeh, 2004). Nearly constant number density and slight increase in modal content of microlite indicate that only growth of microlite occur during annealing at 1120 ℃ or 1170 ℃. However, most of microlite show euhedral and no evidence of Ostwald ripening, suggesting that textural change of microlite during annealing at 1120 ℃ or 1170 ℃ is not due to the case of (1); crystal aging. In the case of constant growth rate of all crystals despite of the difference of crystal size, CSD plot shift parallel to the original CSD with increase in crystallization time. However, in the case of 1200-1120 ℃, 1220-1120 ℃, 1227-1120 ℃, 1200-1170 ℃ and 1227-1170 ℃ experiments, intercepts of CSD slightly decrease and slope of CSD become gentle with increase in crystallization time. Eberl et al. (1998) and Zeh (2004) suggested that these evolutions of CSDs were due to surface (reaction)-control growth or supply (diffusion)-control growth of nucleated crystals.

In the case of 1235-1120 ℃ and 1235-1170 ℃ experiments, intercepts increase with time and slopes of CSDs become steep with time. These results indicate that nucleation-dominated crystallization process of 1235-1120 ℃ and 1235-1170 ℃ experiments occur longer time than that of 1200-1120 ℃, 1220-1120 ℃, 1227-1120 ℃, 1200-1170 ℃ and 1227-1170 ℃ experiments. Size variation of microlite in the run products of 1235-1120 ℃ and 1235-1170 ℃ experiments is larger than that of 1200-1120 ℃, 1220-1120 ℃, 1227-1120 ℃, 1200-1170 ℃ and 1227-1170 ℃ experiments due to long nucleation interval because of large and subsequent effective growth and growth dispersion of early nucleated crystals.

6.5 Summary

1. 1-atmosphere closed system melting/crystallization experiment reveal that crystallization processes of plagioclase microlite are divided into two processes: the first is nucleation process and the second is growth process of nucleated crystals. Duration of nucleation process changes in response to initial melting temperature.

2. Initial melting and final crystallization temperature affect the number density and modal content of plagioclase microlite in the run products.

3. Linear correlation between logarithms of population density and crystal size in closed system melting/crystallization experiments is due to nucleation interval, growth dispersion and size-dependent growth of nucleated crystals.

4. During nucleation-dominated crystallization process, intercept of CSD increase due to nucleation and growth dispersion of nucleated microlite, resulting in steep slope of CSDs. Size dependent-growth and growth dispersion of nucleated crystals taking place during growth-dominated crystallization process cause the decrease in intercept of CSD and gentler slope of CSD.

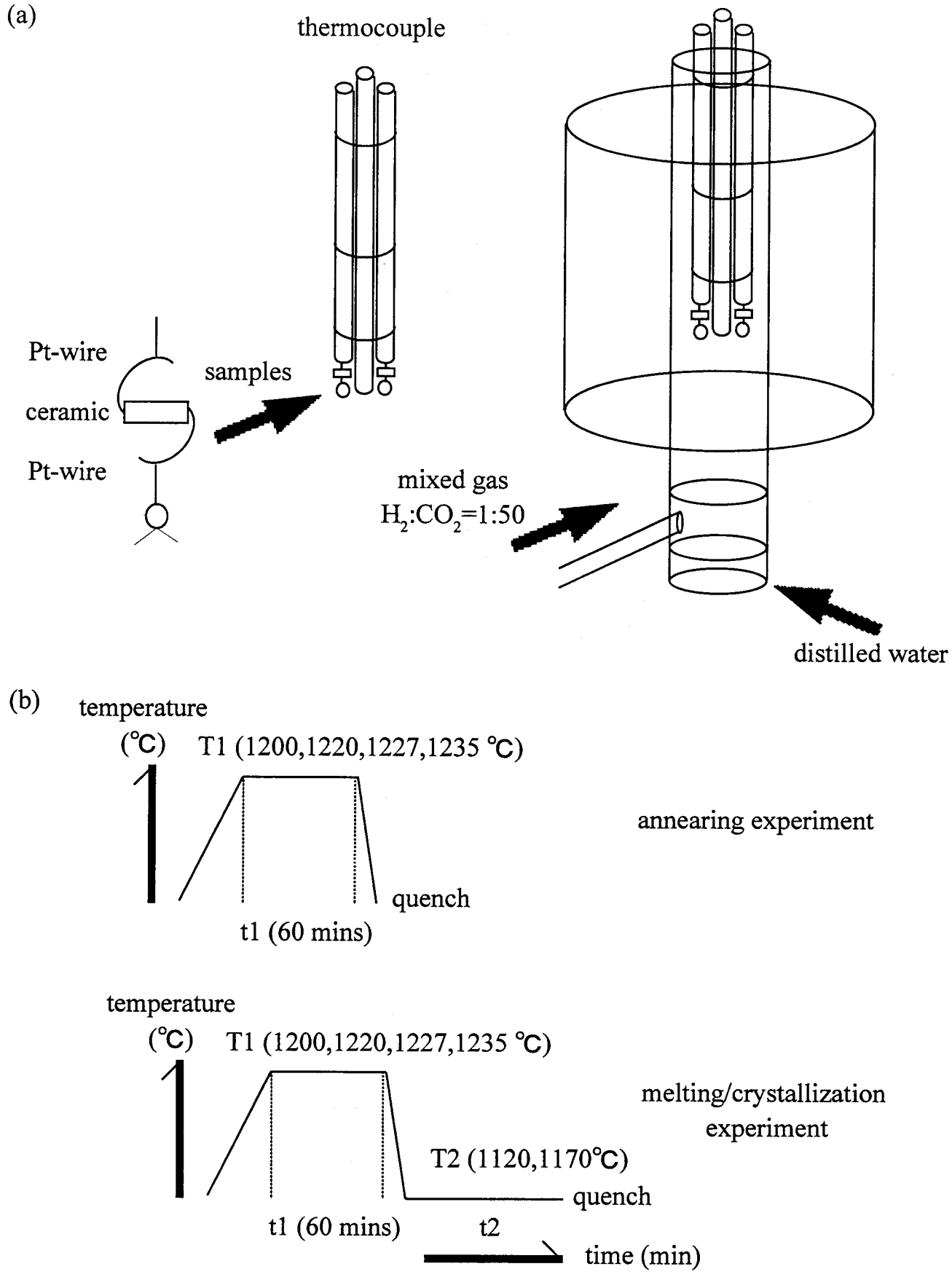

Figure 6-1 Shematic illustration of electric furnace (a) and time-temperature relations of experimets (b).

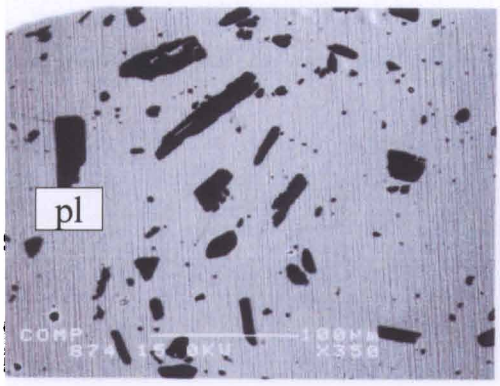

#001 1200℃-1hour

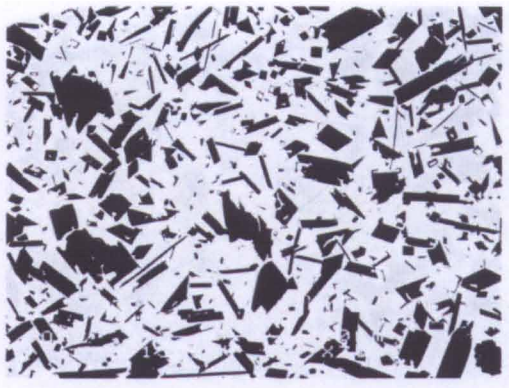

#002 1200℃-1hour-1120℃-0mins

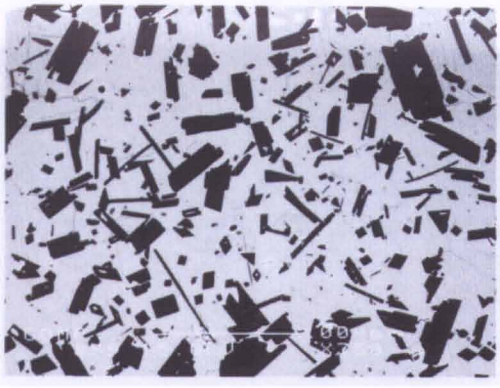

#003 1200℃-1hour-1120℃-15mins

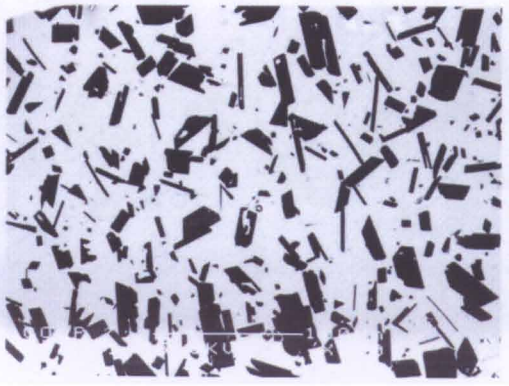

#004 1200℃-1hour-1120℃-30mins

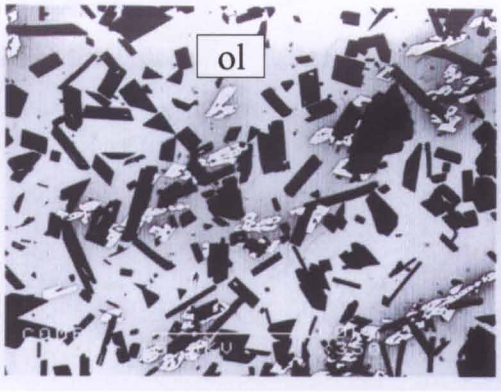

#006 1200℃-1hour-1120℃-1hour

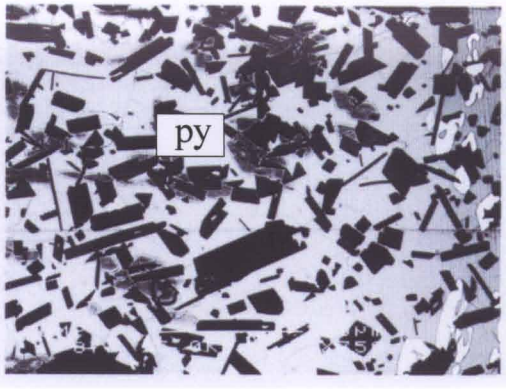

#007 1200℃-1hour-1120℃-3hours

Figure 6-2 Back scattered electron images of run products: cooling induced crystallization from 1200 to 1120 ℃. pl: plagioclase. ol: olivine. py: pigeonitic pyroxene

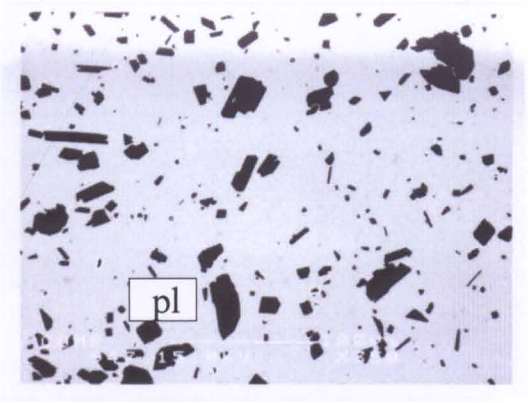

#047 1200℃-1hour-1170℃-0mins

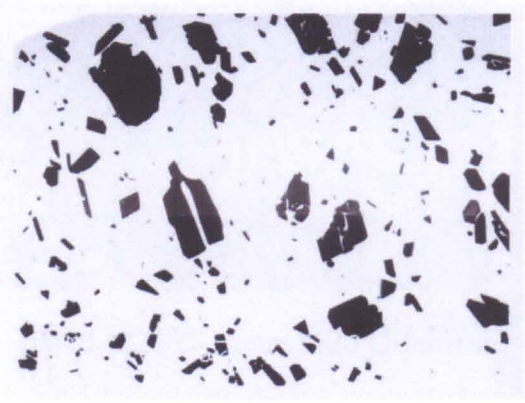

#048 1200℃-1hour-1170℃-15mins

#049 1200℃-1hour-1170℃-30mins

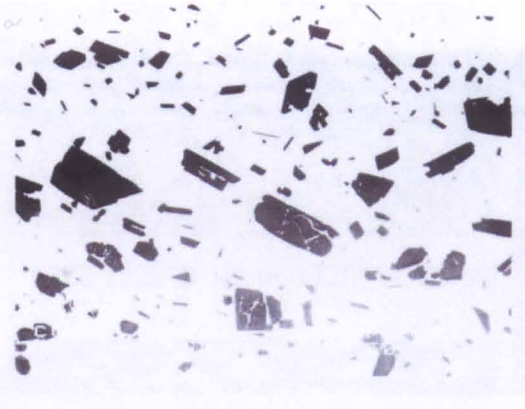

#050 1200℃-1hour-1170℃-1hour

#051 1200℃-1hour-1170℃-3hours

Figure 6-3 Back scattered electron images of run products: cooling induced crystallization from 1200 to 1170 ℃. pl: plagioclase. ol: olivine. py: pigeonitic pyroxene

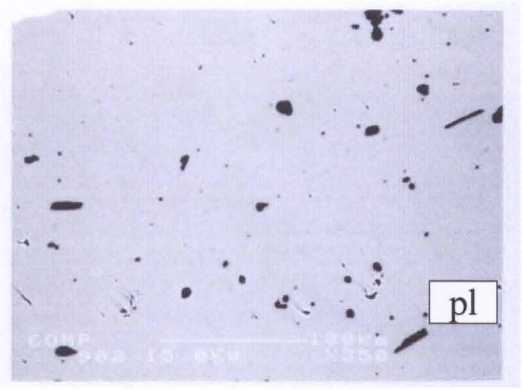

#019 1220℃-1hour

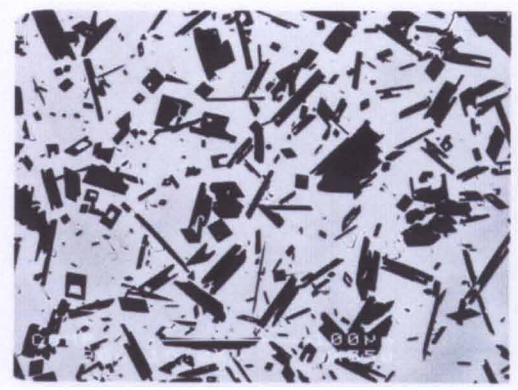

#020 1220℃-1hour-1120℃-0mins

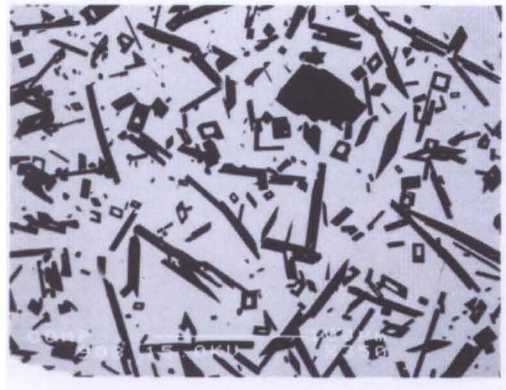

#021 1220℃-1hour-1120℃-15mins

#022 1220℃-1hour-1120℃-30mins

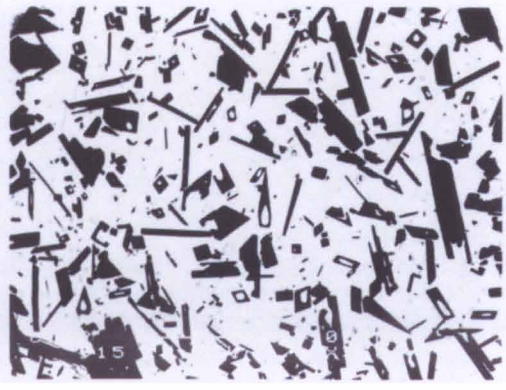

#023 1220℃-1hour-1120℃-1hour

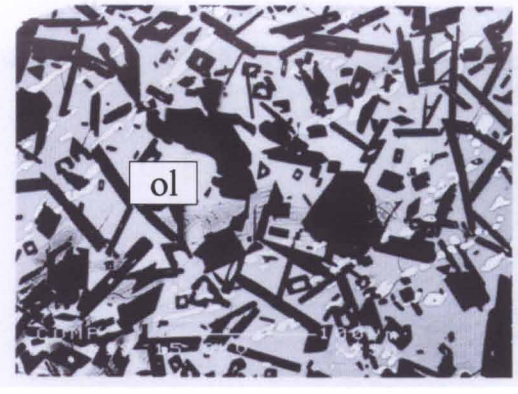

#024 1220℃-1hour-1120℃-3hours

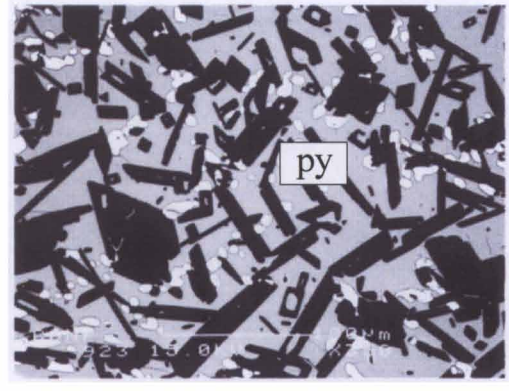

#025 1220℃-1hour-1120℃-6hours

Figure 6-4 Back scattered electron images of run products: cooling induced crystallization from 1200 to 1120 ℃. pl: plagioclase. ol: olivine. py: pigeonitic pyroxene

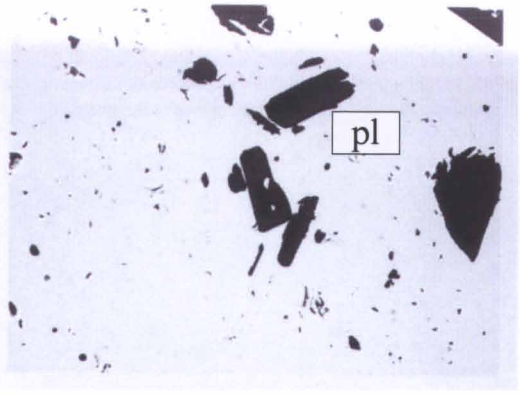

#026 1227℃-1hour

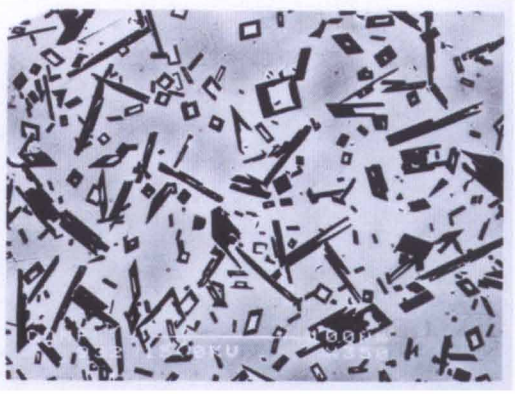

#027 1227℃-1hour-1120℃-0mins

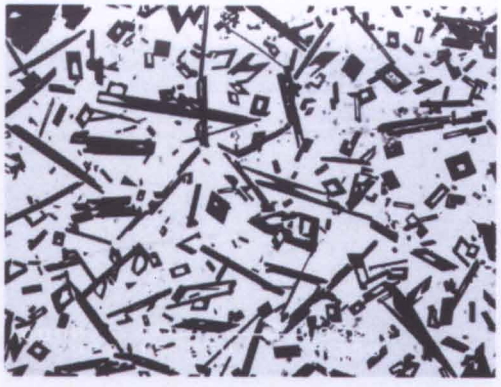

#028 1227℃-1hour-1120℃-15mins

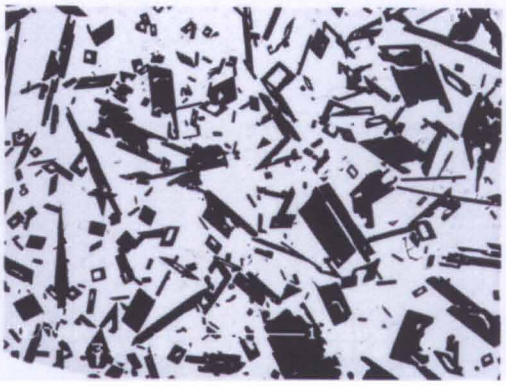

#029 1227℃-1hour-1120℃-30mins

#030 1227℃-1hour-1120℃-1hour

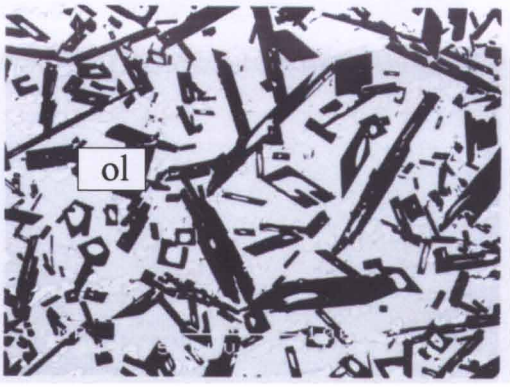

#031 1227℃-1hour-1120℃-3hours

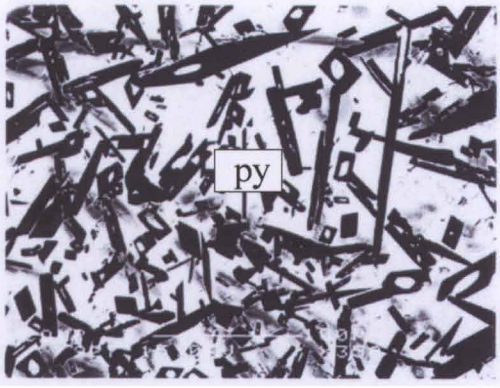

#032 1227℃-1hour-1120℃-6hours

Figure 6-5 Back scattered electron images of run products: cooling induced crystallization from 1227 to 1120 ℃. pl: plagioclase. ol: olivine. py: pigeonitic pyroxene

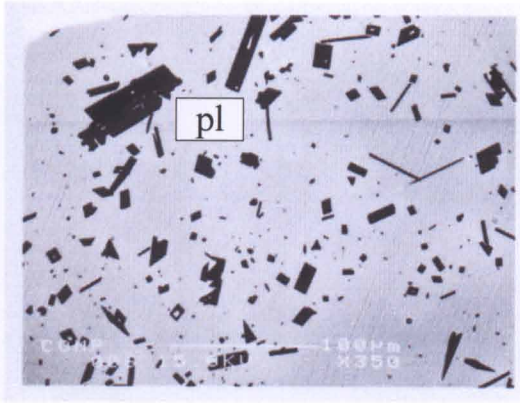

#041 1227℃-1hour-1170℃-0mins

#042 1227℃-1hour-1170℃-15mins

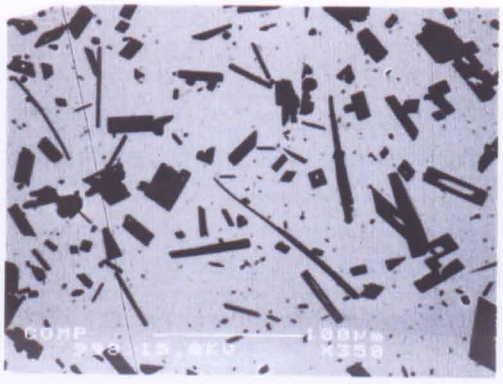

#043 1227℃-1hour-1170℃-30mins

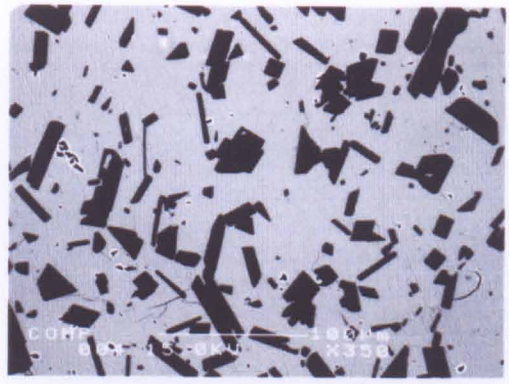

#044 1227℃-1hour-1170℃-1hour

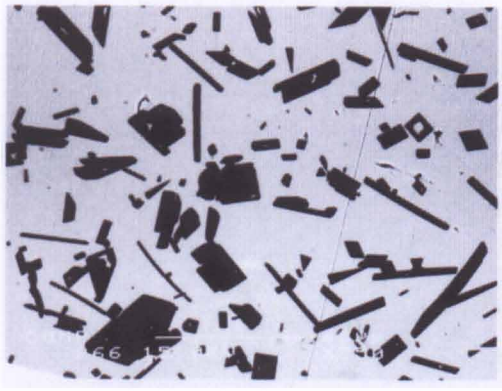

#045 1227℃-1hour-1170℃-3hours

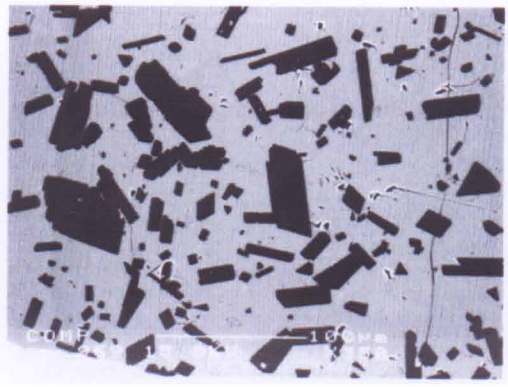

#046 1227℃-1hour-1170℃-6hours

Figure 6-6 Back scattered electron images of run products: cooling induced crystallization from 1227 to 1170 ℃. pl: plagioclase. ol: olivine. py: pigeonitic pyroxene

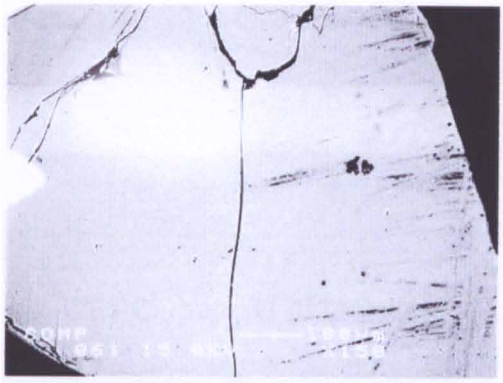

#059 1235℃-1hour

#060 1235℃-1hour-1120℃-0mins

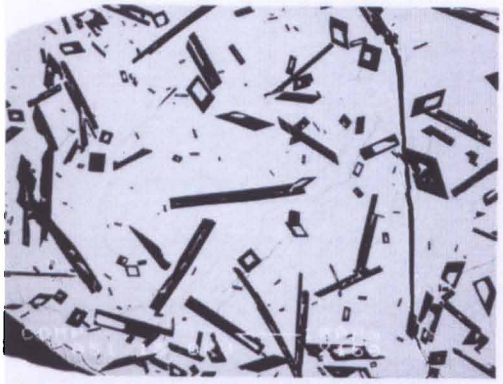

#062 1235℃-1hour-1120℃-30mins

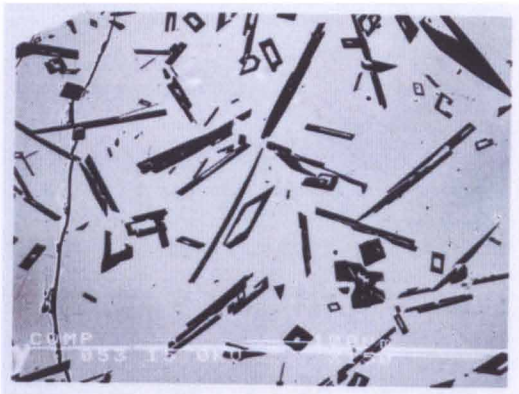

#063 1235℃-1hour-1120℃-1hour

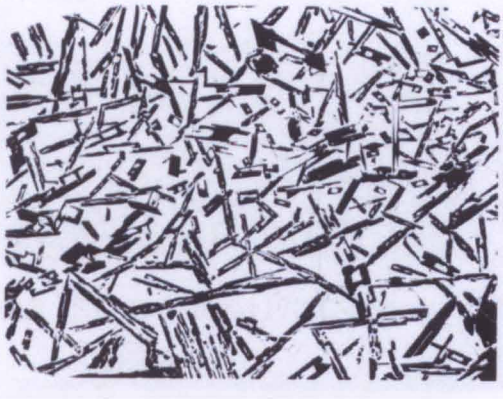

#064 1235℃-1hour-1120℃-3hours

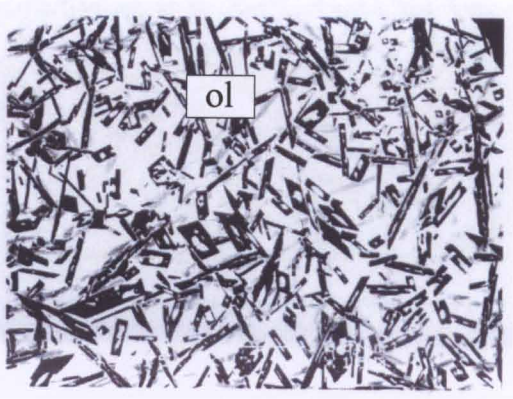

#065 1235℃-1hour-1120℃-6hours

Figure 6-7 Back scattered electron images of run products: cooling induced crystallization from 1235 to 1120 ℃. pl: plagioclase. ol: olivine. py: pigeonitic pyroxene

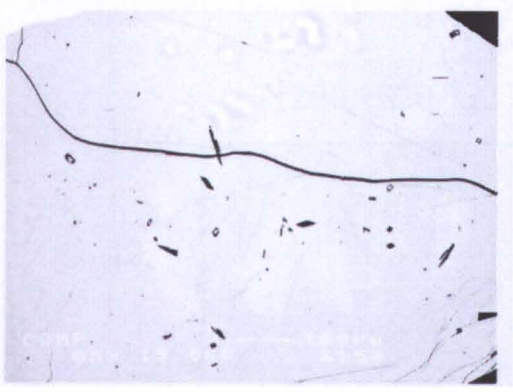

#052 1235℃-1hour-1170℃-0min

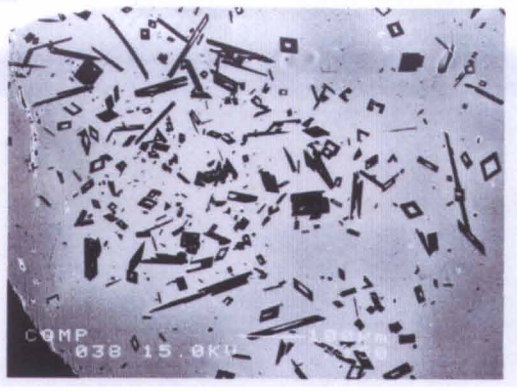

#053 1235℃-1hour-1170℃-15min

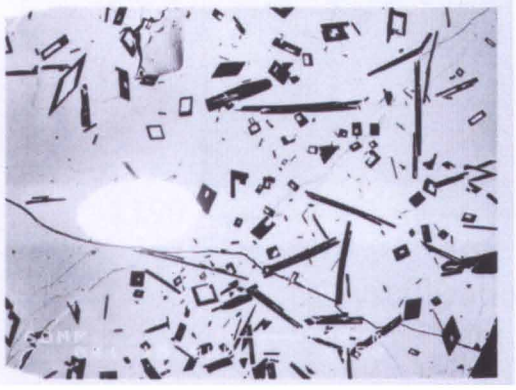

#054 1235℃-1hour-1170℃-30mins

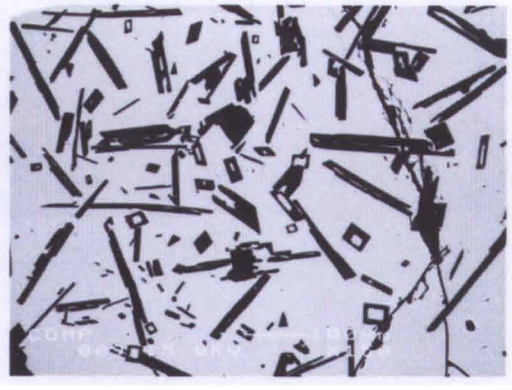

#057 1200℃-1hour-1170℃-1hour

#058 1235℃-1hour-1170℃-3hours

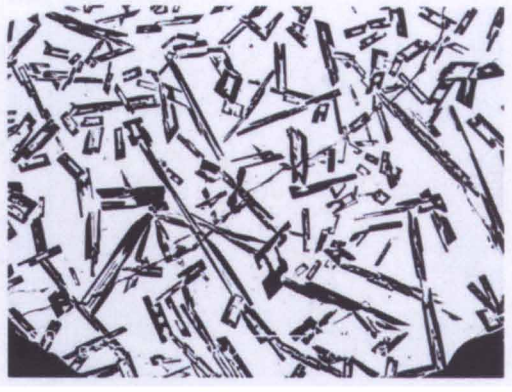

#055 1235℃-1hour-1170℃-6hours

#056 1235℃-1hour-1170℃-12hours

Figure 6-8 Back scattered electron images of run products: cooling induced crystallization from 1235 to 1170 ℃. pl: plagioclase. ol: olivine. py: pigeonitic pyroxene

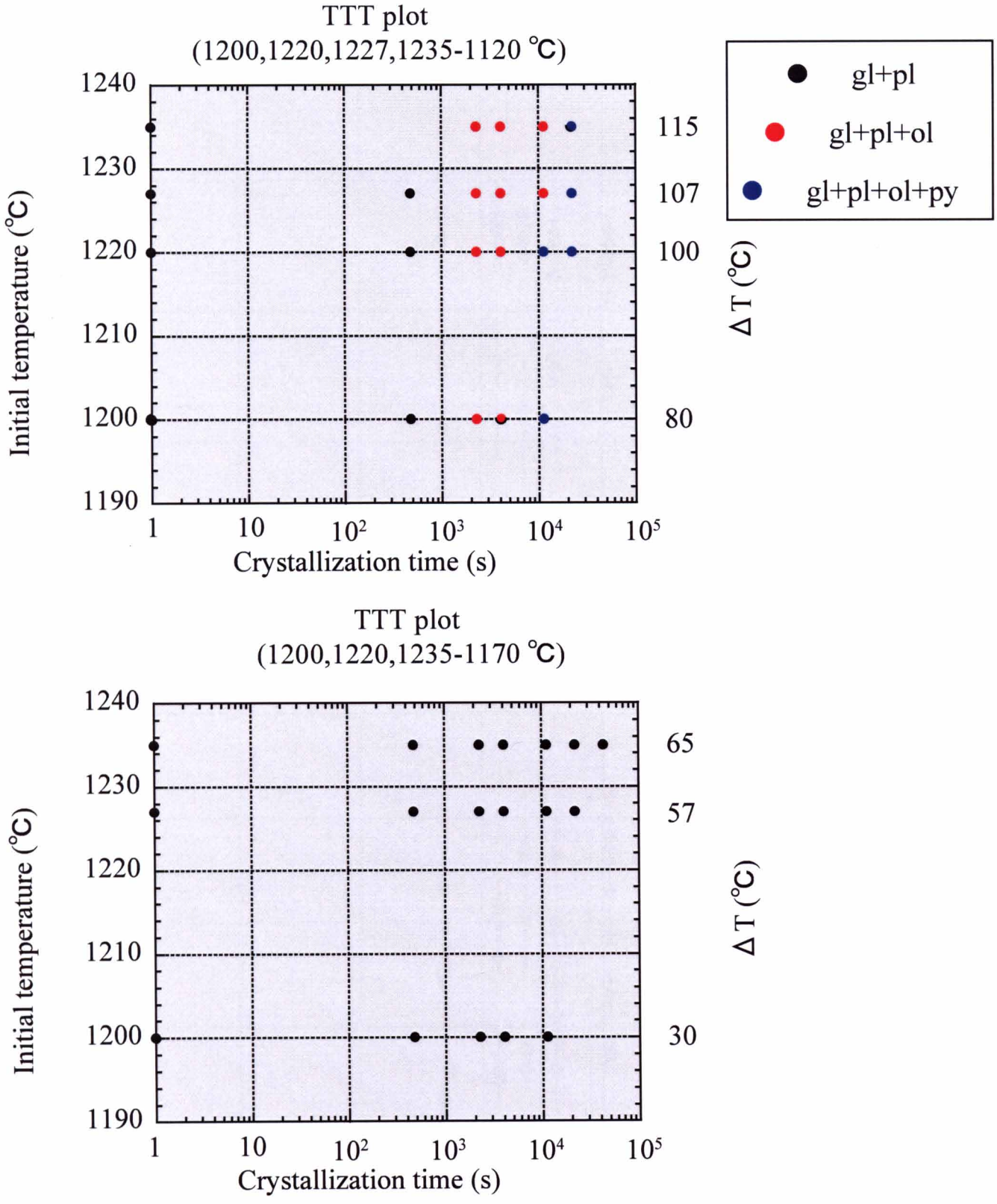

Figure 6-9 TTT (time-temperature-transformation) plots of run products.

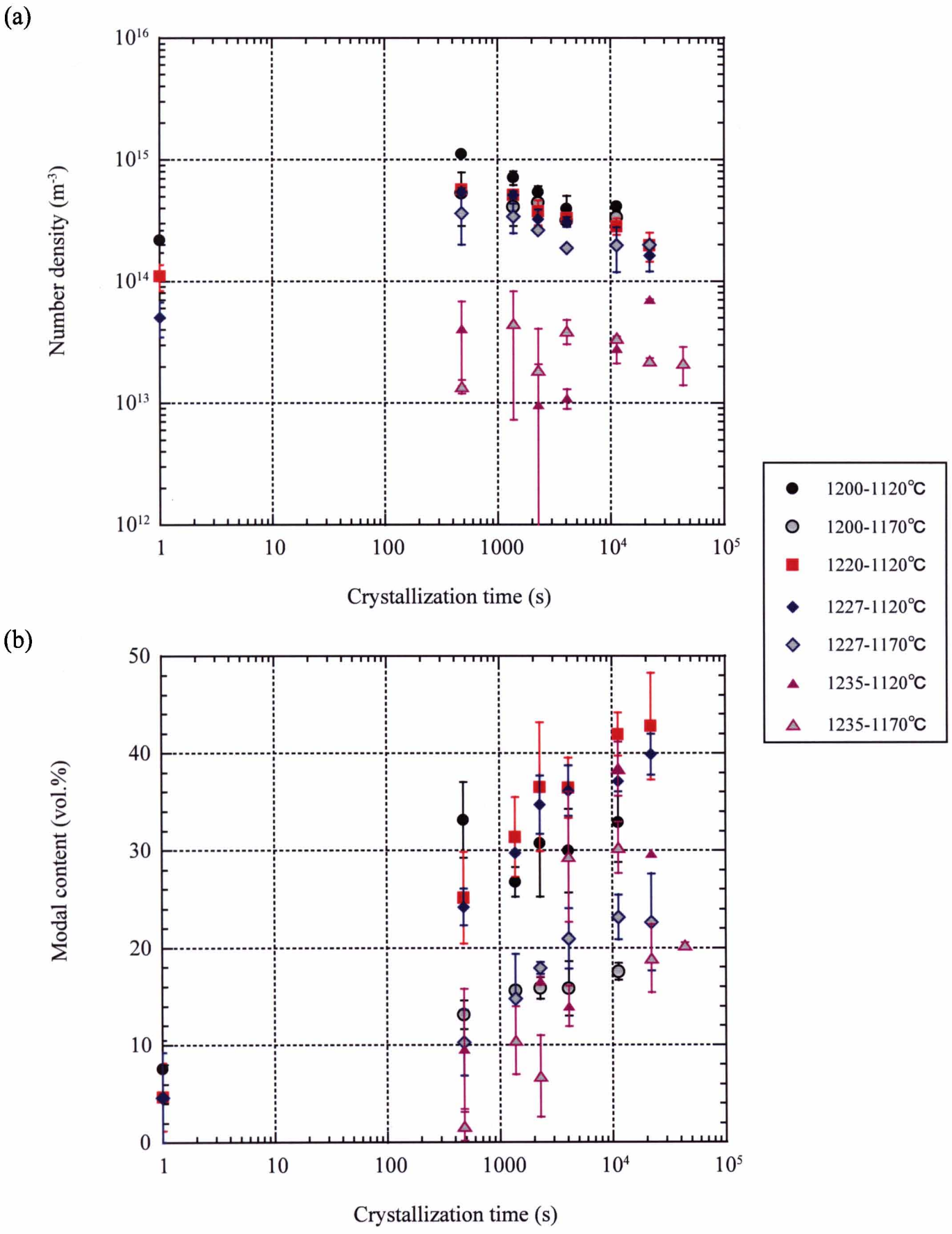

Figure 6-10 Number density (a) and modal content (b) of plagioclase microlites in the run products ploted against crystallizastion time.

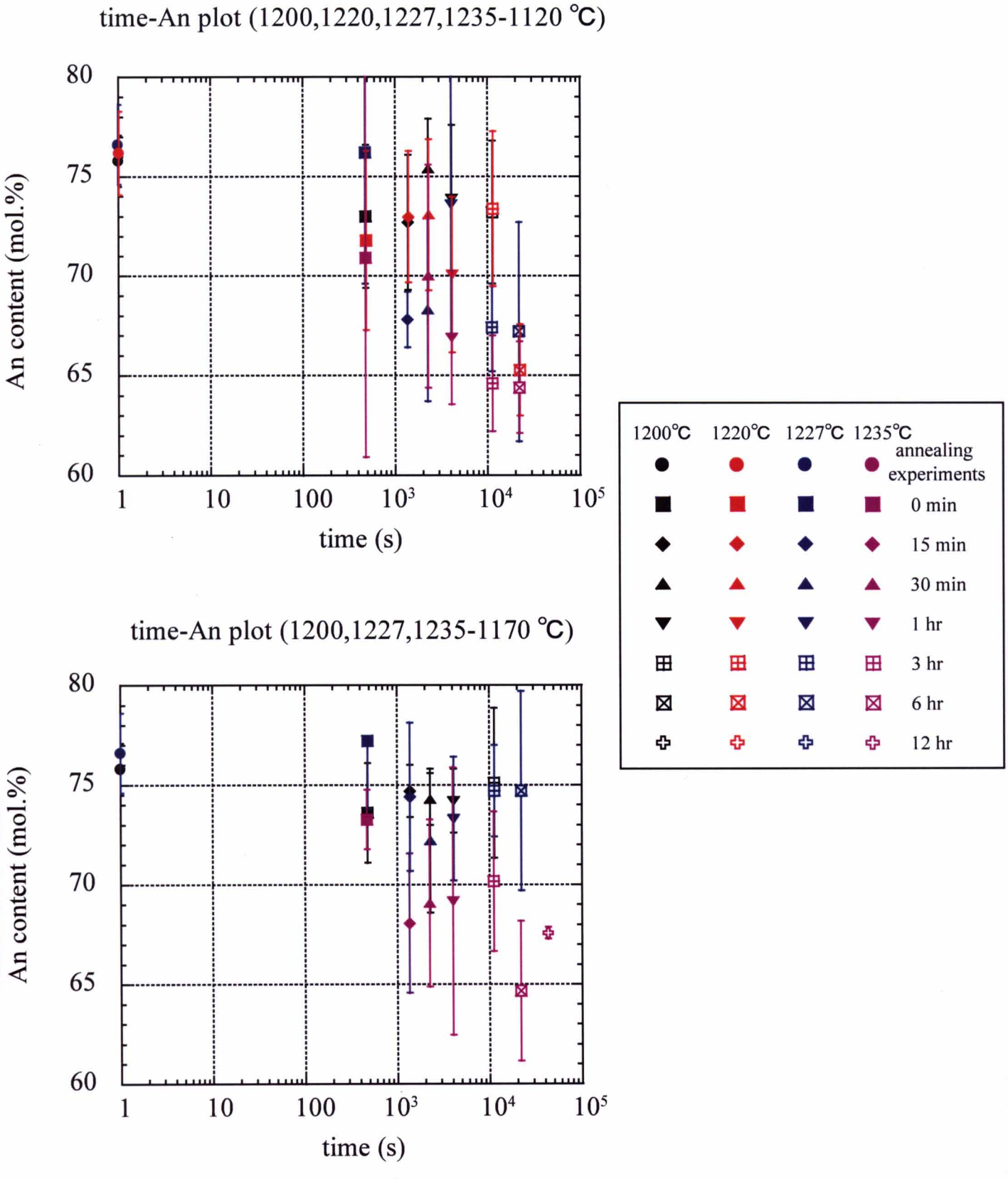

Figure 6-11 An contents of plagioclase microlites in the run products ploted against crystallizastion time.

(a)

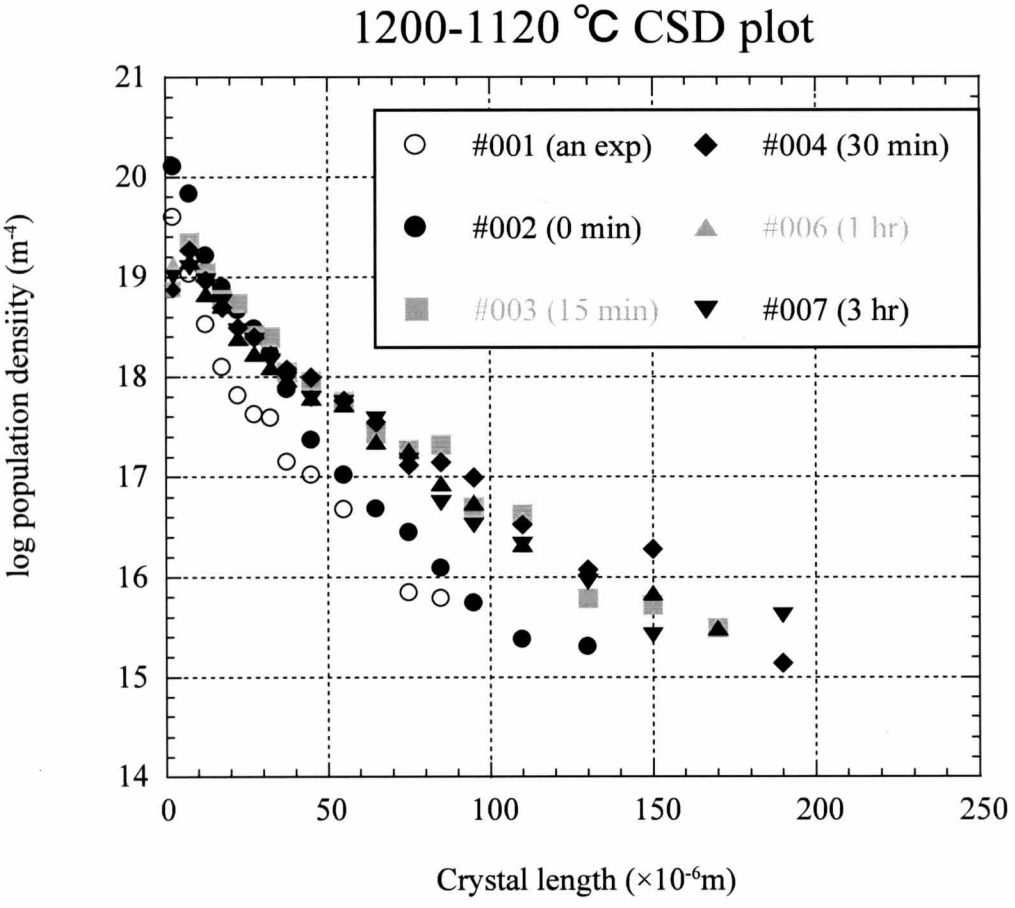

(b)

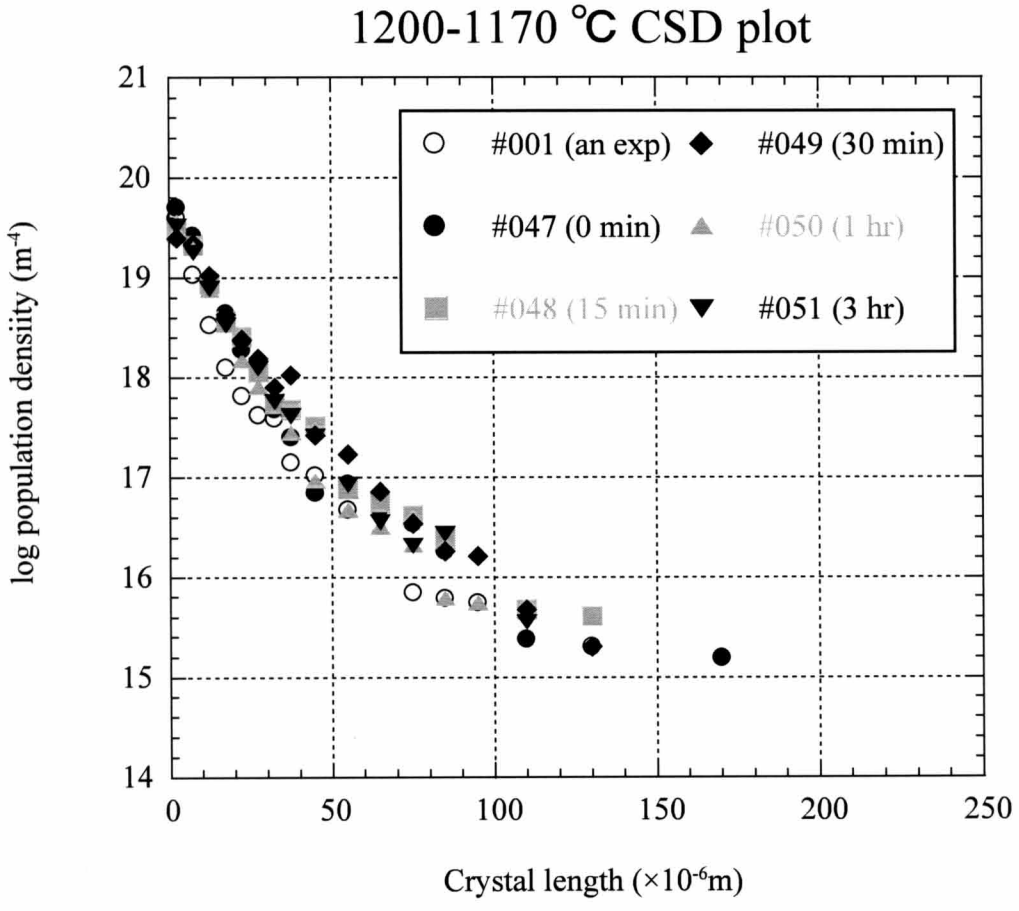

Figure 6-12 CSD (Crystal Size Ditribution) plot of run products. (a) Run products of 1200-1120 ℃ experiments and (b) Run products of 1200-1170 ℃ experiments. an exp is annealing experiment.

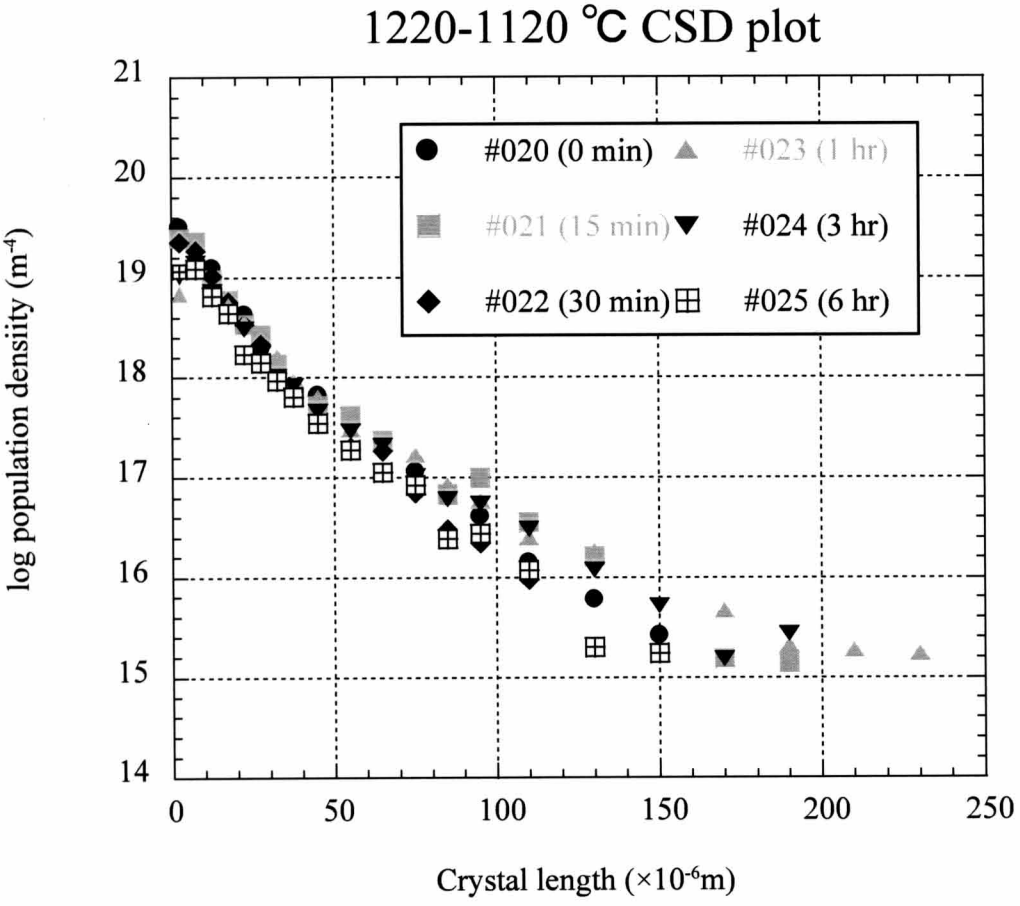

Figure 6-13 CSD (Crystal Size Ditribution) plot of run products of 1220-1120 ℃ experiments.

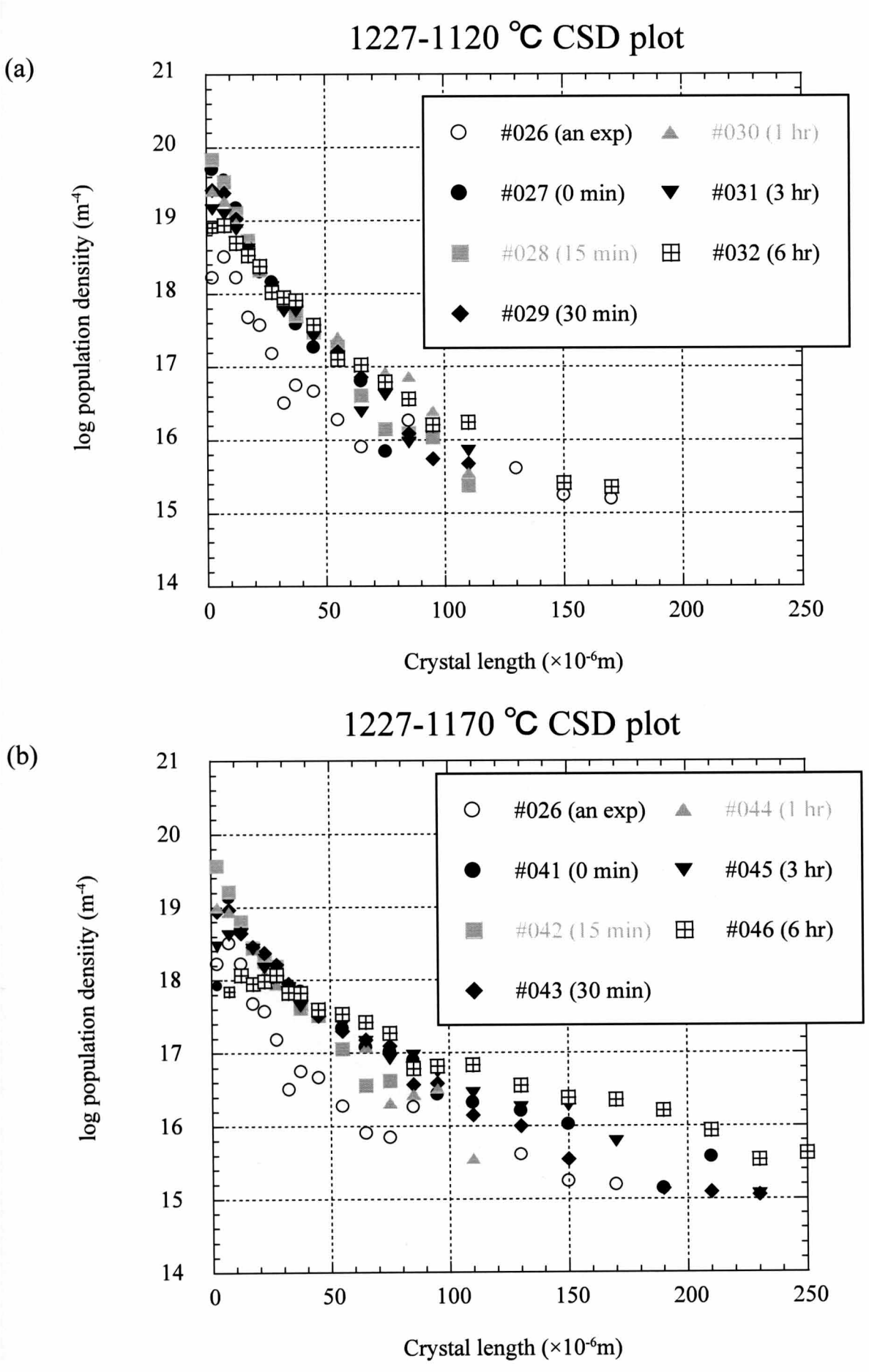

Figure 6-14 CSD (Crystal Size Ditribution) plot of run products. (a) Run products of 1227-1120 ℃ experiments and (b) Run products of 1227-1170 ℃ experiments. an exp is annealing experiment.

(a)

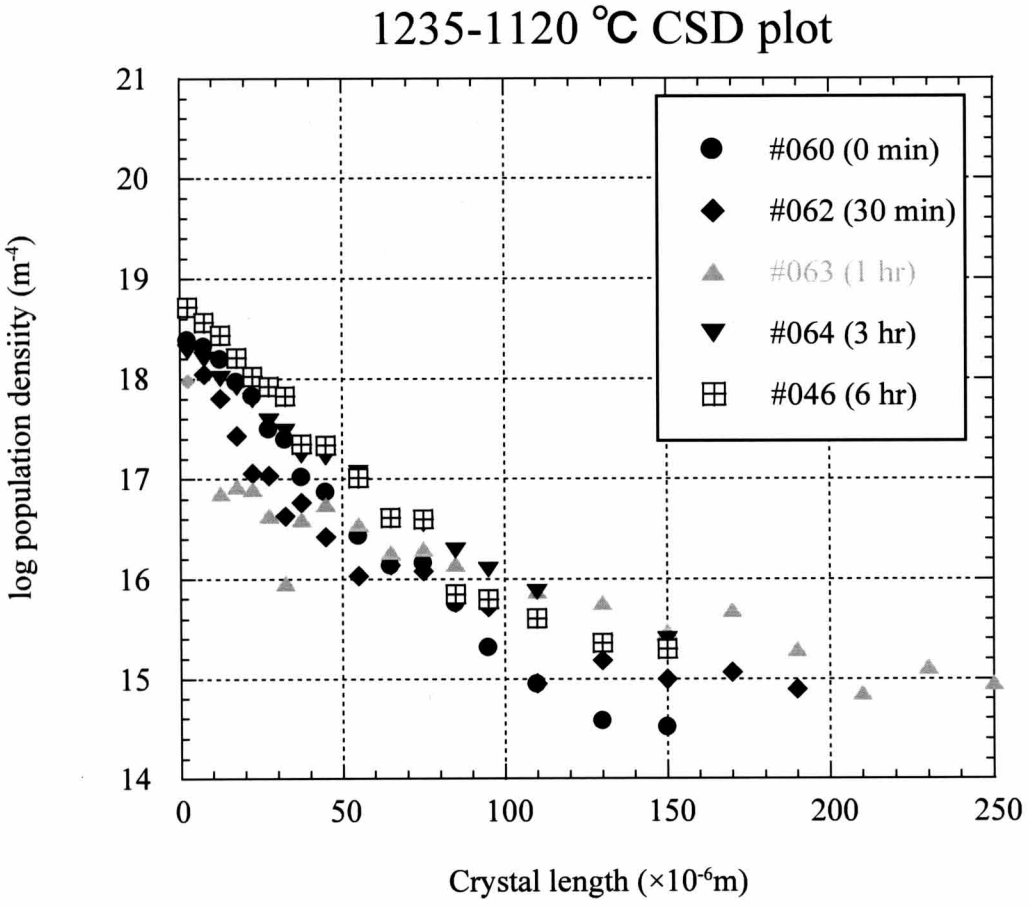

(b)

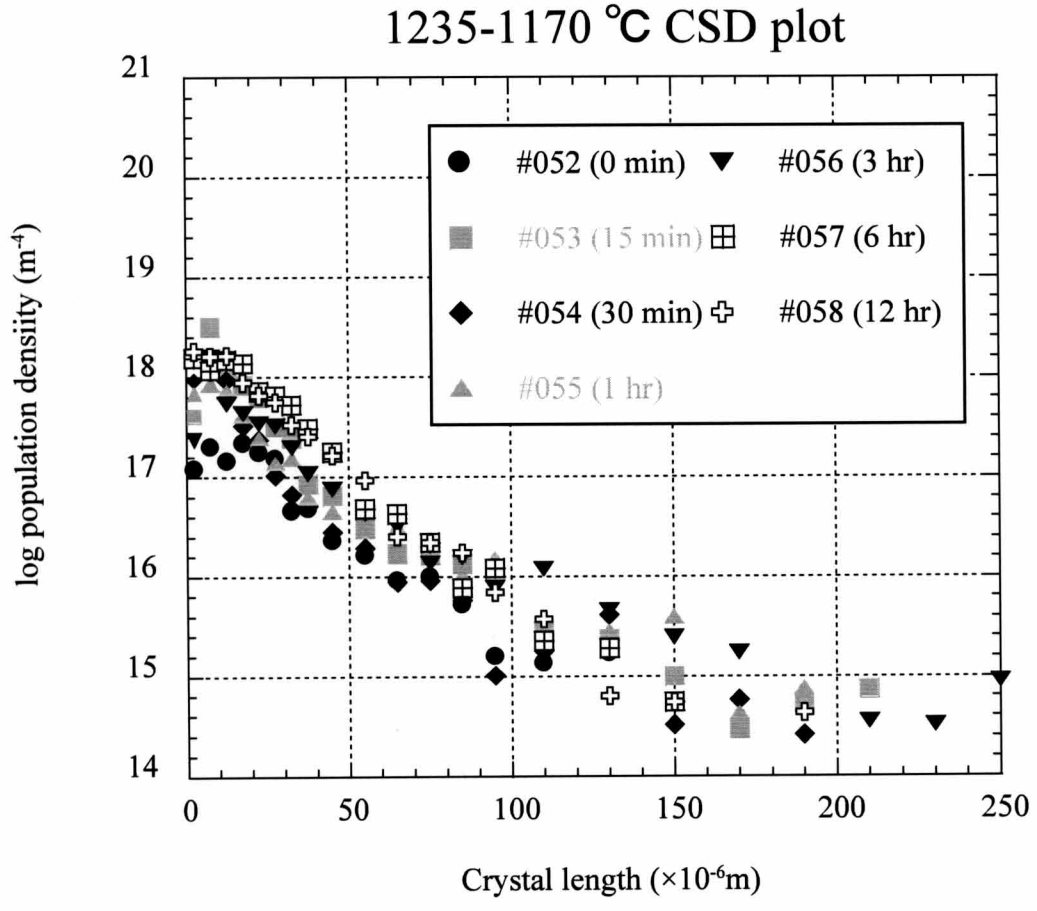

Figure 6-15 CSD (Crystal Size Ditribution) plot of run products. (a) Run products of 1235-1120 ℃ experiments and (b) Run products of 1235-1170 ℃ experiments.

Table 6-1 Whole rock compositions of strarting material

SiO_2	TiO_2	Al_2O_3	FeO	MnO	MgO	CaO	Na_2O	K_2O	P_2O_5	Total
51.23	1.41	16.79	10.89	0.17	5.33	9.78	2.64	0.75	0.27	99.25

Analysis of bulk rock compositions of starting material was done by Hara (1991) at Tokyo University (See detail in Hara,

Table 6-2 Experimental condition of the run products

type of experiment	No.	Temp. 1 (℃)	Temp. 2 (℃)	T1 (min)	T2 (min)		area (μm^2)	counted crystals (n)
annealing experiment	#001	1200	—	60	0	×350-3	192032.0	293
melting/crystallization experiment	#002	1200	1120	60	0	×350-3	192032.0	1424
melting/crystallization experiment	#003	1200	1120	60	15	×350-3	192032.0	983
melting/crystallization experiment	#004	1200	1120	60	30	×350-3	192032.0	855
melting/crystallization experiment	#006	1200	1120	60	60	×350-3	192032.0	681
melting/crystallization experiment	#007	1200	1120	60	180	×350-2	128021.3	490
annealing experiment	#019	1220	—	60	0	×350-2	128021.3	148
melting/crystallization experiment	#020	1220	1120	60	0	×350-3	192032.0	553
melting/crystallization experiment	#021	1220	1120	60	15	×350-3	192032.0	836
melting/crystallization experiment	#022	1220	1120	60	30	×350-3	192032.0	708
melting/crystallization experiment	#023	1220	1120	60	60	×350-2	128021.3	438
melting/crystallization experiment	#024	1220	1120	60	180	×350-3	192032.0	620
melting/crystallization experiment	#025	1220	1120	60	360	×350-3	192032.0	486
annealing experiment	#026	1227	—	60	0	×350-3	192032.0	85
melting/crystallization experiment	#027	1227	1120	60	0	×350-3	192032.0	798
melting/crystallization experiment	#028	1227	1120	60	15	×350-3	192032.0	825
melting/crystallization experiment	#029	1227	1120	60	30	×350-3	192032.0	635
melting/crystallization experiment	#030	1227	1120	60	60	×350-2	128021.3	417
melting/crystallization experiment	#031	1227	1120	60	180	×350-2	128021.3	310
melting/crystallization experiment	#032	1227	1120	60	360	×350-2	130157.8	285
annealing experiment	#059	1235	—	60	0	×150-2	n.a.	n.a.
melting/crystallization experiment	#060	1235	1120	60	0	×150-3	1023959.8	556
melting/crystallization experiment	#062	1235	1120	60	30	×150-3	1009960.2	228
melting/crystallization experiment	#063	1235	1120	60	60	×150-2	673306.8	173
melting/crystallization experiment	#064	1235	1120	60	180	×150-2	673306.8	453
melting/crystallization experiment	#065	1235	1120	60	360	×150-1	336653.4	385
melting/crystallization experiment	#047	1200	1170	60	0	×350-3	192032.0	624
melting/crystallization experiment	#048	1200	1170	60	15	×350-3	192032.0	567
melting/crystallization experiment	#049	1200	1170	60	30	×350-3	192032.0	636
melting/crystallization experiment	#050	1200	1170	60	60	×350-3	192032.0	479
melting/crystallization experiment	#051	1200	1170	60	180	×350-2	128021.3	344
melting/crystallization experiment	#041	1227	1170	60	0	×350-3	192032.0	457
melting/crystallization experiment	#042	1227	1170	60	15	×350-2	128021.3	331
melting/crystallization experiment	#043	1227	1170	60	30	×350-3	192032.0	445
melting/crystallization experiment	#044	1227	1170	60	60	×350-2	128021.3	249
melting/crystallization experiment	#045	1227	1170	60	180	×350-3	192032.0	394
melting/crystallization experiment	#046	1227	1170	60	360	×350-3	192032.0	397
melting/crystallization experiment	#052	1235	1170	60	0	×150-2	671839.6	94
melting/crystallization experiment	#053	1235	1170	60	15	×150-3	991755.9	555
melting/crystallization experiment	#054	1235	1170	60	30	×150-3	1030058.2	287
melting/crystallization experiment	#057	1235	1170	60	60	×150-2	689513.3	228
melting/crystallization experiment	#058	1235	1170	60	180	×150-2	673306.8	303
melting/crystallization experiment	#055	1235	1170	60	360	×150-2	611025.4	469
melting/crystallization experiment	#056	1235	1170	60	720	×150-2	611025.4	432

Table-6-3 textural data of plagioclase microlite in the run products

No.	Phase	morphology	An (mol.%)	stdev	φ (vol.%)	stdev	Nv (m^{-3})	stdev	Sn (μm)	stdev	intercept (m^{-4})	slope (m^{-1})
#001	gl, pl	faceted, tabular	75.8	1.3	7.6	2.9	2.17E+14	4.56E+13	6.98	0.50	18.8	3.28E+04
#002	gl, pl	faceted, tabular	73.0	3.6	33.1	3.9	1.11E+15	5.81E+13	6.68	0.34	19.6	3.92E+04
#003	gl, pl	faceted, tabular	72.7	3.4	26.8	1.5	7.10E+14	9.03E+13	7.24	0.41	19.2	2.36E+04
#004	gl, pl, ol	faceted, tabular	75.4	2.5	30.7	5.5	5.42E+14	6.57E+13	8.29	0.82	19.0	2.10E+04
#006	gl, pl, ol	faceted, tabular	73.9	6.1	30.0	4.3	3.93E+14	1.09E+14	9.24	1.20	18.9	2.17E+04
#007	gl, pl, ol, px	faceted, tabular	73.2	3.6	32.9	4.1	4.13E+14	6.56E+12	9.26	0.33	18.9	2.16E+04
#019	gl, pl	faceted, tabular	76.2	2.1	4.7	3.5	1.11E+14	2.70E+13	7.19	2.50		
#020	gl, pl	faceted, tabular or hopper	71.8	4.5	25.2	4.7	5.69E+14	4.68E+13	7.62	0.68	19.2	2.71E+04
#021	gl, pl	faceted, tabular or hopper	73.0	3.3	31.4	4.1	5.15E+14	3.68E+13	8.48	0.58	19.0	2.26E+04
#022	gl, pl, ol	faceted, tabular or hopper	73.1	3.8	36.6	6.6	3.77E+14	8.84E+13	9.98	1.30	19.3	3.20E+04
#023	gl, pl, ol	faceted, tabular or hopper	70.1	3.9	36.5	3.1	3.31E+14	1.48E+13	10.32	0.14	18.7	1.75E+04
#024	gl, pl, ol, px	faceted, tabular or hopper	73.4	3.9	42.0	2.2	2.85E+14	4.35E+13	11.43	0.80	18.8	2.08E+04
#025	gl, pl, ol, px	faceted, tabular or hopper	65.3	2.3	42.8	5.5	1.98E+14	5.27E+13	13.08	1.66	18.9	2.70E+04
#026	gl, pl	faceted, tabular	76.6	2.0	4.6	4.6	5.08E+13	1.61E+13	8.68	3.87	17.8	1.85E+04
#027	gl, pl	faceted, tabular or hopper	76.2	6.6	24.2	1.9	5.46E+14	3.93E+13	7.63	0.37	19.6	4.59E+04
#028	gl, pl	faceted, tabular or hopper	67.8	1.4	29.8	0.2	5.16E+14	3.63E+13	8.33	0.17	19.4	3.97E+04
#029	gl, pl, ol	faceted, tabular or hopper	68.3	4.6	34.7	3.0	3.25E+14	6.24E+13	10.28	0.93	19.3	3.65E+04
#030	gl, pl, ol	faceted, tabular or hopper	73.6	6.5	36.1	2.6	3.09E+14	2.84E+13	10.54	0.07	19.2	3.20E+04
#031	gl, pl, ol	faceted, tabular or hopper	67.4	2.2	37.2	1.1	1.95E+14	2.45E+12	12.39	0.07	18.9	2.84E+04
#032	gl, pl, ol, px	faceted, tabular or hopper	67.2	5.5	39.9	2.1	1.63E+14	4.28E+13	13.58	0.96	18.7	2.27E+04
#059	gl								n.a.	n.a.		
#060	gl, pl	faceted, tabular, hopper	70.9	10.0	9.6	6.2	4.10E+13	2.72E+13	13.34	0.51	18.3	2.92E+04
#062	gl, pl, ol	faceted, tabular, hopper	70.0	5.6	16.6	0.4	9.69E+12	1.12E+13	31.37	####	17.4	1.64E+04
#063	gl, pl, ol	faceted, tabular, hopper	66.9	1.5	14.0	2.1	1.10E+13	2.01E+12	23.40	0.27	16.8	7.80E+03
#064	gl, pl, ol	faceted, tabular, hopper	64.6	2.4	38.4	2.8	2.82E+13	7.01E+12	24.01	1.43	18.2	2.12E+04
#065	gl, pl, ol, px	faceted, tabular, hopper	64.4	2.3	29.7		7.10E+13	0.00E+00	16.11		18.6	2.59E+04
#047	gl, pl	faceted, equant	73.6	2.5	13.1	1.5	5.35E+14	2.50E+14	6.43	0.89	18.9	2.82E+04
#048	gl, pl	faceted, equant	74.7	1.3	15.6	0.3	4.10E+14	1.25E+14	7.34	0.68	19.1	3.14E+04
#049	gl, pl	faceted, equant	74.3	1.3	15.9	1.1	4.41E+14	8.67E+13	7.15	0.46	19.2	3.29E+04
#050	gl, pl	faceted, equant	74.2	1.6	15.8	2.8	3.16E+14	4.43E+13	7.95	0.73	19.3	4.14E+04
#051	gl, pl	faceted, equant	75.1	1.6	17.5	2.4	3.34E+14	4.36E+13	8.08	0.72	19.2	3.65E+04
#041	gl, pl	faceted, equant	77.2	6.0	10.3	3.4	3.62E+14	1.62E+14	6.69	0.54	18.5	1.75E+04
#042	gl, pl	faceted, equant	74.4	3.6	14.8	4.6	3.42E+14	9.39E+13	7.55	0.09	19.3	4.09E+04
#043	gl, pl	faceted, equant	72.2	4.5	17.9	0.6	2.64E+14	3.99E+13	8.82	0.46	18.5	1.78E+04
#044	gl, pl	faceted, equant	73.3	5.4	21.0	3.1	1.88E+14	5.86E+11	10.36	0.50	18.9	3.04E+04
#045	gl, pl	faceted, equant	74.7	2.8	23.1	2.3	1.98E+14	7.92E+13	10.78	1.56	18.4	1.60E+04
#046	gl, pl	faceted, equant	74.7	3.2	22.6	5.0	1.99E+14	1.06E+13	10.41	0.86	18.1	1.02E+04
#052	gl, pl	faceted, tabular, hopper	73.2	7.2	1.6	1.5	1.37E+13	1.77E+12	10.03	3.01	17.4	1.98E+04
#053	gl, pl	faceted, tabular, hopper	68.0	1.4	10.5	3.5	4.49E+13	3.76E+13	15.93	6.02	17.9	1.85E+04
#054	gl, pl	faceted, tabular, hopper	69.0	6.0	6.8	4.2	1.86E+13	2.20E+13	18.02	3.88	17.6	1.92E+04
#057	gl, pl	faceted, tabular, hopper	69.1	1.2	29.4	6.7	3.92E+13	8.85E+12	19.56	0.01	17.7	1.68E+04
#058	gl, pl	faceted, tabular, hopper	70.1	4.9	30.3	2.6	3.42E+13	2.13E+11	20.70	0.55	17.7	1.40E+04
#055	gl, pl	faceted, tabular, hopper	64.6	0.7	18.9	3.5	2.23E+13	1.64E+13	21.66	4.50	18.4	2.54E+04
#056	gl, pl	faceted, tabular, hopper	67.5	8.4	20.3	0.3	2.14E+13	7.43E+12	21.44	2.44	18.2	2.30E+04

Table 6-4 Chemical composition of run products

No.	Temp. 1	Temp. 2		n	SiO_2	TiO_2	Al_2O_3	FeO	MnO	MgO	CaO	Na_2O	K_2O	Total
#001	1200		gl	8	50.89	1.54	15.37	11.96	0.17	6.05	9.21	2.49	0.81	98.50
			σ		0.41	0.06	0.19	0.41	0.02	0.26	0.09	0.09	0.05	0.32
			pl	7	49.67	0.07	30.07	1.23	0.01	0.27	14.73	2.60	0.12	98.76
			σ		0.36	0.06	0.35	0.28	0.01	0.14	0.24	0.15	0.02	0.54
#002	1200	1120	gl	8	51.24	1.89	11.97	14.61	0.24	7.37	8.05	2.10	1.22	98.67
			σ		0.14	0.06	0.49	0.38	0.02	0.27	0.05	0.14	0.04	0.32
			pl	7	51.14	0.10	29.40	1.37	0.03	0.37	14.08	2.87	0.17	99.53
			σ		1.11	0.07	1.33	0.34	0.02	0.24	1.02	0.32	0.06	0.58
#003	1200	1120	gl	8	50.79	1.91	12.23	14.65	0.23	6.76	8.57	2.19	1.01	98.34
			σ		0.35	0.08	0.22	0.58	0.02	0.35	0.22	0.19	0.06	0.52
			pl	7	50.75	0.08	29.74	1.25	0.02	0.27	14.21	2.94	0.15	99.42
			σ		1.20	0.04	0.84	0.08	0.02	0.08	0.82	0.33	0.05	0.72
#004	1200	1120	gl	8	50.21	2.05	11.85	14.49	0.22	6.25	8.64	2.20	1.06	96.96
			σ		0.71	0.27	0.21	0.27	0.04	1.19	0.40	0.13	0.10	0.61
			pl	6	49.42	0.07	29.47	1.26	0.00	0.25	14.63	2.63	0.13	97.87
			σ		0.90	0.03	0.66	0.14	0.01	0.09	0.60	0.25	0.04	0.49
			ol	1	37.80	0.10	0.55	27.37	0.37	33.70	0.56	0.07	0.04	100.56
			σ		–	–	–	–	–	–	–	–	–	–
#006	1200	1120	gl	5	51.81	2.16	12.37	13.99	0.22	5.14	8.64	2.44	1.15	97.93
			σ		0.82	0.14	0.27	0.77	0.03	0.46	0.29	0.14	0.14	0.47
			pl	8	50.63	0.12	29.50	1.40	0.02	0.36	14.42	2.80	0.18	99.45
			σ		1.98	0.10	2.09	0.49	0.02	0.27	1.49	0.60	0.12	0.40
			ol	2	37.61	0.06	0.31	26.31	0.33	35.73	0.43	0.06	0.01	100.84
			σ		0.33	0.04	0.31	0.97	0.00	0.98	0.10	0.04	0.01	0.82
#007	1200	1120	gl	4	52.06	2.33	12.09	14.21	0.22	4.35	8.75	2.33	1.32	97.65
			σ		0.75	0.13	0.14	0.45	0.02	0.03	0.20	0.11	0.08	0.50
			pl	8	51.10	0.07	30.11	1.15	0.02	0.22	14.36	2.90	0.15	100.08
			σ		0.93	0.01	0.86	0.15	0.02	0.03	0.78	0.37	0.04	0.72
			ol	5	36.94	0.05	0.14	28.98	0.38	33.30	0.44	0.03	0.01	100.28
			σ		0.33	0.03	0.16	0.89	0.04	0.46	0.06	0.04	0.01	0.69
			px	5	51.78	0.76	3.18	16.02	0.37	21.40	6.43	0.13	0.03	100.11
			σ		0.86	0.29	1.25	1.14	0.03	1.80	1.98	0.09	0.04	0.38
#019	1220		gl	5	51.33	1.39	16.03	10.73	0.17	5.47	9.37	2.43	0.86	97.77
			σ		0.18	0.03	0.10	0.81	0.02	0.05	0.11	0.11	0.01	0.96
			pl	4	49.95	0.08	30.29	1.29	0.01	0.32	14.78	2.55	0.12	99.41
			σ		0.33	0.04	0.76	0.27	0.01	0.19	0.63	0.19	0.03	0.67
#020	1220	1120	gl	5	50.62	1.53	13.74	12.93	0.20	6.56	8.49	2.18	1.08	97.34
			σ		0.35	0.10	0.57	0.23	0.02	0.18	0.12	0.11	0.05	0.24
			pl	8	51.09	0.07	29.35	1.18	0.02	0.29	13.86	3.00	0.16	99.02
			σ		1.25	0.04	0.91	0.13	0.01	0.11	0.96	0.46	0.05	0.30
#021	1220	1120	gl	5	50.73	1.81	12.06	13.89	0.19	7.41	8.45	2.13	1.04	97.72
			σ		0.25	0.09	0.29	0.49	0.02	0.10	0.08	0.14	0.04	0.37
			pl	8	51.03	0.06	29.85	1.08	0.01	0.23	14.10	2.88	0.15	99.38
			σ		1.18	0.04	0.63	0.06	0.01	0.03	0.79	0.33	0.05	0.39
#022	1220	1120	gl	5	50.37	1.85	11.97	14.23	0.21	7.12	8.24	2.04	1.05	97.08
			σ		0.12	0.04	0.23	0.38	0.02	0.06	0.19	0.08	0.04	0.05
			pl	8	50.48	0.08	29.50	1.22	0.01	0.25	14.12	2.86	0.15	98.67
			σ		1.04	0.05	0.88	0.14	0.02	0.08	0.96	0.36	0.04	0.44
#023	1220	1120	gl	5	51.73	2.50	11.35	13.89	0.23	4.28	9.19	2.09	1.21	96.47
			σ		0.61	0.04	0.42	0.77	0.03	0.19	0.25	0.19	0.10	0.92
			pl	7	51.58	0.10	28.83	1.23	0.00	0.25	13.48	3.17	0.18	98.83
			σ		1.17	0.07	1.08	0.22	0.00	0.08	0.92	0.38	0.08	0.59
			ol	3	38.06	0.20	0.95	27.35	0.39	31.68	0.95	0.11	0.13	99.82
			σ		1.11	0.06	0.63	0.55	0.02	1.30	0.39	0.07	0.06	1.45
#024	1220	1120	gl	5	52.31	2.47	11.37	13.93	0.23	4.18	9.05	2.15	1.30	96.99
			σ		0.34	0.05	0.14	0.26	0.04	0.04	0.13	0.13	0.04	0.33
			pl	8	50.55	0.08	29.73	1.14	0.00	0.24	14.23	2.84	0.14	98.95
			σ		1.28	0.03	0.83	0.08	0.01	0.08	0.85	0.41	0.05	0.33
			ol	6	36.76	0.06	0.11	28.57	0.39	32.64	0.45	0.02	0.01	99.02

Table 6-4 (continued)

			σ		0.31	0.01	0.07	0.34	0.03	0.24	0.03	0.02	0.01	0.45
			px		—	—	—	—	—	—	—	—	—	—
#025	1220	1120	gl	5	52.41	2.26	11.57	13.85	0.20	4.24	8.99	2.21	1.22	96.95
			σ		0.40	0.30	0.06	0.28	0.01	0.03	0.05	0.11	0.14	0.91
			pl	8	52.93	0.12	27.84	1.36	0.01	0.30	12.51	3.68	0.27	99.01
			σ		0.81	0.08	0.96	0.35	0.02	0.09	0.62	0.20	0.07	0.75
			ol	6	37.28	0.13	0.45	29.31	0.40	31.93	0.68	0.07	0.05	100.29
			σ		1.09	0.10	0.59	0.62	0.04	1.03	0.42	0.09	0.07	0.86
			px		—	—	—	—	—	—	—	—	—	—
#026	1227		gl	5	51.70	1.44	16.48	10.90	0.18	5.36	9.61	2.57	0.83	99.08
			σ		0.11	0.05	0.11	0.22	0.03	0.07	0.09	0.08	0.02	0.22
			pl	6	50.13	0.08	30.74	1.37	0.01	0.32	15.20	2.57	0.13	100.56
			σ		0.72	0.08	0.82	0.40	0.01	0.20	0.60	0.20	0.04	0.25
#027	1227	1120	gl	7	50.98	1.83	12.86	13.98	0.22	6.88	8.64	2.21	1.03	98.61
			σ		0.24	0.08	0.60	0.49	0.04	0.15	0.08	0.10	0.04	0.69
			pl	7	50.08	0.07	30.64	1.25	0.02	0.27	15.19	2.60	0.14	100.25
			σ		1.84	0.09	2.00	0.46	0.02	0.28	1.52	0.68	0.08	0.44
#028	1227	1120	gl	7	50.77	1.96	11.93	14.50	0.21	7.28	8.44	2.11	1.00	98.20
			σ		0.25	0.07	0.15	0.58	0.03	0.04	0.13	0.12	0.05	0.76
			pl	7	52.62	0.12	28.81	1.22	0.01	0.30	13.31	3.49	0.21	100.09
			σ		1.84	0.09	2.00	0.46	0.02	0.28	1.52	0.68	0.08	0.44
#029	1227	1120	gl	7	50.89	1.85	11.96	14.82	0.22	7.31	8.57	2.14	0.99	98.76
			σ		0.23	0.06	0.16	0.44	0.03	0.06	0.12	0.07	0.07	0.56
			pl	7	52.78	0.09	29.26	1.24	0.01	0.25	13.57	3.46	0.21	100.88
			σ		1.52	0.03	1.03	0.10	0.02	0.05	1.11	0.46	0.06	0.33
			ol		—	—	—	—	—	—	—	—	—	—
#030	1227	1120	gl	7	52.10	2.28	12.38	14.45	0.21	4.72	9.21	2.27	1.17	98.78
			σ		0.59	0.15	0.31	0.64	0.06	0.36	0.31	0.07	0.11	0.54
			pl	6	51.26	0.09	30.30	1.21	0.01	0.26	14.69	2.91	0.16	100.88
			σ		2.02	0.04	1.76	0.22	0.01	0.12	1.37	0.70	0.08	0.33
			ol	4	37.97	0.12	0.77	27.57	0.34	32.46	0.71	0.15	0.05	100.15
			σ		0.54	0.03	0.72	0.76	0.05	0.94	0.19	0.11	0.04	0.50
#031	1227	1120	gl	7	52.47	2.41	11.77	13.93	0.23	4.30	9.47	2.18	1.26	98.01
			σ		0.23	0.07	0.10	0.74	0.03	0.04	0.12	0.09	0.04	0.91
			pl	7	53.02	0.09	28.85	1.21	0.00	0.24	13.33	3.57	0.25	100.56
			σ		0.97	0.02	0.68	0.09	0.00	0.04	0.59	0.20	0.06	0.42
			ol	6	37.86	0.12	0.53	29.50	0.40	31.92	0.62	0.09	0.04	101.08
			σ		1.31	0.06	0.73	0.44	0.03	0.50	0.25	0.14	0.04	1.89
#032	1227	1120	gl	7	50.16	2.65	11.73	16.75	0.22	4.24	8.80	2.17	1.43	98.16
			σ		0.26	0.07	0.19	0.34	0.02	0.07	0.14	0.17	0.03	0.60
			pl	8	52.76	0.09	28.91	1.23	0.01	0.26	13.26	3.57	0.24	100.34
			σ		1.75	0.03	1.12	0.10	0.01	0.05	1.19	0.58	0.08	0.25
			ol	9	37.22	0.09	0.20	29.14	0.43	32.10	0.51	0.05	0.03	99.77
			σ		0.65	0.04	0.32	2.28	0.03	1.52	0.17	0.08	0.04	0.40
			px	5	50.95	0.87	3.34	16.05	0.37	19.55	8.29	0.11	0.01	99.55
			σ		0.79	0.18	0.63	1.10	0.05	2.15	3.36	0.04	0.01	0.36
#059	1235		gl	6	51.32	1.42	16.57	10.96	0.19	5.40	9.16	2.53	0.67	98.21
			σ		0.28	0.07	0.11	0.23	0.03	0.09	0.41	0.12	0.03	0.42
#060	1235	1120	gl	6	51.07	1.43	16.20	11.33	0.22	5.64	8.74	2.48	0.72	97.83
			σ		0.41	0.06	0.59	0.74	0.04	0.39	0.48	0.13	0.07	0.47
			pl	7	51.63	0.09	29.23	1.31	0.02	0.29	13.42	3.01	0.14	99.14
			σ		3.08	0.03	2.31	0.22	0.02	0.11	2.19	1.00	0.06	0.27
#062	1235	1120	gl	6	50.87	1.67	14.27	12.71	0.24	6.27	8.29	2.41	0.74	97.45
			σ		0.21	0.09	0.27	0.22	0.03	0.13	0.23	0.14	0.04	0.36
			pl	8	51.41	0.07	29.02	1.08	0.01	0.23	13.20	3.11	0.14	98.25
			σ		1.46	0.03	1.08	0.08	0.01	0.03	1.34	0.55	0.03	0.71
#063	1235	1120	gl	6	50.82	1.53	14.96	12.01	0.20	6.01	8.42	2.49	0.75	97.19
			σ		0.30	0.06	0.36	0.32	0.03	0.10	0.43	0.11	0.03	0.59
			pl	8	52.14	0.09	28.47	1.05	0.01	0.22	12.26	3.35	0.16	97.76

Table 6-4 (continued)

			σ		0.48	0.02	0.23	0.07	0.02	0.02	0.39	0.17	0.01	0.42
#064	1235	1120	gl	6	51.91	2.45	11.62	14.29	0.27	4.40	8.30	2.12	1.06	96.42
			σ		0.27	0.09	0.14	0.34	0.03	0.12	0.21	0.12	0.06	0.43
			pl	7	52.82	0.16	26.95	1.67	0.02	0.43	11.66	3.52	0.23	97.47
			σ		0.53	0.17	0.85	0.90	0.02	0.29	0.63	0.20	0.06	0.95
			ol	5	36.54	0.08	0.07	29.50	0.49	32.54	0.43	0.02	0.01	99.68
			σ		0.22	0.01	0.05	0.23	0.05	0.51	0.05	0.02	0.01	0.48
#065	1235	1120	gl	6	49.53	2.66	11.72	16.38	0.26	4.53	8.07	2.29	1.18	96.61
			σ		0.17	0.07	0.05	0.27	0.04	0.11	0.16	0.06	0.02	0.37
			pl	7	52.89	0.11	27.45	1.39	0.02	0.31	11.92	3.64	0.24	97.96
			σ		0.55	0.04	0.50	0.13	0.02	0.05	0.63	0.20	0.03	0.33
			px	5	51.19	0.68	2.96	16.55	0.42	21.76	5.26	0.08	0.01	98.91
			σ		0.60	0.15	1.07	1.20	0.05	0.62	0.41	0.01	0.01	0.31
#047	1200	1170	gl	6	51.44	1.60	14.63	12.59	0.23	6.22	8.92	2.42	0.80	98.83
			σ		0.14	0.04	0.13	0.13	0.02	0.05	0.38	0.14	0.03	0.63
			pl	5	48.94	0.05	30.17	1.37	0.00	0.21	13.53	2.67	0.10	97.03
			σ		0.81	0.03	0.61	0.13	0.01	0.02	0.83	0.19	0.02	0.41
#048	1200	1170	gl	6	51.43	1.62	14.30	12.61	0.21	6.28	8.91	2.39	0.84	98.58
			σ		0.24	0.06	0.12	0.17	0.02	0.06	0.31	0.14	0.02	0.54
			pl	7	50.61	0.06	30.07	1.32	0.01	0.22	14.71	2.75	0.12	99.88
			σ		0.45	0.02	0.35	0.06	0.01	0.02	0.43	0.13	0.02	0.48
#049	1200	1170	gl	6	51.33	1.70	13.71	13.14	0.21	6.40	8.72	2.51	0.85	98.58
			σ		0.32	0.04	0.08	0.13	0.05	0.07	0.22	0.11	0.03	0.26
			pl	9	50.73	0.09	29.71	1.44	0.01	0.31	14.46	2.77	0.13	99.65
			σ		0.50	0.06	0.60	0.20	0.02	0.15	0.38	0.13	0.03	0.43
#050	1200	1170	gl	6	50.73	1.68	13.74	12.95	0.21	6.44	8.77	2.37	0.84	97.73
			σ		0.17	0.03	0.09	0.11	0.04	0.07	0.17	0.06	0.01	0.30
			pl	10	50.19	0.07	29.70	1.34	0.02	0.26	14.23	2.74	0.12	98.68
			σ		0.55	0.04	0.44	0.12	0.03	0.06	0.53	0.15	0.02	0.39
#051	1200	1170	gl	6	50.87	1.70	13.51	13.18	0.22	6.40	8.64	2.36	0.85	97.73
			σ		0.25	0.04	0.08	0.24	0.04	0.05	0.16	0.08	0.02	0.52
			pl	8	49.84	0.13	29.40	1.64	0.03	0.42	14.23	2.61	0.15	98.45
			σ		0.55	0.15	1.46	1.14	0.03	0.53	0.78	0.17	0.07	0.39
#041	1227	1170	gl	7	51.58	1.51	15.86	11.64	0.17	5.59	9.44	2.56	0.86	99.21
			σ		0.31	0.10	0.55	0.49	0.02	0.23	0.25	0.10	0.02	0.56
			pl	3	49.83	0.08	31.32	1.07	0.00	0.19	15.42	2.52	0.11	100.53
			σ		1.59	0.00	1.24	0.07	0.01	0.05	1.17	0.66	0.06	0.07
#042	1227	1170	gl	8	51.50	1.65	14.55	12.46	0.19	6.21	9.14	2.46	0.86	99.02
			σ		0.33	0.03	0.22	0.59	0.03	0.09	0.06	0.07	0.04	0.82
			pl	5	50.64	0.04	30.70	1.22	0.00	0.21	14.88	2.83	0.14	100.65
			σ		1.28	0.01	0.58	0.07	0.00	0.02	0.73	0.40	0.04	0.51
#043	1227	1170	gl	8	51.68	1.65	14.71	12.53	0.18	6.08	9.09	2.46	0.86	99.25
			σ		0.41	0.06	0.27	0.23	0.04	0.06	0.15	0.12	0.04	0.60
			pl	7	51.76	0.09	30.26	1.09	0.01	0.22	14.37	3.06	0.16	101.03
			σ		1.27	0.03	0.95	0.12	0.02	0.02	0.93	0.49	0.03	0.23
#044	1227	1170	gl	8	51.28	1.68	14.09	12.31	0.17	6.17	8.95	2.37	0.93	97.96
			σ		0.29	0.04	0.15	0.99	0.04	0.06	0.10	0.17	0.05	1.23
			pl	8	51.06	0.07	30.15	1.10	0.01	0.20	14.55	2.93	0.14	100.23
			σ		1.44	0.04	1.12	0.12	0.02	0.04	1.05	0.59	0.05	0.68
#045	1227	1170	gl	9	51.30	1.70	13.90	12.99	0.18	6.30	8.80	2.35	0.79	98.32
			σ		0.22	0.06	0.13	0.19	0.03	0.08	0.18	0.19	0.06	0.43
			pl	8	50.52	0.06	30.71	1.09	0.01	0.22	15.02	2.81	0.14	100.58
			σ		1.07	0.02	0.55	0.10	0.01	0.05	0.60	0.31	0.04	0.51
#046	1235	1170	gl	7	51.23	1.65	13.82	13.12	0.18	6.40	8.93	2.39	0.91	98.64
			σ		0.32	0.04	0.14	0.22	0.03	0.05	0.07	0.06	0.06	0.48
			pl	8	50.71	0.09	30.22	1.34	0.01	0.35	14.83	2.77	0.15	100.47
			σ		0.71	0.08	1.20	0.38	0.01	0.27	0.84	0.31	0.06	0.43

Table 6-4 (continued)

#052	1235	1170	gl	6	51.02	1.41	16.37	10.90	0.16	5.40	9.78	2.53	0.72	98.29
			σ		0.39	0.05	0.17	0.29	0.02	0.08	0.14	0.13	0.01	0.45
			pl	6	51.01	0.10	29.88	1.15	0.02	0.24	14.23	2.87	0.13	99.62
			σ		2.14	0.05	1.67	0.07	0.02	0.07	1.51	0.76	0.05	0.21
#053	1235	1170	gl	6	50.75	1.48	16.06	11.38	0.20	5.56	9.52	2.54	0.78	98.26
			σ		0.17	0.04	0.18	0.36	0.03	0.10	0.22	0.18	0.04	0.50
			pl	5	52.50	0.09	28.76	1.12	0.02	0.29	12.97	3.37	0.16	99.27
			σ		0.54	0.05	0.22	0.10	0.02	0.08	0.40	0.16	0.01	0.51
#054	1235	1170	gl	6	51.03	1.57	15.21	11.90	0.21	5.83	9.45	2.44	0.75	98.40
			σ		0.38	0.09	0.53	0.47	0.04	0.24	0.16	0.16	0.03	0.59
			pl	7	51.90	0.10	29.20	1.13	0.01	0.23	13.07	3.21	0.14	98.98
			σ		1.58	0.02	1.15	0.10	0.01	0.05	1.66	0.55	0.04	0.70
#057	1235	1170	gl	6	50.66	1.88	12.17	14.77	0.26	7.23	8.28	2.10	0.86	98.19
			σ		0.23	0.06	0.26	0.51	0.03	0.17	0.17	0.15	0.04	0.55
			pl	7	52.92	0.18	26.86	2.00	0.03	0.68	11.73	3.55	0.21	98.16
			σ		0.29	0.15	1.40	1.07	0.02	0.53	0.44	0.12	0.06	0.22
#058	1235	1170	gl	6	50.19	1.88	12.19	14.67	0.27	7.32	8.26	2.02	0.83	97.62
			σ		0.17	0.08	0.44	0.44	0.04	0.30	0.23	0.06	0.05	0.38
			pl	8	52.20	0.09	28.19	1.44	0.01	0.36	12.55	3.33	0.18	98.34
			σ		2.34	0.03	2.12	0.32	0.02	0.14	1.77	0.84	0.06	0.91
#055	1235	1170	gl	4	51.27	1.66	14.22	12.72	0.22	6.36	8.60	2.46	0.73	98.23
			σ		0.33	0.04	0.14	0.09	0.02	0.03	0.36	0.13	0.01	0.38
			pl	4	52.06	0.10	28.91	1.14	0.01	0.26	12.92	3.20	0.15	98.75
			σ		0.53	0.04	0.23	0.09	0.01	0.02	0.23	0.18	0.02	0.57
#056	1235	1170	gl	6	51.15	1.71	14.06	12.78	0.25	6.43	8.85	2.32	0.73	98.27
			σ		0.24	0.04	0.07	0.11	0.02	0.05	0.15	0.07	0.02	0.38
			pl	6	51.62	0.11	29.25	1.16	0.02	0.27	13.33	3.14	0.14	99.04
			σ		1.55	0.03	0.78	0.12	0.02	0.06	0.82	0.55	0.03	0.59

Table 6-5 Average growth rate of plagioclase microlite in the run products

No.	Temp. 1 (℃)	Temp. 2 (℃)	T1 (min)	T2 (min)	Sn (μm)	stdev	average growth rate (mm/s)
#001	1200	—	60	0	6.98	0.50	n.a.
#002	1200	1120	60	0	6.68	0.34	n.a.
#003	1200	1120	60	15	7.24	0.41	6.27E-07
#004	1200	1120	60	30	8.29	0.82	1.16E-06
#006	1200	1120	60	60	9.24	1.20	5.28E-07
#007	1200	1120	60	180	9.26	0.33	2.44E-09
#019	1220	—	60	0	7.19	2.50	n.a.
#020	1220	1120	60	0	7.62	0.68	n.a.
#021	1220	1120	60	15	8.48	0.58	9.62E-07
#022	1220	1120	60	30	9.98	1.30	1.66E-06
#023	1220	1120	60	60	10.32	0.14	1.90E-07
#024	1220	1120	60	180	11.43	0.80	1.54E-07
#025	1220	1120	60	360	13.08	1.66	1.53E-07
#026	1227	—	60	0	8.68	3.87	n.a.
#027	1227	1120	60	0	7.63	0.37	n.a.
#028	1227	1120	60	15	8.33	0.17	7.74E-07
#029	1227	1120	60	30	10.28	0.93	2.17E-06
#030	1227	1120	60	60	10.54	0.07	1.44E-07
#031	1227	1120	60	180	12.39	0.07	2.57E-07
#032	1227	1120	60	360	13.58	0.96	1.10E-07
#059	1235	—	60	0	n.a.	n.a.	n.a.
#060	1235	1120	60	0	13.34	0.51	n.a.
#062	1235	1120	60	30	31.37	10.54	n.a.
#063	1235	1120	60	60	23.40	0.27	n.a.
#064	1235	1120	60	180	24.01	1.43	n.a.
#065	1235	1120	60	360	16.11	—	n.a.
#047	1200	1170	60	0	6.43	0.89	n.a.
#048	1200	1170	60	15	7.34	0.68	1.01E-06
#049	1200	1170	60	30	7.15	0.46	n.a.
#050	1200	1170	60	60	7.95	0.73	4.44E-07
#051	1200	1170	60	180	8.08	0.72	1.83E-08
#041	1227	1170	60	0	6.69	0.54	n.a.
#042	1227	1170	60	15	7.55	0.09	9.51E-07
#043	1227	1170	60	30	8.82	0.46	1.41E-06
#044	1227	1170	60	60	10.36	0.50	8.59E-07
#045	1227	1170	60	180	10.78	1.56	5.72E-08
#046	1227	1170	60	360	10.41	0.86	n.a.
#052	1235	1170	60	0	10.03	3.01	n.a.
#053	1235	1170	60	15	15.93	6.02	6.55E-06
#054	1235	1170	60	30	18.02	3.88	2.32E-06
#057	1235	1170	60	60	19.56	0.01	8.57E-07
#058	1235	1170	60	180	20.70	0.55	1.57E-07
#055	1235	1170	60	360	21.66	4.50	8.90E-08
#056	1235	1170	60	720	21.44	2.44	n.a.

Chapter 7: Summary

1. Volume of Plinian fall deposit erupted at the 1914-1915 eruption of Sakurajima volcano is c.a. 0.72 km^3 (0.29 km^3 ;DRE). Column height was 15-18 km. Wind velocity at the eruption was 20-30 m/s from west to east. Volume eruption rate is c.a. 5×10^3 m^3/s.

2. Plinian fall deposit pumices collected at Loc. P1 are divined into two types according to the bulk density (vesicularity) and color; white pumice with low bulk density (c.a. 700 kg/m^3) deposited whole parts of the Plinian fall deposit and darker colored pumice with high density (c.a. 950 kg/m^3) deposited at upper parts of the deposit.

3. The volcanic products from the 1914-1915 eruption of Sakurajima volcano show the evidence of magma mixing; linear composition trends of whole rock and matrix glass compositions of the erupted materials, bimodal distribution of An content of plagioclase phenocrysts and Mg# content of clinopyroxene and orthopyroxene phenocrysts, and existence of dusty zoned plagioclase.

4. There are three end-member magma; felsic low temperature (988-1039 ℃) magma with sodic plagioclase and low Mg# orthopyroxene, augite phenocrusts, basic high temperature (1051-1082 ℃) magma with high An plagioclase and high Mg# orthopyroxene, augite phenocrysts , and more non-differentiation mafic end-member magma (1138-1208 ℃) with high An plagioclase, high Mg# augite and olivine phenocrysts.

5. Trigger for the eruption is an injection of more non-differentiation mafic end-member magma to the magma chamber just before the eruption. Pre-eruptive melt composition of indicate that previously mixed magma in the magma chamber erupted as Plinian fall pumice and Taisho 1 lava. Newly injected mafic magma mixed with previously mixed magma and erupted as Taisho 2 and Taisho 2' lava. Difference of bulk density (vesicularity) between white pumice and darker colored pumice erupted during the Plinian phase is a result of the difference of decompression rate.

6. Plinian fall pumices divided into three types in terms of vesicularity and

plagioclase microlite textures. Type-1 pumice is white pumice with high vesicularity, low modal content and number density of plagioclase microlite. Type-2 pumice is white pumice with high vesicularity, middle modal content and number density of plagioclase microlite. Type-3 pumice is darker colored pumice with low vesicularity, high modal content and number density of plagioclase microlite.

7. Textural differences of vesicularity and plagioclase microlite of Plinian fall pumice are due to the difference of decompression rate. Type-1 and type-2 pumice mainly deposited in the lower to middle parts of the deposit, indicating that decompression rate of magma during early to middle stage of Plinian phase of the eruption. Proportion of type-1 and type-2 white pumices decrease and that of type-3 darker colored pumice increase in the upper part of the deposit, implying that decompression rate of magma decrease in the late stage of Plinian phase of the eruption. Difference of microlite texture between type-1 and type-2 in early to middle stage and between type-1, -2 pumice and type-3 pumice in the late stage of Plinian phase reflects the slightly difference of magma ascent rate, perhaps the difference of center and near the margin of conduits.

8. 1-atmosphere closed system melting/crystallization experiment by using basaltic magma erupted at the 1707 eruption reveal that crystallization processes of plagioclase microlite are divided into two processes: the first is nucleation process and the second is growth process of nucleated crystals. Duration of nucleation process changes in response to initial melting temperature.

9. Initial melting and final crystallization temperature affect the number density and modal content of plagioclase microlite in the run products.

10. Linear correlation between logarithms of population density and crystal size in closed system melting/crystallization experiments is due to nucleation interval, growth dispersion and size-dependent growth of nucleated crystals.

11. During nucleation-dominated crystallization process, intercept of CSD increase due to nucleation, resulting in steep slope of CSDs. Size dependent-growth of nucleated crystals and growth dispersion of nucleated crystals taking place during growth-dominated crystallization process cause the decrease in intercept of CSDs and

gentler slope of CSDs.

References

Amma-Miyasaka. M. and Nakagawa. M. (2002) Origin of anorthite and olivine megacrysts in island-arc tholeiites: petrological study of 1940 and 1962 ejecta from Miyake-jima volcano, Izu-Mariana arc. J. Volcanol. Geotherm. Res., **117**, 263-283.

Aramaki, S. (1975) Classification and mechanism of volcanic eruption. Bull. Volcanol. Soc. Japan, **20**, 205-221 (in Japanese with English abstract).

Aramaki, S. (1984) Formation of the Aira Caldera, southern Kyushu, 22,000 years ago. J. Geophys. Res., **89**, 8485-8501.

Armienti, P., Pareschi, M. T., Innocenti, F. and Pompilio, M. (1994) Effect of magma storage and ascent on the kinetics of crystal growth. Contrib. Mineral. Petrol., **115**, 402-414.

Blake, S. (1981) Volcanism and dynamics of open magma chamber. Nature, **289**, 783-785.

Blake, S. and Ivey, G. N. (1986) Density and viscosity gradients in zoned magma chambers, and their influence on withdrawal dynamics. J. Volcanol. Geotherm. Res., **30**, 201-230.

Blower. J. D., Keating, J. P., Mader, H. M. and Phillips, J. C. (2001) Inferring volcanic degassing processes from vesicle size distributions. Geophys. Res. Lett., **28**, 347-350.

Blower. J. D., Keating, J. P., Mader, H. M. and Phillips, J. C. (2002) The evolution of bubble size distribution in volcanic eruption. J. Volcanol. Geotherm. Res., **120**, 1-23.

Boorman, S., Boorman, A. and Kruger, F. J. (2004) The lower zone-critical zone transition of the Bushveld complex: a quantitative textural study. J. Petrol., **45**, 1209-1235.

Burkhard, D. J. M. (2002) Kinetics of crystallization: example of micro-crystallization in basalt lava. Contrib. Mineral. Petrol., **142**, 724-737.

Campbell, I. H. and Turner, J. S. (1989) Fountains in magma chambers. J. Petrol., **30**,

885-923.

Carey, S. and Sparks, R. S. J. (1986) Quantitative models of the fallout and dispersal of Tephra from volcanic eruption columns. Bull. Volcanol., **48**, 109-125.

Cashman, K. V. (1988) Crystallization of Mount St. Helens 1980-1986 dacite: A quantitative textural approach. Bull. Volcanol., **50**, 194-209.

Cashman, K. V. (1990) Textural constraints on the kinetics of crystallization of igneous rocks. Rev. Mineral., **24**, 259-314.

Cashman, K. V. (1992) Groundmass crystallization of Mount St. Helens dacite, 1980-1986: a tool for interpreting shallow magmatic processes. Contrib. Mineral. Petrol., **109**, 431-449.

Cashman, K. V. and Ferry, J. M. (1988) Crystal size distribution (CSD) in rocks and kinetics and dynamics of crystallization Ⅲ. Metamorphic crystallization. Contrib. Mineral. Petrol., **99**, 401-415.

Cashman, K. V. and Marsh, B. D. (1988) Crystal size distribution (CSD) in rocks and kinetics and dynamics of crystallization Ⅱ. Makaopuhi lava lake. Contrib. Mineral. Petrol., **99**, 292-305.

Clynne, M. A. (1999) A complex magma mixing origin for rocks erupted in 1915, Lassen Peak, California. J. Petrol., **40**, 105-132.

Coombs, M. L., Eichelberger, J. C. and Rutherford, M. J. (2002) Experimental and textural constraints on mafic enclave formation in volcanic rocks. J. Volcanol. Geotherm. Res., **119**, 125-144.

Couch, S. (2003) Experimental investigation of crystallization kinetics in haplogranite system. Am. Mineral., **88**, 1471-1485.

Couch, S., Sparks R. S. J. and Carroll, M. R. (2003) The kinetics of degassing-induced crystallization at Soufrière Hills Volcano, Montserrat. J. Petrol., **44**, 1477-1502.

Crisp, J., Cashman, K. V., Bonini, J. A., Hougen, S. B. and Pieri, D. C. (1994) Crystallization history of the 1984 Mauna Loa lava flow. J. Geophys. Res., **99**, 7177-7198.

Donaldson, C. H., Williams, R. J. and Lofgren, G. (1975) A sample holding technique

for study of crystal growth in silicate melts. Am. Mineral., **60**, 324-326.

Draper, D. S. and Johnston, A. D. (1992) Anhydrous PT phase relations of an Aleutian high-MgO basalt: an investigation of the role of olivine-liquid reaction in generation of arc high-alumina basalts. Contrib. Mineral. Petrol., **112**, 501-519.

Eberl, D. D., Drits, V. A. and Srodon, J. (1998) Deducing growth mechanisms for minerals from the shape of crystal size distributions. Amer. J. Sci., **298**, 499-533.

Eichelberger, J. C., Carrigan, C. R., Westrich, H. R. and Price, R. H. (1986) Non-explosive silicic volcanism. Nature, **323**, 598-602.

Folch, A. and Marti, J. (1998) The generation of overpressure in felsic magma chamber by replenishment. Earth Planet. Sci. Lett., **163**, 301-314.

Fukuyama, H. (1978) Geology of Sakurajima volcano, southern Kyushu. Jour. Geol. Soc. Japan, **84**, 309-316 (in Japanese with English abstract).

Fukuyama, H. and Ono, K. (1981) Geological map of Sakurajima volcano 1:25,000. Geological Survey of Japan., **1**, 1-8 (in Japanese with English abstract).

Gardner, C. A., Cashman, K. V. and Neal, C. A. (1998) Tephra-fall deposits from the1992 eruption of Crater Peak, Alaska: implications of clast textures for eruption processes. Bull. Volcanol., **59**, 537-555.

Geschwind, C. H. and Rutherford, M. J. (1995) Crystallization of microlite during magma ascent: the fluid mechanics of 1980-1986 eruptions at Mount St. Helens. Bull. Volcanol., **57**, 356-370.

Gill, J. B. (1981) Orogenic andesite plate tectonics. Springer-Verg, P390.

Grove, T. L., Gerlach, D. C. and Sando, T. W. (1982) Oriigin of calc-alkaline series lavas at Medicine Lake volcano by fractionation, assimilation and mixing. Contrib. Mineral. Petrol., **80**, 160-182.

Grove, T. L. and Juster, T. C. (1989) Experimental investigations of low-Ca pyroxene stability and olivine-pyroxene-liquid equilibria at 1-atm in natural basaltic and andesitic liquids. Contrib. Mineral. Petrol., **103**, 287-305.

Gurioli, L., Houghton, B. F., Cashman, K. V. and Cioni, R. (2005) Complex changes in

eruption dynamics during the 79 AD eruption of Vesuvius. Bull. Volcanol., **67**, 114-159.

Hammer, J. E., Cashman, K. V., Hoblitt, R. P. and Newman, S. (1999) Degassing and microlite crystallization during pre-climactic events of the 1991 eruption of Mt. Pinatubo, Philippines. Bull. Volcanol., **60**, 355-380.

Hammer, J. E. and Rutherford, M. J. (2002) An experimental study of the kinetics of decompression-induced crystallization in silicic melt. J. Geophys. Res., **107**, 1-24.

Hara, I. (1991) 1-atmosphere experiment on the 1707 basalt of Fuji volcano. pp.43, MS Thesis, Hiroshima University, Hiroshima, Japan.

Hayakawa, Y. (1985) Pyroclastic geology of Towada volcano. Bull. Earthq. Res Inst., Tokyo University, **60**, 507-592

Higgins, M. D. (1994) Numerical modeling of crystal shapes in thin sections: Estimation of crystal habit and true size. Am. Mineral., **79**, 113-119.

Higgins, M. D. (1996a) Magma dynamics beneath Kameni volcano, Thera, Greece, as revealed by crystal size and shape measurements. J. Volcanol. Geotherm. Res., **58**, 194-204.

Higgins, M. D. (1996b) Crystal size distributions and other quantitative textural measurements in lavas and tuff from Egmont volcano (Mt. Taranaki), New Zealand. Bull. Volcanol., **60**, 355-380.

Higgins, M. D. (1998) Origin of anorthosite by textural coarsening: Quantitative measurements of a natural sequence of textural development. J. Petrol., **39**, 1307-1323.

Higgins, M. D. (2000) Measurement of crystal size distributions. Am. Mineral., **85**, 1105-1116.

Higgins, M. D. (2002) A crystal size-distribution study of the Kiglapait layered mafic intrusion, Ladrador, Canada: evidence for textural coarsening. Contrib. Mineral. Petrol., **144**, 314-330.

Higgins, M. D. and Roberge, J. (2003) Crystal size distribution of plagioclase and amphibole from Soufriere Hills volcano, Montserrat: Evidence for dynamic

crystallization-textural coarsening cycles. J. Petrol., **44**, 1401-1411.

Hoblitt, R. P. and Harmon, R. S (1993) Bimodal density distribution of cryptodome dacite from the 1980 eruption of Mount St. Helens, Washington. Bull. Volcanol., **55**, 421-437.

Houghton, B. F. and Wilson, C. J. N. (1989) A vesicularity index for pyroclastic deposits. Bull. Volcanol., **51**, 451-462.

Huebner, J. S. (1982) Use of gas mixtures at low pressure to specify oxygen and other fugacities of furnace atmospheres. In hydrothermal experimental techniques (Ulmer, G. C. and Barnes, H. L. Eds.) John Wiley and Sons, New York, 20-60.

Huppert, H. E., Sparks, R. S. J., and Turner, J. S. (1982) Effect of volatiles on mixing in calc-alkaline magma systems. Nature, **297**, 554-557.

Ishihara, K. (1988) Geophysical evidence on the existence of magma reservoir and conduit at Sakurajima volcano, Japan. Ann. Disast. Prevent. Res. Inst. Kyoto Univ., **31(B-1)**. 59-73 (in Japanese with English abstract).

Ishihara, K. (1991) Pressure sources and induced ground deformation associated with explosive eruptions at an andesitic volcano: Sakurajima volcano, Japan. In "Magma Transport and Strage" (Ryan, M. P. ed.), 335-356, John Wiley and Sons.

Ishihara, K. (1995) Forecast of volcanic activity of Sakurajima volcano. Monthly Science, **65**, 707-710 (in Japanese).

Ishihara, K., Takayama, T., Tanaka, Y. and Hirabayashi, J. (1981) Lava flows at Sakurajima volcano (I), volume of the historical lava flows. Ann. Disast. Prevent. Res. Inst. Kyoto Univ., **24(B-1)**. 1-10 (in Japanese with English abstract).

Ishihara, K., Iguchi M. and Kamo K. (1985) Lava flows at Sakurajima volcano (II), Numerical simulation of the 1914 lava flows on the western side of Sakurajima. Ann. Disast. Prevent. Res. Inst. Kyoto Univ., **28(B-1)**. 1-11 (in Japanese with English abstract).

Jaupart, C. and Tait, S. (1990) Dynamics of eruption phenomena. In: Nicholls. J. and Russell, J. K. (ed) Modern methods of igneous petrology: understanding

magmatic processes, Rev Mineral., **24**, 213-238.

Jaupart, C. and Allègre, C. J. (1991) Gas content, eruption rate and instabilities of eruption regime in silicic volcanoes. Earth Planet. Sci. Lett., **102**, 413-429.

Jerram, D. A., Cheadle, M. J. and Philpotts, A. R. (2003) Quantifying the building blocks of igneous rocks: Are clustered crystal frameworks the foundation? J. Petrol., **44**, 2033-2051.

Kawamoto, T. (1992) Dusty and honeycomb plagioclase: indicators of processes in the Uchino stratified magma chamber, Izu Peninsula, Japan. J. Volcanol. Geotherm. Res., **49**, 191-208.

Klug, C. and Cashman, K. V. (1994) Vesiculation of May 18, 1980, Mount St. Helens magma. Geology, **22**, 468-472.

Klug, C., Cashman, K. V. and Bacon, C. R. (2002) Structure and physical characteristics of pumice from the climactic eruption of Mount Mazama (Crater Lake), Oregon. Bull. Volcanol., **64**, 486-501.

Kobayashi, T. (1982) Geology of Sakurajima volcano: A review. Bull. Volcanol. Soc. Japan, **27**, 277-292 (in Japanese with English abstract).

Kobayashi, T. (1986) Formation and pyroclastic flow of Sakurajima volcano. Report of research project "Characteristics and disaster of volcanic dry pyroclastic flows. (leader Aramaki, S.) (Monbu Kagakusyou) (In Japanese), 137-163.

Koyaguchi, T. (1986) Mixing mechanism of mafic and felsic magmas – Origin of heterogeneous magmas -. Bull. Volcanol. Soc. Japan, **30**, 41-54. (in Japanese with English abstract)

Koto, B. (1916) The great eruption of Sakurajima in 1914. Journal of College of Science, Imperial University of Tokyo, **38**, 1-237.

Lange, R. L. and Carmichael, I. S. E. (1990) Thermodynamic properties of silicate liquids with emphasis on density, thermal expansion and compressibility. In: Nicholls. J. and Russell, J. K. (ed) Modern methods of igneous petrology: understanding magmatic processes, Rev Mineral., **24**, 25-64.

Lindsley, D. H. and Frost, B. R. (1992) Equilibria among Fe-Ti oxides, pyroxenes, olivine, and quartz: Part Ⅰ. Theory. Am. Mineral., **77**, 987-1003.

Loucks. R. R. (1996) A precise olivine-augite Mg-Fe exchange geothermometer. Contrib. Mineral. Petrol., **125**, 140-150.

Mangan, M. T. (1990) Crystal size distribution systematics and the determination of magma storage times: The 1959 eruption of Kilauea volcano, Hawaii. J. Volcanol. Geotherm. Res., **44**, 295-302.

Mangan, M. T., Cashman, K. V., and Newman, S. (1993) Vesiculation of basaltic magma during eruption. Geology, **21**, 157-160.

Mangan, M. T. and Cashman, K. V. (1996) The structure of basaltic scoria and reticulite and inferences for vesiculation, foam formation, and fragmentation in lava fountains. J. Volcanol. Geotherm. Res., **73**, 1-18.

Marsh, B. D. (1988) Crystal size distribution (CSD) in rocks and the kinetics and dynamics of crystallization I . Theory. Contrib. Mineral. Petrol., **99**, 277-291.

Marsh, B. D. (1998) On the interpretation of crystal size distributions in magmatic systems. J. Petrol., **39**, 553-599.

Martel, C., Bourdier, J. L., Pichavant, M. and Traineau, H. (2000) Textures, water content and degassing of silicic andesites from recent Plinian and dome-forming eruptions at Mount Pelèe volcano (Martinique, Lesser Antilles arc). J. Volcanol. Geotherm. Res., **96**, 191-206.

Martel, C. and Schmidt, B. C. (2003) Decompression experiments as an insight into ascent rates of silicic magmas. Contrib. Mineral. Petrol., **144**, 397-415.

McCabe, W. L. (1929) Crystal growth in aqueous solutions. Industrial Engineering Chemistry, **21**, 30-33.

Meen, J. K. (1990) Elevation of potassium content of basaltic magma by fractional crystallization: the effect of pressure. Contrib. Mineral. Petrol., **104**, 309-331

Miyashiro, A. (1974) Volcanic rock series in island arcs and active continental margins. Amer. J. Sci., **274**, 321-355.

Miyazaki, K. (1991) Ostwald ripening of garnet in high P/T metamorphic rocks. Contrib. Mineral. Petrol., **108**, 118-128.

Miyazaki, K. (1996) A numerical simulation of textural evolution due to Ostwald ripening in metamorphic rock: A case for small amount of volume of dispersed

crystals. Geochim. Cosmochim, Acta, **60**, 277-290.

Mock, A., Jerram, D. A. and Breitkreuz, C. (2003) Using quantitative textural analysis to understand the emplacement of shallow level rhyolitic laccoliths- a case study from the Halle volcanic complex, Germany. J. Petrol., **44**, 833-849.

Mogi, K. (1958) Relations between the eruptions of various volcanoes and the deformation of the ground surfaces around them. Bull. Earthq. Res. Inst. Univ. Tokyo, **36**, 99-134.

Moore, G., Vennemann, T. and Carmichael, I. S. E. (1998) An empirical model for solubility of H_2O in magmas to 3 kilobars. Am. Mineral., **83**, 36-42.

Morishita. R. (1992) Crystal Size Distribution of Togawa andesite lava. Bull. Volcanol. Soc. Japan, **37**, 285-293. (in Japanese with English abstract)

Morishita. R. (1995) The CSD theory and some problems with its application to volcanic rocks. Journal of Mineralogical society of Japan, **24**, 101-105. (in Japanese with English abstract)

Morrissey, M. M. (1997) Long-period seismicity at Redoubt volcano, Alaska, 1989-1990 related to magma degassing. J. Volcanol. Geotherm. Res., **75**, 321-335.

Murphy, M. D., Sparks, R. S., Barclay, L., Carroll, M. R., Lejeune, A. M., Brewer, T. S., Macdonald, R., Black, S. and Young, S. (1998) The role of magma mixing in triggering the current eruption at the Soufriere Hills volcano, Montserrat, West Indies. Geophys. Res. Lett., **25**, 3433-3436.

Murphy, M. D., Sparks, R. S., Barclay, L., Carroll, M. R. and Brewer, T. S. (2001) Remobilization of andesite magma by intrusion of mafic magma at Soufriere Hills volcano, Montserrat, West Indies. J. Petrol., **41**, 21-42.

Nakagawa, M., Wada, K. and Wood, C. P. (2002) Mixed magmas, mush chambers and eruption trigger: Evidence from zoned clinopyroxene phenocrysts in andesitic scoria from the 1995 eruptions of Ruapehu volcano, New Zealand. J. Petrol., **43**, 2279-2303.

Nagaoka, S., Okuno, M. and Arai, F. (2001) Tephrostratigraphy and eruptive histry of the Aira caldera volcano during 100-30 ka, Kyushu, Japan. Jour. Geol. Soc.

Japan, **107**, 432-450.

Nakamura, M. and Simakita, S. (1998) Dissolution origin and syn-entrapment compositional change of melt inclusion in plagioclase. Earth Planet. Sci. Lett., **161**, 119-133.

Nishiyama, T. (1991) Pattern formation due to uphill diffusion. Monthly Earth, **13**, 311-319 (in Japanese).

Okuno, M. (2002) Chronology of Tephra Layers in Southern Kyushu, SW Japan, for the last 30,000 years. The Quaternary research, **41**, 225-236 (in Japanese with English abstract).

Okuno, M., Nakamura, T., Moriwaki, H. and Kobayashi, T. (1997) AMS radiocarbon dating of the Sakurajima tephra group, southern Kyushu, Japan. Nuclear Instruments and Methods in Physics Research, **B123**, 470-474.

Omori, F. (1916) Sakurajima eruptions and earthquakes II. Bull. Imp. Earthq. Com., **8**, No.2.

Peterson, T. D. (1996) A refined technique for measuring crystal size distributions in thin section. Contrib. Mineral. Petrol., **124**, 395-405.

Petrik, I., Nabelek, P. I., Janak, M. and Plasienka, D. (2003) Conditions of formation and crystallization kinetics of highly oxidized pseudotachylytes from the High Tatras (Slovakia). J. Petrol., **44**, 901-927.

Polacci. M., Papale, P. and Rosi, M. (2001) Textual heterogeneities in pumices from the climactic eruption of Mount Pinatubo, 15 June 1991, and implications for magma ascent dynamics. Bull. Volcanol., **63**, 83-97.

Presnall, D. C. and Brenner, N. L. (1974) A method for studying iron silicate liquidus under reducing conditions with negligible iron loss. Geochim. Cosmochim, Acta, **33**, 1785-1788.

Randolph, A. D. and Larson, M. A. (1971) Theory of particulate processes. New York: Academic Press, 251 pp.

Resmini, R. G. and Marsh, B. D. (1995) Steady-state volcanism, paleoeffusion rates, and magma system volume inferred from plagioclase crystal size distributions in mafic lavas: Dome Mountain, Nevada. J. Volcanol. Geotherm. Res., **68**,

273-296.

Saharigan, D. L. and Proussevith, A. A. (1998) 3D particle size distributions from 2D observations: stereology for natural applications. J. Volcanol. Geotherm. Res., **84**, 173-196.

Sakuyama, M. (1979) Evidence of magma mixing: petrological study of Shirouma-Oike calc-alkaline andesitic volcano, Japan. J. Volcanol. Geotherm. Res., **5**, 179-208.

Sakuyama, M. (1981) Petrological study of the Myoko and Kurohime volcanoes, Japan: Crystallization sequence and evidence for magma mixing. J. Petrol., **22**, 553-583.

Sato, H. (1995) Textural difference between pahoehoe and aa lavas of Izu-Oshima volcano, Japan - an experimental study on population density of plagioclase. J. Volcanol. Geotherm. Res., **66**, 101-113.

Sekine, T., Katsura, T. and Aramaki, S. (1979) Waters saturated relations of some andesites with application to the estimation of the initial temperature and water pressure at the time of eruption. Geochim. Cosmochim, Acta, **43**, 1367-1376.

Simakin, A. and Botcharnikov, R. (2001) Degassing of stratified magma by compositional convection. J. Volcanol. Geotherm. Res., **105**, 207-224.

Simakin, A. G., Armienti, P. and Epel'baum, M. B. (1999) Coupled degassing and crystallization: experimental study at continuous pressure drop, with application to volcanic bomb. Bull. Volcanol., **61**, 275-287.

Sisson, T. W. and Grove, T. L. (1993) Experimantal investigations of role of H_2O in calc-alkaline differentiation and subduction zone magmatism. Contrib. Mineral. Petrol., **113**, 143-166.

Snyder, D. S. and Tait, S. (1996) Magma mixing by convective ebtrainment. Nature, **379**, 529-531.

Solomatov, V. S. (1995) Batch Crystallization under continuous cooling: Analytical solution for diffusion limited crystal growth. J. Cryst. Growth, **148**, 412-431.

Sparks, R. S. J. (1978) The dynamics of bubble formation and growth in magmas: A review and analysis. J. Volcanol. Geotherm. Res., **3**, 1-37.

Sparks, R. S. J. (1986) The dimensions and dynamics of volcanic eruption columns. Bull. Volcanol., **48**, 3-15.

Sparks, R. J., Sigurdsson, H. and Wilson, L. (1977) Magma mixing: a mechanism for triggering acid explosive eruptions. Nature, **267**, 315-318.

Suzuki, T., Sato, H. and Suzuki-Kamata, K. (1999) Relation between crater size and eruption rate for three recent eruptions of Kirishima volcano, Japan. Akiyama, M. edit., "Dynamics of vaper explosions", March, 1998, 21-19.

Suzuki, Y. and Nakada, S. (2002) Vesiculation and magma ascent process in the Usu 2000 eruption, inferred from texture and size distribution of bubble. Bull. Volcanol. Soc. Japan, **47**, 675-688 (in Japanese with English abstract).

Swanson, S. E. (1977) Relation of nucleation and crystal-growth rate to the development of granitic textures. Am. Mineral., **62**, 966-978.

Takahashi, E. and Takahashi, M. (1995) What determines the structure beneath the arc-volcano? Monthly Science, **65**, 638-647 (in Japanese).

Takahashi M., Otsuka T., kawamata H. and Kobayashi T. (2001) Petrologic model for magma plumbing system of Sakurajima volcano. Abstract of Volcanological Society of Japan, PP9 (in Japanese).

Taddeucci, J., Pompilio, M. and Scarlato, P. (2004) Conduit processes during the July-August 2001 explosive activity of Mt. Etna (Italy): inferences from glass chemistry and crystal size distribution of ash particles. J. Volcanol. Geotherm. Res., **137**, 33-54.

Takeuchi, S. and Nakamura, M. (2001) Role of precursory less-viscous mixed magma in the eruption of phenocryst-rich magma: evidence from the Hokkaido-Komagatake 1929 eruption. Bull. Volcanol., **63**, 365-376.

Tait, S., Jaupart, C. and Vergniolle, S. (1989) Pressure, gas content and eruption periodicity of shallow crystallizing magma chamber. Earth Planet. Sci. Lett., **92**, 107-123.

Tomiya, A. and Takahashi, E. (1995) Reconstruction of an evolving magma chamber beneath Usu volcano since the 1663 eruption. J. Petrol., **36**, 617-636.

Toramaru, A. (1990) Measurement of bubble size distributions in vesiculated rock with

implications for quantitative estimation of processes. J. Volcanol. Geotherm. Res., **43**, 71-90.

Toramaru, A. (1991) Model of nucleation and growth of crystals in cooling magmas. Contrib. Mineral. Petrol., **108**, 106-117.

Toramaru, A. (1995) Numerical study of nucleation and growth of bubbles in viscous magmas. J. Geophys. Res., **100**, 1913-1931.

Toramaru, A. (2001) A numerical experiment of crystallization for binary eutectic system with application to igneous textures. J. Geophys. Res., **106**, 4037-4060.

Tsune, A. and Toramaru, A. (2004) Magmatic differentiation process inferred from plagioclase zoning and its pattern. Bull. Volcanol. Soc. Japan, **49**, 249-266 (in Japanese with English abstract).

Tuchiyama, A. (1983) Crystallization kinetics in the system $CaMgSi_2O_6$-$CaAl_2Si_2O_8$: the delay in nucleation of diopside and anorthite. Am. Mineral., **68**, 687-698.

Tuchiyama, A. (1985) Dissolution kinetics of plagioclase in the melt of the system diopside-albite-anorthite, and origin of dusty plagioclase in andesites. Contrib. Mineral. Petrol., **89**, 1-16.

Uto, K., Miki, D., Nguyen, H., Suto, M., Fukushima, D. and Ishihara, K. (2005) Temporal evolution of magma composition in Sakurajima volcano, Southwest Japan. Ann. Disast. Prevent. Res. Inst. Kyoto Univ., **48(B-1)**. (in press) (in Japanese with English abstract).

Venezky, D. Y. and Rutherford, M. J. (1997) Preeruption conditions and timing of dacite-andesite magma mixing in the 2.2 ka eruption at Mount Rainier. J. Geophys. Res., **102**, 20069-20086.

Waters, C. and Boudreau, A. E. (1996) A reevaluation of crystal-size distributions in chromite cumulates. Am. Mineral., **81**, 1452-1459.

Webber, K. L., Simmons, W. B., Falster, A. U. and Foord, E. E. (1999) Cooling rates and crystallization dynamics of shallow level pegmatite-apatite dikes, San Diego County, California. Am. Mineral., **84**, 708-717.

Westrich, H. R. and Eichelberger, J. C. (1994) Gas transport and bubble collapse in rhyolitic magma: an experimental approach. Bull. Volcanol., **56**, 447-458.

Wilhelm, S. and Worner,G. (1996) Crystal size distribution in Jurassic Ferrar flows and sills (Victoria Land, Antarctica): evidence for processes of cooling, nucleation, and crystallization. Contrib. Mineral. Petrol., **125**, 1-15.

Wilkin, R. T., Barnes, H. L. and Brantley, S. L. (1996) The size distribution of framboidal pyrite in modern sediments: An indicator of redox conditions. Geochim. Cosmochim, Acta, **60**, 3897-3912.

Yamashina, K. (2001) Eruptive activity of Sakurajima volcano in terms of magma strage and discharge. Abstract of Volcanological Society of Japan, PP10 (in Japanese).

Yanagi, T., Ichimaru, Y. and Hirahara, S. (1991) Petrochemical evidence for coupled magma chambers beneath the Sakurajima volcano, Kyushu, Japan. Geochemical Journal, **25**, 17-30.

Yamada, R. and Sato, H. (1998) Petrology of glassy rocks from Takamatsu crater, Kagawa prefecture, Japan. J. Mineral. Petrol. Eco. Japan, **93**, 279-290 (in Japanese with English abstract)

Yasui, M. (1995) Magma mingling recorded in "B-scoria fall deposit" from Maekake stage, Asama volcano. J. Japan. Assoc. Mineral. Petrol. Econ. Geol., **89**, 439-453.

Yasui, M. (2001a) Contrastive eruptive style occurred on the western flank and the eastern flank in the 1914 eruption of Sakurajima volcano. Abstract of Volcanological Society of Japan, PP8 (in Japanese).

Yasui, M. (2001b) Occurrence of the eruptive products of the 1914 eruption of Sakurajima volcano. Abstract of Volcanological Society of Japan, PP130 (in Japanese).

Yasui, M. (2005) Eruptive style and its temporal variation through the 1914-1915 eruption Sakurajima volcano, southern Kyushu, Japan. Abstract of Volcanological Society of Japan, PP24 (in Japanese).

Yaasui, M. and Suganuma, Y. (2003) Broken texture of free crystals contained in pumice fall deposits. Bull. Volcanol. Soc. Japan, **48**, 221-227 (in Japanese with English abstract).

Yokoyama, I. (1971) A model for the crustal deformations around volcanoes. J. Phys. Earth., Vol. **19**, PP199-207.

Yokoyama, I. (1986) Crustal deformation caused by the 1914 eruption of Sakurajima volcano, Japan and its secular changes. J. Volcanol. Geotherm. Res., **30**, 283-302.

Zeh, A. (2004) Crystal size distribution (CSD) and textural evolution of accessory apatite, titanite and allanite during four stage of metamorphism: an example from the Moine supergroup, Scotland. J. Petrol., **45**, 2102-2132.

Zeig, M. J. and Marsh, B. D. (2002) Crystal size distributions and scaling laws in the quantification of igneous textures. J. Petrol., **43**, 85-101.

Appendix Results of caluibration of oxygen fugacity

Temp. (℃)	H_2 (ml/min)	CO_2 (ml/min)	H_2 : CO_2	starting material	
				Ni	NiO
1225	10	500	1: 50	NiO	
1225	10	400	1: 40	NiO	
1225	10	300	1: 30	Ni	
1225	10	350	1: 35	NiO	
1120	10	425	1: 42.5	Ni	Ni
1120	10	375	1: 37.5	Ni	Ni
1120	5	500	1: 100	NiO	NiO
1120	7	500	1: 83	NiO	NiO
1120	9	500	1: 56	NiO	NiO
1120	10	500	1: 50	NiO	NiO
1120	10	475	1: 47.5	NiO	NiO
1120	10	425	1: 42.5	Ni	Ni
1225	10	350	1: 35	NiO	NiO
1225	10	300	1: 30	Ni	Ni